Τμήμα Φυσικής
Σχολή Θετικών και Τεχνολογικών Επιστημών
Πανεπιστήμιο Κρήτης

Μελέτη ατομικών διεγέρσεων δέσμης ηλιοειδών ιόντων C^{4+} και O^{6+} σε κρούσεις με στόχους He

Διδακτορική Διατριβή

Άγγελος Λαουτάρης

Επιβλέπων: Καθ. Θεόδωρος Τζούρος, Πανεπιστήμιο Κρήτης

Ηράκλειο, 2024

Department of Physics
School of Sciences and Engineering
University of Crete

Excitation of heliumlike C^{4+} and O^{6+} projectile ions in collisions with He targets

Ph.D. Dissertation

Angelos Laoutaris

Supervisor: Prof. Theo Zouros, University of Crete

Heraklion, 2024

Approved by

Date of Signature

Theo J. M. Zouros, Professor, University of Crete
Thesis Supervisor

Emmanouil P. Benis, Associate Professor, University of Ioannina
Thesis Committee member

Anastasios Lagoyannis, Director of Research, NCSR "Demokritos"
Thesis Committee member

Theodore - Peter Rakitzis, Professor, University of Crete
Thesis Committee member

Iannis Kominis, Associate Professor, University of Crete
Thesis Committee member

Dionysis Antypas, Assistant Professor, University of Crete
Thesis Committee member

Alain Dubois, Professor, Sorbonne Universitè, Paris
Thesis Committee member

To my parents Dimitris and Popi.

七転び八起き

(“Nanakorobi yaoki”)

Fall down seven times, stand up eight.

Contents

List of Figures

List of Tables

Acknowledgments

This work was completed not only through my own effort, but also due to the help of many people who I would like to thank. First of all, I would like to thank my supervisor Prof. Theo Zouros for his tutoring, support, trust and friendly attitude all these years. It is his extended knowledge on atomic physics and in physics overall, his passion for experiments, focus on detail and balanced lifestyle that inspired and tutored me all these years to do my best every single day in the laboratory, while enjoying this "journey".

Secondly, I have to express my gratitude to the other two members of my advisory committee Prof. Emmanouil Benis, for his transmission of knowledge on ion-atom collision physics and experimental method, and Dr. Anastasios Lagoyannis for all these years of co-operation and guidance in the tandem accelerator laboratory since 2013 when I first started working there as an intern student.

Furthermore, I want to thank Prof. Alain Dubois for his contribution to this thesis by performing the theoretical calculations matching the experimental data together with his student Dr. Stylianos Passalidis as well as Profs. Nicolas Sisourat and Brett DePaola for valuable discussions.

Especially, I have to acknowledge the support of Dr. Sotirios Harissopulos all these years and for giving me the opportunity to work at the CALIBRA project.

Furthermore, I want to give credit to my co-workers in the atomic physics team all these years, Dr. Ioannis Madesis, Dr. Stefanos Nanos and M.Sc. student Andreas Biniskos, and in the TANDEM accelerator laboratory Dr. Michail Axiotis, Miltiades Andrianis, Vasilis Andreopoulos and Manos Tsompanakis for the co-operation, exchange of knowledge and help during my studies.

Furthermore, I want to thank Dr. Athanasios Stamatopoulos for our fruitful conversations that inspired me to take my studies a step further.

Last, but not least, I would like to thank my companion Anastasia, her parents Ioannis and Eirini and my parents Dimitris and Popi, for their love and support all these years.

Funding

This work has been recently supported by the grant Cluster of Accelerator Laboratories for Ion-Beam Research and Applications - CALIBRA (MIS 5002799) which is implemented under the Action “Reinforcement of the Research and Innovation Infrastructure”, funded by the Operational Programme Competitiveness, Entrepreneurship and Innovation (NSRF 2014-2020) and co-financed by Greece and the European Union (European Regional Development Fund).

Additionally, this project was originally (2009-2013) co-financed by the European Union (European Social Fund-ESF) and Greek national funds through the Operational Program Education and Lifelong Learning of the National Strategic Reference Framework (NSRF)-Research Funding Program: THALES. Investing in knowledge society through the European Social Fund (Grant No. MIS 377289).

I also acknowledge support by the project “IKYDA2020" of the IKY-DAAD Greek-German collaboration.

Abstract

Using the APAPES (Atomic Physics with Accelerators: Projectile Electron Spectroscopy) project zero-degree Auger projectile spectrograph setup and the C^{4+} and O^{6+} He-like ion beams supplied by the 5.5 MV "Demokritos" tandem Van de Graaff accelerator, K-Auger projectile electron spectra measurements were performed, for 0.5-1.5 MeV/u collisions with He gas targets. He-like beams in general contain a mixture of $1s^2\,{}^1S$, $1s2s\,{}^1S$ and $1s2s\,{}^3S$ components, so all three initial channels are considered. In particular, this work focuses on the following two collision processes:

$$\mathrm{X}^{q+}(1s^2) + \mathrm{He} \rightarrow \mathrm{X}^{(q+1)+}(1s2p^2\,{}^2D) + \mathrm{He}^{+}(\mathrm{All}) \quad \text{(Transfer-Excitation)} \tag{1}$$

$$\hookrightarrow \mathrm{X}^{q+}(1s^2) + e_A^{-}(\theta = 0^\circ) \tag{2}$$

and

$$\mathrm{X}^{q+}(1s^2, 1s2s\,{}^{3,1}S) + \mathrm{He} \rightarrow \mathrm{X}^{q+}(2s2p\,{}^{3,1}P) + \mathrm{He}(\mathrm{All}) \qquad \text{(Projectile Excitation)} \tag{3}$$

$$\hookrightarrow \mathrm{X}^{(q-1)+}(1s) + e_A^{-}(\theta = 0^\circ) \tag{4}$$

where X^{q+} refers to carbon C^{4+} or oxygen O^{6+} projectiles. The second line of each process indicates the emission of the Auger electron and its detection at theta=0 degrees.

In this thesis, the cross section for the production of the $1s2p^2\,{}^2D$, $2s2p\,{}^3P$ and $2s2p\,{}^1P$ states were determined, in order to study the transfer-excitation (TE), single and double projectile excitation atomic processes. The measurements are also accompanied by close-coupling (CC) calculations in which three-active electrons have been included for the first time (3eAOCC)[1], in an attempt to cast further light on these complex multi-electron processes.

The calculated cross sections for the production of $1s2p^2\,{}^2D$ from $1s^2\,{}^1S$ through TE, both for carbon and oxygen are found to be in agreement with zero-degree Auger projectile spectroscopy measurements covering the maximum of the resonance peak

[1]The CC calculations are provided through our collaboration with Prof. Alain Dubois and his group in the Sorbonne, Paris

and its high energy wing. At lower energies, the theoretical results show a second maximum which is interpreted recently [11] through a nonresonant one-step transfer excitation mechanism.

In the case of $2s2p\,^3P$ and $2s2p\,^1P$ the 3eAOCC calculated cross sections were converted to Auger electron normalized yields for a direct comparison between theory and experiment, as $2s2p\,^3P$ and $2s2p\,^1P$ states can be populated by all three $1s^2\,^1S$, $1s2s\,^1S$ and $1s2s\,^3S$ components through different processes. Although both theory and experiment trends appear to have a similar energy dependence, the theoretical results in this case are in general smaller than the experimental, leaving room for discussion on the possible reasons that this happens.

Keywords: accelerator-based atomic physics, ion-atom collisions, highly-charged ions, doubly-excited states, Auger electron spectroscopy, projectile-ion electron spectroscopy, zero-degree Auger projectile spectroscopy, state-selective cross sections, electron transfer-excitation, electron excitation, mixed-state ion beams, He-like ions, Li-like ions, long-lived (metastable) states

Περίληψη

Αξιοποιώντας τον ήδη υπάρχοντα φασματογράφο ηλεκτρονίων δέσμης μηδέν μοιρών της πειραματικής διάταξης APAPES (Atomic Physics with Accelerators: Projectile Electron Spectroscopy) και τις ηλιοειδείς δέσμες ιόντων C^{4+} και O^{6+} προερχόμενες από τον 5.5 MV επιταχυντή tandem Van de Graaff του «Δημόκριτου», πραγματοποιήθηκαν μετρήσεις K-Auger ηλεκτρονίων δέσμης ιόντων, μέσω κρούσεων με στόχους αερίου He στην ενεργειακή περιοχή 0.5-1.5 MeV/u. Οι ηλιοειδείς δέσμες εν γένει συνυπάρχουν σε ένα μείγμα των $1s^2\,{}^1S$, $1s2s\,{}^1S$ και $1s2s\,{}^3S$ καταστάσεων, οπότε συμπεριλαμβάνονται διαδικασίες προερχόμενες και από τις τρείς αυτές αρχικές καταστάσεις. Ποίο συγκεκριμένα η παρούσα δουλειά εστιάζει στις επόμενες δύο διαδικασίες κατά την διάρκεια κρούσεων:

$$\mathrm{X}^{q+}(1s^2) + \mathrm{He} \rightarrow \mathrm{X}^{(q+1)+}(1s2p^2\,{}^2D) + \mathrm{He}^{+}(\mathrm{All}) \quad \text{(Transfer-Excitation)} \tag{5}$$

$$\hookrightarrow \mathrm{X}^{q+}(1s^2) + e_A^{-}(\theta = 0^\circ) \tag{6}$$

και

$$\mathrm{X}^{q+}(1s^2, 1s2s\,{}^{3,1}S) + \mathrm{He} \rightarrow \mathrm{X}^{q+}(2s2p\,{}^{3,1}P) + \mathrm{He}(\mathrm{All}) \qquad \text{(Projectile Excitation)} \tag{7}$$

$$\hookrightarrow \mathrm{X}^{(q-1)+}(1s) + e_A^{-}(\theta = 0^\circ) \tag{8}$$

όπου το X^{q+} αναφέρεται στη δέσμη ιόντων άνθρακα C^{4+} ή οξυγόνου O^{6+}. Η δεύτερη γραμμή κάθε διεργασίας δείχνει την εκπομπή του ηλεκτρονίου Auger και την ανίχνευσή του σε ϑ=0 μοίρες. Στην παρούσα διατριβή προσδιορίστηκαν οι ενεργές διατομές για την παραγωγή των καταστάσεων $1s2p^2\,{}^2D$, $2s2p\,{}^3P$ και $2s2p\,{}^1P$, προκειμένου να μελετηθούν οι ατομικές διεργασίες transfer-excitation (TE) και single ή double excitation της δέσμης ιόντων. Οι μετρήσεις συνοδεύονται επίσης από close-coupling (CC) υπολογισμούς στους οποίους έχουν συμπεριληφθεί για πρώτη φορά τρία ηλεκτρόνια (3eAOCC)[2] με ενεργό ρόλο κατά την κρούση, σε μια προσπάθεια να ριχθεί περαιτέρω φως σε αυτές τις πολύπλοκες διεργασίες πολλών ηλεκτρονίων. Οι υπολογισμένες ενεργές διατομές για την παραγωγή $1s2p^2\,{}^2D$ από $1s2s\,{}^1S$ μέσω TE, τόσο για άνθρακα όσο και για οξυγόνο, βρέθηκαν να συμφωνούν με τις πειραματικές με-

[2]Οι CC υπολογισμοί πραγματοποιήθηκαν από τον καθηγητή Alain Dubois και την θεωρητική του ομάδα στο Παρίσι.

τρήσεις φασματοσκοπίας Auger μηδέν μοιρών που καλύπτουν το μέγιστο της κορυφής συντονισμού και την πλευρά των υψηλών ενεργειών. Σε χαμηλότερες ενέργειες, τα θεωρητικά αποτελέσματα δείχνουν ένα δεύτερο μέγιστο που ερμηνεύεται πρόσφατα [11] μέσω ενός nonresonant one-step transfer-excitation μηχανισμού. Στην περίπτωση των καταστάσεων $2s2p\,^3P$ και $2s2p\,^1P$ οι 3eAOCC υπολογισμοί ενεργών διατομών μετατράπηκαν σε Auger electron normalized yields για μια άμεση σύγκριση μεταξύ θεωρίας και πειράματος, καθώς οι καταστάσεις $2s2p\,^3P$ και $2s2p\,^1P$ μπορούν να εποικηθούν και από τις τρεις $1s^2\,^1S$, $1s2s\,^1S$ και $1s2s\,^3S$ καταστάσεις μέσω διαφορετικών διεργασιών. Παρόλο που θεωρία και πειραματικές μετρήσεις φαίνεται να έχουν παρόμοια ενεργειακή εξάρτηση, τα θεωρητικά αποτελέσματα σε αυτήν την περίπτωση είναι γενικά μικρότερα από τα πειραματικά, αφήνοντας χώρο για συζήτηση σχετικά με τους πιθανούς λόγους που συμβαίνει αυτό.

Λέξεις κλειδιά: ατομική φυσική με επιταχυντές, κρούσεις ατόμων ιόντων, υψηλά φορτισμένα ιόντα, διπλά διεγερμένες καταστάσεις, φασματοσκοπία ηλεκτρονίων Auger, φασματοσκοπία ηλεκτρονίων δέσμης ιόντων, φασματοσκοπία δέσμης ιόντων μηδέν μοιρών, ενεργές διατομές ατομικών καταστάσεων, σύλληψη ηλεκτρονίων με ατομική διέγερση, μικτές δέσμες ιόντων, ηλιοειδή ιόντα, λιθιοειδή ιόντα, μετασταθείς ατομικές καταστάσεις.

Chapter 1

Introduction

1.1 Historical Background

The Auger effect is a spontaneous de-excitation process of an atom having a vacancy in one of its inner shells, being the alternative to the radiative de-excitation process for excited atoms. In the case of the radiative de-excitation shown in Fig.1.1a, the initial inner shell vacancy is filled by an electron from a higher shell, with the simultaneous emission of a photon with energy equal to the energy difference of the two shells, $h\nu' = E_1 - E_2$. In the competitive Auger process shown in Fig. 1.1b, two active electrons interact through their mutual Coulomb force in the field of the atomic nucleus screened by any other "spectator" electrons, resulting in the filling of the initial inner shell vacancy by one of them and the ejection to the continuum of the second one (absorbing the excess amount of energy), with a kinetic energy equal to $E_A = E_1 - E_2 - E_3$ with the E_3 being the binding energy of the emitted electron [12–14].

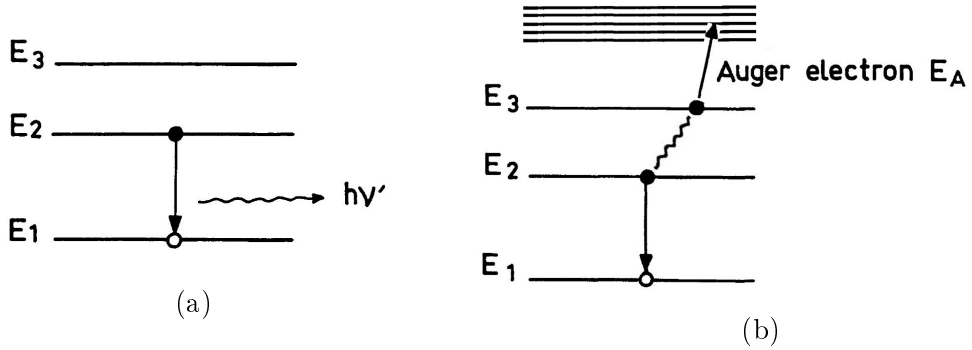

Figure 1.1: (a) Radiative and (b) Auger de-excitation.

The Auger effect was discovered by Pierre Auger, shown in 1.2, during the middle 1920's [1, 12, 13]. Pierre Auger started his studies in 1922 constructing the first Wilson cloud chamber in France together with Francis Perrin. By filling the chamber with argon, he noticed that tracks corresponding to ejected electrons could be seen along a beam of X-rays. This novel effect could be detected by the presence of a

double track emanating from a single source. One track was due to photoelectron ejection, while the origin of the second remained unknown [12, 13].

In his PhD thesis in 1926, he proposed a complete description of the effect that would eventually take his name. More specifically he noted that i) electrons can be obtained following the initial ionization of an atom instead of photons, ii) for core states with low-binding energies the more probable decay mechanism following ionization is through ejection of an electron and iii) that Auger electrons are emitted isotropically in all directions. The observation of such a phenomenon verified S. Rosseland's theoretical prediction since 1923 [15] for the possibility of such a non-radiative atomic transition.

Although Pierre Auger's simple picture implied that this novel effect might be an internal reabsorption of an intermediate photon emitted following the initial ionization of an atom leading to the emission of a second electron, it was soon realized that the Auger process is a non-radiative rearrangement of the electrons within the atomic system, with an electron filling an initial inner shell vacancy leading to the emission of another electron with an energy characteristic of the atomic transition. This picture is supported by the fact that there are indeed many examples where the observed Auger electrons correspond to atomic transitions which would be forbidden by radiative selection rules, where a real photon is involved in the process.

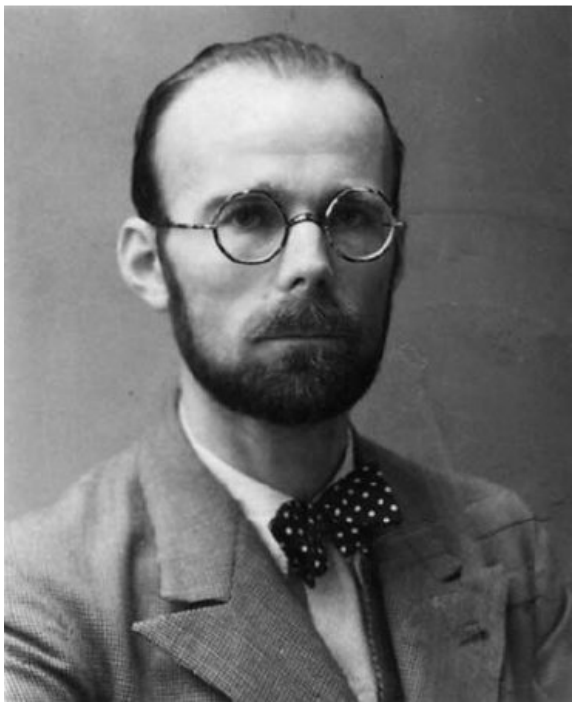

Figure 1.2: Pierre Auger. From Ref. [1]

The first investigations with emphasis on the Auger electron emission were performed by H.R. Robinson and A.M. Cassie in 1926 [16], marking the birth of Auger electron spectroscopy. In parallel, G. Wenzel [17] was the first to theoretically confirm the effect formulating the process. The theory of the Auger effect has been

discussed extensively by P. G. Burke [18], E. H. S. Burhop and W. N. Asaad [19], D. Chattarji [20], E. J. McGuire [21], and T. Åberg, J. Utriainen and G. Howat [22, 23]. It was soon understood that when an Auger transition takes place in an isolated atom, it depends solely on its atomic properties. In addition, it was shown that in most cases nature preferentially chooses the Auger process in atom de-excitation. It is only when the transition energy exceeds approximately 10 keV that X-ray emission becomes predominant. A useful concept in the fields of Auger and X-Ray spectroscopy is that of widths. If there are multiple decay channels available from an initial state, the corresponding partial Auger or radiative width corresponds to the relative probability for that type of transition. Thus, as illustrated in Fig. 1.3, the radiative width Γ_R is greater than 0.5 eV only for vacancies in the K shells of atoms whose atomic number $Z > 30$, and in a few cases in the L shell for very heavy elements. For lower Z the Auger width Γ_A appears to be orders of magnitude larger than the radiative width. As a result, the study of the Auger effect has proven to be ideal for the structure and dynamics investigation of atoms particularly in the low Z region.

Initially, the Auger effect was studied together with nuclear decay mechanisms, performing experiments using radioactive sources in solid samples studying inner shell transitions of heavy elements producing Auger electrons of relatively high velocities, able to escape from the solid with little energy loss.

In the early 60's the Auger effect was studied through Auger electron measurements from gaseous or vapour targets excited by photon, electron and ion impact with the use of ions presenting the advantage of being able to excite inner shell electrons not possible through photons or electrons. M. E. Rudd [24, 25] was the first to measure with high resolution the He Auger electrons produced by H^+ and H_2^+ impact on He targets.

In the 70's high resolution electron spectrometers were used attaining $\simeq$1eV or less FWHM line widths together with high energy multiple charged ions as projectiles of Z higher than H and He were used, in the energy range of 10-20 MeV/u [26].

In the 80's the Auger processes gained attention both experimentally and theoretically, leading to the development of special equipment dedicated to Auger electron angular distribution studies [3, 27, 28]. Ion-impact induced Auger spectroscopy studies initially focused on electrons emitted from the target atom, but later the focus shifted to Auger electrons emitted from the projectile ion upon collision with the target due to numerous advantages explained in more detail below [27].

Projectile electron spectroscopy has been extensively used for many years to study ion-atom collisions, starting around the late 60's and early 70's [26] . However, kinematic line broadening effects, that become particularly strong at high collision energies, limited the high resolution capabilities of this technique, to rather low resolution investigations. It was discovered however, that these broadening effects can be substantially reduced by performing the observation of the emitted electrons at 0° with respect to the beam direction [29]. From that observation, the technique

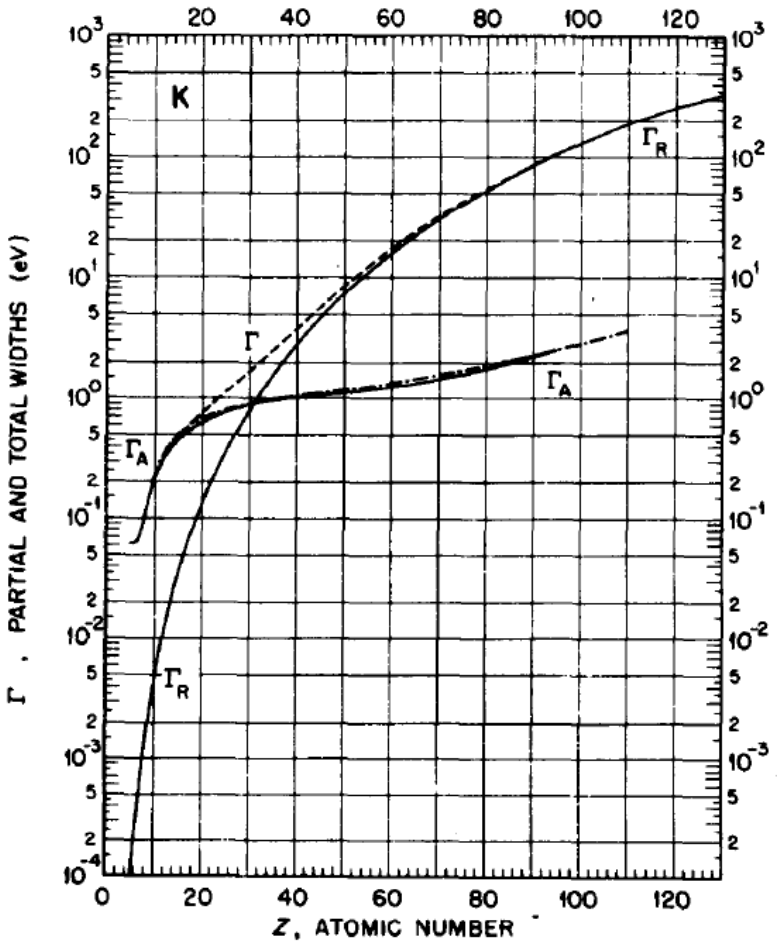

Figure 1.3: K-shell theoretical Auger (Γ_A), radiative (Γ_R) and total (Γ) atomic level widths as a function of atomic number Z. For Z$\leq$30, Γ_A appears to be orders of magnitude larger than Γ_R, while for higher Z, Γ_R increases rapidly with Γ_A increasing only slightly. From Ref. [2].

of zero-degree Auger projectile spectroscopy was introduced in order to perform high resolution ion-atom collision measurements [29–33]. In Fig. 1.4 a schematic representation of the ion-induced Auger electron spectroscopy method is presented.

It is essential to mention here that in general, in the case of ion impact induced Auger processes, the emission of Auger electrons can arise from both the target and the projectile atoms simultaneously. However, in the case where the Auger electrons are emitted from a fast moving ion they will appear shifted in energy in the recorded spectrum, according to the kinetic energy of the projectile, as illustrated in Fig. 1.5. In the present thesis, Auger projectile spectroscopy is employed in order to study the inter-atomic processes taking place in energetic ion-atom collisions. This is possible due to the fact that, when the collision time to excite the atom($\approx 10^{-17}$ s) is small compared to the Auger state lifetime($\approx 10^{-13}$ s), the decay process can be considered to be independent of the excitation process [14], a condition that is fulfilled in our experiments. In section 1.2 the various processes taking place in ion atom collisions are described.

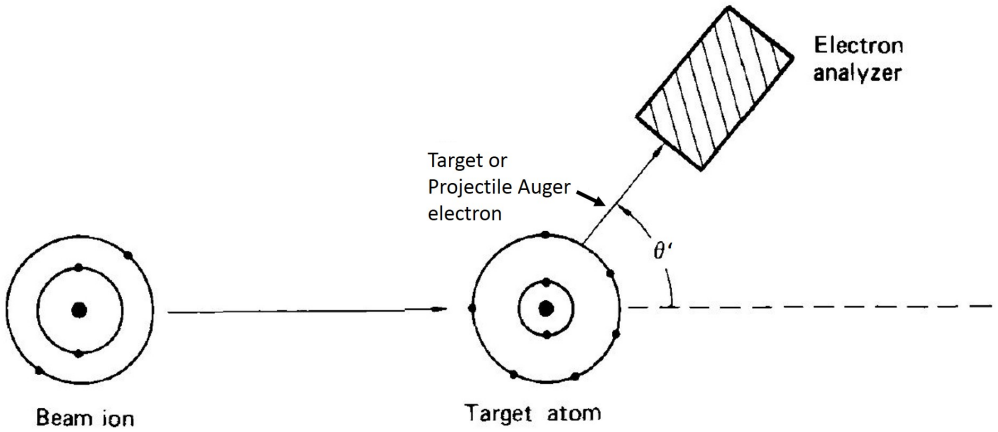

Figure 1.4: Schematic illustration of the basic principle of ion-induced Auger electron spectroscopy. In general, Auger electrons from the target atom and the projectile ion will be emitted in all directions. In principle, an electron analyzer is placed at an angle θ' with respect to the beam's direction detecting the emitted electrons at this angle. Zero degree electron spectroscopy is performed when $\theta' = 0°$. From Ref. [3].

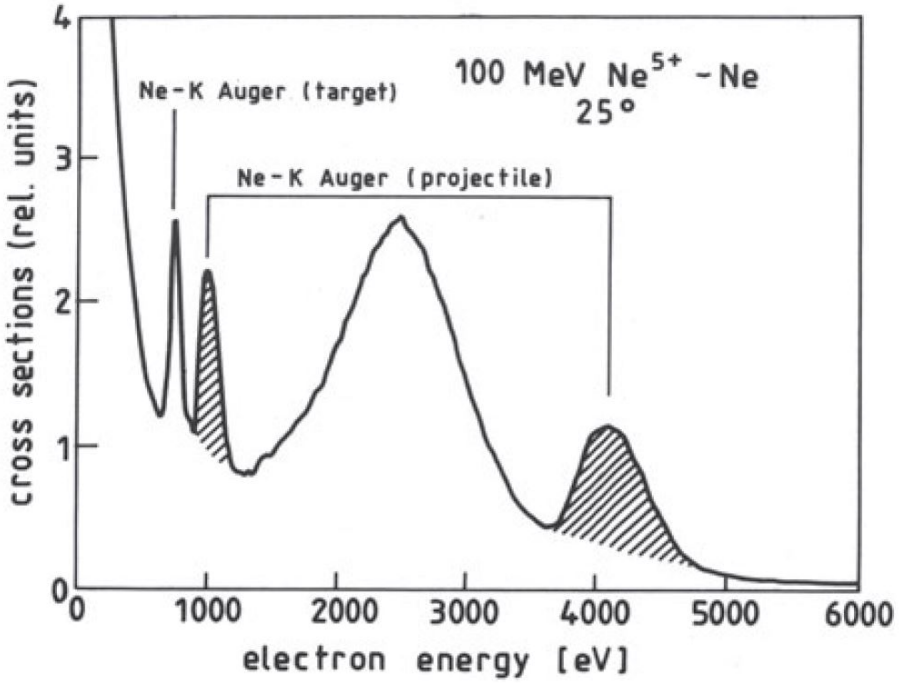

Figure 1.5: Typical Auger electron spectrum produced in 100 MeV Ne^{5+} + Ne collision. Both target and projectile Ne - K Auger electrons appear in the same spectrum, well separated in the laboratory electron energy due to kinematic effects. From Ref. [4].

1.2 Electron processes in ion-atom collisions

As already mentioned, when a fast projectile ion collides with an atom, generally one or more electrons are ejected in the collision. Atomic processes such as electron capture (transfer), excitation and ionization may take place during ion-atom collisions, with any combination of these processes also being possible in a single-collision event. These processes are of fundamental interest in many branches of physics and related sciences, with the understanding and modelling of the dynamics of these many-body systems remaining even nowadays a great challenge.

Since the collision dynamics of these systems can prove extremely complicated to be described theoretically, few-electron ions and atoms systems are selected, in an attempt to reduce the complexity of these systems.

Thus, few-electron projectile ions combined with low Z atomic targets present the ideal laboratories to study the processes occurring during ion-atom collisions.

In more detail, the possible processes occurring during ion-atom collisions (where P is the projectile and T the target) are:

Electron capture (n-electron transfer)

$$\mathrm{P}^{q+} + \mathrm{T} \rightarrow \mathrm{P}^{(q-n)+} + \mathrm{T}^{n+} \tag{1.1}$$

Excitation (projectile excitation with simultaneous target excitation or n-electron target ionization)

$$\mathrm{P} + \mathrm{T} \rightarrow \mathrm{P}^{*} + \mathrm{T}^{n+} + \mathrm{n}e^{-} \tag{1.2}$$
$$\rightarrow \mathrm{P}^{*} + \mathrm{T}^{*} \tag{1.3}$$

Ionization (m projectile ionization (loss) or n-electron target ionization)

$$\mathrm{P} + \mathrm{T} \rightarrow \mathrm{P}^{m+} + \mathrm{T} + \mathrm{m}e^{-}, \text{ or} \tag{1.4}$$
$$\rightarrow \mathrm{P} + \mathrm{T}^{n+} + \mathrm{n}e^{-} \tag{1.5}$$

Furthermore, any combination of the above fundamental processes can, in general, occur:

Transfer-Excitation

$$\mathrm{P}^{q+} + \mathrm{T} \rightarrow \mathrm{P}^{(q-n)+*} + \mathrm{T}^{n+}, \text{ or} \tag{1.6}$$
$$\rightarrow \mathrm{P}^{(q-n)+} + \mathrm{T}^{(n+)*} \tag{1.7}$$

Transfer-Ionization

$$\mathrm{P}^{q+} + \mathrm{T} \rightarrow \mathrm{P}^{(q-1)+} + \mathrm{T}^{2+} + \mathrm{e}^{-} \tag{1.8}$$

Overall, the determination of cross sections of the above reaction channels is of particular importance in various fields of physics, including atomic physics, astrophysics, plasma physics, and accelerator based physics.

1.3 Motivation for ion-atom collision investigations

In general, ion-atom collisions play a crucial role in various scientific and technological fields, both in fundamental physics and technological applications.

In fundamental physics, they provide insights into the processes occurring at the atomic and nuclear levels, allowing for a better understanding of the interaction dynamics between charged particles, leading to advancements in atomic and molecular physics.

On the other hand, ion-atom collision studies contribute also to numerous applications. Plasma physics depend on ion-atom collisions, particularly for understanding the behaviour of matter at extremely high temperatures and pressures, as well as astrophysics research, rely on ion-atom collisions in order to better understand the behaviour of matter in extreme environments. Furthermore, ion-atom collisions contribute to material science for characterising materials and medical applications such as hadron therapy for cancer treatment.

In summary, ion-atom collisions have far-reaching implications across various scientific and technological domains, contributing to our understanding of fundamental physics and enabling practical applications with widespread impact.

1.4 Dissertation goals

The goal of the present thesis is to study the processes of electron transfer-excitation (TE) and electron excitation (eE) in energetic ion-atom collisions over a wide energy range. These processes are mediated by electron-electron ($e-e$) and electron-nucleus ($e-n$) interactions of fundamental interest. The TE process is further divided into resonant transfer-excitation and nonresonant transfer-excitation processes attributed to the $e-e$ and $e-n$ interactions respectively. The eE process is also attributed to both $e-n$ and $e-e$ interactions.

Studies on $e-e$ and $e-n$ interactions contribute to the understanding of the structure, properties, and behaviour of matter at the atomic levels, playing a crucial role in various scientific disciplines including physics, chemistry, materials science, and engineering.

In this thesis, these processes are studied experimentally through high resolution zero-degree projectile Auger electron spectroscopy. The detected Auger electrons

originate from doubly-excited projectile states produced in ion-atom collisions between He-like carbon and oxygen projectiles and He target, in the collision energy range of 0.5 to 1.5 MeV/u. The He-like ion beams provided by the 5.5 MV tandem Van de Graff accelerator together with the He target present simple enough systems to study. However, once produced in the accelerator, they exist in a mixture of a ground and excited components each one capable of populating unique intermediate states through specific production channels. The challenge when using mixed-state He-like ion beams lies in the determination of the absolute amount of each component surviving to the target area. The amount of each component must be evaluated separately and taken into account in the determination of cross sections. The experimental results are then compared to ab initio non-pertubative semiclassical atomic orbital close-coupling calculations, performed and provided by our collaborating theoretical physicists group in Sorbonne University, Prof. Alain Dubois and his student Dr. Stylianos Passalidis. In the following, a brief background on the transfer-excitation and electron excitation processes is given.

1.4.1 Transfer-Excitation

The idea of the existence of an electron transfer and simultaneous excitation process in ion-atom collisions came from the already known process of dielectronic recombination occuring in electron - atom collisions [34]. In the first step of dielectronic recombination, known as dielectronic capture (DC), a free electron is captured by a positively charged ion to one of its bound orbits with simultaneous excitation of another atomic electron leading to the formation of a doubly excited state. In the second step, a photon is emitted characteristic of the doubly excited state. This looks similar to radiative recombination, a process where an electron is captured by a positively charged ion with simultaneous emission of a photon, however the radiative recombination is a single-step process, while dielectronic recombination (DR) occurs in two distinct steps [9, 35, 35–37]. We note that electron capture of a free electron can only happen with the simultaneous change of energy in the atom.

An analogous process to dielectronic recombination was expected in ion-atom collisions. In fact, the existence of a "capture with excitation" process, as transfer-excitation (TE) was initially called, was observed through X-ray detection in S + Ar collisions by J. A. Tanis et al. in 1981 [34]. Thus, transfer-excitation in energetic ion-atom collisions is defined as a "two-electron process involving the excitation of an electron to a bound state and the capture of an electron from the collision partner" [38]. It was soon discovered that TE can occur through both a resonant and a non-resonant mechanism attributed to electron-electron and electron-nucleus interactions, respectively. Two different models have been developed to elucidate the impact energy dependence of the TE cross sections. The resonant transfer-excitation (RTE) contribution has been described to first order by a one-step mechanism mediated by the two-center $e-e$ interaction (TCee) It has been modelled through the

impulse approximation (IA), as a quasifree resonant electron scattering analogous to the inverse Auger process [39–42]. However, the IA, even though fairly successful in describing the relative collisional energy dependence of RTE, is not an ion-atom collision theory, but is based on an electron impact theory adjusted for the initial energy distribution of the impinging electron according to its momentum distribution (Compton profile) carried into the collision due to its binding to the target. On the other hand, the nonresonant transfer-excitation (NTE) contribution has been interpreted by a sequence of uncorrelated excitation and transfer events, each independently driven by separate $e-n$ interactions [43, 44] Both TE mechanisms can be expected to occur in the same ion-atom collision contributing coherently to the production of the same final (doubly-excited) projectile state and could therefore also be expected to interfere. To date, calculated cross sections for these different TE mechanisms have only been computed separately in independent treatments. Thus, their contributions to the total TE cross sections could only be added incoherently, allowing at most for interesting speculations about possible RTE-NTE interferences [31, 43, 45–49].

In this thesis transfer-excitation is studied through the detection of Auger electrons emitted from the doubly-excited $1s2p^2\,{}^2D$ projectile state produced in the following collision systems,

$$\mathrm{C}^{4+}(1s^2\,{}^1S) + \mathrm{He}(1s^2) \rightarrow \mathrm{C}^{3+}(1s2p^2\,{}^2D) + \mathrm{He}^{+}(\mathrm{All}) \tag{1.9}$$

$$\mathrm{O}^{6+}(1s^2\,{}^1S) + \mathrm{He}(1s^2) \rightarrow \mathrm{O}^{5+}(1s2p^2\,{}^2D) + \mathrm{He}^{+}(\mathrm{All}) \tag{1.10}$$

in the collision energy range of 0.5 to 1.5 MeV/u. The $1s2p^2\,{}^2D$ can be formed from $1s^2$ only through transfer-excitation, and is therefore ideal for studying the particular process. With He^{+}(All) the final status of the target, i.e., ground, excited or ionized, is symbolized.

The $1s2p^2\,{}^2D$ cross section measurements cover the maximum of the resonance peak and its high energy wing, and are compared with ab initio three electron atomic orbital close-coupling calculations. At the lower energies, the theoretical results show a second maximum which is interpreted through a new, nonresonant, one-step transfer-excitation mechanism [11]. The present work provides an important advance in the modeling and understanding of multielectronic processes in quantum systems under strong and ultrafast perturbations through a fully coherent, many-body treatment.

1.4.2 Excitation

The electron excitation of an atom or ion from one bound state to another, is a fundamental quantum mechanical process pervading most atomic physics. Together with electron capture and ionization it constitutes one of the most important ion-atom collision processes.

In the past, excitation of H or He by particle beams such as electrons [50, 51] or bare ions [52–54] has reached a high level of sophistication and accuracy utilizing also ab initio nonperturbative treatments. However, excitation with ions carrying electrons into the collision (known as dressed ions) is not yet as advanced, mostly relying on perturbative treatments. In fact, the additional projectile electrons introduce considerable complexity acting not only as passive screening agents, but also as dynamic exciting agents themselves, clearly demonstrating phenomena such as collision energy thresholds and electron exchange interactions [55]. Additionally, in most experiments the final state of the target following projectile excitation is not usually determined. Therefore, contributions from both ground and excited-target states (including ionization) need to be considered for an accurate comparison to experiment, further increasing the difficulty of the calculations. In this thesis, the electron single or double excitation mechanisms mediated by electron-electron and electron-nucleus interaction are studied through the detection of Auger electrons emitted from the $2s2p\,^3P$ and $2s2p\,^1P$ states formed during energetic ion-atom collisions, while a comprehensive investigation of projectile excitation combining close-coupling calculations for three active electrons is provided. Thus, the following processes are studied:

$$\mathrm{C}^{4+}(1s^2\,^1S, 1s2s\,^{1,3}S) + \mathrm{He}(1s^2) \rightarrow \mathrm{C}^{4+}(2s2p\,^{1,3}P) + \mathrm{He(All)} \tag{1.11}$$

$$\mathrm{O}^{6+}(1s^2\,^1S, 1s2s\,^{1,3}S) + \mathrm{He}(1s^2) \rightarrow \mathrm{O}^{6+}(2s2p\,^{1,3}P) + \mathrm{He(All)} \tag{1.12}$$

where He(All) includes all target excited states, i.e., ground, excited or ionized.

1.5 Dissertation outline

The current thesis begins by introducing the necessary background used in the present experiments, followed by theory describing the atomic processes occurring in ion-atom collisions, and finally the experimental study of the processes leading to the production of $1s2p^2\,^2D$, $2s2p\,^3P$ and $2s2p\,^1P$ in collisions of He-like pre-excited carbon and oxygen ions with He gas target in the MeV/u energies regime.

In chapter 2 the zero-degree Auger projectile spectroscopy (ZAPS) technique utilized in this thesis is described in detail, together with the frame transformations and kinematic broadening effects governing Auger electron spectra obtained from moving emitters, as well as the intrinsic Auger line broadening effects.

In chapter 3 the N.C.S.R. "Demokritos" 5.5 MV tandem Van de Graaff accelerator is described together with is operation principles, as well as the whole setup dedicated for atomic physics fundamental research frequently referred as the APA-PES setup.

In chapter 4 the data analysis method, including the apparatus's energy calibration and the transformation of the raw experimental data to double-differential

cross sections, is described.

Chapter 5 is dedicated to the description of the advantages of He-like ($1s^2$, $1s2s\,^{3,1}S$) mixed component beams used in the present thesis, together with the method used for the determination of the surviving population of each of these components to the experiment's target known as the "two-spectra measurement" technique, and a new three-component beam model offering higher accuracy in the existing model.

In chapter 6 a brief overview of a recently developed ab initio method referred as three-electron Atomic Orbit Close-Coupling (3eAOCC) theory is given, for the further understanding of the ongoing processes studied in this thesis.

In chapter 7 the transfer-excitation process is studied experimentally through the detection of the $1s2p^2\,^2D$ Auger electrons produced in collisions of He-like ($1s^2$) carbon and oxygen projectiles on He targets in a wide MeV energy region. Furthermore, the experimental data are accompanied by theoretical calculations provided by our collaborators revealing a new process never considered up to now.

In chapter 8 the atomic processes leading to the production of the $2s2p\,^3P$ and $2s2p\,^1P$ states are studied through He-like ($1s^2$, $1s2s\,^{3,1}S$) carbon and oxygen projectiles on He targets collisions in a wide MeV energy region. An attempt to determine the contribution of single and double excitation, and transfer-loss processes in the production of the $2s2p\,^3P$ and $2s2p\,^1P$ states from each of the initial beam components of the He-like beam is made together with corresponding full close-coupling (FCC) calculations.

Finally in chapter 9 an overall summary of the present thesis is given, highlighting the new knowledge gained through this work and future planning.

Chapter 2

The Zero-degree Auger Projectile Spectroscopy Technique

Overview

During the 1970's, I. A. Sellin, D. J. Pegg and collaborators performed experiments measuring Auger electrons from fast projectiles focusing on reducing kinematic broadening effects sufficiently to resolve the observed Auger lines [14, 56–58]. Projectile Auger electron spectroscopy presents multiple advantages over target Auger spectroscopy as it allows for the use of ion beams in a pre-selected charge state (and therefore number of incoming electrons) and kinetic energy [30]. Combined with few-electron targets, such as H_2 or He, ion-atom collision investigations of interacting atomic systems can be simple enough, to study the effects of electron-nucleus and electron-electron interactions. The main drawback of the Auger projectile spectroscopy though, lies in the kinematic broadening effects associated with electrons ejected from moving emitters that can reduce dramatically the Auger spectra resolution [59]. These effects originate from the spectrometer's finite acceptance angle $\Delta\theta$ and depend strongly on the electron detection angle θ [60]. However, as will be explained further below, these broadening effects decrease with the reduction of the observation angle θ, and become second-order at observation angles of $\theta = 0^\circ$ or 180° with respect to the ion beam's direction [14]. In Fig. 2.1 the drastic improvement in resolution by decreasing the observation angle close to $\theta = 0^\circ$ can be clearly seen. The first measurements of Auger electrons at 0° were performed in the early 70's by Lucas and Harrison [61], mostly in the context of investigations of electron capture to the continuum [62–64], which demanded 0° observations.

Combining the advantages of Auger projectile spectroscopy above with the detection of the emitted electrons at $\theta = 0^\circ$ for minimization of kinematic broadening effects, the Zero-degree Auger Projectile Spectroscopy (ZAPS) technique emerged to perform high resolution state-selective cross section measurements. Initially, the ZAPS technique utilized two-stage (tandem) slit spectrometers, consisting of two sets of 45° parallel-plate spectrometers, known as tandem - Parallel Plate Analyzers

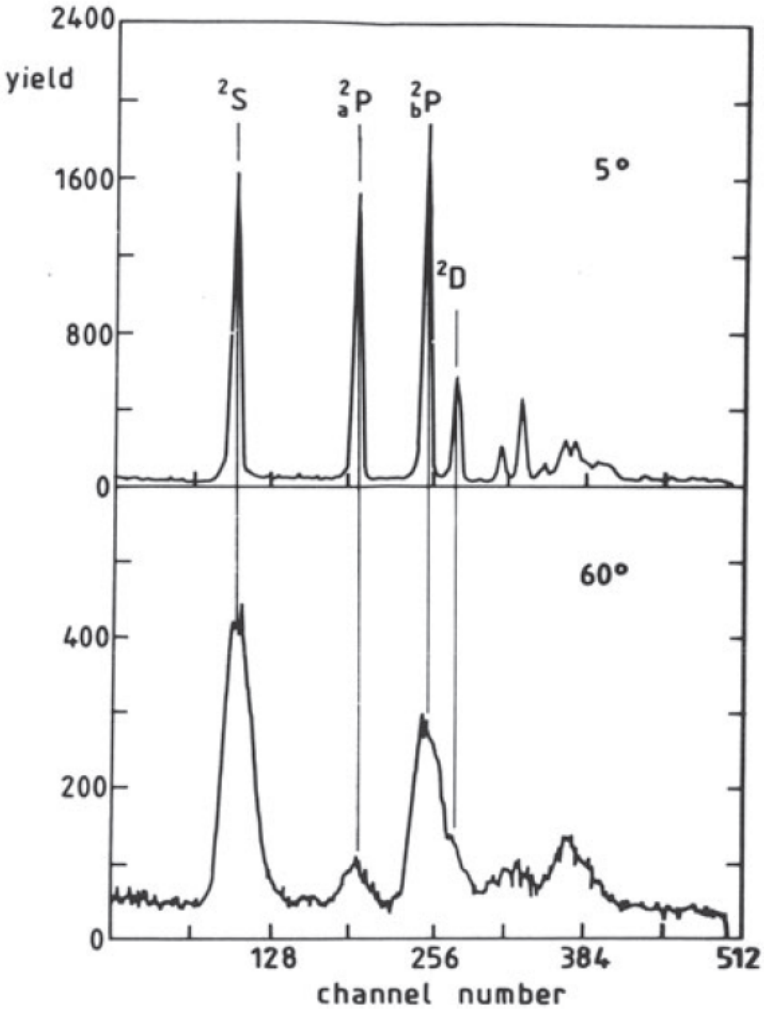

Figure 2.1: Li Auger spectra from 250 keV Li^+ + He at $\theta = 5°$ and $\theta = 60°$ laboratory observation angles. From Ref. [65].

(tandem-PPA) [29, 67]. Although this type of spectrometer is able to provide ZAPS high resolution spectra ($\approx 0.1\%$ or better), its greatest disadvantage is the large time required for the collection of a single spectrum due to its overall low transmission and small detection solid angle. This type of spectrometer works by scanning over the studied Auger lines energy region, a process that takes time. Furthermore, the use of very small apertures in order to increase the spectrometer's resolution, along with the dramatic reduction in transmission when operating in pre-retardation mode, requires high beam currents (50-100 nA) to maintain the experimental acquisition time at 12-24 hrs level. Therefore, experiments with low beam currents (< 10 nA) or small cross section processes (DDCS $< 10^{-22}$ cm^2/eVsr) are practically impossible with this type of spectrometer. The need for treatment of these problems led to the development of a *single* stage spectrometer using a Hemispherical Deflector Analyzer (HDA) spectrometer, combined with an injection lens and a position-sensitive detector (PSD) by E. P. Benis and T. J. M. Zouros (1996-2000) [66, 68], with its most advanced version used in this thesis, shown in Fig. 2.2. Here, an ion beam is

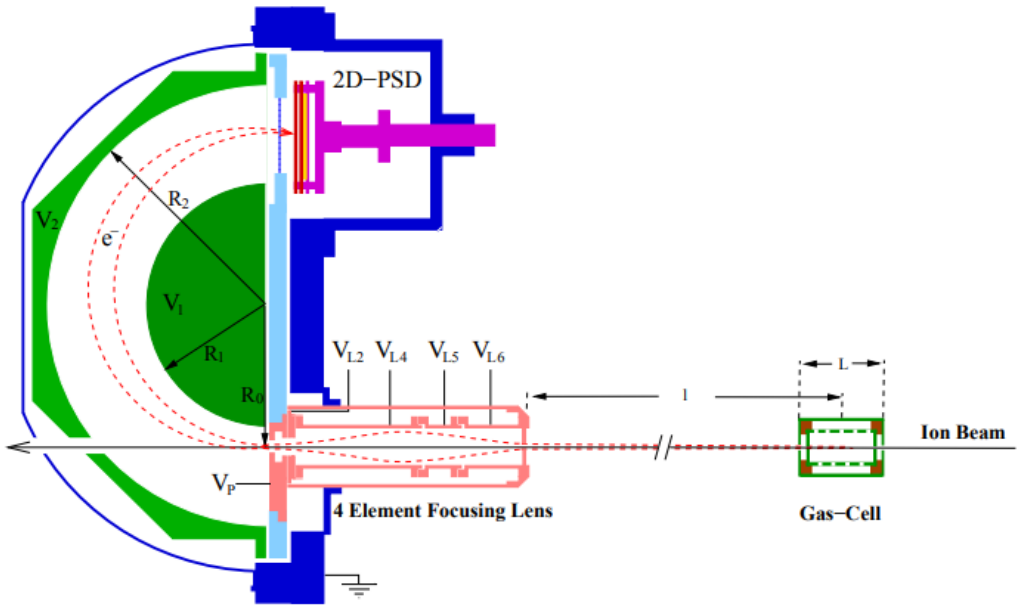

Figure 2.2: Schematic of the experimental apparatus used for Zero-degree Auger projectile spectroscopy. In this system, a Hemispherical Deflector Analyzer (HDA) is used together with a four-element injection lens to focus electrons produced during the collision in the target gas cell and exiting at $\theta = 0°$, while the ion beam traverses through the lens and HDA to be eventually recorded for normalization in a Faraday Cup behind the HDA (not shown). From Refs. [59, 66].

directed through a cylindrical cell containing the target gas and then traverses the electrostatic analyzer exiting through a hole at its back and collected in a Faraday cup used for normalization. Collisions occur inside the gas cell which result in the emission of Auger electrons that exit the cell at $\theta = 0°$, enter the electrostatic analyzer, are focused and decelerated by an injection lens and are finally energetically analysed by the HDA and detected by the PSD. In contrast to the tandem-PPA, the use of a focusing electrostatic lens creating a *virtual* aperture together with the use of PSD, allows for the detection of a wider energy acceptance window of Auger electrons in a single spectrum, reducing dramatically the data acquisition time even with low beam currents (< 10 nA). A more detailed description of the operation of the HDA used in combination with the other parts of the setup is given in section 3.2. The effects originating from the ZAPS technique, can be divided into frame transformation effects that alter the energy, width, shape and height of the Auger lines detected in the laboratory, and kinematic broadening effects that reduce the energy resolution of the recorded Auger lines in the spectrum. All these effects along with their origin are described in this chapter, and need to be taken into account when double-differential cross section information is extracted from the data.

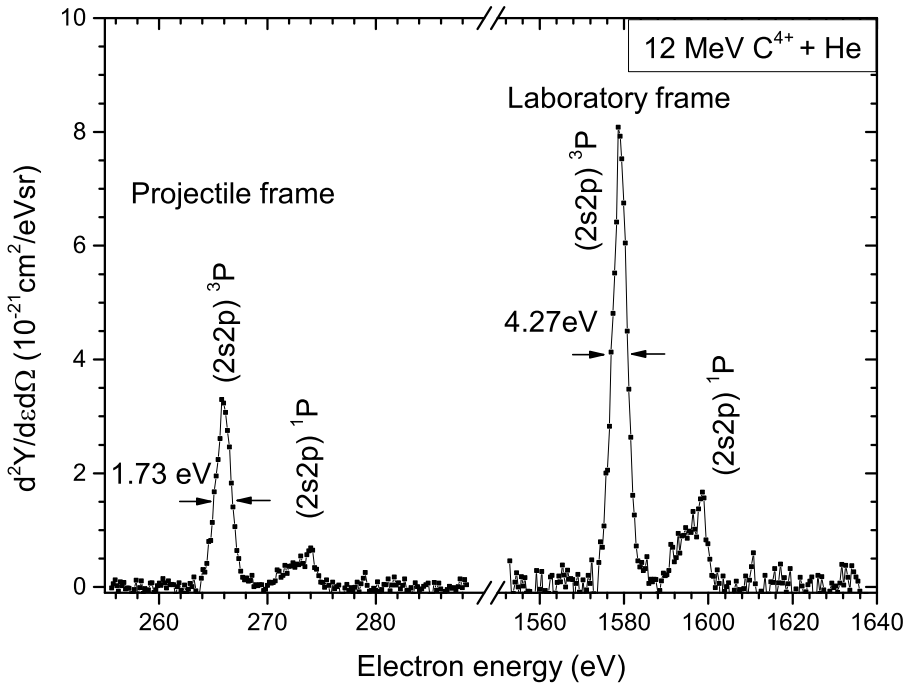

Figure 2.3: Carbon Auger electron spectra obtained in 12 MeV C^{4+} + He collisions as they appear in the laboratory (right) and after transformation to the projectile frame (left). Both spectra have been normalized and energy calibrated, taking into consideration all experimental parameters. The line energy shifting, stretching and enhancement effects in the laboratory frame are clearly seen. From recent data (this work).

2.1 Kinematics effects of electrons ejected from moving emitters

As mentioned above ZAPS developed in order to provide high resolution Auger spectra allowing line identification, atomic structure information and state production cross sections to be obtained. Although it presents numerous advantages such as the pre-selection of the projectile ion, its kinetic energy and charge state, the main drawback is the kinematic effects that can alter the height, width and energy of the projectile Auger lines. These effects have to be treated successfully in order to obtain accurate information on Auger line energies and cross sections. In Fig. 2.3 a representative Auger spectrum is shown in the laboratory frame (right) and corrected for the kinematic effects of line shifting, stretching, angular compression and enhancement in the projectile rest frame (left). The origin and nature of these effects are described below.

2.1.1 Line shifting

It is easy to understand that due to the vector addition of the velocities of the projectile and the emitted Auger electron, the detection energy of the electrons will

appear shifted to higher or lower energies in the laboratory frame, depending on the emission angle $\theta' = 0°$ or 180°. Although the analytic description of these effects can be quite complicated, in the case of energetic ion-atom collisions, where the projectile ions are considered to be scattered into negligible small angles effectively close to zero, the resulting effects on both projectile energy loss and projectile trajectories are considered negligible. The problem now is translated to a velocity vector addition model, simple enough to determine the projectile-to-laboratory frame transformations [33, 59]. The kinetic energy of an electron emitted from a

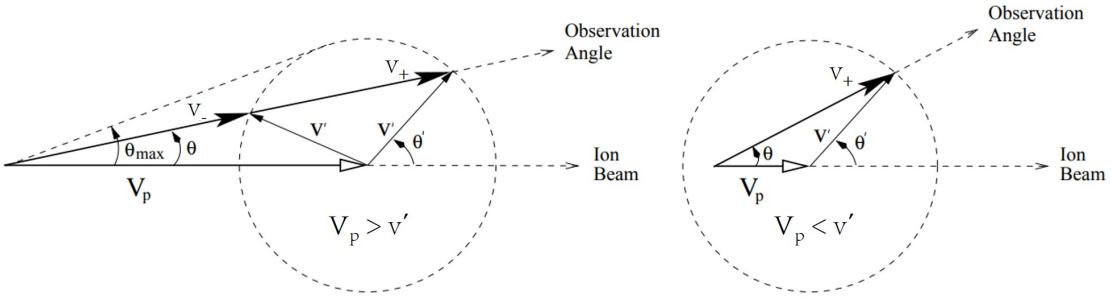

Figure 2.4: Velocity vector addition diagram when the projectile velocity V_p is larger (left) or smaller (right) than the emitted Auger electron, v′. Primed symbols are quantities in the projectile frame. The electron velocity in the projectile rest frame v′ is transformed to v in laboratory frame through the vector addition $\mathbf{v} = \mathbf{V}_p + \mathbf{v}'$. When $V_p > v'$ (left), the velocity vector addition leads to a maximum possible laboratory frame emission angle $\theta_{\max}$, while when $V_p < v'$ (right), θ can take any possible angle value (see [33, 59, 69]).

projectile in the laboratory frame is given classically by $\varepsilon = \frac{1}{2}mv^2$. From this energy the electron kinetic energy in the projectile frame $\varepsilon' = \frac{1}{2}mv'^2$ is extracted using the velocity addition diagrams in Fig. 2.4 as:

$$\mathbf{v}' = \mathbf{v} - \mathbf{V}_p \tag{2.1}$$

or in energy

$$\varepsilon' = \varepsilon + t_p - 2\sqrt{\varepsilon t_p}\cos\theta \tag{2.2}$$

or equivalently

$$\mathbf{v} = \mathbf{v}' + \mathbf{V}_p \tag{2.3}$$

or

$$\varepsilon = \varepsilon' + t_p + 2\sqrt{\varepsilon' t_p}\cos\theta' \tag{2.4}$$

where t_p is equal to the energy of an electron moving with the same velocity as the projectile,

$$t_p = \frac{1}{2}mV_p^2 = \frac{m}{M_p}E_p = 548.58 \cdot \frac{E_p(\text{MeV})}{M_p(\text{amu})}(\text{eV}) \tag{2.5}$$

with m being the electron mass, E_p and M_p are the kinetic energy and the mass of the projectile and θ and θ' are the ejection angles of the electron in the laboratory and the projectile rest frame, respectively.

In the case of zero-degree *forward* emission, i.e., $\theta' = 0°$) Eq. (2.4) results in:

$$\varepsilon = \varepsilon' + t_p + 2\sqrt{\varepsilon' t_p} = (\sqrt{\varepsilon'} + \sqrt{t_p})^2 = \varepsilon'(1+\zeta)^2 \tag{2.6}$$

where the dimensionless parameter ζ is introduced for convenience:

$$\zeta \equiv \frac{V_p}{v'} = \sqrt{\frac{t_p}{\varepsilon'}} \tag{2.7}$$

which gives the observed Auger line's energy ε', in the laboratory frame, ε. The characteristic Auger lines energies usually provided by theoretical calculations [70–73] are transformed to the laboratory frame according to the ion beam's kinetic energy in order to know in which energy region to expect the emitted projectile electrons. The uncertainty in the energy in the laboratory frame is given by:

$$\delta\varepsilon = \sqrt{\left(\frac{\partial\varepsilon}{\partial\varepsilon'} \cdot \delta\varepsilon'\right)^2 + \left(\frac{\partial\varepsilon}{\partial t_p} \cdot \delta t_p\right)^2} \tag{2.8}$$

or

$$\delta\varepsilon = \sqrt{\left[\left(1 + \sqrt{\frac{t_p}{\varepsilon'}}\right) \cdot \delta\varepsilon'\right]^2 + \left[\left(1 + \sqrt{\frac{\varepsilon'}{t_p}}\right) \cdot \delta t_p\right]^2} \tag{2.9}$$

The uncertainty in the line's energy $\delta\varepsilon$, is seen to depend on the uncertainties of the theoretical Auger electron energy $\delta\varepsilon'$ and the ion beam's kinetic energy δt_p. For the tandem accelerator of "Demokritos" $\delta t_p/t_p$ is considered to be $\approx 1 \times 10^{-3}$. Alternatively, rest frame Auger energies can be extracted from the laboratory frame for the projectile rest frame as:

$$\varepsilon' = \varepsilon + t_p - 2\sqrt{\varepsilon t_p} = (\sqrt{\varepsilon} - \sqrt{t_p})^2 \tag{2.10}$$

with the uncertainty in the energy at the projectile rest frame being:

$$\delta\varepsilon' = \sqrt{\left(\frac{\partial\varepsilon'}{\partial\varepsilon} \cdot \delta\varepsilon\right)^2 + \left(\frac{\partial\varepsilon'}{\partial t_p} \cdot \delta t_p\right)^2} \tag{2.11}$$

$$\delta\varepsilon' = \sqrt{\left[\left(1-\sqrt{\frac{t_p}{\varepsilon}}\right)\cdot\delta\varepsilon\right]^2 + \left[\left(1-\sqrt{\frac{\varepsilon}{t_p}}\right)\cdot\delta t_p\right]^2} \tag{2.12}$$

By converting the energy from the laboratory frame to the projectile rest frame, unidentified Auger lines can be easily recognized from their characteristic energies.

2.1.2 Relativistic corrections

At high collision energies, relativistic effects in the electron energies are observable and therefore, should be taken into account. Eq. (2.2), using the more accurate relativistic formula [74], then becomes:

$$\varepsilon' = \gamma_p\varepsilon + t_p - \sqrt{(1+\gamma)(1+\gamma_p)\varepsilon t_p}\cdot\cos\theta, \tag{2.13}$$

while Eq. (2.4) becomes

$$\varepsilon = \gamma_p\varepsilon' + t_p + \sqrt{(1+\gamma')(1+\gamma_p)\varepsilon' t_p}\cdot\cos\theta', \tag{2.14}$$

where γ_p, γ, γ' are the Lorentz factors for the moving projectile and electron, respectively [69], with:

$$\gamma_p = 1 + \frac{t_p}{mc^2} \tag{2.15}$$

$$\gamma = 1 + \frac{\varepsilon}{mc^2} \tag{2.16}$$

$$\gamma' = 1 + \frac{\varepsilon'}{mc^2} \tag{2.17}$$

For example, in the case of E_p=1 MeV/u and ε'=242.15 eV the ε_{clas}=1519.671 eV, while ε_{rel}=1520.213 eV.

2.1.3 Line stretching

As shown above, the Auger line energies in the laboratory frame and the projectile rest frame need to be transformed from the one frame to the other when extracting characteristic information from the detected Auger lines. Similarly, the energy width of an Auger line in the laboratory frame, $\Delta\varepsilon$, must be converted to the projectile rest frame $\Delta\varepsilon'$ in order to obtain the Auger line's characteristic information. By differentiating Eq. (2.2), for zero-degree measurements, it can be shown that:

$$\frac{\Delta\varepsilon}{\Delta\varepsilon'} \simeq \frac{d\varepsilon}{d\varepsilon'} = |1\pm\zeta| \tag{2.18}$$

$$\Delta\varepsilon = |1\pm\zeta|\Delta\varepsilon' \qquad (\theta = 0^\circ) \tag{2.19}$$

which means that the Auger lines in the laboratory frame will appear stretched for the forward emission (+), i.e., $\theta' = 0°$, and compressed for the backwards emission (-), i.e., $\theta' = 180°$. It is worth noting that the structure of the spectrum is not affected by this stretching effect, as it does not increase the overlap between close-lying lines, but only the separation between the lines increases or decreases accordingly.

2.1.4 Angular compression

Due to the motion of the projectile, electrons emitted isotropically in all directions in the projectile frame will appear ejected forward within a small angle in the laboratory frame. The relation between the two solid angles is [14]:

$$\Delta\Omega = \frac{\varepsilon'}{\varepsilon} \cdot \Delta\Omega' = \frac{\Delta\Omega'}{(1 \pm \zeta)^2} \qquad (\theta = 0°) \tag{2.20}$$

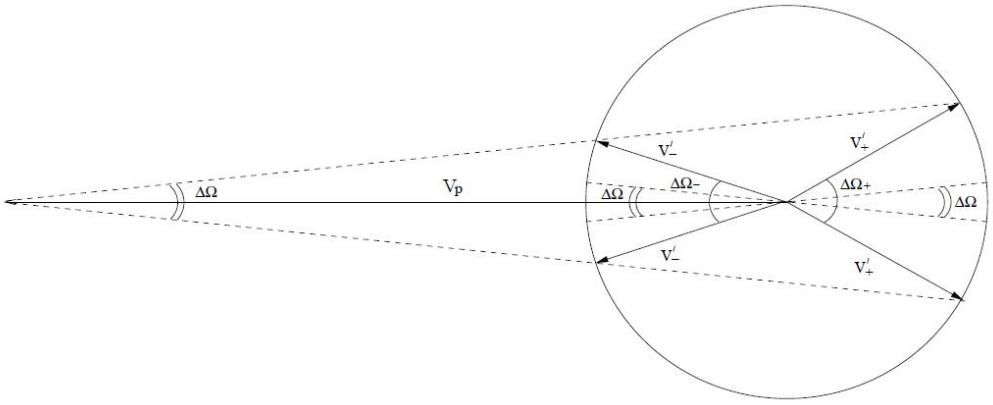

Figure 2.5: Angular range of emitted electrons in the laboratory and projectile frames. From Ref. [59].

2.1.5 Line enhancement

As shown in Fig. 2.3 the laboratory frame electron yield is enhanced compared to the projectile rest frame as a result of projectile electron kinematics. This is proven directly from Eq. (2.19) and Eq. (2.20) as:

$$\frac{\mathrm{d}^2\sigma}{\mathrm{d}\varepsilon \mathrm{d}\Omega} = |1 \pm \zeta| \frac{\mathrm{d}^2\sigma}{\mathrm{d}\varepsilon' \mathrm{d}\Omega'} \qquad (\theta = 0°) \tag{2.21}$$

Again, the (+) or (-) solutions refers to the forward or backward emission resulting in enhancement or diminution of the electron yield.

2.2 Auger line broadening effects

Projectile Auger lines are broadened according to the uncertainties in the parameters of the line shifting formula given in Eq. (2.2) which are seen to depend on $t_p = mV_p^2/2$ and the emission angle θ [75]. Thus, as explained schematically in Fig. 2.6, these line broadening effects depend primarily on the finite acceptance angle of the spectrometer $\Delta\theta$ and the uncertainty in the kinetic energy of the emitting projectile which can also be affected by straggling effects [76], when going through a foil during the stripping process in the tandem terminal or beyond (post-stripping). The recorded Auger line base width is usually approximated by the quadrature sum of these uncertainties. These effects set a lower limit on the possible energy resolution of the recorded spectra, independent from the experimental apparatus energy resolution capability. Further explanation of these effects is given below.

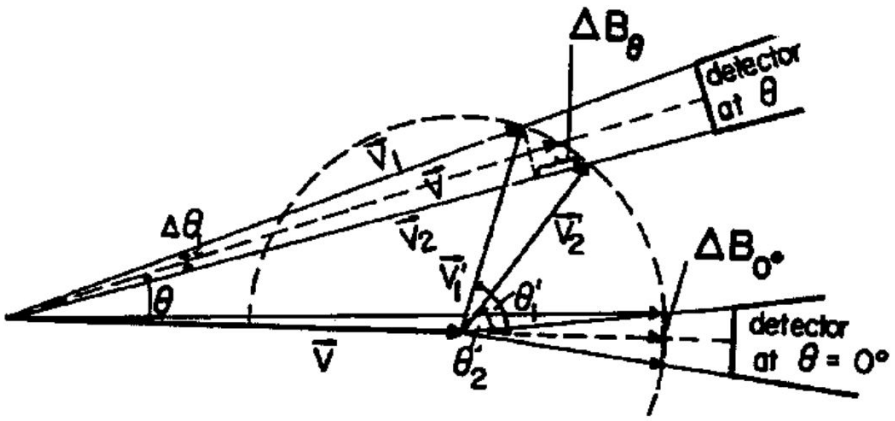

Figure 2.6: Schematic depiction of the geometric parameters explaining the kinematic broadening effect for a spectrometer with acceptance angle $\Delta\theta$. Two electrons emitted with identical velocities $v'_1 = v'_2$, but different emission angles θ'_1 and θ'_2 in the projectile frame, will be detected in the laboratory frame with different velocities $v_1 \neq v_2$ resulting in different corresponding kinetic energies and therefore kinematic energy broadening $\Delta B_\theta \sim \frac{1}{2}m|v_2^2 - v_1^2|$. From Ref. [33].

2.2.1 Kinematic line broadening ΔB_{0° due to the spectrometer's finite acceptance angle $\Delta\theta$

The particular line broadening effect can be easily understood through the following example. As shown in Fig. 2.6 two electrons detected at $\theta \neq 0^\circ$ will have different initial ejection angles θ' due to the finite angular acceptance $\Delta\theta$ of the spectrometer. Therefore, two electrons of the same energy ε' in the projectile frame due to vector addition, will have different velocities v_1 and v_2 and consequently different energies ε_1 and ε_2 in the laboratory frame [77]. This phenomenon creates an energy broadening $\Delta B = \varepsilon_1 - \varepsilon_2$ of the Auger line detected dependent on the detection angle θ, minimized for detection angles $\theta = 0^\circ$ or 180°. The kinematic line broadening

can be computed exactly as:

$$\Delta B_{\theta}^{exact} = |\varepsilon_1(\theta_1) - \varepsilon_2(\theta_2)| = 2\sqrt{t_p}\left(\sqrt{\varepsilon_2(\theta_2)}\cos\theta_2 - \sqrt{\varepsilon_1(\theta_1)}\cos\theta_1\right) \tag{2.22}$$

and can also be expanded in a Taylor series in powers of $\Delta\theta$ [30, 33, 77]:

$$\Delta B_{\theta}^{exact} \approx \left|\sum_n \frac{\partial^n \varepsilon(\theta)}{\partial\theta^n}\frac{(\Delta\theta)^n}{n!}\right| = \left|\sum_n \Delta B_{\theta}^{(n)}\right| \tag{2.23}$$

by differentiating the Eq. (2.2) with respect to θ and obtaining the Taylor expansion coefficients. Therefore the first order coefficient is:

$$|\Delta B_{\theta}^{(1)}| = 2\Delta\theta\sqrt{\varepsilon t_p}\frac{\sin\theta}{\left(1 - \sqrt{\frac{t_p}{\varepsilon}}\cos\theta\right)} \tag{2.24}$$

which is seen to be zero at $\theta = 0^\circ$ in which case the second order coefficient must be taken into account:

$$|\Delta B_{\theta=0^\circ}^{(2)}| = \Delta\theta^2\frac{t_p}{4}\left(\sqrt{\frac{\varepsilon'}{t_p}} + \sqrt{\frac{t_p}{\varepsilon'}} \pm 2\right) \tag{2.25}$$

This broadening effect increases the width of the Auger lines without increasing the separation between them. As a result, the overlap between two neighbouring lines increases, and can wash out intrinsic structures of the spectra. For the spectrometer in use in the present thesis, $\Delta\theta = 0.79^\circ = 1.38 \times 10^{-2}\ rad.$

2.2.2 Line broadening due to the energy spread of the emitting projectile ΔB_t

Another parameter that contributes to the broadening of the recorded Auger lines is the energy spread of the emitter-ion due to the variation of its kinetic energy t_p. This originates from the uncertainty in the energy of the ion beam delivered by the accelerator depending mainly on the slit opening after the 90° bending magnet that acts as an ion beam energy filter. Recently, our group performed a detailed study on the determination of the ion beam energy width in tandem Van de Graaff accelerators via Auger projectile spectroscopy, showing that the final ion beam energy width varies with the beam energy t_p and the stripping method [78]. This broadening can be computed to first order as:

$$\Delta B_t^{(1)} = \frac{\partial\varepsilon}{\partial t_p}\Delta t_p \tag{2.26}$$

using Eq. (2.2) for $\theta = 0^\circ$ observation angle it is obtained that:

$$\Delta B_t^{(1)} = \left(\frac{\Delta t_p}{t_p}\right) \varepsilon' \zeta |1 \pm \zeta| \qquad (\theta = 0^\circ) \tag{2.27}$$

In the case of the 5.5 MV tandem Van de Graaff accelerator of NCSR "Demokritos" $\Delta t_p/t_p$ value varies from 1×10^{-3} to 3×10^{-3} depending on application.

2.2.3 Auger natural line width Γ'_A line broadening

The Auger natural line width Γ'_A, i.e., the FWHM of the Lorentzian line profile, is obtained through calculations from theoretical probabilities of auto-ionization provided by recent literature [70–72, 79, 80]. In Table 2.1 the natural widths of the states with the highest intensity recorded in the experiments of the present thesis are shown.

Table 2.1: $1s2l2l'\,^{2s+1}L$ and $2l2l'\,^{2s+1}L$ Auger widths Γ'_A in s^{-1} and calculated in meV.

		Γ'_A (10^{13} s^{-1})	Γ'_A (meV)
$\mathbf{C}^{4+}$	$1s2s^2\ ^2S$	7.48[1]	49.2
	$1s2s2p\ ^4P$	1.06(-5)[2]	6.98(-5)
	$1s(2s2p\ ^3P)\ ^2P_-$	1.44[1]	9.47
	$1s(2s2p\ ^1P)\ ^2P_+$	3.86[1]	25.4
	$1s2p^2\ ^2D$	9.31[1]	61.3
	$2s2p\ ^3P$	1.31[3]	8.62
	$2s2p\ ^1P$	14.4[3]	94.8
$\mathbf{O}^{6+}$	$1s2s^2\ ^2S$	9.22[1]	60.7
	$1s2s2p\ ^4P$	3.00(-5)[2]	1.97(-4)
	$1s(2s2p\ ^3P)\ ^2P_-$	1.31[1]	8.62
	$1s(2s2p\ ^1P)\ ^2P_+$	5.41[1]	35.6
	$1s2p^2\ ^2D$	11.4[1]	75.0
	$2s2p\ ^3P$	1.32[3]	8.69
	$2s2p\ ^1P$	15.7[3]	103

[1]Ref. [72]. [2]Ref. [80]. [3]Ref. [71].

2.2.4 Line broadening of the total line width Γ_{tot}

By combining in quadrature the kinematic broadenings and the stretched natural line width Γ_A the total laboratory line width Γ_{tot} is obtained, i.e., the FWHM of

the observed Auger line in the laboratory frame).

$$\Gamma_{tot} = \sqrt{(\Delta B_t/2)^2 + (\Delta B_{0^\circ}/2)^2 + \Gamma_A^2} \approx \sqrt{(\Delta B_t{}^{(1)}/2)^2 + (\Delta B^{(2)}_{exact0^\circ}/2)^2 + \Gamma_A^2} \tag{2.28}$$

Note that the ΔB_t and ΔB_{0° refer to the base width of the Auger line so it is necessary to divide them by 2 in order to obtain their FWHM equivalent. Sometimes, it can be more convenient to apply the frame transformation formulas in order to obtain the rest frame total line broadening, Γ'_{tot}, since it is directly comparable with the rest frame FWHM of the observed experimental lines. This is expressed as:

$$\Gamma'_{tot} \approx \sqrt{(\Delta B_t'^{(1)}/2)^2 + (\Delta B'^{(2)}_{exact0^\circ}/2)^2 + \Gamma_A'^2} \tag{2.29}$$

where $\Delta B_t'^{(1)} = \Delta B_t^{(1)}/(1+\zeta)$ and $\Delta B'^{(2)}_{exact0^\circ} = \Delta B^{(2)}_{exact0^\circ}/(1+\zeta)$.

Chapter 3

Experiment

Overview

In this chapter the main principles of operation of the 5.5 MV (5.5 Million Volts) tandem Van de Graaff accelerator of the NCSR. "Demokritos" are explained together with the experimental apparatus of the APAPES (Atomic Physics with Accelerators Projectile Electron Spectroscopy) setup. The tandem accelerator of "Demokritos" is the only heavy ion research accelerator in Greece and operates since the mid 70's [81]. It is nowadays the major research facility of the Institute of Nuclear and Particle Physics (INPP) of the National Centre for Scientific Research "Demokritos" (NCSRD). In 2022, the tandem was significantly upgraded by the National Electrostatic Corporation (NEC). This upgrade included replacing the charging belt with a pelletron chain, the replacement of the old ion sources by new TORVIS (Toroidal Volume Ion Source) and SNICS II (Source of Negative Ions by Cesium Sputtering), able to provide high currents of light (H^-, D^-, He^-) or heavy elements (Li^- to Cu^-) from 20μA to 400 μA, and replacing the accelerator diffusion pumps by turbo pumps, thus improving the overall beamline vacuum to below 10^{-6} Torr. In addition, all analogue systems were replaced by digital ones, thus introducing a new control system for the tandem. However, all data for this PhD thesis was taken before the upgrade.

The APAPES project was initiated by Prof. Theo Zouros in collaboration with Prof. Manolis Benis of the University of Ioannina, as well as researchers Drs. Sotiris Harissopulos and Tasos Lagoyannis of the Demokritos Institute of Nuclear Physics via a successful THALES grant (2009-2014). Its main goal, was to extend the use of the tandem to also include atomic physics research and focus on the establishment of a new beamline (L45) dedicated to atomic physics research using zero-degree Auger projectile spectroscopy and utilizing highly charged ions from the "Demokritos" 5.5 MV tandem Van de Graaff accelerator [69].

3.1 The 5.5 MV tandem Van de Graaff accelerator of the NCSR "Demokritos"

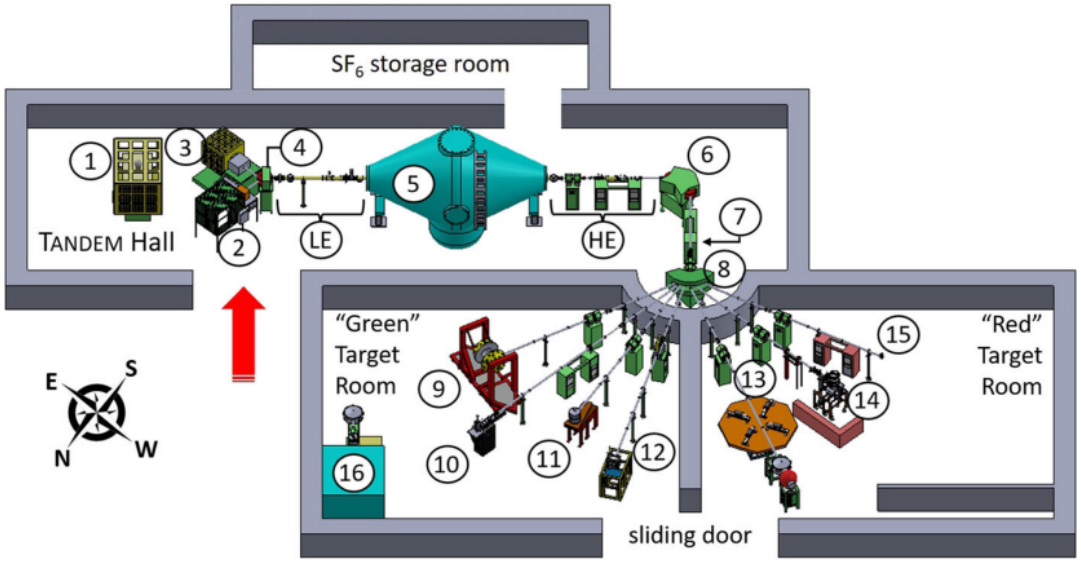

Figure 3.1: A schematic overview of the tandem Van de Graaff accelerator laboratory of the NCSR "Demokritos" in Athens. At (14) the L45 Atomic physics beamline and apparatus are depicted. From Ref. [81]. (Drawings by A. Laoutaris, I. Madesis and S. Nanos)

The experiments for the present thesis were performed at the NCSR "Demokritos" using the 5.5 MV tandem accelerator during the years 2016-2021. A 3-D schematic of the accelerator and the experimental beamlines is shown in Fig. 3.1. An initially negatively charged ion with charge $q_i = -1 \cdot e$, where $e = 1.6 \times 10^{-19}$ Coulomb the charge of the electron, is produced by a sputter or duoplasmatron ion source (2),(3). It is then pre-accelerated to 60 keV and injected into the low energy (LE) side of the tandem Van de Graaff accelerator. There, it is attracted by the positively charged terminal gaining a kinetic energy equal to $V_{term} \cdot q_i$, where q_i is the initial charge of the ion and V_{term} the accelerator's terminal voltage (5). In the terminal the ion beam undergoes a charge-stripping process, changing its charge to q_f, by passing through a gas, i.e., N_2, or solid, i.e., thin C foil, medium. As a result, the previously negative ion beam becomes positively charged and is further accelerated by the now repulsive positively charged terminal gaining an additional kinetic energy equal to $V_{term} \cdot q_f$. It thus exits on the high energy (HE) side of the tandem accelerator with a total energy gain of $E_{tot} = V_{term} \cdot (q_f + 1) \cdot e$. Since more than one charge states can be produced during the stripping process, especially for heavier ions, a 90° bending magnet is used as an ion beam energy analyzer (6) selecting the required energy and charge state. The ion beam is then directed to the right beamline by a switching magnet (8) and further guided to the target of the experiment (14). A system of multiple focusing elements, both electrostatic and

magnetic is also used for maximizing the ion beam transport to the target.

3.2 The Atomic Physics Experimental Apparatus

A dedicated beamline for atomic physics research was built within the APAPES project in the years 2012-2014 funded by the THALES program. In Fig. 3.2 a 3-D schematic of the setup is shown. In 2014, the first test experiments were performed with great success leading to the first publications [69, 82, 83].

During the experiments, a selected ion beam with specific energy and charge is delivered to the APAPES beamline. Two sets of four-jaw movable slits are used to collimate the ion beam, while two magnetic steerers together with a magnetic quadrupole are also used for focusing and guiding the ion beam smoothly through the gas cell target trying to minimize the hitting of any of its apertures in an effort to obtain best conditions for high resolution - low background measurements. The positioning and dimensions of the beam were also monitored by a Beam Profile Monitor (BPM) (see Fig. 3.2) for better transmission at the final Faraday Cup (FC2) at the end of the beamline. During measurements, the ion beam is initially maximized at a FC1, before the ZAPS setup and consequently driven through the target and the HDA spectrometer, to FC2. In Fig. 3.2 the complete APAPES setup is shown, while a photo of the experimental beam line is shown in Fig. 3.3. A more

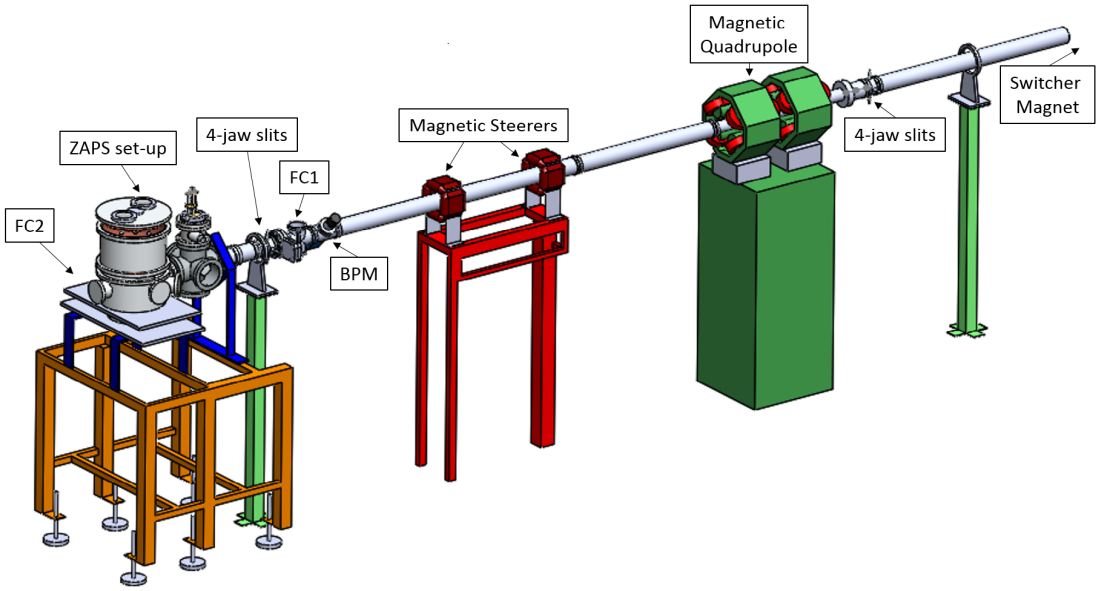

Figure 3.2: ZAPS setup used at the tandem Van de Graaff accelerator laboratory of the NCSR "Demokritos" in Athens (Drawings by A. Laoutaris and I. Madesis)

detailed view of the target-spectrometer area is shown in Fig. 3.4. The ion beam collides with the gas target producing intermediate excited atomic states that relax through the emission of Auger electrons or photons. The Auger electrons emitted at zero degrees with respect to the ion beam exit the target and enter a Hemispherical

Deflector Analyzer (HDA), where they are energetically separated and detected by a Multichannel plate Position sensitive detector (MCP-PSD). The ion beam passes through the HDA, exiting at the back of its outer electrode through a small hole. The beam is collected in Faraday cup FC2 used for normalization.

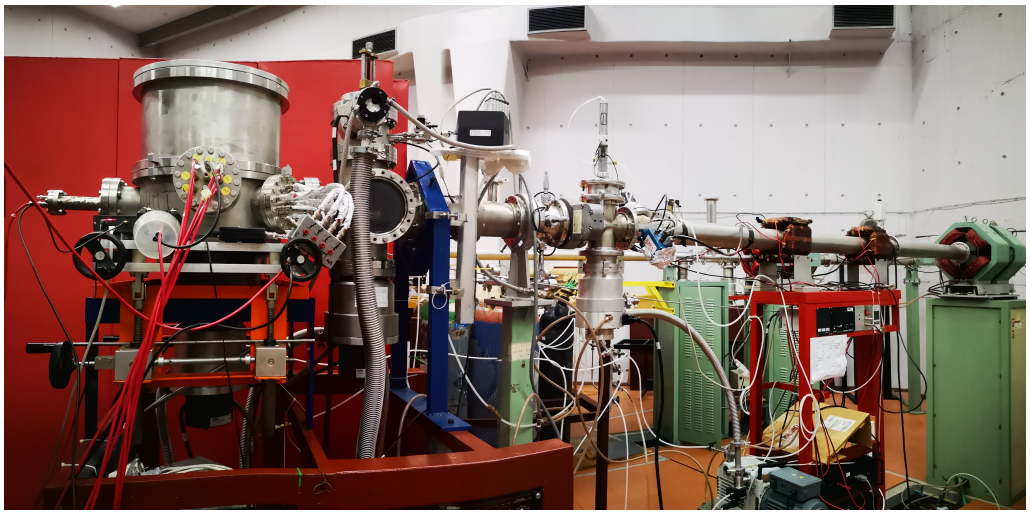

Figure 3.3: Photo of the whole APAPES beam line (January 2021).

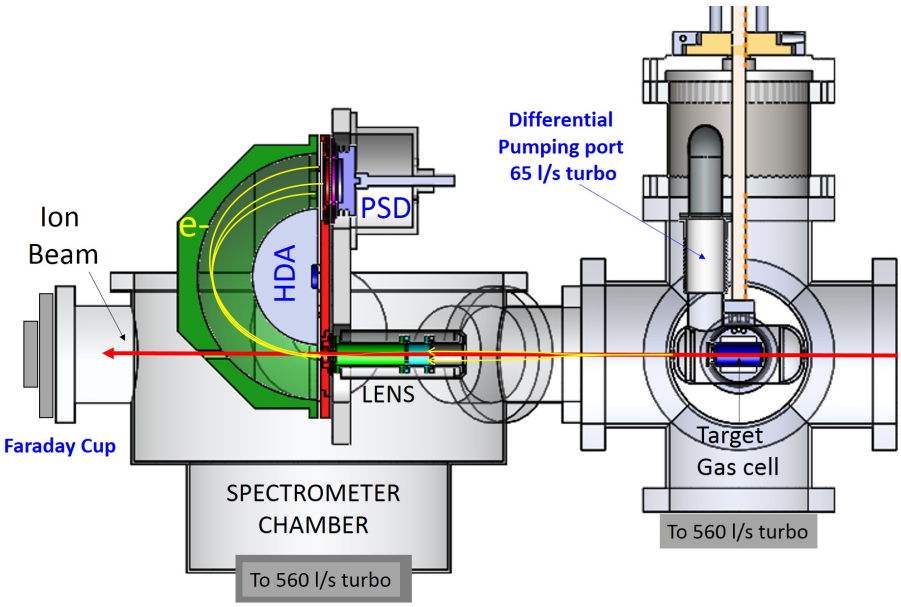

Figure 3.4: Schematic of the ZAPS setup used at the tandem accelerator laboratory of the NCSR "Demokritos". The projectile ion beam collides with the target atoms inside a doubly- differentially pumped cylindrical gas cell. The Auger electrons emitted in the forward direction at zero degrees are focused by the LENS and guided into the HDA, where they are energetically analysed and detected at the PSD. (Drawings by A. Laoutaris and I. Madesis)

3.3 Vacuum

High vacuum in the range of 10^{-7} Torr is required for our experiments. This is crucial for good beam transport as well as for low background. The vacuum at the APAPES experimental line is maintained by four turbomolecular pumps backed by three rotary pumps. Two 560 l/s turbo pumps are connected to the spectrometer chamber and the target cross, one 345 l/s turbo pump is connected to the beamline just before the target area, while a 65 l/s is connected to the gas cell's outer part in order to achieve double-differential pumping. The characteristics of the pumps used are shown in Table 3.1.

Table 3.1: Vacuum pump characteristics. From www.leyboldproducts.com.

Turbo molecular pumps	
Name	pumping speed N_2
Leybold TURBOVAC 600C	560 l/s
Leybold TURBOVAC 361C	345 l/s
Leybold TURBOVAC SL 80H	65 l/s
Rotary pumps	
Leybold SCROLLVAC 30D	500 l/min
Leybold SCROLLVAC 15D	250 l/min
Leybold TRIVAC D16B	266 l/min

3.4 The gas cell target system

One of the main parts of the APAPES setup is the target gas cell. It consists of two co-axial cylindrical cells of 25 mm and 63 mm in diameter with lengths of 50 mm and 140 mm, respectively. Its main function is to contain the gas target inside it. This system, known as a doubly-differentially pumped gas cell, is shown in Fig. 3.5, manages to handle sufficiently high target gas pressures (5-40 mTorr), while still maintaining very low pressures (10^{-6} - 10^{-7} Torr) in the rest of the apparatus. The two coaxial gas cells are separated by an insulating material making them electrically isolated from one another as shown in Fig. 3.6. The outer cell is grounded, while the inner one can be floated to high voltages for experimental purposes. The inner gas cell is connected to the gas target supply system through an electric valve controlled by an MKS Baratron manometer shown in Fig. 3.7 which manages the flow of gas in the cell in order to maintain a constant pressure inside it. The outer shell is connected to a small 65 l/s turbomolecular pump to pump the gas escaping the inner cell. The diameters of the apertures of the two cylinders given in Table 3.2 are small enough to contain efficiently the gas.

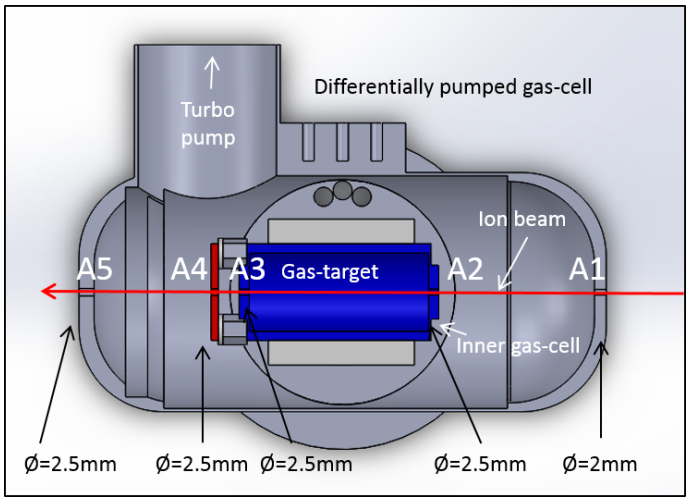

Figure 3.5: Schematic of the target gas cell. The gas is inserted into the inner gas cell (blue), where the ion-atom collisions take place. A second outer gas cell is used to pump down any excess gas pouring out of the inner cell and is connected to a turbo molecular pump. The apertures are noted with A1 to A5 symbols with the diameter of each one shown at the bottom. From Ref. [84].

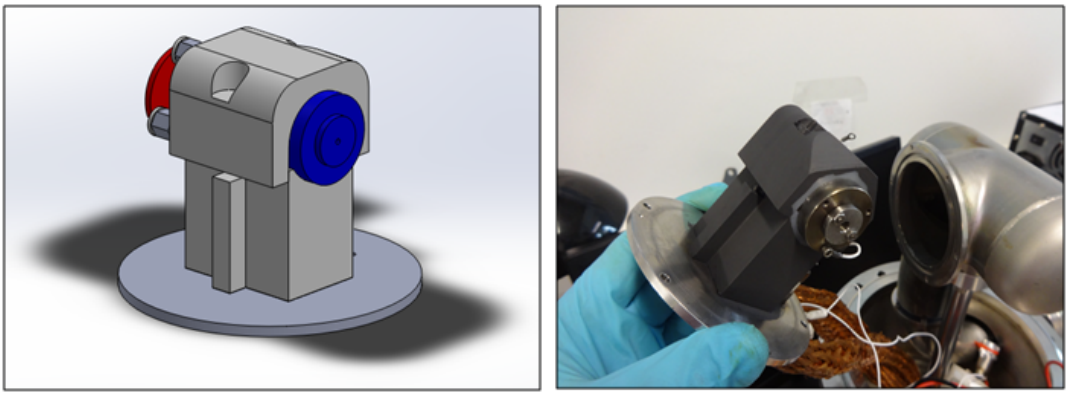

Figure 3.6: Schematic of the target gas cell together with actual photo. An insulating material keeps the inner gas cell electrically isolated from the outer one. From Ref. [84].

Table 3.2: Gas cell characteristics

Gas cell system	
Apertures (circular)	Diameter (mm)
A1 outer cell entrance	2.0
A2 inner cell entrance	2.5
A3 inner cell exit	2.5
A4 extra aperture	2.5
A5 outer cell exit	2.5
Inner cell diameter (outside dimension)	25
Outer cell diameter (outside dimension)	63
Inner cell length (outside dimension)	49.8
Inner cell length (inside dimension)	47
Outer cell length (outside dimension)	140

3.4.1 The MKS Baratron gas supply system

In order to control and maintain the gas target pressure at a constant value, an MKS Baratron pressure transducer together with a gas supply valve controller are used. The system consists of an MKS 390H pressure transducer, an MKS 248 control valve, an MKS 250E controller with an MKS 270D signal conditioner shown in Fig. 3.7 (left top and bottom) connected to a gas supply system Fig. 3.7 (right). With this system the gas supply in the target gas cell is controlled with the pressure gauge monitoring continuously the pressure inside the gas cell supplying more or less gas by controlling the gas supply valve [85].

Figure 3.7: [Left top and bottom:]The MKS Baratron manometer system. This system is used to maintain a constant target gas pressure inside the cell. [Right:] The target gas supply system. H_2, He, Ne and Ar are available for use.

3.4.2 Single-collision conditions

In order to obtain correct and accurate data, single-collision conditions must be ensured in our experiments. This means that the intermediate excited Auger states must be produced in a single-collision between a projectile ion and an atom of the target. This condition is directly related to the gas target pressure, and is satisfied when a sufficient low gas pressure is applied to the target gas cell [59]. When single collision conditions are achieved the intensity of the Auger peaks must be proportional to the gas target pressure. In the case where the single-collision conditions are violated, the Auger yields in the recorded spectra are no longer proportional to the gas pressure, as shown in Fig. 3.8. The explanation for this is that when too much pressure is applied in the target area the projectile ions can collide more than once during their passage through the target and as a result, states produced from the first collision are destroyed in the second one before managing to Auger decay.

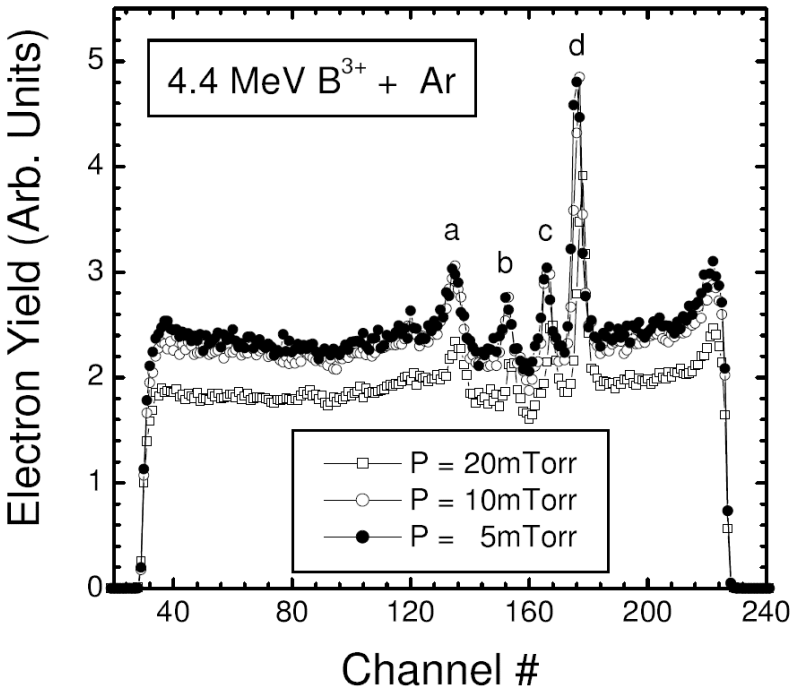

Figure 3.8: Representative spectra that show the dependence of the Auger yields on the gas target pressure. When too much pressure is applied, the intensity of the Auger peaks is no longer proportional to the gas pressure. From Ref.[59].

3.5 The Spectrometer

The spectrometer uses a paracentric HDA combined with a focusing four-element electrostatic lens and a MCP-PSD. A short description of its operation is given here since the properties of the paracentric HDA have been described extensively in the literature [59, 66, 68, 85]. The electrons produced in the ion-atom collisions exit the gas cell at $\theta = 0°$, enter along the axis of the electrostatic lens and are focused at the entrance plane of the HDA. The HDA, shown in Fig. 3.9 consists of four electrodes. The V_1 and V_2 electrodes, attached to the inner and outer hemispheres of radii R_1 =72.4 mm and R_2 =130.8 mm, are set to appropriate voltages in order to create an electrostatic field where the Auger electrons will be forced to follow elliptical trajectories before reaching the surface of the detector. These trajectories, depend on their kinetic energy and will be therefore energetically analyzed before reaching the detector forming a vertical focal line at its surface. The mean radius is $\overline{R} = R_\pi$=101.6 mm, while the paracentric entry is at R_0 =82.6 mm. The V_P electrode is used for retardation of the electrons, a method used for increasing the electron energy resolution of the spectrometer [3, 33, 59, 66, 85], while V_{bias}, a voltage applied in front of the detector, is set to an appropriate value so that the electrons of the central trajectory will impact the surface of the detector with a preset value so that the electrons always hit the detector with about 1000 eV kinetic energy for which energy the response of the detector is optimal. The projectile ions remain unaffected by the electrostatic field generated by the HDA due to their much larger mass, and therefore, exit the HDA at 0 degrees through a small hole at the back of the HDA. The HDA spectrometer together with the four-element electrostatic lens are shielded from the Earth's magnetic field with μ-metal, as it has been observed that the trajectories of the produced electrons can be otherwise affected. In Table 3.3 the parameters of the paracentric HDA in use are presented.

3.5.1 HDA operating voltages

In order for the HDA to function properly the inner and outer hemispherical electrode voltage values, i.e., V_1 and V_2, respectively, must satisfy the Eq. (3.1), regarding an electron of energy W entering the HDA at R_0 and exiting at R_π.

$$q \cdot V_i = \frac{W}{F}\left[F - \gamma \cdot \left(\frac{R_0}{R_\pi}\right) \cdot \left(\frac{R_0 + R_\pi}{R_i} - 1\right)\right] \qquad (i = 1, 2) \qquad (3.1)$$

where $q = -|e|$ is the electron charge, V_i refers to the voltage of the inner and outer hemispherical electrodes, R_0 and R_π are the entry and exit radii, respectively, F is the pre-retardation factor and γ is an independent parameter setting the entry bias $V_0 \equiv V(R_0)$. γ is defined as:

$$\gamma \equiv 1 - \frac{qV_0}{E_0} \qquad (3.2)$$

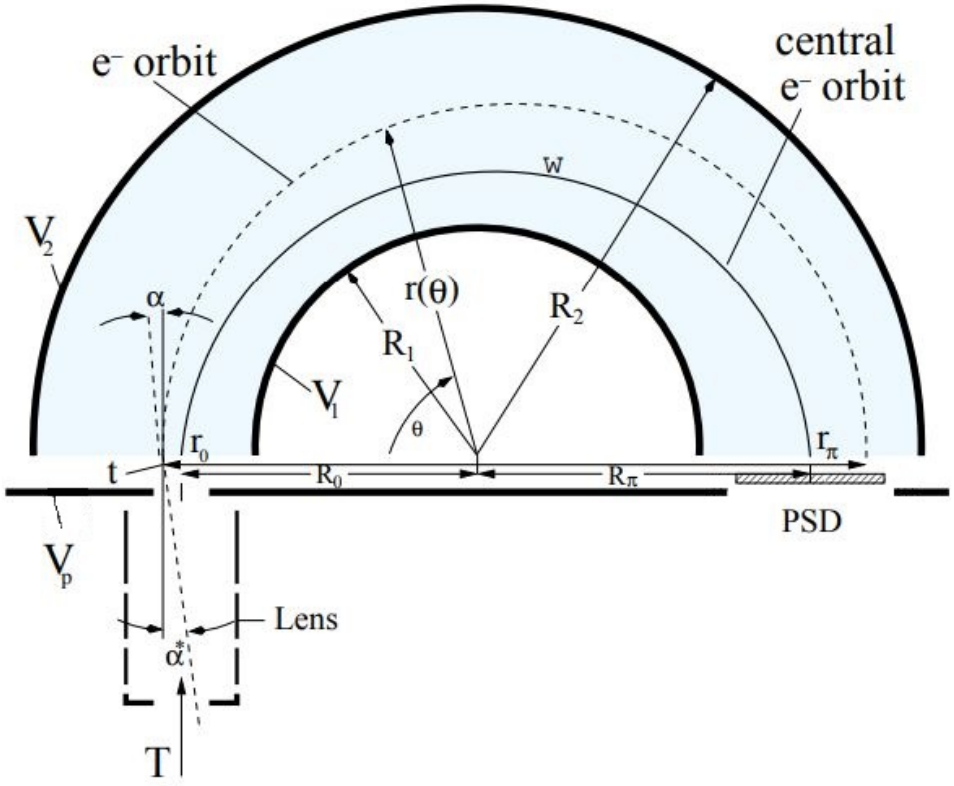

Figure 3.9: The HDA consists of two hemispherical electrodes one inner and one outer set on V_1 and V_2 potentials, a deceleration plate set on potential V_P, a four element focusing electrostatic lens and a position sensitive detector (PSD). Electrons within a certain energy acceptance window around the tuning energy w will be deflected and depicted on the surface of the PSD. The central trajectory used as reference (continuous black line) is defined as the trajectory of a particle which enters with energy E_0 at $r_0 = R_0$ with $\alpha = 0°$ and exits at $r_\pi = R_\pi$. From Ref.[86]

with V_0 being the potential value at R_0 and E_0 being the kinetic energy of an electron entering the HDA at $r_0 = R_0$ with $\alpha = 0°$ and exits at $r_\pi = R_\pi$. For the specific HDA in use $\gamma = 1.5$. This value was determined empirically using SIMION to obtain the best resolution. SIMION is a software package used to study electrostatic fields and orbits of charged particles [87]. F is the pre-retardation factor defined as:

$$F = \frac{W}{w} \tag{3.3}$$

where W is the undecelerated tuning energy, and w is the actual central trajectory pass energy. The electron pre-retardation, as explained below, is used for the improvement of the energy resolution of the recorded spectra. In order to achieve the electron pre-retardation, a potential V_P is applied at the plate electrode. The biasing value of V_P has to satisfy Eq. (3.4) and depends on the tuning energy W (the energy of the central electron trajectory before pre-retardation) and the actual

pass energy w in the HDA, directly related to the pre-retardation factor F.

$$V_P = w - W = \frac{W}{F} - W = W\left(\frac{1}{F} - 1\right) \leq 0 \tag{3.4}$$

The improvement in the analyzer's resolution can be explained by the base energy resolution equation for an ideal HDA given by [88]:

$$R_B \equiv \frac{\Delta E_B}{E_0} = \frac{\Delta r_0 + \Delta r_\pi}{D_\gamma} + \alpha_{max}^2 \tag{3.5}$$

where

- Δr_0 is the diameter of the entry aperture or slit. This particular HDA has a "virtual" aperture whose diameter is defined by the focusing lens and is much smaller than the actual 6 mm exit aperture of the lens.

- Δr_π is the diameter of the exit slit. Since a PSD is used instead of an exit slit, this value is set to the PSD's spatial resolution, Δx_π.

- α_{max} is the maximum angle of incidence at the HDA entry. This quantity squared is much smaller and can usually be ingored.

- D_γ is the dispersion length which is the magnitude of the image displacement resulting from a small change in the reduced pass energy τ, a characteristic length of the HDA which determines the shift of the image position of a particle trajectory for an infinite small change in the particle energy [86, 88]. For an ideal HDA is:

  $$D_\gamma = \left(\frac{R_\pi + R_0}{\gamma}\right)\frac{R_\pi}{R_0} \tag{3.6}$$

  The reduced pass energy τ is:

  $$\tau \equiv \frac{t}{w} = F\left(\frac{T}{W} - 1\right) + 1 \tag{3.7}$$

  where T is the initial kinetic energy of an electron ejected at zero potential far from the spectrometer and t is the post-retardation kinetic energy of the electron prior to entering the analyzer, equal to:

  $$t = T - qV_P \tag{3.8}$$

As seen in Eq. (3.5) the base energy resolution R_B is constant for an HDA, depending solely on its geometrical properties and γ which here is a constant set to 1.5 [89]. It can be easily concluded then, that decrease in the energy E_0 results inevitably in a simultaneous smaller ΔE_B and therefore better energy resolution. Furthermore,

in analyzer systems with pre-retardation capability, the concept of overall base resolution $\mathfrak{R}_B$ is introduced, referring to the HDA's improved resolution due to the deceleration of the injected electrons. Therefore the overall base resolution is given by Eq.(3.9) [6, 88].

$$\mathfrak{R}_B = \frac{\Delta E_B}{W} = \frac{1}{F}\frac{\Delta E_B}{w} = \frac{1}{F}R_B \tag{3.9}$$

In Fig. 3.10 normalized yield spectra of KLL Auger lines produced in collisions of 21.78 MeV F^{7+} + He obtained for pre-retardation factors F=1, 2 and 4 show clearly the improvement in the energy resolution with increasing value of F. In Fig. 3.11 the dependence between the half of the overall-base resolution, i.e., FWHM, is presented as a function of $1/F$ for a varying pre-retardation factor F.

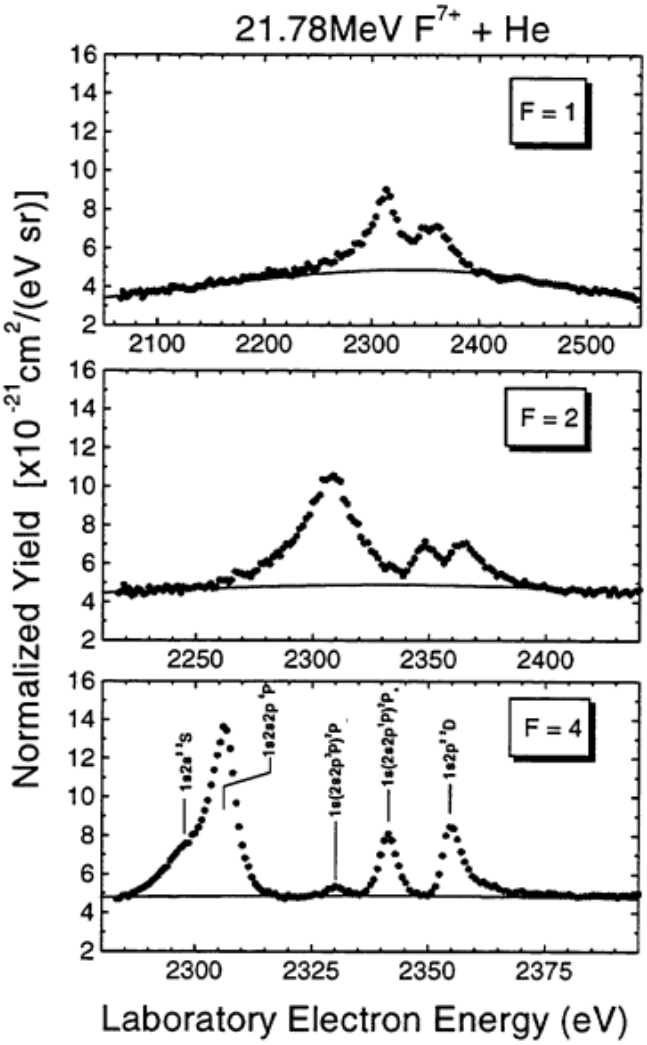

Figure 3.10: Normalized yields of various KLL Auger lines produced in collisions of 21.78 MeV F^{7+} +He. Clearly the energy resolution is improved as the retardation factor F increases. From Ref. [68].

3.5.2 The HDA's energy acceptance window

A unique advantage of the spectrometer in use is its ability to record a large portion of the spectrum simultaneously. The energy range of a spectrum detected by a HDA equipped with a PSD detector of diameter d_{PSD} is defined as the HDA's energy acceptance window $\Delta\tau_{window}$ [59]. In the case where electron pre-retardation is also used, the more useful quantity ΔT_{window} including the pre-retardation factor F defined as:

$$\Delta T_{window} = \Delta\tau_{window}\frac{W}{F} \tag{3.10}$$

is used. The energy acceptance window of the HDA in use is close to 20% ($\Delta T = |\frac{0.9W}{F} - \frac{1.1W}{F}|$) varying, according to the tuning energy W and pre-retardation factor F.

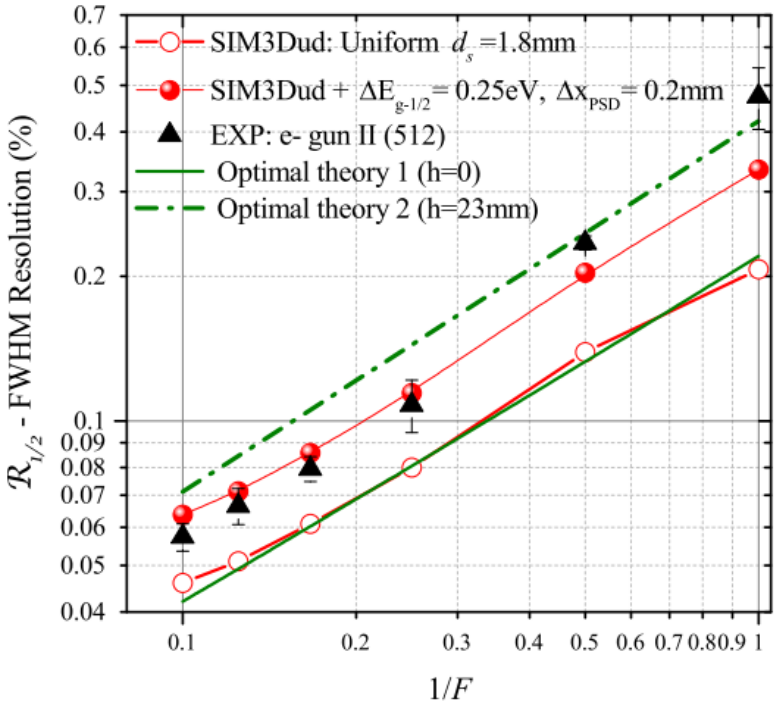

Figure 3.11: $R_{1/2}$ FWHM energy resolution is plotted as a function of 1/F for pre-retardation factor F. From Ref. [5]

Table 3.3: Paracentric HDA parameters. From [6]

R_1	72.4 mm	inner radius
R_0	82.55 mm	principal ray entry radius
R_2	130.8 mm	outer radius
$\overline{R}$	101.6 mm	mean radius
R_π	$\overline{R}$	principal ray exit radius
d_{PSD}	40 mm	active PSD diameter
V_0	$0.5w$	nominal Voltage at $V(R_0)$
$\alpha_{max} \equiv \Delta\theta_{max}$	$0.79°(1.38 \times 10^{-2} rad)$	maximum angle of incidence at the HDA's lens entry
γ	1.5	entry bias
W		HDA's undecelerated tuning energy "tuning" energy
w		HDA's actual central trajectory pass-energy
T		pre-retardation electron kinetic energy
t		post-retardation electron kinetic energy
τ		ideal HDA's reduced pass energy

3.6 The four-element electrostatic lens

A four-element electrostatic lens is used to provide the highest possible electron transmission and HDA energy resolution. Usually in HDAs, a small entry slit or aperture is used, which also determines the detected electron energy resolution. In our case though, since the ion beam also enters together with the electrons, a large enough entry aperture is needed to allow for the uninhibited passage of the ions (which otherwise could produce many background problems). The electrostatic lens focuses the electrons (it has no effect on the ions) on to the HDA's entry plane into a small spot thus providing in effect a virtual aperture. In Fig. 3.12 a 3-D schematic of the used electrostatic lens is shown. Note that the various electrodes are electrically isolated from each other unless otherwise noted. V_{L6} is typically set to ground, V_{L2} is electrically connected to V_P, while V_{L3} is connected to V_{L4}. Therefore, V_{L4} and V_{L5} have to be set at appropriate voltages in order to obtain the best conditions for electron transmission and energy resolution. For this purpose, electron trajectory simulations were run in various SIMION studies to obtain the best voltages to be used during measurements [5, 33, 90]. The effect of the actual lens on the spectrum is shown in Fig. 3.13.

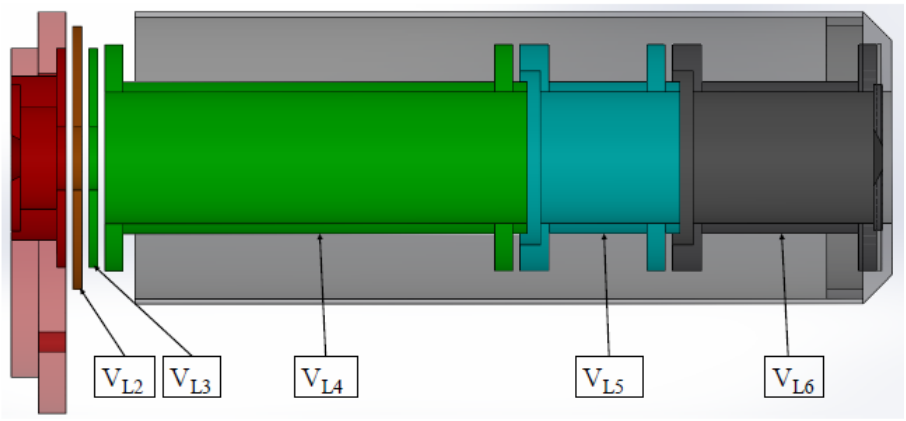

Figure 3.12: The electrostatic lens has a 4 mm entry diameter and four cylindrical electrodes electrically isolated from each other. By applying the appropriate voltages on elements V_{L4} and V_{L5}, optimal focusing of electrons at the entrance of the analyzer is achieved. From Ref. [85]

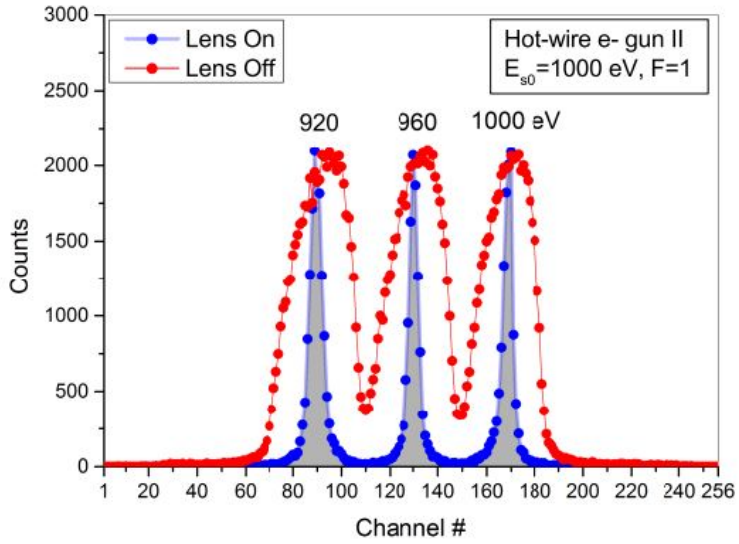

Figure 3.13: Example spectrum obtained with the use of a hot-wire e-gun with and without applied voltage on the four-element electrostatic lens. It is clear that the resolution of the spectrum is drastically improved when applying proper voltages on the lens. From Ref. [5]

3.7 The Detector

The detector used for electron recording is a two-dimensional PSD. It consists of two microchannel plates of 40 mm diameter in a Chevron configuration and a RAE as shown in Fig. 3.14. The MCP is a matrix of approximately 10^4 to 10^7 electron multipliers oriented parallel to one another working as microdynodes. Typical channel diameters are in the range of 10-100 μm and their length to diameter ratios is between 40 and 100. The typical distance between the microdynode centers is 50 to 150 μm. MCPs have the ability to multiply electrons to an output charge of 10^3-10^7 electrons allowing high position resolution particle detection. The RAE encodes the impact position of each electron in two-dimensions.

Another advantage of this type of detector is its high detection efficiency (around 50%). In our experiments the electrons that are guided and analysed energetically by the HDA reach the surface of the PSD forming a vertical focal line of incoming electrons. The signal from these impacting electrons is amplified by the MCPs and is finally encoded and translated to the image shown by our Data Acquisition system [59, 91]. A voltage divider as shown in Fig. 3.15 applies the appropriate voltages to the detector in order for the MCP plates to function properly.

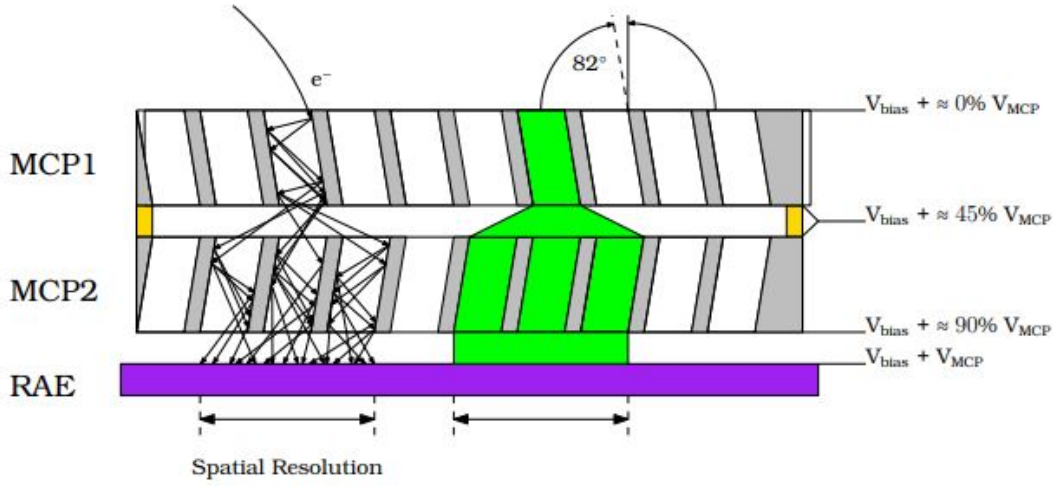

Figure 3.14: Schematic of the operation of a chevron configuration of 2 microchannel plates inside the two-dimensional PSD. Note that the voltage at the different stages depends on the V_{MCP} across the MCP which is set by a biased power supply. In our experiments V_{MCP} was set at 2050 Volts. From Ref. [59].

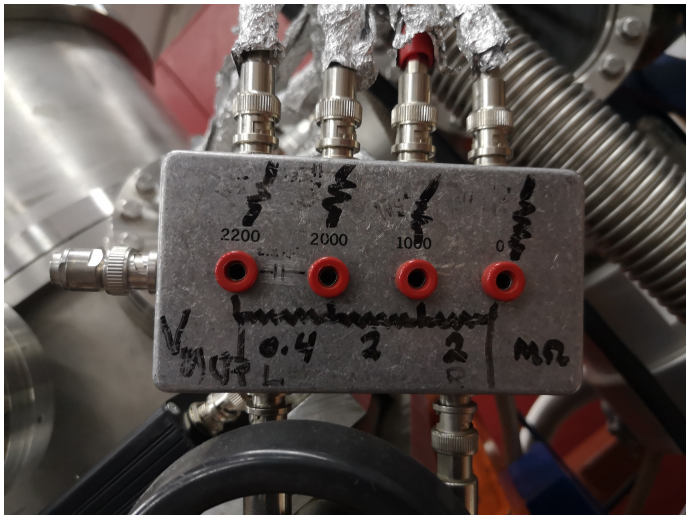

Figure 3.15: A home built voltage divider (resistor chain) is used to supply the appropriate voltages on the MCP plates.

3.8 Electronics

The complete electronics diagram is shown in Fig. 3.16. High voltage precision power supplies are used to apply the proper voltages at the HDA's and focusing lens electrodes, while a floating high voltage power supply together with a resistor chain voltage divider is used for the MCP-PSD, shown in Fig. 3.15. Furthermore, a pre-amplifier and a Digital Signal Processor (DSP) unit are used to obtain the signal from the detected electrons.

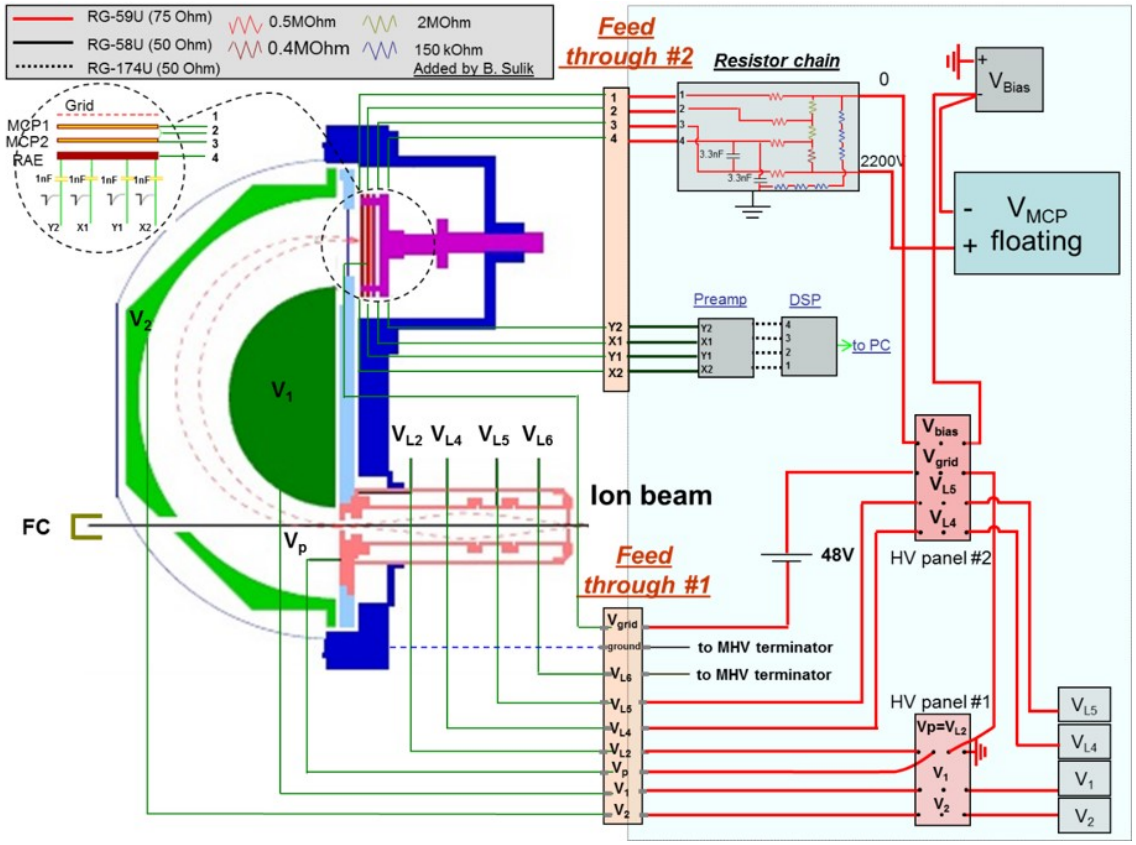

Figure 3.16: The complete electronics diagram and power supplies. From Ref. [59].

3.9 High Voltage Power Supplies

High precision (high stability and low noise) - high voltage power supplies, shown in Fig. 3.17 (right), are used to apply the appropriate voltages on the HDA, the electrostatic lens and the MCP detector. The HDA requires four dedicated voltage power supplies, the electrostatic lens requires two, while the PSD requires a floating power supply in order to apply an isolated voltage value at the detector shown in Fig. 3.17 (left). The whole voltage application is controlled through a LABVIEW interface developed for the particular setup by Fasmatech company as shown in Fig. 3.18. More specifically the power supplies in use are:

- HMI high precision HVPSs build by the Hahn-Meitner-Institut with fixed predefined polarity and the lowest ripple even at higher voltages, i.e., absolute error 0.2% and an additional 0.1%/kV.
- Tennelec HVPSs with the ability for both positive and negative polarity. They exhibit sufficient stability for the high resolution spectroscopy and were used mostly for testing and to apply voltage suppression at the Faraday cup collecting the ion beam.
- Applied Kilovolts HVPSs that can digitally reverse their polarity but at the cost of 1 bit. This drops their internal DAC's resolution to 15 bits. Taking all

that into consideration they were connected to specific voltages of the apparatus. They are integrated inside a mountable unit purchased from Fasmatech company. Specifically, inside the Fasmatech unit there are: 3 Applied Kilovolts with a ±10 kV range and 1 Applied Kilovolts with a ±5 kV range.

- An 6515A DC Hewlett-Packard 3 kV floating unit in order to provide appropriate voltage, V_{MCP}, on the MCP detector.

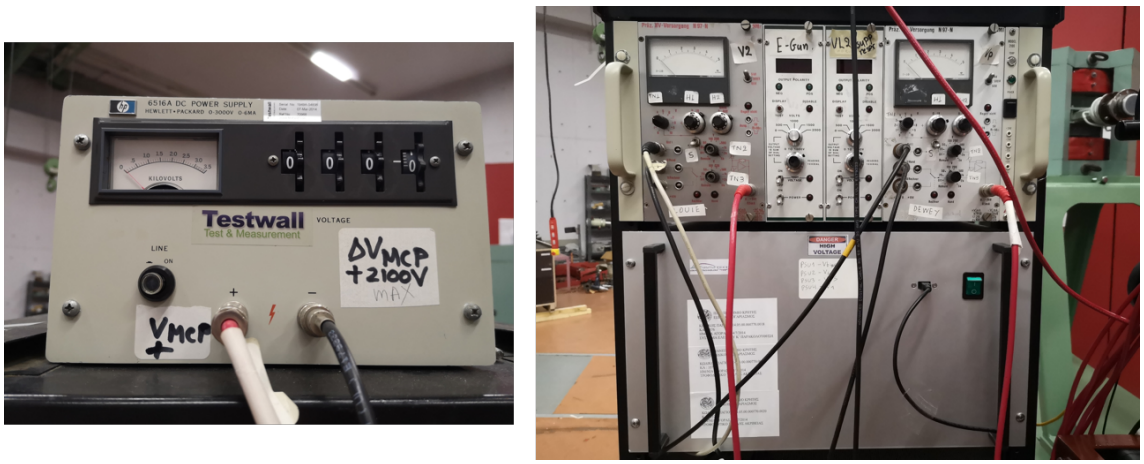

Figure 3.17: The power supplies used in APAPES setup. (Left): The floating high voltage power supply applying 2050V at the MCP-PSD. (Right): HMI high precision-low ripple ±5kV power supplies used for the voltage applied to the V_1 and V_2 hemispherical electrodes of the HDA [top] and the Fasmatech multiple HV power supply (±5kV, ±10kV) and controller "box" used for HDA's V_{bias}, V_P and V_{L4}, V_{L5} of the electrostatic lens [bottom].

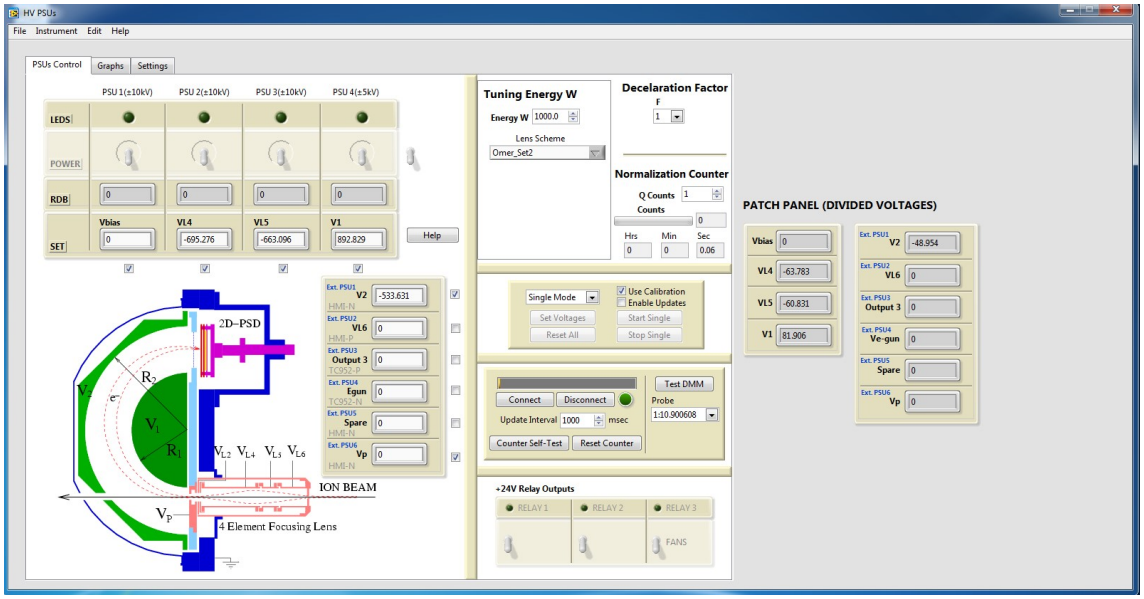

Figure 3.18: The HV PSU's LabVIEW high voltage power supplies control program's interface. This program is used for remote control of the high voltages applied on all the elements of the HDA and electrostatic lens. It serves also as an ion beam counter used in connection with the data acquisition system.

3.10 Data Acquisition

The detected electrons at the PSD produce four electric signals that are sent to a pre-amplifier unit, are amplified, and consequently, sent to a Digital Signal Processor (DSP) unit which serves as an Analogue to Digital Converter (ADC), shown in Fig. 3.19. The four signals obtained from the four corners of the RAE shown in Fig. 3.20 (left) are translated to X and Y coordinates according to Eqs. 3.11, 3.12 producing a two-dimensional image Fig. 3.20(right).

$$X = \frac{X_1 + Y_1}{X_1 + Y_1 + X_2 + Y_2} \tag{3.11}$$

$$Y = \frac{X_2 + Y_1}{X_1 + Y_1 + X_2 + Y_2} \tag{3.12}$$

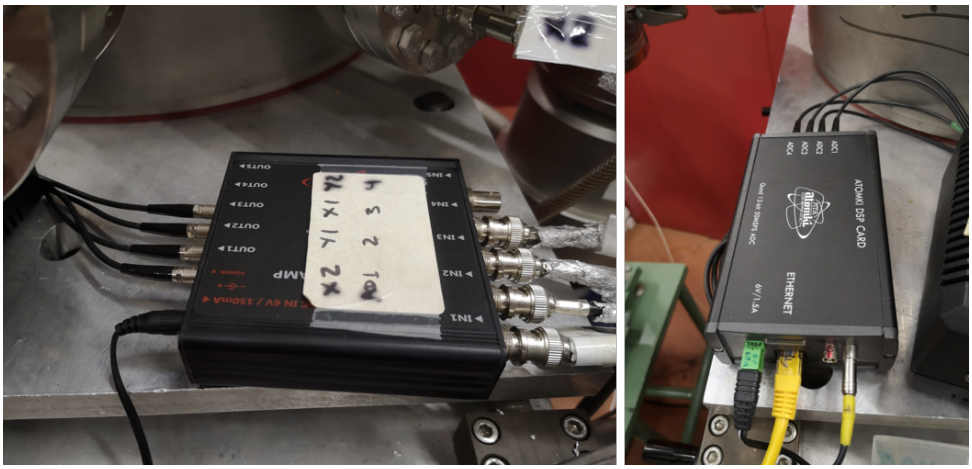

Figure 3.19: (Left): The pre-amplifier unit. (Right): The Digital Signal Processor (DSP) unit.

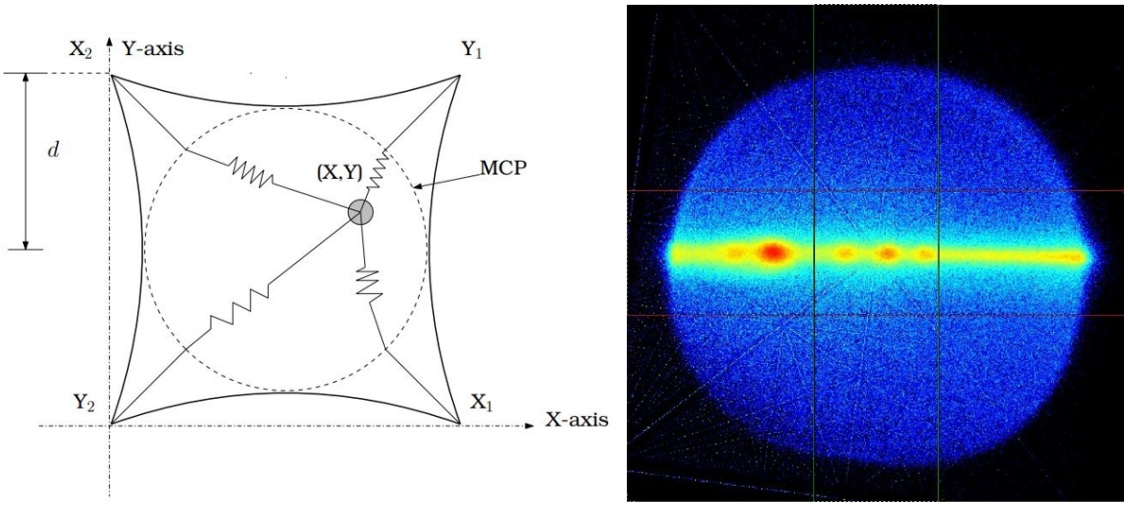

Figure 3.20: (Left): Schematic of a RAE. An electron arriving at the detector will produce four signals at the corners of the RAE interpreted as (X,Y) coordinates according to Eqs. 3.11 and 3.12. (Right): A typical Auger electron induced signal as seen on the data recording program. From Ref. [59].

Chapter 4

Data Analysis

Overview

In this chapter, the method used for transforming the recorded raw experimental spectra to energy calibrated double-differential cross section spectra is described. This process includes kinematic transformations regarding the energy calibration of raw data to the projectile rest frame and the electron yield normalization with respect to the parameters of the experiment. Thus, the recorded spectra are transformed from detector channels initially to the laboratory energy and finally to the projectile energy rest frames, together with the conversion of electron counts, to double-differential cross sections (DDCS) and eventually, to Auger electrons normalized yields and state production cross sections.

4.1 Recorded spectra Energy Calibration

The energy calibration method of the recorded spectra is straightforward. Auger electron spectral lines of known energies are converted from the rest frame to the laboratory frame according to the frame transformation Eq. (2.4). The spectrometer is then set at an appropriate pass energy in order to record this specific slice of the spectrum. Then, the detector channels are matched with the corresponding peaks and their laboratory frame energies. Upon recording a spectrum a 2nd order polynomial equation, i.e., Eq. (4.1), is then used to create a relation between the lab frame energy and the detector channels i.

$$E\left(i\right) = a + b \cdot i + c \cdot i^2 \tag{4.1}$$

Where i refers to the i-th channel of the detector and E is the corresponding laboratory electron energy. In Fig. 4.1 a representative spectrum of 12 MeV C^{4+} on He Auger KLL raw data with the recorded counts versus the detector channel number is shown. In Table 4.1 the computed laboratory frame energies of the Auger states used are shown, together with the channel value that the peak is recorded on the

detector.

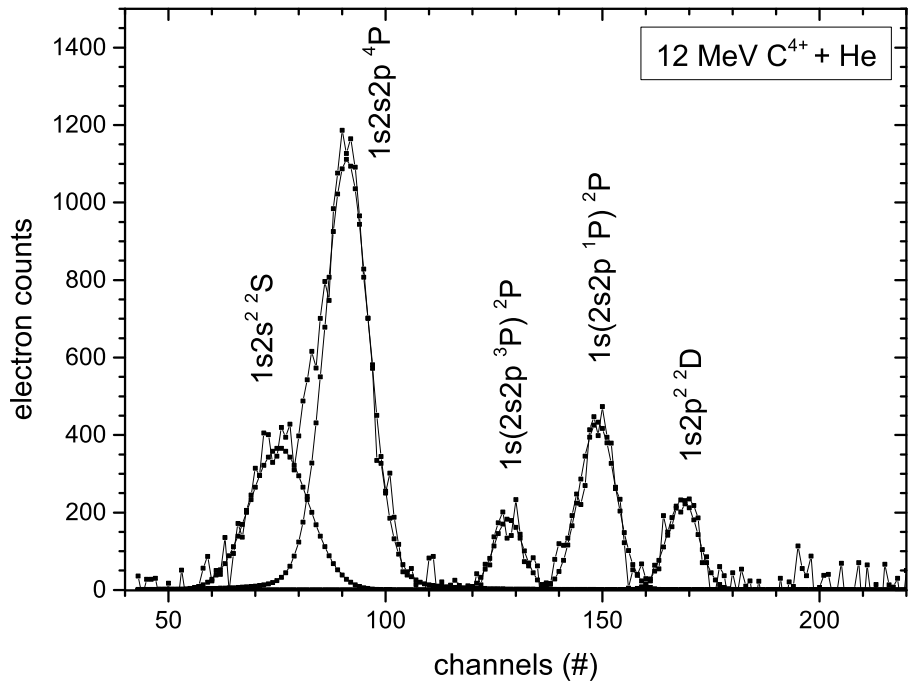

Figure 4.1: Spectrum of 12 MeV C^{4+} on He Auger KLL raw data with the recorded counts versus the detector channel number.

Table 4.1: KLL Auger electron energies together with their fitted peak center channel values and their corresponding energies in the lab frame for 12 MeV C^{4+}.

State	Auger energy (eV)	Lab frame energy (eV)	Fitted peak center (channel)
$1s2s^2\ ^2S$	227.23	1482.30	75.50
$1s2s2p\ ^4P$	229.64	1488.60	91.09
$1s(2s2p^3P)\ ^2P_-$	235.44	1503.32	128.30
$1s(2s2p^1P)\ ^2P_+$	238.86	1511.95	148.83
$1s2p^2\ ^2D$	242.15	1520.21	168.42

For example, using the data from Table 4.1 the a,b,c parameters computed are $a = 1454.37, b = 0.35$ and $c = 2.15 \times 10^{-4}$. From the above a,b,c, "universal" A, B, C values can be computed including also the passing energy W and pre-retardation factor F that the spectrometer is set to.

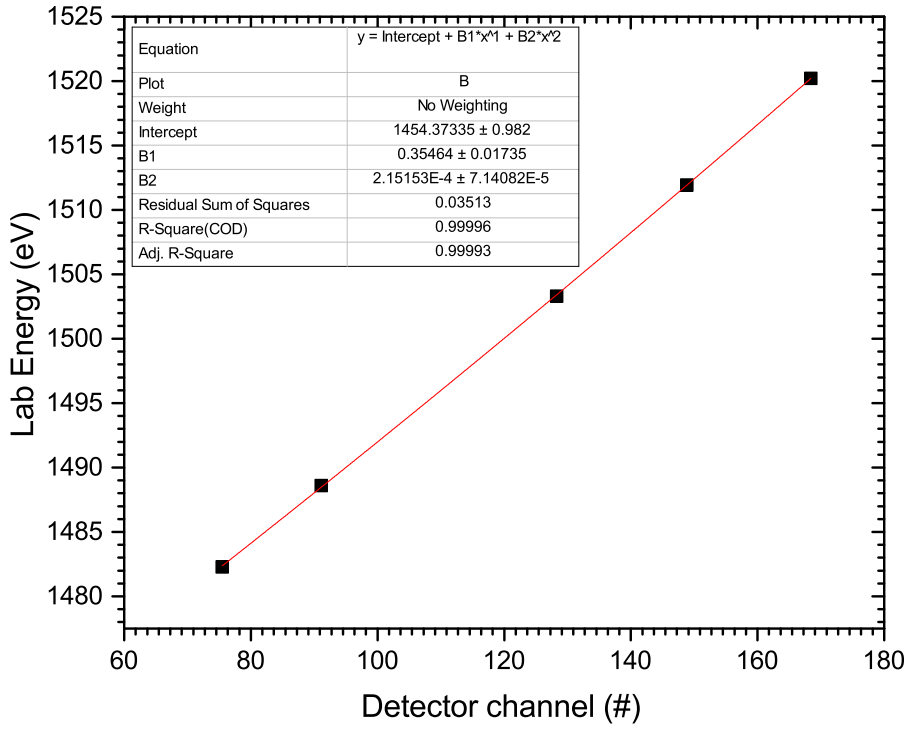

Figure 4.2: Auger lines lab frame energies versus channel detector values for a KLL Auger spectrum of $1s2s^{2}\ ^{2}S$, $1s2s2p\,^{4}P$, $1s(2s2p\,^{3}P)\ ^{2}P_{-}$, $1s(2s2p\,^{1}P)\ ^{2}P_{+}$, $1s2p^{2}\ ^{2}D$. By applying a 2nd order polynomial fit the a,b,c values are extracted.

$$A = \frac{a}{W}F - F + 1 \tag{4.2}$$

$$B = \frac{b}{W}F \tag{4.3}$$

$$C = \frac{c}{W}F \tag{4.4}$$

and solving for a, b, c, Eq. (4.1) is now converted to

$$E\left(i\right) = \frac{W}{F}\left(A - 1 + F + B \cdot i + C \cdot i^{2}\right) \tag{4.5}$$

By applying directly Eq. (4.5) to the spectra obtained at different W and F values these can now be converted from channels to lab frame energy [59].

4.2 Double-differential cross section determination

The laboratory double-differential cross section (DDCS) for Auger electron production is given by Eq. (4.6 [33, 59])

$$DDCS_i = \frac{d^2\sigma_i}{d\varepsilon d\Omega} = \frac{N_{ei} DTC}{N_I L_{eff} n T \Delta\Omega \Delta E_i \eta} \tag{4.6}$$

where i refers to the i-th channel of the X-projection of the PSD, N_{ei} is the number of the recorded electrons at the i-th channel of the detector, DTC is the dead-time correction, N_I is the number of ions collected at the Faraday cup, L_{eff} is the effective length of the gas cell, n is the number of the target gas molecules per cm^3, $\Delta\Omega$ is the solid angle determined by the opening of the spectrometer's lens-entrance and its distance from the target gas cell, ΔE_i is the energy step of the spectrum per channel, T is the transmission of the spectromemeter and η is the multi-channel plates efficiency. The single differential cross sections (SDCS) of the Auger lines are determined by integrating the spectral line's area corrected by the Auger electron yield. The projectile rest frame double-differential cross section is obtained by applying the frame transformations as:

$$\frac{\mathrm{d}^2\sigma}{\mathrm{d}\varepsilon' \mathrm{d}\Omega'} = \left(\frac{\varepsilon'}{\varepsilon}\right)^{1/2} \frac{\mathrm{d}^2\sigma}{\mathrm{d}\varepsilon \mathrm{d}\Omega} \tag{4.7}$$

$$\varepsilon' = (\sqrt{\varepsilon} - \sqrt{t_p})^2 \tag{4.8}$$

where ε' is the rest frame electron energy with $t_p = mV_p^2/2$ the laboratory kinetic energy of an electron with the same speed V_p as the projectile ion. The single differential cross sections (SDCS) of an Auger line is extracted by integrating the Auger line's area over its energy region and dividing it by its Auger electron yield.

4.2.1 Number of electrons recorded at the i-th channel of the detector - N_{ei}

Using the Data Acquisition program, a number of electrons in a specific channel i is recorded. This has with a statistical uncertainty $\delta N_{ei} = \sqrt{N_{ei}}$.

4.2.2 Dead-time correction - DTC

The dead-time of a detection system recording discrete events, such as particles, is the time after each event during which the system is unable to record another event [92]. In fact, the DTC was experimentally tested and found to be equal to 1, i.e., no dead time, for rates of events up to 112 kHz [85]. Since the typical counting rate in our experiments is 1 to 20 kHz, there is no need for such a correction.

4.2.3 Number of incident ions - N_I

The ions passing through the gas target are collected at the Faraday cup at the end of the beamline. This number is calculated by the formula:

$$N_I = \frac{Q(\text{nC})}{q \cdot 1.6 \times 10^{-10}(\text{nC})} \tag{4.9}$$

where q is the ion beam's charge state, Q is the total charge recorded at the final Faraday cup in nC and 1.6×10^{-10} is the electron charge in nC. Q is calculated from the number of counts Q_{qnt} produced by a Brookhaven Model 1000 beam current integrator (BCI). The uncertainty in C_{nts} is ginen to be $\delta C_{nts}/C_{nts}$=0.02% for all scales. I_{FS} the scale of the BCI in nA and C_{nts} is the number of pulses generated at full scale. In the case of this thesis, this is $C_{nts} = 100$ Hz.

$$Q(nC) = \frac{Q_{cnt} \cdot I_{FS}(\text{nA})}{C_{nts}} \tag{4.10}$$

The determination of N_I relies on the assumption that the beam current remains unaffected by the ion-atom collisions in the target gas cell. However, this is not completely accurate as the projectile electron loss or capture processes increase or decrease the beam charge respectively. A rough estimation on the beam charge can be attempted in the case when current I_0 is passing through a gas target of density n.

In this scenario, the beam current, I, resulting from a path length, L, is given by

$$I = I_0 \sigma n L \tag{4.11}$$

where σ is the total cross section. Assuming a gas cell length of L $\approx$ 5 cm, a typical target pressure of 20 mTorr, which corresponds to approximately 6 $\times 10^{14}$ molecules/cm^3, and a typical total cross section of 10^{-19} cm^2, it is found that I/I_0 = δN_I = 0.03%. Consequently, the beam current percentage variation amounts to $0.03/q_p$%, where q_p denotes the initial beam charge. Assuming an average value of $q_p = 4$, the uncertainty in the beam current and therefore in the number N_I is: $\delta N_I/N_I \leq 0.0075\%$.

4.2.4 Effective gas cell length - L_{eff}

The incident ion beam passes through the gas target contained in the gas cell of length equal to L. Therefore the probability of interaction between the projectile ion and the target atoms is directly connected also to the length of the gas cell. The effective gas cell length is a computed value that takes into account the actual length of the gas cell and the dimensions of the entry and exit apertures and corresponds to the length of the path available for interaction. For a gas cell of actual length L and apertures on either side of diameters D_1 and D_2, the effective length is given

by:

$$L_{eff} = L + \frac{D_1 + D_2}{2} \tag{4.12}$$

where, in our case $L = 47.0$ mm and the entrance and exit apertures D_1 and D_2 have a diameter of 2.5 mm. Therefore $L_{eff} = 49.5$ mm. $(D_1 + D_2)/2$ can be accepted as the uncertainty in length determination, resulting in $\delta L/L$=5.3%

4.2.5 Target gas density - n

n refers to the gas number of molecules per cm^3. Assuming that the experiments are done at room temperature (300°K), the density can be calculated by using the state equation which is summed up in the following formula [59]:

$$n(\#\text{ molecules/cm}^3) = 3.222 \times 10^{13} P(\text{mTorr}) \tag{4.13}$$

P is the pressure of the gas target maintained at a specific value by the MKS Baratron capacitive manometer system controlling the operation of the gas supplying electric valve. According to the baratron readings during the measurements, the pressure uncertainty was never larger than 1.25%. Consequently, $\delta n/n \leq 1.25\%$.

4.2.6 Detection solid angle - $\Delta\Omega$

The detection solid angle $\Delta\Omega$ is defined by the distance l between the gas cell's center and the entrance of the spectrometer's lens ($l = 289.48$ mm) entrance and the diameter of the lens aperture ($d_{lens} = 4$ mm).

$$\Delta\Omega = \frac{\pi \cdot d_{lens}^2}{4l^2} = 1.5 \times 10^{-4} \text{ sr} \tag{4.14}$$

The uncertainty in the solid angle is primarily attributed to the uncertainty in the measurement of l, which less than 2%. This results in an uncertainty in the determination of the solid angle of $\Delta\Omega/\Omega \leq 2\%$.

4.2.7 The energy step per channel - ΔE_i

The detector channels are converted to energy by a calibration procedure in which Auger lines of known energies at a specific ion beam energy are used as a standard. This way, a detector channel versus energy relation is created through a 2nd order polynomial equation (as already presented in Eq. (4.1)). Consequently the energy step per channel is:

$$\Delta E_i = b + 2c \cdot i \tag{4.15}$$

computed from the first derivative of $E(i)$ in Eq. (4.1). For a typical spectrum such as in Fig. 4.1 using the data values from Table 4.1 for channel i=128, ΔE=0.405 eV$\pm$4%.

4.2.8 Analyzer transmission - T

The analyzer transmission refers to the ratio between the number of electrons reaching the detector to the number of electrons that entered the spectrometer initially, i.e., the lens entrance. The transmission of electrons is decreased by the three grids used at the face of the detector, useful for deflecting background electrons created inside the spectrometer, each having a transmission of 90% resulting in a total transmission of $T = 0.90^3 = 0.729$. The accuracy of the determined transmission value is expected to be better than 0.01, therefore $\delta T/T = 1\%$

4.2.9 Micro Channel Plate (MCP) efficiency - η

The MCP efficiency is the probability of an electron hitting the surface of the MCP to create a measurable signal, i.e., a pulse higher than the noise signal. This depends on the area of the MCP occupied by microchannels over the total area of the MCP also referred as the active MCP area, as well as the kinetic energy of the electrons hitting the MCP. In our case the MCP presents a maximum efficiency at around 350 eV dropping slowly for higher energies, while for lower energies it drops rather fast. Due to the fact that the efficiency function varies quite fast around 350 eV a higher value of 1000 eV impact energy was chosen for the central ray of electrons reaching the MCP. In order to maintain the 1000 eV impact energy value, a controlled V_{bias} potential value is applied to the front of the MCP that adds or subtracts kinetic energy from the arriving electrons, thus maintaining their impact energy roughly at 1000 eV [33, 59, 85]. In order to experimentally determine the MCP efficiency, two known normalization methods were used. Either a comparison to the Binary encounter peak or using known cross sections of target Auger electrons [59, 93]. By applying both methods during our experiments, a value of $\eta = (50 \pm 5)\%$ was determined and used in the analysis of the present data. In Table 4.2 typical quantities used in the determination of the absolute DDCS spectra, according to Eq. (4.6) along with their maximum uncertainties are presented.

Table 4.2: Typical experimental quantities used in the determination of the absolute DDCS spectra, according to Eq. (4.6). Typical values are shown together with their maximum percentage uncertainties.

Quantity	Symbol	Typical value	Uncertainty
Number of ions	N_I	3.9×10^{12} [1]	± 0.0075%
Effective gas cell length	L_{eff}	49.5 mm	± 5.3%
Target density	n	$3.222 \times 10^{13} \cdot P$ mTorr	± 1.25%
Energy step per channel	ΔE_i	0.405 eV [2]	± 4%
Acceptance solid angle	$\Delta\Omega$	1.5×10^{-4} sr	± 2%
Grid transmission	T	0.729	± 1%
MCP efficiency	η	50%	±5%

[1]Refers to ≈2500 nC of ion charge q=4 collected at the FC2.
[2]Typical value corresponding to channel i=128 according to the experimental parameters of Table 4.1.

4.2.10 Error analysis

The uncertainties in ZAPS DDCS measurements involves both statistical and systematic errors. The statistical uncertainties arise from the electron counts, i.e., $N_{ei} \pm \sqrt{N_{ei}}$, while systematic errors include the uncertainties of the quantities present in Eq. (4.6). The average absolute systematic uncertainty can then be estimated by adding in quadrature all the estimated systematic uncertainties for each term in Eq. (4.6) as:

$$\frac{\delta\sigma}{\sigma} = \sqrt{\left(\frac{\delta N_I}{N_I}\right)^2 + \left(\frac{\delta L}{L}\right)^2 + \left(\frac{\delta n}{n}\right)^2 + \left(\frac{\delta(\Delta E)}{\Delta E}\right)^2 + \left(\frac{\delta(\Delta\Omega)}{\Delta\Omega}\right)^2 + \left(\frac{\delta T}{T}\right)^2 + \left(\frac{\delta \eta}{\eta}\right)^2}$$

$$\leq 17.4\% \tag{4.16}$$

Chapter 5

He-like beams with mixed state content

Overview

As already mentioned, He-like ion beams, i.e., ions with only two electrons, are used in our experiments. In tandem Van de Graaff accelerators, such highly charged ions are readily produced by passing a lower charge state beam through a thin foil or gas medium, at the accelerator's terminal or/and at a point further downstream. Through this process, known as charge-stripping, a Gaussian-like charge state distribution centered around a mean value is created, according to the ion's kinetic energy during the stripping process, its atomic number Z_p and the density of the stripping medium (solid or gas) [94]. In general, the higher the ion beam energy and the density of the medium, the higher the mean charge state produced [95, 96]. Occasionally, the stripping energy at the terminal is not sufficient for the creation of a highly charged state of sufficient intensity and a second stripping after the full acceleration of the beam, known as post-stripping, is required. Multiple computer codes have been developed providing relatively accurate charge state distributions such as ETACHA [97], CHARGE [95, 98–100] and TARDIS [101] based on known charge state equilibrium equations. After charge-stripping, the desired ion charge state and energy are magnetically selected by a 90° analyzing or a switching magnet (in the case of post-stripping), before injecting into the beamline of the experiment.

5.1 Properties of the excited He-like ion beams: $1s2s\,^3S$ and $1s2s\,^1S$ metastable states

He-like ions present a number of characteristics that make them attractive for ion-atom collision mechanism studies. First of all, a He-like ion is one of the simplest few-electron systems which, combined also with a few-electron target such as He or H_2, can therefore be expected to be much better understood, both experimentally and

theoretically, as the important channels available for ionization, capture or excitation are more limited [94]. Secondly, when created through charge-stripping, the He-like ion beam exists in a mixture of three components, the (stable) $1s^2\,{}^1S$ ground-state and the two excited $1s2s\,{}^1S$, $1s2s\,{}^3S$ metastable states with lifetimes, as shown in Table 5.1, long enough, especially for the $1s2s\,{}^3S$ state, to survive to the target. Both $1s2s\,{}^1S$ and $1s2s\,{}^3S$ states owe their metastability to the atomic orbital transition rules, since the electric dipole (E1) transition $\Delta\ell = \pm 1$ and spin transition $\Delta S = 0$ rules forbid their transition to the $1s^2\,{}^1S$ ground state. The $1s2s\,{}^1S$ can only decay to ground through two-photon emission, while the $1s2s\,{}^3S$ decays to ground through a magnetic-dipole (M1) transition, both being low probability transitions, though increasing with atomic number Z_p [102, 103], as spin-orbit interactions become non-negligible. The number of ions $N(z_0)$ produced in state S, surviving a distance z_0 downstream from the stripper is given quite generally by the exponential decay law:

$$N_S(z_0) = N_S(z = 0) \cdot \exp\left(\frac{-z_0}{V_p\,\tau_S}\right) \tag{5.1}$$

where $N_S(z = 0)$ is the number of ions produced at the stripping point $z = 0$, τ_S is the lifetime of state S (see Table 5.1) and V_p is the ion beam's velocity. In our particular experimental setup, the distance between the stripping points and the target are approximately s_{ter}=26.35 m or s_{post}=12.1 m depending on whether the terminal or the post-stripper system is used. Alternatively, $N_S(z = 0)$ can be simply obtained from the measured number $N_S(z_0)$ at the target point $z = z_0$ inverting Eq. (5.1):

$$N_S(z = 0) = N_S(z_0) \cdot \exp\left(\frac{z_0}{V_p\,\tau_S}\right) \tag{5.2}$$

He-like ion beams in collisions with a target, lead to the production of various intermediate states X populated from each component by different production mechanisms, which many times can be uniquely identified depending on collision energy E_p and population S of the initial beam component at the collision site $z = z_0$, $N_S(z_0)$. The determination of the absolute production cross section for the state X therefore clearly also requires the accurate knowledge of the initial population of the particular beam component S, i.e., the fractional beam composition, from which it was produced.

The fractional composition of the beam with n-components is defined quite generally as:

$$f_{S_i}(z_0) \equiv \frac{N_{S_i}(z_0)}{N_I(z_0)} \tag{5.3}$$

where $N_I(z_0)$ is the total number of ions in all n components

$$N_I(z_0) = \sum_i^n N_{S_i}(z_0) \qquad (i = 1, \ldots n) \tag{5.4}$$

and therefore we also have the correct normalization

$$\sum_i^n f_{S_i}(z_0), = 1 \tag{5.5}$$

For our three-component He-like ion beam since the two metastable states, ^3S and ^1S, can only decay to the third component, the ground state, N_I is a constant independent of z_0. Thus, we have:

$$f_{^3S}(z_0) \equiv \frac{N_{^3S}(z_0)}{N_I} \tag{5.6}$$

$$f_{^1S}(z_0) \equiv \frac{N_{^3S}(z_0)}{N_I} \tag{5.7}$$

$$f_g(z_0) = [1 - f_{^3S}(z_0) - f_{^1S}(z_0))] \tag{5.8}$$

with the normalization

$$1 = f_g(z_0) + f_{^3S}(z_0) + f_{^1S}(z_0) \tag{5.9}$$

In most experiments using low-Z_p projectile ions, it is primarily the ^3S component that survives practically intact in most cases due to its much longer lifetime (see Table 5.1).

While various methods to determine the fractional composition of the beam (mostly the ^3S component) have been reported [104–111], they usually involve measurements on a completely different apparatus and therefore many times this component can be quite different from the composition of the beam in the actual experiment. Here, we use an *in situ* technique, i.e., the beam fractions are determined from the Auger spectra themselves in the same measurement, originally developed [7, 8] in 2001 and further improved over time in our group [112]. This *in situ* technique can therefore be expected to be more accurate than the other reported methods and is detailed next.

Table 5.1: Theoretical and experimental lifetimes (in s) of the metastable He-like $1s2s\,^1S$ and $1s2s\,^3S$ states for projectile atomic number $Z_p = 3 - 10$. In this thesis, the theoretical values $\tau_{^3S}$=20.59(-3) s and $\tau_{^1S}$=3.02(-6) s for carbon ($Z_p = 6$) and $\tau_{^3S}$=957.8(-6) s and $\tau_{^1S}$=0.43(-6) s for oxygen ($Z_p = 8$)were used. The notation 20.59(-3) stands for 20.59×10^{-3}.

	$\tau_{^3S}$		$\tau_{^1S}$	
Z_p	Experiment	Theory	Experiment	Theory
2	7870±510[1]	7862[9]	38±8(-3)[14]	19.5(-3)[12]
		7899[10]	19.7±1.0(-3)[15]	
		7859[4]		
3	58.6±12.9[2]	49.04[9]	503±26(-6)[16]	513(-6)[12]
	52.2±5[3]			
4	1.808±0.49[4]	1.780[9]		55.2(-6)[12]
		1.693[11]		
5	149.8±0.45(-3)[5]	149.4(-3)[9]		10.8(-6)[12]
		149.3(-3)[10]		
6	20.589±0.047(-3)[5]	20.59(-3)[9]		3.02(-6)[12]
		20.52(-3)[12]		
		20.16(-3)[13]		
7	3.94±0.05(-3)[6]	3.949(-3)[9]		1.06(-6)[12]
8	956±5(-6)[7]	957.8(-6)[9]		0.433(-6)[12]
		943.4(-6)[13]		
9	276±2(-6)[6]	277.1(-6)[9]		0.198(-6)[12]
		277.2(-6)[4]		
10	91.7±0.4(-6)[8]	92.0(-6)[9]		0.100(-6)[12]
		90.9(-6)[13]		

[1]Ref. [113]. [2]Ref. [114]. [3]Ref. [115]. [4]Ref. [116]. [5]Ref. [117]. [6]Ref. [118]. [7]Ref. [119]. [8]Ref. [120]. [9]Ref. [103]. [10]Ref. [121]. [11]Ref. [122]. [12]Ref. [102]. [13]Ref. [123]. [14]Ref. [124]. [15]Ref. [125]. [16]Ref. [126].

5.2 The "two-spectra measurement" technique in the determination of the fractional component of the $1s2s\,^3S$ state

The development of this *in situ* method emerged from the observation of changes in the relative intensities of specific Auger lines in spectra produced in collisions of He-like ions with atoms, when the ion beam stripping method was changed from foil-stripping to gas-stripping [8]. It was quite surprising to see some peaks almost "vanish", while others becoming quite enhanced. Knowing that He-like beams consist of three components, it was clear that the stripping method chosen led to a variation of the relative amounts of the three beam components.

In this method, the amount of the metastable $1s2s\,^3S$ component is extracted directly from the high resolution KLL-Auger electron projectile spectra as shown in Fig. 5.1, by recording two successive spectra at the same beam energy, but with beams having a quite different $1s2s\,^3S$ fraction [7, 8]. This is achieved by stripping the ion beam with a thin carbon foil in the first measurement and with a gas in the second, with the foil-stripping producing a significantly higher $1s2s\,^3S$ component fraction. The relative electron yields of the$1s2s2p\,^4P$ and $1s2p^2\ ^2D$ doubly excited states produced in collisions of a He-like beam with H_2 or He gas targets are then used to determine the $1s2s\,^3S$ content under the assumption that the $1s2s2p\,^4P$ state derives exclusively from the $1s2s\,^3S$ state (through direct 2p capture) and the $1s2p^2\ ^2D$ state uniquely from the $1s^2\,^1S$ state (through the Transfer Excitation process (TE), i.e., the transfer of a target electron to the projectile $2p$ orbital with the simultaneous excitation of a $1s$ projectile electron to the $2p$, respectively [7, 94, 127]). In Fig. 5.1 it is clearly seen that not only the $1s2s2p\,^4P$ but also the $2s2p\,^3P$ appear to be significantly stronger when the spectrum is obtained by stripping in a foil rather than in gas, indicating that both states are strongly connected to the amount of $1s2s\,^3S$ component. On the other hand, clearly this is not the case for the carbon $2s2p\,^1P$ that seems to have the same yield independent of foil or gas stripping implying a different mechanism.

In the original method [7], only two components were considered in the production of the $1s2l2l'$ states, with the ion beam assumed to be mainly in the ground $1s^2\,^1S$ state and some in the $1s2s\,^3S$ state. The $1s2s\,^1S$ component was considered negligible due to its much shorter lifetime. However, in the present work which also considers excitation, the production of the $2s2p\,^1P$ state from the $1s2s\,^1S$ is considerable and therefore, this component must also be considered, requiring a revised three-component treatment that also takes into account the $1s2s\,^1S$ population.

The theoretical normalized electron yield $dY[X]/d\Omega'$ for the production of projectile Auger state X in a collision at a point $z = z_0$ from the last stripping point is

given quite generally, by the following simple formula:

$$\frac{dY[X]}{d\Omega'}(z_0) = f_g(z_0) \cdot \frac{d\sigma_g[X]}{d\Omega'} + f_{^3S}(z_0) \cdot \frac{d\sigma_{^3S}[X]}{d\Omega'} + f_{^1S}(z_0) \cdot \frac{d\sigma_{^1S}[X]}{d\Omega'} \tag{5.10}$$

which just sums the contributions from each fractional component at z_0, properly normalized according to:

$$1 = f_g(z_0) + f_{^3S}(z_0) + f_{^1S}(z_0) \tag{5.11}$$

since all the produced states are considered to quickly decay to the above three states. Here, the three projectile rest frame SDCS, $d\sigma_g/d\Omega'$, $d\sigma_{^3S}/d\Omega'$ and $d\sigma_{^1S}/d\Omega'$ for the production of state X are weighted according to the fraction in each of the assumed three components.

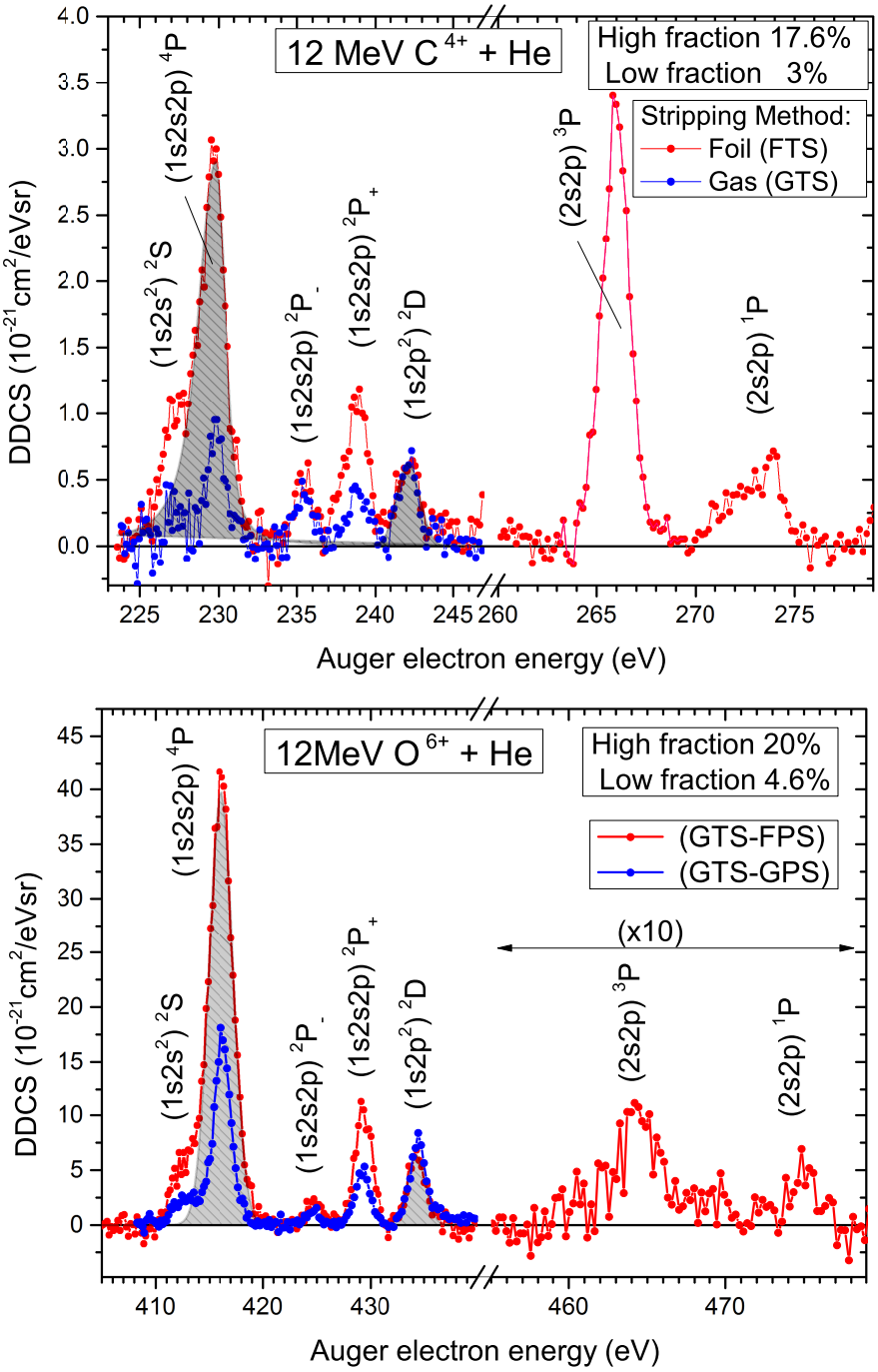

Figure 5.1: Normalized Auger electron spectra measured at $\theta = 0°$ with respect to the ion beam for 12 MeV C^{4+} (top) and O^{6+} (bottom) projectiles in collision with He at a distance $z = z_0$ from the closest stripping point. The red spectra obtained through foil terminal stripping (FTS) and/or post-stripping (FPS) have a higher metastable fraction ($f_{^3S} \sim 17 - 20\%$), while the blue spectra have a lower fraction ($f_{^3S} \sim 3 - 5\%$) and were obtained through gas terminal stripping (GTS) and/or post-stripping (GPS).

5.3 Determination of the metastable $1s2s\,^3S$ fraction using the "two-spectra measurement" technique

This technique was developed from the observation that collisions of He-like ion beams with H_2 or He targets lead to the production of an Auger projectile electron spectrum which includes the two characteristic Auger lines $1s2s2p\,^4P$ and $1s2p\,^2D$ (in short ^4P and ^2D). Theoretically, these can be produced primarily either from the ^3S by $2p$ capture or ground state by transfer excitation, respectively. Thus, Eq. (5.10) can be simplified for these states to:

$$\frac{dY[^4P](z_0)}{d\Omega'} = f_{^3S}(z_0) \cdot \frac{d\sigma^A_{^3S}[^4P]}{d\Omega'} \tag{5.12}$$

and

$$\frac{dY[^2D](z_0)}{d\Omega'} = f_g(z_0) \cdot \frac{d\sigma^A_g[^2D]}{d\Omega'} \tag{5.13}$$

where $\frac{d\sigma^A_{^3S}[^4P]}{d\Omega'}$ and $\frac{d\sigma^A_g[^2P]}{d\Omega'}$, are the Auger electrons single differential cross sections (SDCS) deriving from the ground and ^3S state, respectively, with $f_g(z_0)$ given by: Eq. (5.11):

$$f_g(z_0) = 1 - f_{^3S}(z_0) - f_{^1S}(z_0) \tag{5.14}$$

However, since $f_{^1S}$ is usually small in some general cases it can be neglected without serious loss. This was originally done in the so called two-component model described in section 5.3.1. More recently, and in particular for cross section measurements of the $2s2p\,^1P$ state which is dominantly produced from the $1s2s\,^1S$ state a three-component model was necessary, described in section 5.3.2

5.3.1 The two-component model

In the two-component (2c) model the $1s2s\,^1S$ state population is considered negligible and therefore we have at $z = z_0$ from Eq. (5.14):

$$f_g(2c) \approx 1 - f_{^3S}(2c) \tag{5.15}$$

Then, the normalized electron yields for the ^4P and ^2D states (Eqs. 5.3-5.13), obtained in two different measurements $i = 1, 2$, with different metastable fraction

$f_{^3S}^{[1]} \neq f_{^3S}^{[2]}$, will be:

$$\frac{dY_1[^4P]}{d\Omega'} = f_{^3S}^{[1]}(2c) \cdot \frac{d\sigma_{^3S}^{A}[^4P]}{d\Omega'} \tag{5.16}$$

$$\frac{dY_1[^2D]}{d\Omega'} = [1 - f_{^3S}^{[1]}(2c)] \cdot \frac{d\sigma_{g}^{A}[^2D]}{d\Omega'} \tag{5.17}$$

$$\frac{dY_2[^4P]}{d\Omega'} = f_{^3S}^{[2]} \cdot \frac{d\sigma_{^3S}^{A}[^4P]}{d\Omega'}(2c) \tag{5.18}$$

$$\frac{dY_2[^2D]}{d\Omega'} = [1 - f_{^3S}^{[2]}(2c)] \cdot \frac{d\sigma_{g}^{A}[^2D]}{d\Omega'} \tag{5.19}$$

where we have explicitly introduced the notation $2c$ to denote the quantities and results in the two-component model and removed the reference to the position $z = z_0$, implicitly always assumed, to avoid cumbersome equations. The above system of four equations can be readily solved for the unknown fractions $f_{^3S}^{[1]}$ $f_{^3S}^{[2]}$, eliminating the unknown two Auger SDCS [7, 8, 112], giving:

$$f_{^3S}^{[i]}(2c) = \frac{dY_i[^4P]}{d\Omega'} \cdot \frac{\frac{dY_1[^2D]}{d\Omega'} - \frac{dY_2[^2D]}{d\Omega'}}{\frac{dY_1[^2D]}{d\Omega'}\frac{dY_2[^4P]}{d\Omega'} - \frac{dY_2[^2D]}{d\Omega'}\frac{dY_1[^4P]}{d\Omega'}}, \qquad (i = 1, 2) \tag{5.20}$$

The normalized electron yields, $\frac{dY_i[^4P]}{d\Omega'}$ and $\frac{dY_i[^2D]}{d\Omega'}$ are obtained directly from the Auger spectra in which the beam is in a high ($i = 1$) or low ($i = 2$) metastable fraction as shown in Fig. 5.1. Beams with quite different metastable fractions $f_{^3S}$ can be obtained by using foil or gas stripping (as first reported in Ref. [8]), the former typically giving in most cases twice as much or more metastable component [128]. In Fig. 5.2 older experimentally measured $1s2s\,^3S$ fractions are presented, obtained using the "two-spectra measurement" technique assuming a two-component [129].

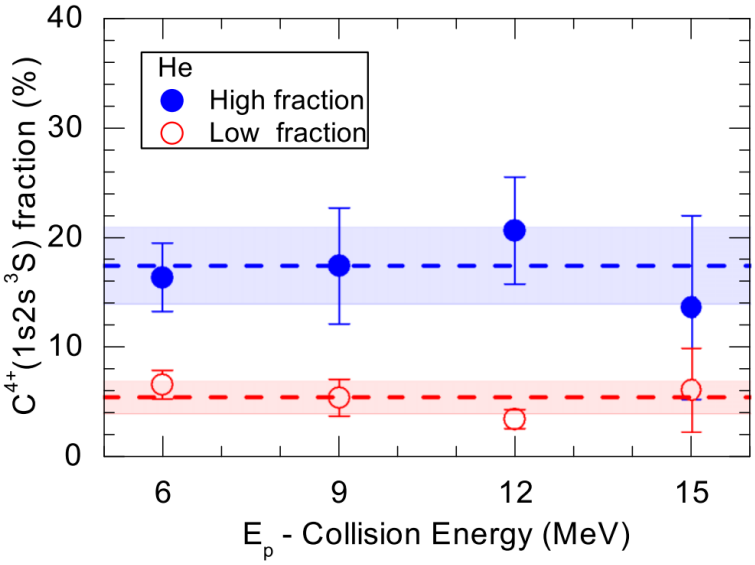

Figure 5.2: Experimentally determined $1s2s\,^3S$ fractions using the KLL "two-spectra measurement" technique as a function of the projectile energy E_p. The mean $f_{^3S}$ fraction for gas stripping (low fraction) is seen to be about 5.5%, while the mean $f_{^3S}$ fraction using foil stripping (high fraction) is about 17% or almost 3 times larger. From Ref. [129]

5.3.2 The three-component model

The development of a three-component fractional beam model, able to provide fractions for all three $1s2s\,^3S$, $1s2s\,^1S$ and $1s^2\,^1S$ components, proved to be necessary during the $2s2p\,^1P$ production cross section determination process, as theoretical calculations showed that one of the dominant mechanisms responsible for its production is 1s→2p excitation from the $1s2s\,^1S$.

The previously, i.e., in the two-component model, neglected $1s2s\,^1S$ component can be readily introduced by assuming that it is produced together with the $1s2s\,^3S$ at the stripping point $z = 0$ in a ratio dictated by spin-statistics [7], i.e.,:

$$\frac{f_{^1S}(z=0)}{f_{^3S}(z=0)} = \frac{1}{3} \tag{5.21}$$

where the $f_{^1S}(z=0)$ and $f_{^3S}(z=0)$ are the corresponding beam fractions at the stripping point. Furthermore, by using Eq. (5.1), for both metastable fractions $f_{^{1,3}S}$ we have:

$$N_{^1S}(z_0) = N_{^1S}(z=0) \cdot \exp\left(\frac{-z_0}{V_p\,\tau_{^1S}}\right) \tag{5.22}$$

$$N_{^3S}(z_0) = N_{^3S}(z=0) \cdot \exp\left(\frac{-z_0}{V_p\,\tau_{^3S}}\right) \tag{5.23}$$

and defining their ratio a we have:

$$a \equiv \frac{f_{^1S}(z_0)}{f_{^3S}(z_0)} = \frac{\frac{N_{^1S}(z_0)}{N_I}}{\frac{N_{^3S}(z_0)}{N_I}} = \frac{f_{^1S}(z=0) \cdot \exp\left(\frac{-z_0}{V_p\,\tau_{^1S}}\right)}{f_{^3S}(z=0) \cdot \exp\left(\frac{-z_0}{V_p\,\tau_{^3S}}\right)} \tag{5.24}$$

and thus a is seen to be just a proportionality constant introduced for short given by:

$$a = \frac{1}{3} \cdot \frac{\exp[-z_0/(V_p\,\tau_{^1S})]}{\exp[-z_0/(V_p\,\tau_{^3S})]} \tag{5.25}$$

therefore:

$$f_{^1S}(z_0) = a \cdot f_{^3S}(z_0) \tag{5.26}$$

Now, in the three-component (3c) model the $1s2s\,^3S$, $1s2s\,^1S$ and $1s^2\,^1S$ fractions will be noted as $f^{[i]}_{^3S}(3c)$, $f^{[i]}_{^1S}(3c)$, $f^{[i]}_{g}(3c)$ with:

$$f^{[i]}_{g}(3c) + f^{[i]}_{^3S}(3c) + f^{[i]}_{^1S}(3c) = 1 \quad \text{(for measurement } i = 1, 2) \tag{5.27}$$

and using Eq. (5.25) we have:

$$f_g^{[i]}(3c) + (1+a) f_{^3S}^{[i]}(3c) = 1 \quad \text{(for measurement } i = 1, 2) \tag{5.28}$$

Thus, using also Eq. (5.28), for each of the two measured Auger spectra at z_0, we have in the three-component model :

Measured Auger spectrum 1:

$$\frac{dY_1[^4P]}{d\Omega'} = f_{^3S}^{[1]} \frac{d\sigma_{^3S}^A[^4P]}{d\Omega'}, \qquad \frac{dY_1[^2D]}{d\Omega'} = f_g^{[1]} \frac{d\sigma_g^A[^2D]}{d\Omega'} \tag{5.29}$$

$$f_g^{[1]}(3c) + (1+a) f_{^3S}^{[1]}(3c) = 1 \tag{5.30}$$

Measured Auger spectrum 2:

$$\frac{dY_2[^4P]}{d\Omega'} = f_{^3S}^{[2]} \frac{d\sigma_{^3S}^A[^4P]}{d\Omega'}, \qquad \frac{dY_2[^2D]}{d\Omega'} = f_g^{[2]} \frac{d\sigma_g^A[^2D]}{d\Omega'} \tag{5.31}$$

$$f_g^{[2]}(3c) + (1+a) f_{^3S}^{[2]}(3c) = 1 \tag{5.32}$$

where $\frac{dY_1[^4P]}{d\Omega'}$ and $\frac{dY_1[^2D]}{d\Omega'}$ refer to the electron normalized yields of ^4P and ^2D, while $\frac{d\sigma_{^3S}^A[^4P]}{d\Omega'}$ and $\frac{d\sigma_g^A[^2D]}{d\Omega'}$ refer to their Auger single differential cross sections. The two measured spectra again should have quite different ^3S metastable fractions.
Measured Auger spectrum 1:

$$\frac{dY_1[^4P]}{d\Omega'} = f_{^3S}^{[1]}(3c) \cdot \frac{d\sigma_{^3S}^A[^4P]}{d\Omega'}, \tag{5.33}$$

$$\frac{dY_1[^2D]}{d\Omega'} = [1 - (1+a) f_{^3S}^{[1]}(3c)] \cdot \frac{d\sigma_g^A[^2D]}{d\Omega'} \tag{5.34}$$

Measured Auger spectrum 2:

$$\frac{dY_2[^4P]}{d\Omega'} = f_{^3S}^{[2]}(3c) \cdot \frac{d\sigma_{^3S}^A[^4P]}{d\Omega'}, \tag{5.35}$$

$$\frac{dY_2[^2D]}{d\Omega'} = [1 - (1+a) f_{^3S}^{[2]}(3c)] \cdot \frac{d\sigma_g^A[^2D]}{d\Omega'} \tag{5.36}$$

which again is seen to be a very similar system of four equations in the four unknowns, $f_{^3S}^{[1]}(3c)$, $f_{^3S}^{[2]}(3c)$, $\frac{d\sigma_{^3S}^A[^4P]}{d\Omega'}$ and $\frac{d\sigma_g^A[^2D]}{d\Omega'}$. This system is readily solved as in the case of the two-component model with the solution:

$$f_{^3S}^{[i]}(3c) = \frac{f_{^3S}^{[i]}(2c)}{(1+a)} \quad \text{(for measurement } i = 1, 2) \tag{5.37}$$

where $f_{^3S}^{[i]}(2c)$ is just the two-component (2c) model fraction already given in Eq. (5.20). It is interesting to note that in the new three-component model, the ground state fractions $f_g^{[i]}(3c)$ are independent of a and therefore the same in both three- and two-component models, i.e., $f_g^{[i]}(3c) = f_g^{[i]}(2c)$. The correction for the existence of

the ^1S component is thus accounted for in the new formula, by $f_{^3S}^{[i]}(3c)$, which is a bit smaller. In Fig. 5.3 and Table 5.2 the experimentally determined $1s2s\,^3S$ fractions using the "two-spectra measurement" technique technique applying the new three-component method are presented. These values were used later in the observed Auger states production cross section determination.

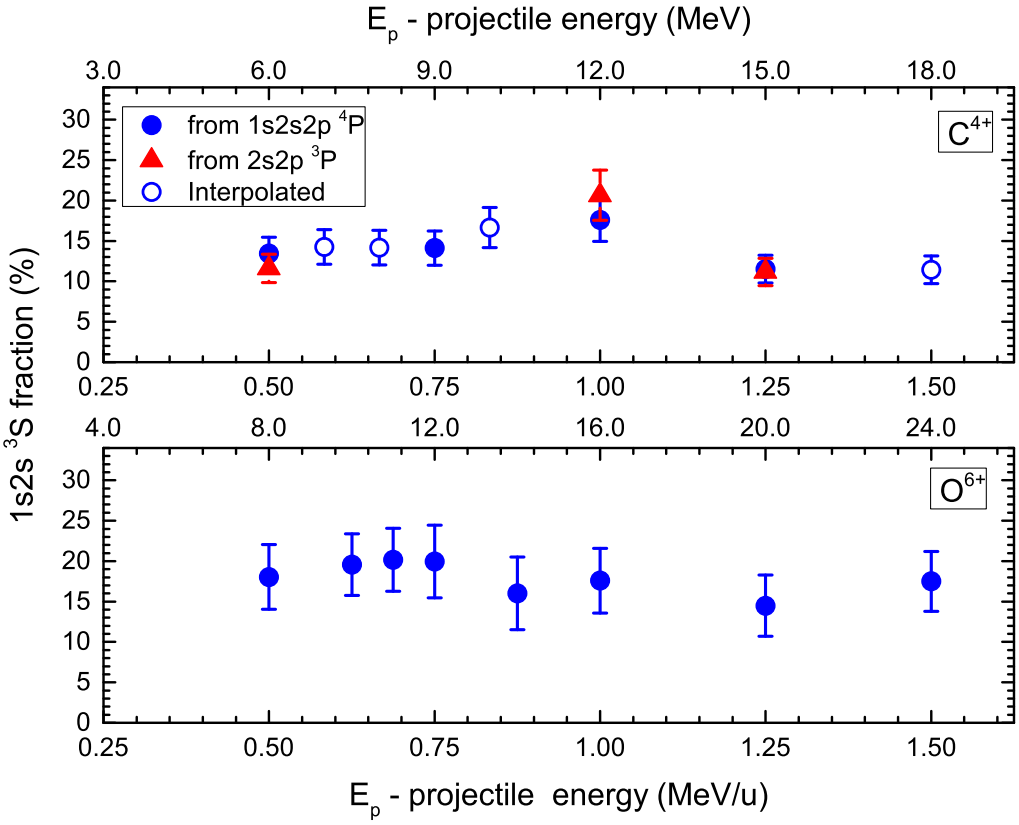

Figure 5.3: Experimentally determined $1s2s\,^3S$ fractions using the "two-spectra measurement" technique as a function of the projectile energy E_p for C^{4+} (top) and O^{6+} (bottom) projectile ions. The above values refer to the high fraction spectrum $1s2s\,^3S$ component when foil terminal or foil post-stripping was used. At some energies, where available, fractions were also determined from the $2s2p\,^3P$ state also, showing good agreement with that determined from the $1s2s2p\,^4P$ state, proving that both states originate from $1s2s\,^3S$ state. The values of the $1s2s\,^3S$, $1s2s\,^1S$, $1s^2\,^1S$ fractions and the stripping conditions for each projectile are given in Table 5.2

Table 5.2: Metastable $1s2s\,^3S$, $1s2s\,^1S$ and ground $1s^2\,^1S$ beam component fractions, $f_{^3S}$, $f_{^1S}$, f_g in mixed-state ($1s^2, 1s2s\,^3S$) C^{4+} and O^{6+} ion beams, extracted through the "two-spectra measurement" technique [7, 8]. Fractions $f_{^1S}$ and $f_{^3S}$ were evaluated in the three-component model as described in the text. The stripping methods include terminal stripping (z_0 = 26.35 m) in gas (GTS) and carbon foils (FTS), while post-stripping (z_0 = 12.1 m) in gas (GPS) and foil (FPS) are also indicated where used. Here, the high fraction spectra values of interest are presented. The value of a (Eq. (5.25)) is also indicated. The notation 2.22(-1) stands for 2.22×10^{-1}.

Stripping method	Incident ion	Final ion	Stripping energy (MeV)	Final energy (MeV)	a	$f_{^3S}$ (%)	$f_{^1S}$ (%)	f_g (%)
GTS-GPS	C^{3+}	C^{4+}	6	6	2.22(-1)	13.4±1.9	3.0±0.5	83.6±2.1
GTS-GPS	C^{3+}	C^{4+}	9	9	2.39(-1)	14.1±2.0	3.4±0.5	82.5±2.2
FTS	C^-	C^{4+}	2.4	12	1.78(-1)	17.6±2.6	3.1±0.5	79.3±2.7
FTS	C^-	C^{4+}	3	15	1.90(-1)	11.5±1.7	2.2±0.3	86.3±1.8
GTS-FPS	O^{4+}	O^{6+}	8	8	1.94(-2)	18.1±4.0	0.35±0.08	81.6±4.0
GTS-FPS	O^{4+}	O^{6+}	10	10	2.62(-2)	19.6±3.8	0.51±0.10	79.9±3.8
GTS-FPS	O^{4+}	O^{6+}	11	11	2.95(-2)	20.2±3.9	0.60±0.12	79.2±3.9
GTS-FPS	O^{4+}	O^{6+}	12	12	3.27(-2)	20.0±4.5	0.65±0.15	79.4±4.5
FTS-FPS	O^{4+}	O^{6+}	14	14	3.88(-2)	16.0±4.5	0.62±0.17	83.4±4.5
GTS-FPS	O^{4+}	O^{6+}	16	16	4.46(-2)	17.6±4.0	0.79±0.18	81.6±4.0
FTS	O^-	O^{6+}	2.85	20	6.59(-2)	14.5±3.8	0.10±0.03	85.4±3.8
FTS	O^-	O^{6+}	3.42	24	9.27(-2)	17.5±3.7	0.16±0.03	82.3±3.7

Chapter 6

Theory

Overview

In this chapter the ion-atom collision basic theoretical treatment used in the present thesis known as the three-electron Atomic Orbit Close-Coupling (3eAOCC) is presented, together with basic formulas for the Auger angular distributions in LS coupling. The electronic transitions induced by collisions between ions and atoms are of fundamental interest for the understanding of many atomic and molecular phenomena. Therefore, the development of theoretical models and codes that match the experimental data and describe these processes successfully is of great importance. The electronic processes are likely to occur in specific conditions. The cross sections of these processes depend strongly on the impact relative velocity (energy), between the collision partners. This parameter is defined as the ratio of the projectile velocity V_p to the velocity v_e of the participating target electron, thus dividing the theoretical approaches into three important energy regions of low, intermediate and high, according to the ratios $V_p/v_e \ll 1$, $V_p/v_e \gg 1$ and $V_p/v_e \approx 1$, respectively as shown in Fig. 6.1. In general, at low V_p velocities, i.e., $V_p/v_e \ll 1$, the dominant process is electron capture. At intermediate V_p velocities, i.e., $V_p/\mathrm{v}_e \approx 1$, all inelastic processes such as charge exchange, excitation and ionization are roughly of the same order, while at high V_p velocities, i.e., $V_p/v_e \gg 1$, the dominant processes are ionization and excitation with the interaction time between the two collision partners being short and the interaction considered as a small perturbation [130, 131].

In the past, the electron excitation and ionization processes in ion-atom collisions have been treated by particle scattering theories, such as the Impulse Approximation (IA) and the Plane Wave Born Approximation (PWBA). These two approximations can describe the experimental results, under certain conditions, quite well in different collision energy regions. However, they are only approximate models, making the development of new comprehensive theories essential.

In the present thesis, a semiclassical non-perturbative approach is used in the study of the present collisions, with the relative motion between the projectile and the target being described by classical trajectories, while the dynamics of the elec-

trons of the collision system is treated quantum mechanically. This approach is valid under the condition that the de Broglie wavelength associated with the relative motion between the projectile and the target is very small compared to the distance over which the interaction takes place during the collision. The corresponding processes here occur during collisions with impact energies between 0.5 and 1.5 MeV/u, i.e., V_p between 4.4 and 7.7 a.u., lying in the high energy region ($V_p/v_e \gg 1$) making the semiclassical approximation valid [131]. A brief summary of a recently developed semiclassical approach, involving three active electrons known as the 3 electron Atomic Orbit Close-Coupling (3eAOCC), is presented below. The 3eAOCC theory has been developed by Professor Alain Dubois of Sorbonne University and his group, while the provided calculations presented in this thesis, were performed by Professor Alain Dubois and his Ph.D. student, at the time, Stylianos Passalidis at their department in Paris.

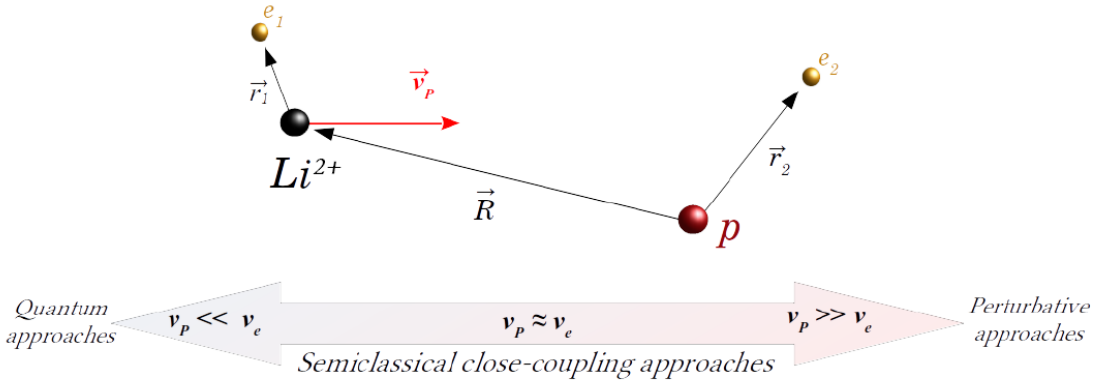

Figure 6.1: Typical scheme of an ion-atom collision system, i.e., Li^{2+}+H together with the different theoretical approaches depending on the relative impact velocity. Three regions of low, intermediate and high energy appear according to the ratios $V_p/v_e \ll 1$, $V_p/v_e \gg 1$ and $V_p/v_e \approx 1$. From Ref. [131].

6.1 The 3 electron Atomic Orbit Close-Coupling

The three-electron Atomic Orbit Close-Coupling (3eAOCC) is a non-perturbative treatment within the semiclassical approach, i.e., the relative target-projectile motion is described classically by straight-line constant velocity, trajectories. In this treatment the time-dependent Schrödinger equation is solved, using an asymptotic atomic picture, where the electron dynamics are treated quantum mechanically, constrained to a configuration space defined by a finite set of basis functions that represent well the electronic states of the isolated target and projectile, while the electronic wave function is expanded into the electronic states of the target and the projectile.

The 3eAOCC was developed in an attempt to describe more accurately the exci-

tation processes taking place in the collisions between an ion and a target involving three electrons in total. 3eAOCC is an evolution of the two-electron AOCC which in turn evolved from a one-electron AOCC as computer power increased over the last 30 years. This method is used to investigate the processes taking place in ion-atom collisions such as electron transfer also known as single electron capture (SEC), transfer-exitation (TE) and excitation, producing doubly excited He-like or Li-like autoionizing states, taking into account both electron-nucleus and electron-electron interactions. In this thesis, the 3eAOCC was used to describe TE and projectile excitation in collisions between two-electron projectiles, i.e., He-like ions, and He targets. The He target, even though it has also two electrons, is modelled by an effective hydrogen-like target.

The solution of these systems in atomic units using the time-dependent Schrödinger equation (TDSE) in the semiclassical approximation is:

$$i\frac{d}{dt}\psi(\boldsymbol{r_1}, \boldsymbol{r_2}, \boldsymbol{r_3}, t) = H\psi(\boldsymbol{r_1}, \boldsymbol{r_2}, \boldsymbol{r_3}, t) \tag{6.1}$$

The time t is related to the target (T)-projectile (P) relative position by the usual straight-line, constant velocity, relation:

$$\boldsymbol{R} = \boldsymbol{b} + \boldsymbol{V_p} \cdot t \tag{6.2}$$

with $\boldsymbol{b}$ and $\boldsymbol{V_p}$ being the impact parameter and velocity, respectively, as seen in Fig. 6.2. In Eq. (6.1) the Hamiltonian operator includes all Coulomb interactions

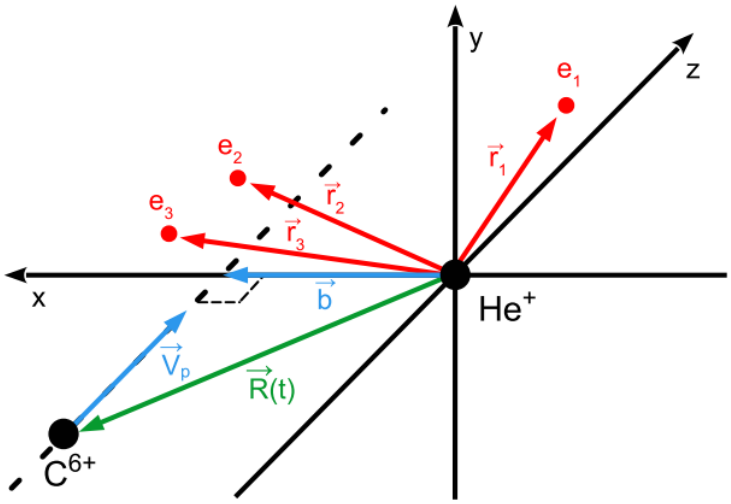

Figure 6.2: Collision geometry of C^{4+} + monoelectronic He. The impact parameter **b** and velocity $\mathbf{V}_p$ define the collision plane (xz) and **R**(t) the projectile (P) trajectory with respect to the target (T). The positions of the three electrons with respect to the target center are denoted $\mathbf{r}_1$, $\mathbf{r}_2$, $\mathbf{r}_3$. From Ref. [129]

.

between the nuclei and the three active electrons. Since two of the three active elec-

trons correspond to the projectile, the performed calculations used a mono-electronic He target, which is considered to be isotropic (nonoriented) in the performed experiments. The scattering wave function is expanded onto a set of asymptotic states (and pseudostates) ϕ_k^{PPP} and products $\phi_i^T \phi_j^{PP}$ of asymptotic states (and pseudostates) as [129]:

$$\psi(\boldsymbol{r_1}, \boldsymbol{r_2}, \boldsymbol{r_3}, t) = \sum_{i,j} c_{i,j}^{TPP}(t)\phi_i^T \phi_j^{PP} + \sum_k c_k^{PPP}(t)\phi_k^{PPP} \tag{6.3}$$

Pseudostates are used to improve the convergence of the calculations in two ways. Firstly, they are used to describe excitation and electron capture into Rydberg states which cannot be included explicitly in the set of exact low-lying eigenstates. Secondly, the pseudostates of positive energies can provide a discretized electron continuum, and thus be used to describe ionization in an approximate way [130]. The superscripts T, PP, PPP denote states describing one, two, and three electrons on their respective centers (He target, He-like and Li-like projectile, respectively), including the usual energy phases, and for the projectile states, the electron translation factors $\exp(i\boldsymbol{V}_p \cdot \boldsymbol{r}_i - iV_p^2/2)$, to ensure Galilean invariance of the results [132].

Note that in Eq. (6.3), the electrons are treated as indistinguishable, and thus, the total wave function, as well as the atomic ϕ states, are fully antisymmetrized. The TDSE can then be written as a set of coupled differential equations for the expansion coefficients c (c$\equiv c_{i,j}^{TPP}$ or c_k^{PPP}), $\dot{\boldsymbol{c}}(t) = -i\boldsymbol{S^{-1}M}\boldsymbol{c}(t)$, where $\boldsymbol{S}$ is the overlap matrix and $\boldsymbol{M}$ the coupling matrix, involving all couplings, notably the two center interelectronic Coulomb repulsion. These equations are solved for an initial state i using the robust predictor-corrector time-step method and code developed by Shampine and Gordon [133]. The $c(t)$ coefficients are asymptotic probability amplitudes from which one gets the partial cross sections for production of the state $X(=^{2S+1} L)$, with L and S being the total orbital angular momentum and the total spin respectively, is given by [129]:

$$\sigma[X](L, M_L) = 2\pi \int_0^{+\infty} |c_X(b, t \to \infty)|^2 b db \tag{6.4}$$

For all the channels covered by the basis set, the state indicator [X] can sometimes be left out when it's clear, and in such cases, the partial cross section is simply denoted as σ (L, M_L), where M_L represents the magnetic quantum number. In this method the total spin of the three-electron system remains constant, necessitating two separate calculations. One for the doublet and another for the quartet spin symmetries. The resulting cross sections from these two sets of calculations are averaged by a factor of 1/2 to ensure unitarity. Additionally, since the capture probabilities are relatively small for the considered range of impact energies, they are multiplied by 2 to accommodate the two target electrons in the case of capture or transfer-excitation. However, this was not done for excitation since the situation

there is more complicated [134].

In more detail, the target He, and the projectile He-like and Li-like states are expressed as linear combinations of Gaussian-type orbitals (GTOs) and of spin-adapted products of these GTOs, by diagonalisation of the respective atomic Hamiltonian operators within a full configuration interaction approach. In the spherical coordinates, the GTOs are defined as [131]:

$$G_{a,l,m}(\vec{r}) = Y_{l,m}(\theta,\phi) r^l e^{-ar^2} \tag{6.5}$$

with $Y_{l,m}$ the spherical harmonics and l, m the azimuthal and the magnetic quantum numbers. The one-electron states of the collision partners are therefore written as the weighted sum of the GTOs as [131]:

$$\phi(\vec{r}) = \sum_{i=1}^{N} c_i G_{a_i,l_i,m_i}(\vec{r}) \tag{6.6}$$

and the two electron states as [131]:

$$\phi^{\pm}(\vec{r_1},\vec{r_2}) = \sum_{i=1}^{N}\sum_{j=1}^{N} C_{i,j}\left[G_{a_i,l_i,m_i}(\vec{r_1})G_{a_j,l_j,m_j}(\vec{r_2}) \pm G_{a_i,l_i,m_i}(\vec{r_2})G_{a_j,l_j,m_j}(\vec{r_1})\right] \tag{6.7}$$

The symmetry $\pm$ of the states is determined by the spin state (singlet corresponding to $+$ and triplet to $-$) of the collision system, in accordance with the Pauli principle. This spin symmetry, imposed by the initial conditions, remains unchanged throughout the collision since this model does not incorporate spin-orbit interactions. The coefficients c_i and C_{ij} are derived through diagonalization of sets of one-electron and two-electron functions, respectively, using the one-electron and two-electron Hamiltonians of the isolated partners. 3-electron wave functions are written similarly to Eq. (6.7).

The GTO exponents are optimized to minimize the number of GTOs, while ensuring accurate binding energies for the important states under consideration. The present calculations are based on a set of seven, seven, 22 and 22 GTOs, that are centered on helium, hydrogen, carbon and oxygen respectively. Their parameters are presented in Table 6.2. In the one-electron model of the helium target, the active electron of He is bound to He^+ by using a model potential, expressed as:

$$V(r) = -\frac{1}{r}\sum_{i=1}^{13} c_i e^{(-\beta_i r^2)} \tag{6.8}$$

with the values of the coefficients c_i and β_i given in Table 6.1. These values were used to obtain a ground-state energy close to the first ionization energy and correct

Coulombic limits at r $\to$ 0 and r $\to \infty$.

Table 6.1: Coefficients and exponents used to represent the system $He^+ + e^-$ by the model potential Eq. (6.8). From [129]

i	1	2	3	4	5	6	
c_i	1.0	0.0212	0.2386	0.2418	0.1841	0.1220	
β_i	0.0	0.7351	4.5960	13.3789	47.8218	260.8236	
i	7	8	9	10	11	12	13
c_i	0.1319	0.0193	0.1065	0.1067	-0.0412	-0.0779	-0.0743
β_i	1.7848	0.5064	1.0731	2.3884	12.0949	30.8796	153.6072

In conclusion, the 3eAOCC calculations provide the probability amplitudes as a function of the impact parameter b from which the production cross sections can be readily evaluated using Eq. (6.4) for any of the $1s2l2l'$ or $2l2l'$ ^{2S+1}L channels treated. Next, in order to directly compare these calculations with experimental data the theoretical results have to be translated to Auger electron production cross sections taking into consideration each specific Auger transistion's yield ξ and angular distribution presented in the following section.

Table 6.2: Orbital angular momentum quantum numbers ℓ and exponents a of the GTOs used in Eq. (6.5), for hydrogen, helium, carbon and oxygen centers. The notation 4.931(−3) stands for 4.931×10^{-3}. Note that the number of GTOs for carbon and oxygen is 22 considering the multiplicity of 3 for each of the $\ell = 1$ orbitals. From Ref. [129]

	Hydrogen		Helium		Carbon		Oxygen	
i	ℓ	a	ℓ	a	ℓ	a	ℓ	a
1	0	4.931(-3)	0	7.250(-3)	0	5.500(-2)	0	3.000(-1)
2	0	2.457(-2)	0	2.903(-2)	0	1.298(-1)	0	7.500(-1)
3	0	1.591(-1)	0	1.163(-1)	0	3.064(-1)	0	1.770
4	0	4.360(-1)	0	4.656(-1)	0	7.231(-1)	0	4.178
5	0	1.152	0	1.864	0	1.707	0	9.861
6	0	1.905	0	7.466	0	4.028	0	2.327(1)
7	0	6.850	0	2.990(1)	0	9.507	0	5.493(1)
8					0	2.244(1)	0	1.297(2)
9					0	5.296(1)	0	3.056(2)
10					0	1.250(2)	0	1.733(3)
11					1	2.600(-1)	1	7.222(-1)
12					1	7.500(-1)	1	2.083
13					1	2.449	1	6.804
14					1	8.000	1	2.667(1)

6.2 Auger angular distributions

In an ion-atom collision a produced doubly excited state SLJ may Auger decay to a final state $S_f L_f J_f$ as:

$$(SLJ) \rightarrow (S_f L_f J_f) + e_A^-(\theta'_e, \varepsilon_A;\, s = 1/2, \ell, j) \tag{6.9}$$

emitting an Auger electron e_A^- at angle θ'_e (the prime refers to the projectile rest frame) with respect to the initial beam direction with energy ε_A and ℓ orbital- and j total-angular momenta.

In general, ionization or excitation by particle impact leads to an alignment of the Auger or autoionising state [135, 136], which is possible to be measured by means of the non-isotropic angular distribution of emitted electrons [137].

$$I(\theta) = I_0 \left(1 + \sum_k A_k P_k(\cos\theta)\right), \qquad \text{with } k = 2, 4, 6, ... \tag{6.10}$$

where A_k are the anisotropy coefficients in the case of a negligible fine structure, i.e., the fine structure splitting is much smaller than the natural widths Γ of the states, and $P_k(\cos\theta)$ the Legendre polynomials. In the case where the final ion state is with $L_f = 0$ as in the examined states here, A_k depend only on the cross sections of the magnetic states, $\sigma(L, M_L)$ of the autoionizing levels. The A_k coefficients for the decay of a state with $L = 1$ or $L = 2$ and arbitrary S into a final state with $L_f = 0$ are given in Table 6.3. [138].

Consequently, the Auger electron SDCSs can be computed at any observation angle θ (or θ' in the projectile rest frame) using the Eq. (6.10) as:

$$\frac{d\sigma_A}{d\Omega'}(\theta_e) = \bar{\xi}\frac{\sigma^{tot}}{4\pi}\left(1 + \sum_{k=2,4,...}^{2L} \alpha_k P_k(\cos\theta_e)\right) \tag{6.11}$$

where σ_i^{tot} is the total state production cross section, while $\bar{\xi}$ is the mean Auger yield of the state usually computed as the statistical average over its J components ξ_J) given by:

$$\bar{\xi}[^{2S+1}L] \equiv \frac{\sum_{J=|L-S|}^{J=L+S}(2J+1)\xi_J}{(2S+1)(2L+1)} \tag{6.12}$$

The coefficients α_k expressed as [138]:

$$\alpha_k = A_k D_k \tag{6.13}$$

include the A_k factors providing information on the ionization (or excitation) and decay processes and also the de-alignment factor D_k which accounts for the average loss of orbital alignment into spin alignment in the partially overlapping LSJ

multiplets. D_k is defined as [138]:

$$D_k = \sum_J \frac{(2J+1)^2}{2S+1} \begin{Bmatrix} J & J & K \\ L & L & S \end{Bmatrix}^2 \tag{6.14}$$

reaching unity when the spin-orbit interaction is negligible with the de-alignment being minimum.

Table 6.3: Anisotropy coefficients A_k for the decay of an autoionising state with $L = 1$ or 2 and arbitrary S into a final ionic state with $L_f = 0$ and $S_f = S \pm 1/2$ in the case of a negligible fine structure, i.e., $\Gamma \gg$ fine structure splitting. The cross sections of substates are given by $Q(L|M_L|)$ and are assumed to be independent of M_S. From Ref.[138]

$L = 1$	$L = 2$
$A_2 = 2\frac{Q(10)-Q(11)}{Q(10)+2Q(11)}$	$A_2 = \frac{10}{7}\frac{Q(20)+Q(21)-2Q(22)}{Q(20)+2Q(21)+2Q(22)}$
	$A_4 = \frac{6}{7}\frac{3Q(20)-4Q(21)+Q(22)}{Q(20)+2Q(21)+2Q(22)}$

Chapter 7

Transfer-Excitation: Experiment and Theory

Overview

As already mentioned some of the main processes taking place during ion-atom collisions are electron capture (transfer), excitation and ionization [130]. Furthermore, any combination of these processes may also take place in a single-collision leading, for example, to simultaneous transfer-excitation (TE) or transfer-loss (TL). In transfer-excitation (TE) the projectile captures a target electron, together with the excitation of one of its other electrons, leading to a doubly excited projectile state. The general TE process is thus:

$$\mathrm{Z}^{q+} + \mathrm{T} \rightarrow (Z^{(q-1)+})^{**} + \mathrm{T}^{+}(\mathrm{All}) \qquad \text{(Transfer-Excitation - TE)} \qquad (7.1)$$

where Z^{q+} is the incident positively charged ion beam of charge-state q. T is the target atom and $(\mathrm{Z}^{(q-1)+})^{**}$ is the resulting doubly excited projectile state. The final state of the target is unknown as it is not determined in the experiment. Thus, in principle, all final states T^{+}(All) of the target should be considered.

A concrete example of such a TE process studied experimentally here is the production of the $1s2p\,^2D$ projectile state produced in the following collision systems:

$$\mathrm{C}^{4+}(1s^2) + \mathrm{He}(1s^2) \rightarrow \mathrm{C}^{3+}(1s2p^2\,^2D) + \mathrm{He}^{+}(\mathrm{All}) \qquad (7.2)$$

$$\mathrm{O}^{6+}(1s^2) + \mathrm{He}(1s^2) \rightarrow \mathrm{O}^{5+}(1s2p^2\,^2D) + \mathrm{He}^{+}(\mathrm{All}) \qquad (7.3)$$

where again He^{+}(All) includes all target states as previously. Here, the He-like carbon and oxygen ions originally in their ground state $1s^2$ are excited to the $1s2p^2\,^2D$ state (among the many excited states produced in the collision) which is seen to be the net result of a $1s \rightarrow 2p$ projectile excitation accompanied by a transfer of a target electron to the projectile $2p$ orbital. This particular state is identified using ZAPS and its production cross section is measured as a function of the projectile energy E_p.

Theoretical models for this TE process are also investigated and compared to the measurements. The results of these TE investigations were published in Ref. [11].

In the early days of ion-atom collisions studies, the electrons surrounding the atoms of the projectile and the target were considered to have only a passive role, assumed to just screen the nucleus. They were later found to also acquire an active dynamic role, contributing significantly to the state production cross sections [139, 140]. While electron-nucleus interactions are generally more important, particularly in ion-atom collisions including bare projectiles, electron-electron interactions also play a major role in projectile ionization and excitation processes, especially in collisions where light targets, i.e., H_2 or He, are used. Both electron-nucleus and electron-electron interactions are present during an ion-atom collision, making it difficult to distinguish the contribution of each interaction. In asymmetric collisions of heavy projectiles with light targets, two distinct peaks are typically observed in the TE cross sections as a function of impact energy [141, 142]. The high-energy peak has been attributed to the process of resonant transfer-excitation (RTE), and the low-energy peak to the process of nonresonant transfer-excitation (NTE). We now know that RTE [41, 127, 139, 143, 144] is due to projectile-target electron-electron (also known as two-center $e-e$ interaction - TCee) interaction, while NTE [127, 139, 143, 145] is due to nucleus-electron interaction.

Recently, a new TE process was predicted by theory referred to as nonresonant correlated transfer-excitation (NCTE) [11], proposing a new one-step mechanism, including the sharing of an electron between the projectile and the target nuclei. All TE mechanisms are expected to occur simultaneously in the ion-atom collisions, contributing coherently to the production of the same doubly-excited final projectile state. Next, a detailed description of the different TE mechanisms is given together with experimental and theoretical data.

7.1 Resonant Transfer-Excitation (RTE)

As mentioned above, TE presents a resonant behaviour at a certain collision energy region. This is explained by a process known as resonant transfer-excitation [38, 41, 127, 139, 143, 144]. This process, shown schematically in Fig. 7.1, is a correlated one-step process mediated by the TCee where the $1s \rightarrow 2p$ projectile excitation and the transfer of the target electron to the projectile $2p$ orbital happens simultaneously. RTE can be seen as the time-reversed Auger process [39–41, 146] so it can only occur if the energy of the transferred electron matches the energy of the corresponding Auger. This condition is fulfilled when the relative impact energy becomes equal to the energy of the corresponding Auger electron.

Initially, RTE has been modelled by the impulse approximation (IA), a simple particle scattering model, used for lightly bound target electrons and fast enough collisions so that in the frame of the projectile the incoming target electron can be considered to be approximately free. This condition is fulfilled when $V_p \gg v_t$, where

V_p and v_t are the velocities of the projectile ion and active target electron, respectively. Thus, the target electron is then treated as a quasifree particle approaching the projectile along the z-axis with a net velocity $V_e = V_p + v_z$ [127] and a momentum probability distribution given by the Compton profile $J(p_z)$, where $p_z = mv_z$. The electron impact energy E_e of this quasifree electron can be written as:

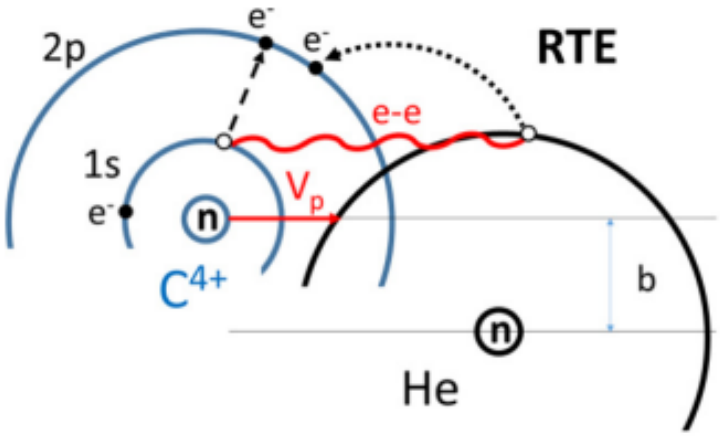

Figure 7.1: Schematic of the resonant transfer-excitation (RTE) process leading to the C^{3+} $(1s2p^2\ ^2D)$ level during collisions of C^{4+} $(1s^2)$+He, examined here. RTE is mediated by a two-center electron-electron $(e-e)$ interaction (TCee), indicated here by the red curvy line, leading to the simultaneous 1s→2p excitation of a projectile electron and the target electron transfer to the projectile 2p indicated by a curved dotted arrow. The projectile velocity V_p and the impact parameter b are also indicated. From Ref. [11].

$$\begin{aligned} E_e &= \frac{1}{2}m(V_p + v_z)^2 - I \\ &= t + p_z \cdot V_p + \frac{{p_z}^2}{2m} - I \end{aligned} \tag{7.4}$$

where $t = \frac{1}{2}m{V_p}^2$, m is the mass of the electron and I is the ionization energy of the active target electron. In the case of the He target, as is our case mostly, $I_{He} = 24.6$ eV. Through Eq. (7.4) the p_z terms are retained. The RTE peak occurs when $E_e = E_A$ and $p_z = 0$ so at the collision energy:

$$E_p^{RTE} = (E_A + I) \cdot \frac{M_p}{m} \tag{7.5}$$

The RTE production cross section in cm^2 is thus given within the IA by:

$$\sigma_{RTE}^{IA} = 2.475 \times 10^{-30} \cdot \frac{(2L_d+1)(2S_d+1)}{(2L_i+1)(2S_i+1)} \cdot \frac{\Gamma_A}{E_R} \cdot \frac{J(p_z)}{V_p + p_z} \tag{7.6}$$

where $J(p_z)$, is the Compton profile, V_p is the projectile velocity, p_z is the target

electron's momentum along the axis of the collision all expressed in a.u.

The L_d, S_d and L_i, S_i refer to the orbital and spin angular momenta of the intermediate LS doubly-excited state (d) and the initial projectile state (i), respectively. Γ_A is the Auger transition rate (s^{-1}) and E_R is the energy in eV of the time-reversed Auger transition.

These calculated RTE cross sections can be compared with experimental SDCS's at 0°, $(d\sigma_{RTEA}/d\Omega')(0°)$ as:

$$\frac{d\sigma_{RTEA}}{d\Omega'}(0°) = \sigma_{RTE}^{IA} \cdot \frac{(2L_d + 1)}{4\pi} \cdot \xi \tag{7.7}$$

with ξ being the Auger yield.

The narrower the target electron's momentum distribution $J(p_z)$, the sharper the RTE peak will appear in the TE cross section spectrum. Light two-electron targets, such as H_2 and He have been found ideal for RTE studies due to the fairly narrow momentum distribution of their two electrons [127, 139].

7.2 Nonresonant Transfer-Excitation (NTE)

Nonresonant transfer-excitation (NTE) is interpreted as a sequence of two uncorrelated events. An electron transfer from the target to the projectile, with a consecutive projectile electron excitation, each process being independently driven by electron-nucleus interactions [43, 44]. Each of the two separate sequential and independent $e - n$ interactions are illustrated in Fig. 7.2. Here, there is no resonance although NTE appears to be stronger at lower projectile energies than the RTE maximum. Theoretically, in the past, NTE has been computed in terms of the impact-parameter dependent capture $[P_{\rm cap}(b)]$ and excitation $[P_{\rm exc}(b)]$ probabilities [44, 127] as:

$$\sigma_{NTE} = 2\pi \int P_{exc}(b) P_{cap}(b) db. \tag{7.8}$$

Both TE mechanisms are expected to occur in the same ion-atom collision contributing coherently to the production of the same final (doubly excited) projectile state. To date, calculated cross sections for these different TE mechanisms have only been computed separately in independent treatments. Thus, their contributions to the total TE cross sections could only be added incoherently, allowing at most for interesting speculations about possible RTE-NTE interferences [32, 43, 45, 46, 49, 147]. In the new 3eAOCC treatment presented in this thesis both processes are treated for the first time coherently. These results are shown later on in sections 7.4 and 7.5.

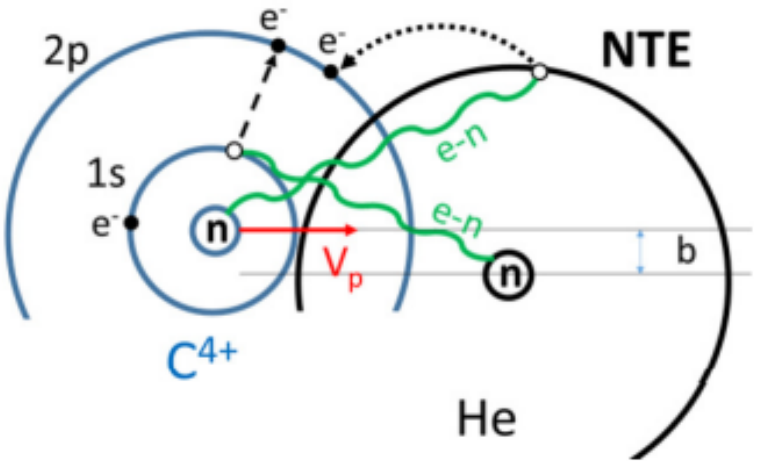

Figure 7.2: Schematic of the nonresonant transfer-excitation (NTE) process leading to the C^{3+} ($1s2p^2\,{}^2D$) level during collisions of C^{4+} ($1s^2$)+He. NTE is a process mediated by two electron-nucleus ($e-n$) interactions between a projectile electron and the target's nucleus together with a target's electron with the projectile's nucleus. Note that these two ($e-n$) interactions occur independently. The green lines represent the two electron-nucleus interactions, leading to the 1s→2p excitation of the projectile indicated by the straight dashed arrow together with an electron transfer from the target to the projectile 2p indicated by the curved dotted arrow. From Ref. [11].

7.3 $1s2p^2\,{}^2D$ DDCS Auger electron spectra

In this section, DDCS for C^{3+} and O^{5+} $1s2l2l'$ KLL Auger spectra produced through collisions of a He-like carbon and oxygen ($1s^2$, $1s2s\,{}^{1,3}S$) mixed state ion beams with a He gas target are presented. These collisions result in the production of intermediate Li-like $1s2l2l'$ doubly excited states, Auger decaying to the $1s^2$ ground state producing electrons of characteristic energies. A typical recorded KLL Auger spectrum of the energy region of interest, is shown in Fig. 7.3 (right) with the produced $1s2s^2\,{}^2S$, $1s2s2p\,{}^4P$, $1s2s2p\,{}^2P_\pm$ $1s2p^2\,{}^2D$ levels referred to in short as ${}^2S$, ${}^4P$, ${}^2P_\pm$, ${}^2D$ (left). While $1s2s^2\,{}^2S$ and $1s2s2p\,{}^2P_\pm$ can be produced from both $1s^2$ and $1s2s\,{}^{1,3}S$ components of the beam through electron transfer or TE respectively, due to spin selection rules the $1s2s2p\,{}^4P$ can only be produced from the $1s2s\,{}^3S$ through electron transfer, while the $1s2p^2\,{}^2D$ state is predominantly produced from the $1s^2\,{}^1S$ through RTE and NTEg, ideal for TE studies [11]. The Auger electron spectra presented here were transformed from electron counts versus channel number, to projectile rest frame DDCS versus Auger energy according to the procedures explained in chapter 4.

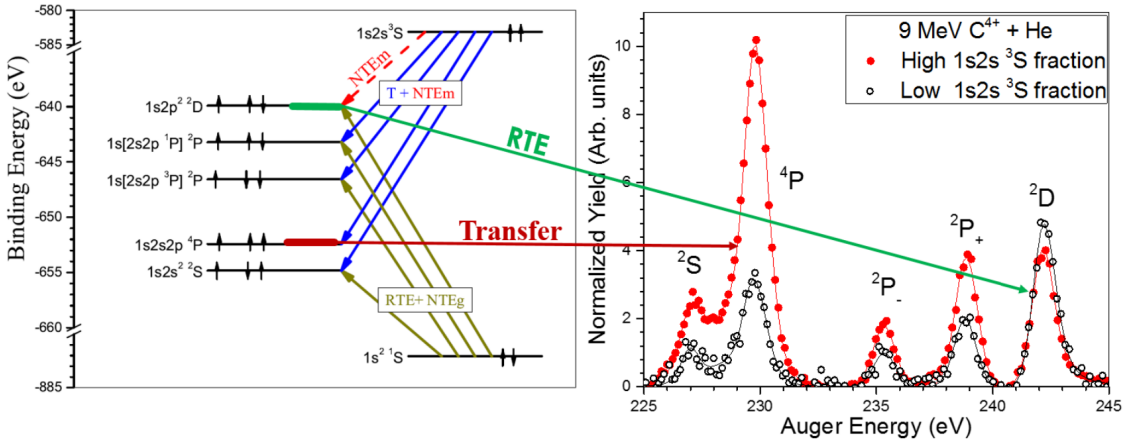

Figure 7.3: Energy level diagram showing the dominant mechanisms for the production of the $1s2l2l'$ doubly excited states formed in collisions of energetic He-like ($1s^2\,{}^1S$, $1s2s\,{}^{1,3}S$) beams with He target. Single $2p$ or $2s$ electron transfer (T) in blue or non-resonant transfer excitation (NTEm) to the metastable state (m) in red, transfer and excitation (both resonant (RTE) and non-resonant (NTEg) from the ground state (g) in gold. The NTEm process is rather weak above 6 MeV and is neglected. From Refs. [85, 112]

7.3.1 C^{4+} + He $1s2p^2\,{}^2D$ DDCS measurements

Here, we present Auger DDCS spectra in the projectile rest frame, in the energy region 6-18 MeV collisions between a two-electron mixed-beam C^{4+} ($1s^2\,{}^1S$, $1s2s\,{}^3S$) and a helium target. We focus on the production of the $C^{3+}(1s2p^2\,{}^2D)$ state which shows the strongest RTE resonance [127, 148] among the KLL Auger transitions, considered to be produced predominantly from the $1s^2\,{}^1S$ initial state. In Eq. (7.9) and Eq. (7.10) the TE and Auger decay processes are shown.

$$C^{4+}(1s^2) + \mathrm{He} \rightarrow C^{3+}(1s2p^2\,{}^2D) + \mathrm{He}^+(\mathrm{All}) \tag{7.9}$$

$$\hookrightarrow C^{4+}(1s^2) + e_A^-(\theta = 0°), \tag{7.10}$$

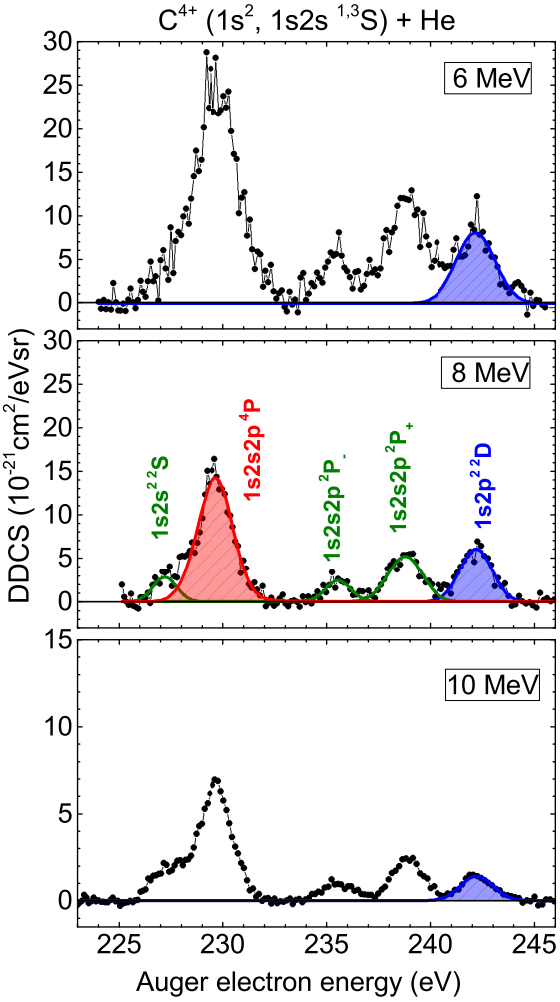

Figure 7.4: $C^{3+}(1s2l2l')$ DDCS Auger spectra after background subtraction and transformation to the projectile rest frame, showing the $1s2s^2\ ^2S$, $1s2s2p\ ^4P$, $1s2s2p\ ^2P_{\pm}$, and the $1s2p^2\ ^2D$ lines obtained in collisions of mixed-state C^{4+} $(1s^2, 1s2s\ ^{3}S)$ ion beams with helium target for projectile energies $E_p = 6, 8, 10$ MeV. The $1s2p^2\ ^2D$ (blue shaded area) assumed to be exclusively produced from the ground state component by transfer-excitation is the peak of interest.

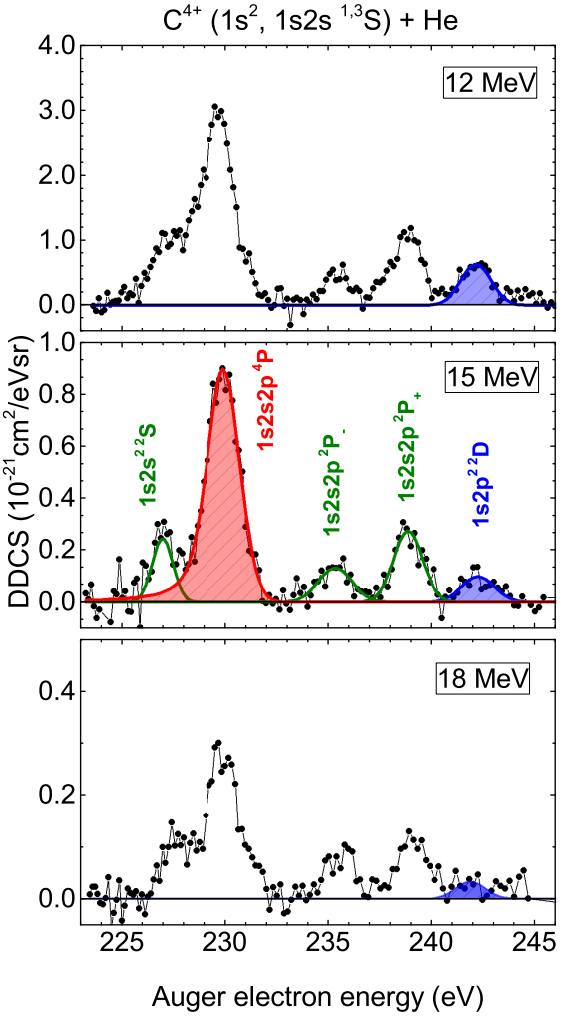

Figure 7.5: Same as 7.4, but for projectile energies $E_p = 12, 15, 18$ MeV.

7.3.2 O^{6+} + He $1s2p^2\,{}^2D$ DDCS measurements

Here, in analogy with carbon, Auger DDCS spectra in the projectile rest frame, in the energy region 10-24 MeV collisions between a two-electron mixed-beam O^{6+} ($1s^2\,{}^1S$, $1s2s\,{}^3S$) and a helium target are presented. The $O^{5+}(1s2p^2\,{}^2D)$ is considered to be predominantly produced through TE from the $1s^2\,{}^1S$ as in Eq. (7.11), and consequently Auger decays as shown in Eq. (7.12), allowing us to detect the emitted electron at $\theta = 0°$.

$$O^{6+}(1s^2) + \mathrm{He} \rightarrow O^{5+}(1s2p^2\,{}^2D) + \mathrm{He}^{+}(\mathrm{All}) \tag{7.11}$$

$$\hookrightarrow O^{6+}(1s^2) + e_A^{-}(\theta = 0°), \tag{7.12}$$

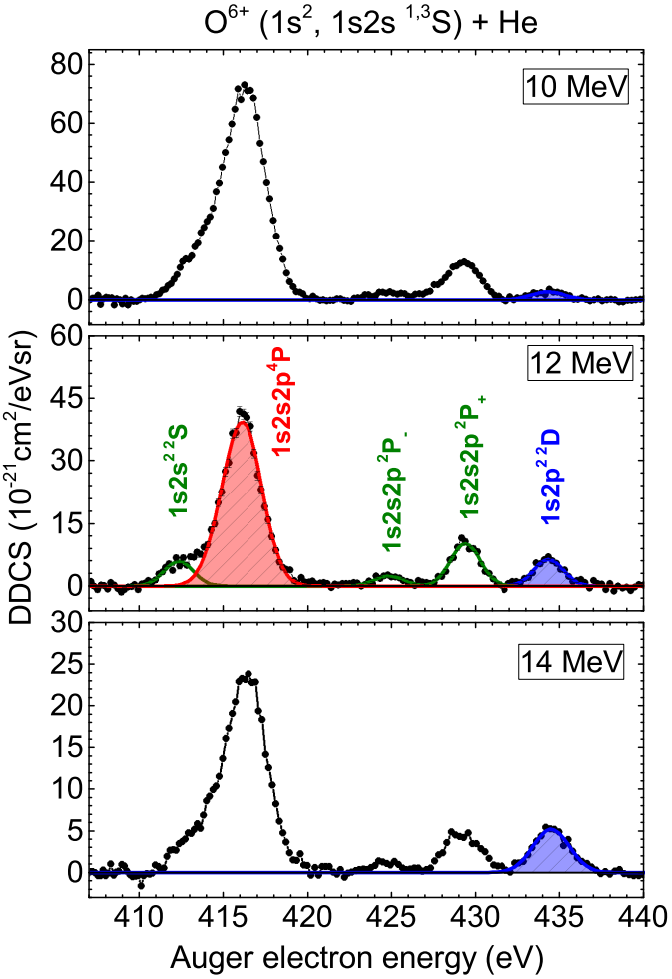

Figure 7.6: $O^{5+}(1s2l2l')$ DDCS Auger KLL spectra after background subtraction and transformation to the projectile rest frame obtained in collisions of mixed-state O^{6+} ($1s^2, 1s2s\,{}^3S$) ion beams with helium target for projectile energies $E_p = 10, 12, 14$ MeV. The $1s2p^2\,{}^2D$ (blue shaded area) is the peak of interest.

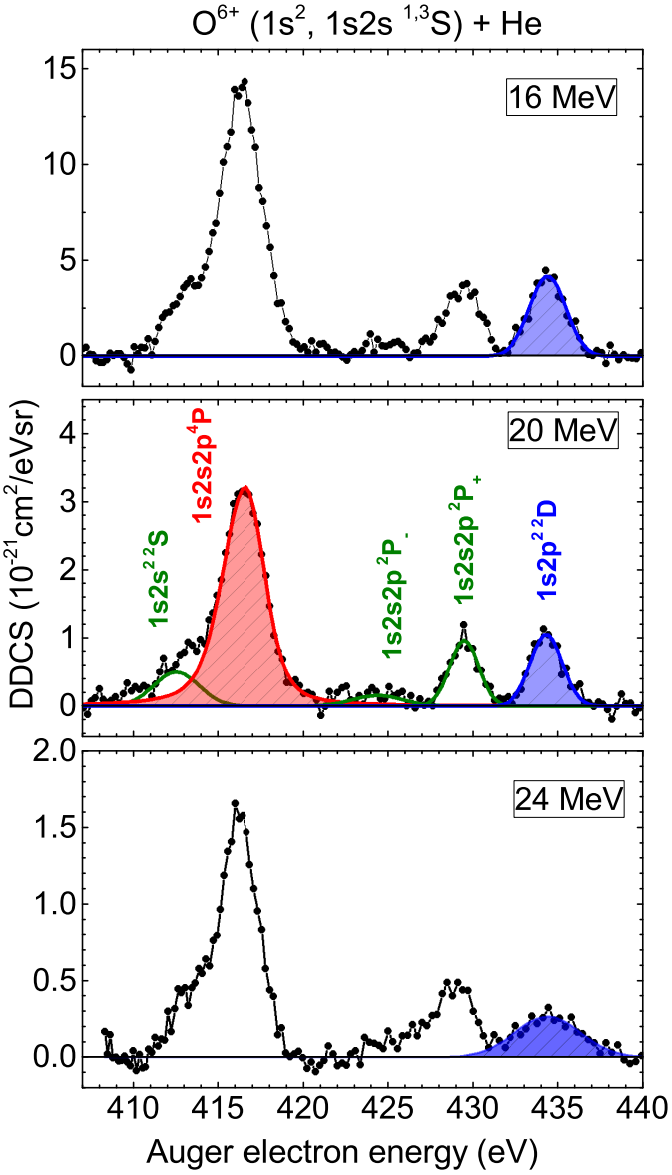

Figure 7.7: Same as Fig. 7.6, but for projectile energies $E_p = 16, 20, 24$ MeV.

7.4 $1s2p^2\,{}^2D$ SDCS results

Single differential cross sections (SDCS) of the observed lines can be obtained by integrating the area under each peak in the DDCS Auger electron spectra. This integration provides us with experimental normalized $\theta = 0°$ Auger yields which are converted to Auger SDCSs taking into account the initial amount the ion beam components that $1s2p^2\,{}^2D$ derives from, according to Eq. (7.18). From the theoretical end, the 3eAOCC theoretical cross sections are converted to the corresponding theoretical $\theta = 0°$ Auger SDCSs taking into account the Auger angular distribution and Auger yield ξ, shown in Eq. (7.17). These conversions allows us to directly compare experiment with theory as shown in Figs. 7.8 and 7.13.

7.4.1 The $1s2p^2\,{}^2D$ Auger theoretical SDCS

The ${}^2D$ SDCS are computed using the Auger angular distribution (Legendre polynomial $P_k(\cos\theta)$ expansion for $L = 2$) formula Eq. (6.11) [138]:

$$\frac{d\sigma_A}{d\Omega'}(\theta) = \overline{\xi}\,\frac{\sigma_{\rm tot}}{4\pi}\left[1 + A_2\,P_2(\cos\theta) + A_4 P_4(\cos\theta)\right], \tag{7.13}$$

where $\overline{\xi}$ is the mean ${}^2D$ Auger yield [71] and the anisotropy coefficients A_2, A_4 are functions of the ${}^2D$ M_L cross sections. In LS-coupling these coefficients depend only on L and $|M_L|$ [138] and are given for L=2 (see Table 6.3 by:

$$A_2 = \left(\frac{10}{7}\right)\frac{\sigma(2,0) + \sigma(2,1) - 2\sigma(2,2)}{\sigma_{\rm tot}} \tag{7.14}$$

$$A_4 = \left(\frac{6}{7}\right)\frac{3\sigma(2,0) - 4\sigma(2,1) + \sigma(2,2)}{\sigma_{\rm tot}}. \tag{7.15}$$

The total ${}^2D$ production cross section, $\sigma_{\rm tot}$, is:

$$\sigma_{\rm tot} = \sum_{M_L=-L}^{L}\sigma(L,|M_L|) = \sigma(2,0)+2\sigma(2,1)+2\sigma(2,2), \tag{7.16}$$

where, due to the axial symmetry around the beam direction, we also have $\sigma(L, M_L)$ $= \sigma(L, -M_L)$. For $\theta = 0°$ in Eq. (7.13), with $P_k(\cos 0°) = 1$ for k even, we then directly have:

$$\frac{d\sigma_A}{d\Omega'}(0°) = \overline{\xi}\,\frac{5\,\sigma(2,0)}{4\pi}, \tag{7.17}$$

showing that at this observation angle the SDCS depend only on the $M_L = 0$ component of the partial cross section, $\sigma(2,0)$. Further corrections due to fine-structure interaction during the time interval between production and Auger decay, i.e., the so called dealignment factors D_2 and D_4 [138], differ very little from 1

for the $C^{3+}(1s2p^2\,{}^2D)$ state [149], with this correction well within the experimental uncertainty and therefore considered negligible.

7.4.2 The $1s2p^2\,{}^2D$ Auger $\theta = 0°$ experimental SDCS

Since the dominant production mechanism for $1s2p^2\,{}^2D$ is considered to be TE from the $1s^2\,{}^1S$ ground state component of the He-like ($1s^2\,{}^1S$, $1s2s\,{}^{1,3}S$) beam, only the contribution of the $1s^2\,{}^1S$ component needs to be taken into account in the computation of the $1s2p^2\,{}^2D$ 0° Auger SDCS. Therefore, the ${}^2D$ state $d\sigma_A^{exp}/d\Omega'(0°)$ is extracted from its recorded $\theta = 0°$ Auger yield as $dY_A/d\Omega'(0°)$ as:

$$\frac{d\sigma_A^{exp}}{d\Omega'}(0°) = \frac{1}{f_g} \cdot \frac{dY_A}{d\Omega'}(0°) \tag{7.18}$$

where f_g is the determined fractional components of the ion beam in the ground state. Here, mostly low $f_{^3S}$ measurements were used to maximize f_g.

7.4.3 C^{3+} $1s2p^2\,{}^2D$ experimental and theoretical SDCS

The experimental C^{3+} $1s2p^2\,{}^2D$ ($\theta = 0°$) Auger SDCS $d\sigma_A^{exp}(0°)/d\Omega'$, are shown in Fig. 7.8 as a function of the impact energy E_p, together with theoretical calculations including 1794 states, or 716 energy levels, referred as full CC (FCC) results. Also included is the RTE impulse approximation (IA RTE) [150], seen to be about 30% larger than experiment, a known deficiency for low-Z_p ions [127]. The FCC results (thick black line) show two distinct peaks. The side of the peak above 6 MeV is seen to be in excellent agreement with the ZAPS measurements, not only in the energy dependence, but also in the absolute scale. The low-energy peak located around 2 MeV could not be recorded experimentally since the C^{4+} beam intensity was too low for reliable ZAPS measurements in this difficult to access 0.5–4 MeV range.

In Table 7.1 the C^{3+} $1s2p^2\,{}^2D$ theoretical and experimental SDCS $d\sigma_A(0°)/d\Omega'$ results according to the corresponding collision energy and the $1s^2\,{}^1S$ fractional beam component are presented.

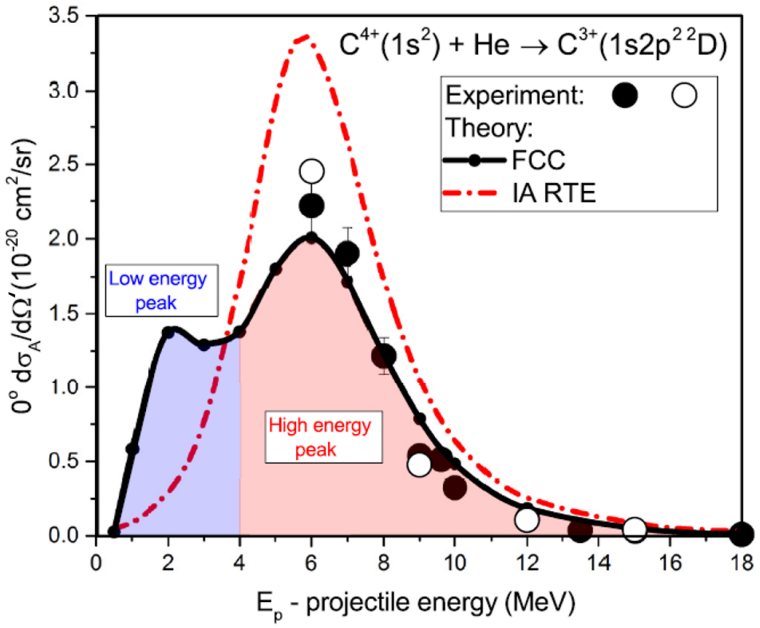

Figure 7.8: Projectile energy dependence of absolute 0° Auger SDCS, $d\sigma_A/d\Omega'$ [Eq. (7.17)], for the production of ^2D states by TE [Eq. (7.9)]. Experiment (large circles, see Table 7.1): Filled (single spectra measurements), open (two-spectra measurements). Error bars shown only when larger than symbol. Below 6 MeV, measurements were not possible due to accelerator beam current limitations. Theory: Full 3eAOCC TE (FCC, small circles joined by black interpolation line). IA RTE [red dash-dotted line, see Eq. (7.1)]. From Ref. [11]

Table 7.1: Theoretical and experimental results for the $1s2p^2\,{}^2D$ state produced in collisions of $C^{4+}(1s^2)$ with He according to Eq. (7.9) at a projectile velocity V_p and energy E_p, respectively. Listed are the full 3eAOCC (FCC) partial cross sections $\sigma(2,|M_L|)$ for $M_L = 0, \pm 1, \pm 2$, already multiplied by 2 to account for the two electrons on the helium target, the total production cross section $\sigma_{\rm tot}$ and the theoretical 0° Auger SDCS, $d\sigma_A(0°)/d\Omega'$. Also listed are the ion beam stripping combinations used in the measurements with the first/second measurement indicated by the separator /, in the case of "two-spectra measurements". Finally, the ground state fraction f_g, the measured 0° Auger electron normalized yields Z(0°) [7], and the experimentally determined 0° Auger SDCS, $d\sigma_A^{\rm exp}(0°)/d\Omega'$ [112] are also indicated. Both experimental and theoretical SDCS are shown in Fig. 7.8. Experimental uncertainties in the SDCS include both the statistical error and the uncertainty in the fraction f_g, when single spectrum measurements are involved. In the case of "two-spectra measurements" only statistical uncertainties are involved[112]. Entries indicated by $-$ means no result was acquired, while an empty (blank) entry means this entry is the same as in the previous line and column. The notation $4.31(-1)$ stands for 4.31×10^{-1}.

		Theory (FCC)					Experiment					
V_p	E_p	$\sigma(2,0)$	$\sigma(2,1)$	$\sigma(2,2)$	$\sigma_{\rm tot}$[1]	$\frac{d\sigma_A}{d\Omega'}(0°)$[2]	Stripping	$f_g^{[1]}$[3]	$f_g^{[2]}$[3]	$Z^{[1]}(0°)$	$Z^{[2]}(0°)$	$\frac{d\sigma_A^{\rm exp}}{d\Omega'}(0°)$[4]
(a.u.)	(MeV)	(cm^2)				(cm^2/sr)	method	(%)	(%)	(cm^2/sr)		
		($\times 10^{-21}$)								($\times 10^{-21}$)		
								$1s2p^2\,{}^2D$ ($\bar{\xi} = 0.9989$)[7]				
1.291	0.50	6.58(-1)	1.84(-1)	1.69(-2)	1.06	2.62(-1)	-	-	-	-	-	-
1.826	1.00	1.47(1)	4.90	5.57(-1)	2.56(1)	5.84	-	-	-	-	-	-
2.582	2.00	3.46(1)	1.48(1)	8.61(-1)	6.59(1)	1.38(1)	-	-	-	-	-	-
3.162	3.00	3.26(1)	1.36(1)	1.07	6.18(1)	1.30(1)	-	-	-	-	-	-
3.652	4.00	3.48(1)	1.03(1)	7.56(-1)	5.69(1)	1.38(1)	-	-	-	-	-	-
4.082	5.00	4.54(1)	8.05	4.31(-1)	6.24(1)	1.81(1)	-	-	-	-	-	-
4.472	6.00	5.06(1)	6.51	2.25(-1)	6.40(1)	2.01(1)	GTS-FPS[5]	-	85.5±5.1	-	18.9±1.3	22.2±2.1
							GTS-GPS/GTS[7]	83.6±3.1	93.3±1.3	20.5±0.2	22.9±0.5	24.5±0.8
4.830	7.00	4.33(1)	4.93	1.18(-1)	5.34(1)	1.72(1)	GTS-FPS[5]	-	85.5±5.1	-	16.2±1.1	19.0±1.7
5.164	8.00	3.08(1)	3.50	6.70(-2)	3.79(1)	1.23(1)	GTS-FPS[5]	-	85.5±6.2	-	10.4±0.7	12.2±1.2
5.477	9.00	1.98(1)	2.37	4.23(-2)	2.46(1)	7.88	GTS-FPS[5]	-	85.5±5.1	-	4.58±0.19	5.37±0.39
							GTS-GPS/GTS[7]	82.5±5.3	94.5±1.7	3.95±0.06	4.53±0.20	4.79±0.29
5.657	9.60	-	-	-	-	-	GTS-FPS[5]	-	85.5±5.1	-	4.37±0.46	5.12±0.62
5.774	10.00	1.22(1)	1.56	2.87(-2)	1.53(1)	4.85	avrg[6]	-	89.0±5.1	-	2.88±0.37	3.24±0.45
6.325	12.00	4.62	6.60(-1)	1.47(-2)	5.97	1.84	GTS[5]vrg[6]	-	84.6±5.1	-	1.04±0.01	1.13±0.21
							FTS/GTS[7]	79.3±4.9	96.5±0.9	0.854±0.017	1.04±0.05	1.08±0.06
6.709	13.50	-	-	-	-	-	GTS[5]	-	92.7±13.9	-	0.335±0.030	0.363±0.063
7.071	15.00	1.26	1.87(-1)	6.24(-3)	1.64	5.00(-1)	GTS[5]vrg[6]	-	83.8±12.6	-	0.255±0.061	0.305±0.086
							FTS/GTS[7]	86.3±8.4	93.9±3.8	0.355±0.010	0.386±0.019	0.412±0.036
7.746	18.00	4.12(-1)	5.99(-2)	3.18(-3)	5.39(-1)	1.64(-1)	FTS[5]	-	71.0±4.3	-	0.0584±0.024	0.083±0.034

[1] For the ^2D state $\sigma_{\rm tot}$ is given by Eq. (7.16).
[2] Theoretical 0° Auger SDCS for the ^2D state, $d\sigma_A(0°)/d\Omega'$, determined from the partial cross sections $\sigma(2, M_L)$ according to Eq. (7.17)
[3] The ground state fraction $f_g^{[i]}$ in measurement i ($i = 1, 2$) is computed from the experimentally determined $1s2s\,{}^3S$ metastable state fraction $f_{3S}^{[i]}$ [94, 112] as $f_g^{[i]} = 1 - f_{3S}^{[i]}$.
[4] Experimental 0° Auger SDCS for the ^2D state, $d\sigma_A^{\rm exp}(0°)/d\Omega' = Z^{[i]}(0°)/f_g^{[i]}$.
[5] Results obtained using single Auger KLL spectrum measurements [151] with an f_g value interpolated from similar nearest energy "two-spectra measurements".
[6] An average value was computed when more than one measurements were made having similar values of ground state fraction f_g at the same collision energy.
[7] Results [85, 152] obtained using the "two-spectra measurement" technique [112].

7.5 Further 3eAOCC results and discussion

7.5.1 Two-level model calculations: Suppressing the two-step mechanism

In order to gain additional understanding of the electronic dynamics involved in the TE process, two-level calculations were also performed, to model the production of the $C^{3+}(1s2p^2\,{}^2D)$ and $C^{3+}(1s2p^2\,{}^2P)$ states. These two identically configured $1s2p^2\,{}^2D$ and $1s2p^2\,{}^2P$ states are similar in that they both require the same net 1s $\rightarrow$ 2p excitation and 2p transfer to be produced by TE. However, due to parity selection rules, the $1s2p^2\,{}^2P$ state cannot autoionize within the LS coupling scheme and its Auger decay is therefore very weak. Its Auger energy is $\varepsilon'_A = 242.94$ eV, while its Auger rate and yield are particularly small at $A_a = 6.7 \times 10^9\ s^{-1}$ and $\xi = 0.0110$, respectively [72], making it practically undetectable by Auger spectroscopy. In comparison, the $1s2p^2\,{}^2D$ state's Auger rate, energy and yield are $A_a = 9.316 \times 10^{13}\ s^{-1}$, $\varepsilon'_A = 242.1eV$, and $\xi = 0.9985$, respectively [72]. The $1s2p^2\,{}^2P$ state can decay radiatively [153] and also by the more rare process of radiative autoionization [22, 154].

The comparison of these identically configured states offers additional interesting insights into the mechanisms of their production [43]. In contrast to the (716-level) FCC results, which include both ^2D and ^2P levels, these two-level CC calculations used a restricted basis set, including only the initial level, i.e., the target and projectile ground states, and either one of the final ^2D or ^2P levels, with their five or three M_L magnetic states, respectively. Without including any single excitation and single capture states, this simplified model blocks these specific channels and therefore deliberately suppresses any two-step mechanisms involving excitation and capture such as NTE [43]. As in the FCC calculations, they include all interactions and couplings between the states. In addition, a second two-level model was developed in which, for the same restricted basis set, the coupled equations are similarly solved, but without the two-center $e-e$ coupling matrix elements, referred to from here on as two-level CC without two center electron-electron interaction (TCee), thus further blocking also processes mediated by TCee such as RTE.

In the following, theoretical results for the ^2D and ^2P states are presented. Their total production cross sections stemming from these different calculations are presented in Fig. 7.9, while their related reduced probabilities $bP(b)$ in Figs. 7.10 and 7.11. The latter offer additional information on the nature of the production mechanisms, related to head-on (hard) or distant (soft) collisions. In Fig. 7.9 (top), the ^2D cross sections are shown for the full and restricted 3eAOCC calculations. As a first general observation, one can see that the cross sections from the FCC and the two-level CC calculations show similar structures, with two peaks. However, observed quantitative differences clearly demonstrate that even in this high energy regime, couplings to other states included in the FCC calculations, but removed in

the two-level CC, are important. Only above 12 MeV do both calculations converge, as expected. In comparison, for the ^2P cross sections, as shown in Fig. 7.9 (bottom), no high-energy peak is seen, in any of the 3eAOCC calculations, in agreement with expectations due to its weak Auger decay probability. In the next two subsections the two observed structures are analyzed in detail.

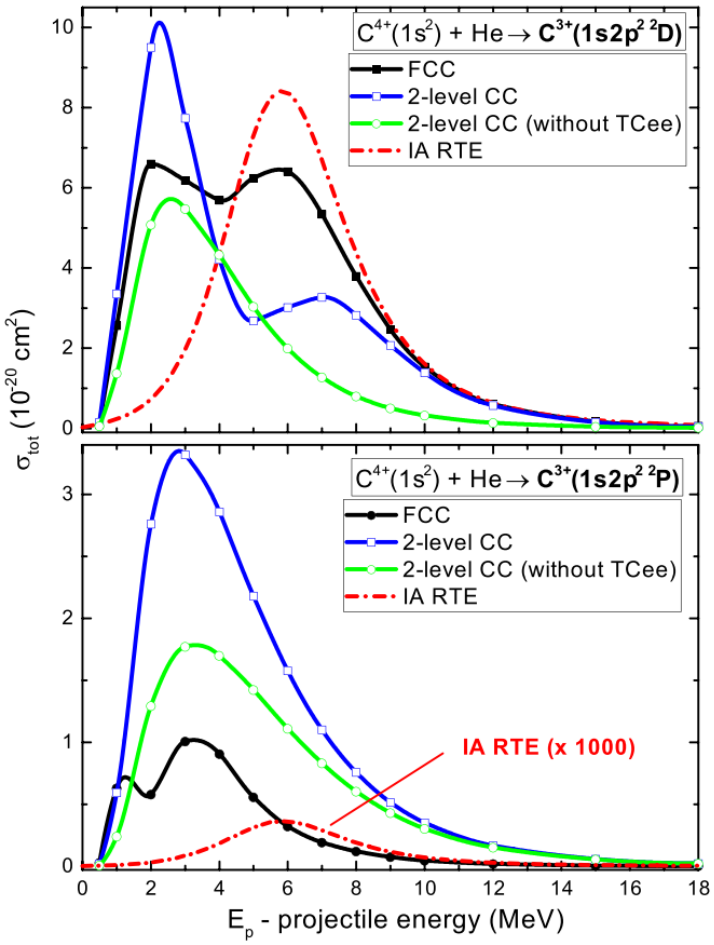

Figure 7.9: Projectile energy dependence of theoretical total cross sections σ_{tot} for the production of the similarly configured $1s2p^2\,{}^2D$ (top) and $1s2p^2\,{}^2P$ (bottom) states. Black lines with filled squares: Full close-coupling (FCC) calculations (used in the SDCS shown in Fig. 7.8). Blue lines with open squares: Two-level calculations. Green lines with open circles: Two-level CC without TCee. Red dashed dot lines: IA RTE cross sections σ^{IA}_{RTE}, also shown for both states. From Ref. [11]

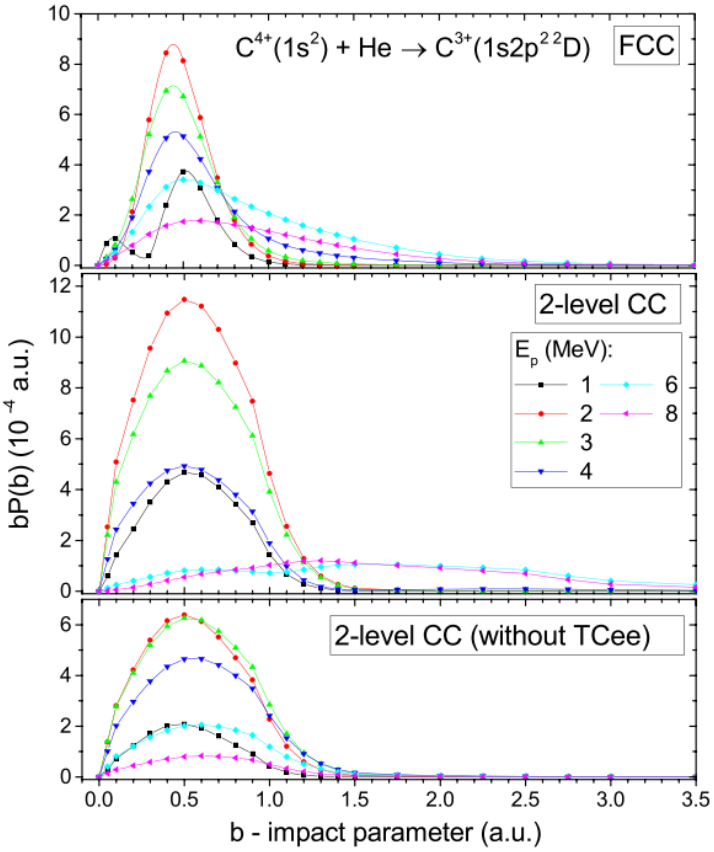

Figure 7.10: Impact parameter-weighted TE reduced probabilities $bP(b)$ (multiplied by 2 to account for the two target electrons) as a function of impact parameter b for the $1s2p^2\,{}^2D$ state at selected projectile energies E_p = 1, 2, 3, 4, 6, and 8 MeV. The three panels from top to bottom correspond to the three different calculations. From Ref. [11].

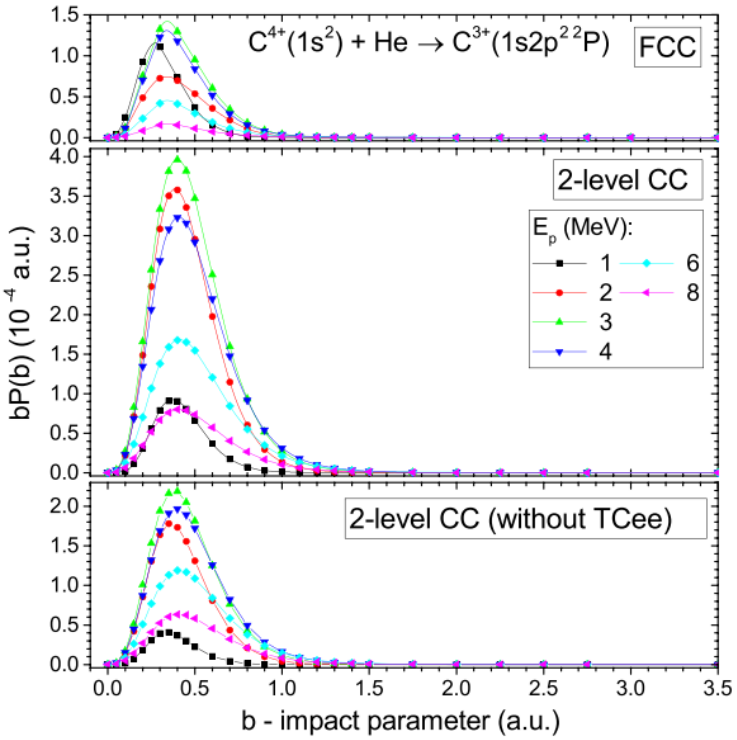

Figure 7.11: Same as Fig. 7.10, but for the identically configured $1s2p^2\,{}^2P$ state. Note that the large-b dependence at $E_p = 6$ and 8 MeV in Fig. 7.10 (middle panel) is totally absent in the corresponding middle panel above, as expected by the inverse Auger description of this process (see text). From Ref. [11].

7.5.2 The high-energy peak and RTE

We first consider the ^2D high-energy ($\sim$6 MeV) peak attributed to RTE shown in Fig. 7.8. When the two-center bielectronic repulsion matrix elements are not taken into account, the resulting cross sections, (green line in Fig. 7.9 (top)), do not show the high-energy peak, contrary to the FCC and two-level CC calculations which do include the TCee interaction. The origin of these differences is clearly elucidated when analyzing the ^2D TE probabilities as a function of impact parameter b seen in Fig. 7.10. The large-b contribution present in the FCC and two-level CC calculations above 4 MeV, as seen in Fig. 7.10 (top and middle), is wiped out when the TCee interactions are removed (Fig. 7.10 (bottom)). Additional evidence for the TCee interactions character of the high-energy peak is provided by (i) the strong $M_L = 0$ contributions in this energy regime observed in the FCC calculations shown in Fig. 7.9, and (ii) the absence of the high energy TE peak in the case of the identically configured $1s2p^2\,^2P$ cross section, shown in Fig. 7.9 (bottom). The production of this state is expected to be of negligible importance since it has an Auger decay rate about 100 times smaller than the ^2D. This is clearly demonstrated by the IA RTE results shown in Fig. 7.9 (bottom). However, the FCC ^2P calculation is seen (black line Fig. 7.9 (bottom)) to be only about a factor of 15 smaller than that for the ^2D around the RTE maximum at 6 MeV. This surprisingly large difference between the FCC calculations and the IA RTE for the ^2P cross sections can be traced to the fact that in ion-atom collisions in general, no selection rules apply during the excitation stage of the collision, while in the inverse Auger model of the IA RTE approximation, Auger selection rules are tacitly assumed in the production of the ^2P and included in the expression for the σ^{IA}_{RTE} cross section [127]. This is further supported when analyzing the probabilities for the ^2P state shown in Fig. 7.11: the FCC and both two-level calculations do not show any large-b tail as seen for the ^2D, mainly due to the suppression of the TCee interaction in this case. From these different results one can state that the high-energy ^2D peak is therefore unambiguously mediated by the TCee interaction and consistent with the inverse Auger mechanism giving rise to its resonant character.

7.5.3 The low-energy peak and the Non-Resonant Correlated Transfer-Excitation (NCTE) mechanism

We next consider the low-energy (∼2 MeV) peak for the ^2D state, to date interpreted by a two-step mechanism [43, 155]. Since the two-level calculations still show this peak even though successive excitation and single electron capture (the main mechanism responsible for NTE (see Fig. 7.2)) have been deliberately excluded in these calculations, its origin must necessarily arise from a one-step mechanism. Furthermore, additionally removing also the TCee interaction (green line in Fig. 7.9 (top)), the total cross sections still show the low-energy peak, albeit somewhat reduced in magnitude, indicating that the production of the ^2D in the two-level CC (blue line) is mediated by $(e-e)$ and still to some effect by $(e-n)$ interactions in this energy range.

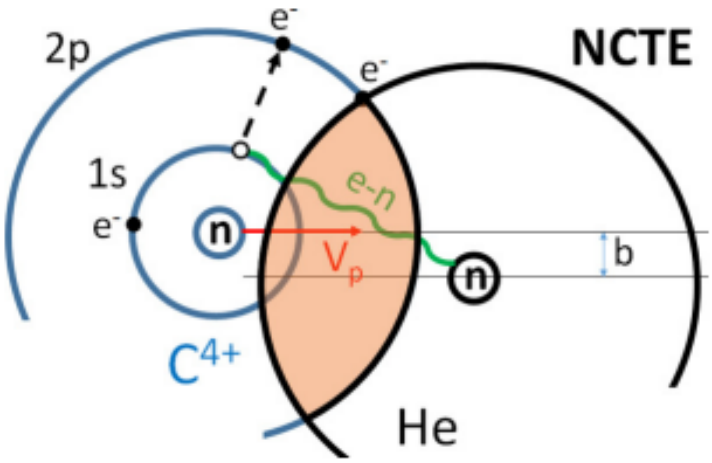

Figure 7.12: In Non-resonant correlated transfer-excitation (NCTE) the transfer of a target electron occurs during the overlap of the projectile and target electron clouds, represented by the orange area, when the projectile and target are close, while the projectile excitation is mediated by the electron-nucleus $(e-n)$ interaction, represented by the green line. From Ref. [11].

These unexpected results challenge the present understanding of transfer-excitation at low collision energies. Moreover, looking into the b dependencies of Fig. 7.10, we note that the removal of the TCee interaction (bottom) leaves the shape of the reduced probability curves qualitatively unchanged in the low-b region. Thus, the low-energy peak observed in Fig. 7.9, arises primarily from this small impact parameter structure. Similar to the two-level CC results, the FCC results (top) also show the same unique low-b structure in the 1–3 MeV energy range, where the low-energy peak appears in the cross sections. These unexpected low energy results point to the existence of a nonresonant but correlated, i.e., since must be single-step, transfer-excitation (NCTE) mechanism. Further theoretical calculations based on the OBK model exposed the mechanism described in Fig. 7.12. For higher E_p energies, the

two well-separated $bP(b)$ structures in the two-level CC results (middle), are seen to merge in the FCC results (top), demonstrating the necessity for a coherent description of the two mechanisms.

We note that for the $1s2p^2\,{}^2P$ state a low-energy peak is also evident (see bottom panel of Fig. 7.9), even though the high-energy peak is absent. This is consistent with the proposed NCTE mechanism (see Fig. 7.12) for which an $(e-n)$ interaction is responsible for the 1s $\rightarrow$ 2p excitation of the projectile (similar for both identically configured states), while transfer is possible due to the overlap of the projectile 2p and target orbitals. In addition, as seen in Fig. 7.11, the impact parameter dependence of the $1s2p^2\,{}^2P$ state is also very similar to that for the ${}^2D$ (Fig. 7.10), with the notable exception that the large-b dependence at $E_p = 6$ and 8 MeV is totally absent as expected by the much suppressed inverse Auger description of this process already discussed.

Further experimental results at low energies should be of interest to probe and validate the NCTE mechanism presented in the previous section. However, such measurements in the energy range of 1-4 MeV, would require almost pure $C^{4+}(1s^2)$ ion beams (to avoid additional TE from the metastable components [156, 157], non-negligible at these much lower energies) and will be difficult to presently obtain at existing highly-charged ion facilities (e.g. ECR sources) mostly due to the rather elevated, high-voltage ($\sim$0.25-1 MV) platforms required.

7.5.4 O^{5+} $1s2p^2\,{}^2D$ experimental and theoretical SDCS

In analogy with carbon results, experimental O^{5+} $1s2p^2\,{}^2D$ ($\theta = 0°$) Auger SDCS, $d\sigma_A^{exp}(0°)/d\Omega'$, are presented in Fig. 7.13 as a function of the impact energy E_p, together with theoretical calculations. IA RTE results (red dash-dotted line) included, are in excellent agreement in the 10 - 24 MeV range. FCC results (thick black line) seem to be in quite good agreement with the experiment in the same energy range, however, slightly shifted in energy. Experimental data were impossible to obtain at projectile energies lower than 8 MeV due to very low O^{6+} beam intensities.

In Table 7.2 the O^{5+} $1s2p^2\,{}^2D$ theoretical and experimental SDCS $d\sigma_A(0°)/d\Omega'$ results according to the corresponding collision energy and the $1s^2\,{}^1S$ fractional beam component are presented.

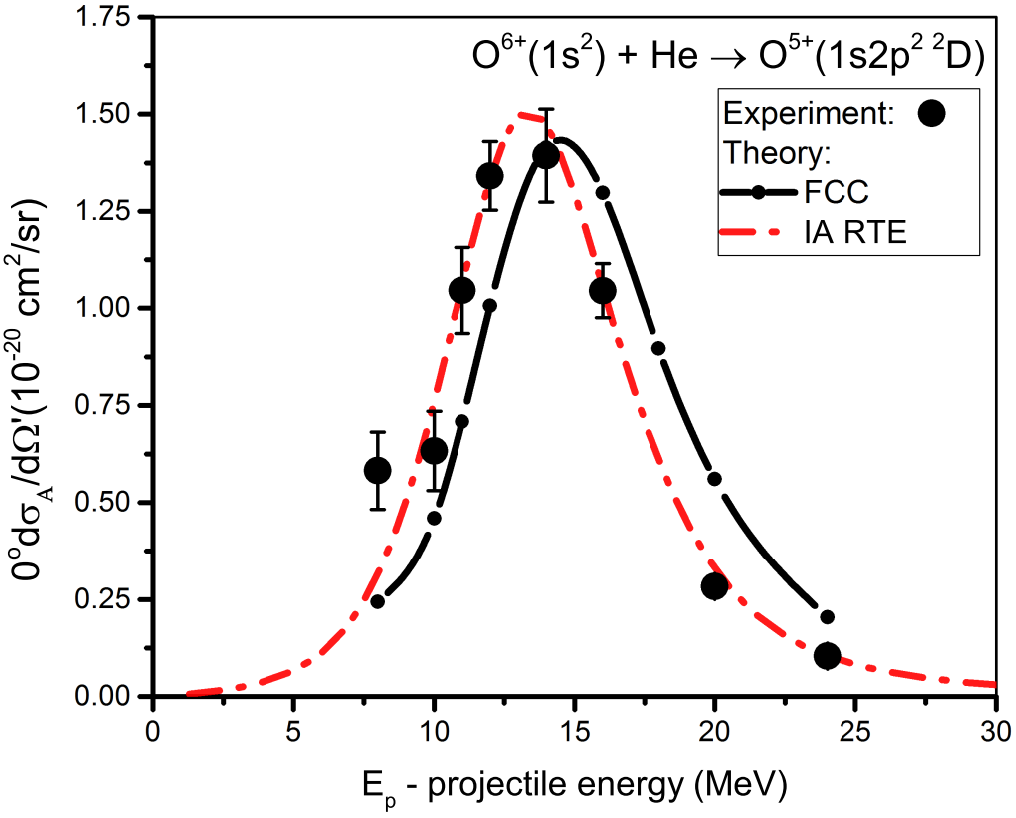

Figure 7.13: Same as Fig. 7.8, but for $O^{6+}(1s^2)$ + He collision energies 6-24 MeV.

Table 7.2: Same as Table 7.1, but for collisions of $O^{6+}(1s^2)$ with He.

		Theory (FCC)					Experiment			
V_p	E_p	$\sigma(2,0)$	$\sigma(2,1)$	$\sigma(2,2)$	$\sigma_{\rm tot}$[1]	$\frac{d\sigma_A}{d\Omega'}(0°)$[2]	Stripping	$f_g^{[2]}$[3]	$Z^{[2]}(0°)$	$\frac{d\sigma_A^{\rm exp}}{d\Omega'}(0°)$[4]
(a.u.)	(MeV)	(cm^2)				(cm^2/sr)	method	(%)	(cm^2/sr)	
		($\times 10^{-21}$)						($\times 10^{-21}$)		
						$1s2p^2\,^2D$ ($\bar{\xi}=0.9848$)[7]				
4.472	8.00	6.21	4.51	3.10(-1)	1.10(1)	2.43	GTS-FPS[5]	81.6±4.0	4.75±0.78	5.82±0.97
5.000	10.00	1.17(1)	4.09	2.62(-1)	1.61(1)	4.60	GTS-FPS[5]	79.9±3.8	5.05±0.78	6.33±1.02
5.244	11.00	1.81(1)	4.25	2.44(-1)	2.26(1)	7.08	GTS-FPS[5]	79.2±3.9	8.28±0.78	10.5±1.11
5.477	12.00	2.57(1)	4.47	2.21(-1)	3.04(1)	1.01(1)	GTS-FPS[5]	79.4±4.5	10.7±0.36	13.4±0.88
5.916	14.00	3.61(1)	4.52	1.57(-1)	4.08(1)	1.41(1)	FTS-FPS[6]	83.4±4.5	11.6±0.78	13.9±1.20
6.325	16.00	3.31(1)	3.77	9.17(-2)	3.70(1)	1.30(1)	GTS-FPS[5]	81.6±4.0	8.53±0.39	10.5±0.70
6.709	18.00	2.29(1)	2.72	4.68(-2)	2.56(1)	8.97	-	-	-	-
7.071	20.00	1.43(1)	1.86	2.28(-2)	1.62(1)	5.60	FTS[5]	85.4±3.8	0.242±0.11	2.84±0.18
7.746	24.00	5.20	7.69(-1)	6.66(-3)	5.98	2.04	FTS[5]	82.3±3.7	0.86±0.13	1.04±0.16

[1] For the ^2D state $\sigma_{\rm tot}$ is given by Eq. (7.16).
[2] Theoretical 0° Auger SDCS for the ^2D state, $d\sigma_A(0°)/d\Omega'$, determined from the partial cross sections $\sigma(2,M_L)$ according to Eq. (7.17)
[3] The ground state fraction $f_g^{[i]}$ in measurement i ($i=1,2$) is computed from the experimentally determined $1s2s\,^3S$ metastable state fraction $f_{^3S}^{[i]}$ [94, 112] as $f_g^{[i]}=1-f_{^3S}^{[i]}$.
[4] Experimental 0° Auger SDCS for the ^2D state, $d\sigma_A^{\rm exp}(0°)/d\Omega' = Z^{[i]}/f_g^{[i]}$.
[5] Results obtained using single Auger KLL spectrum measurements [151] with an f_g value interpolated from similar nearest energy "two-spectra measurements".
[6] An average value was computed when more than one measurements were made having similar values of ground state fraction f_g at the same collision energy.
[7] Results [85, 152] obtained using the "two-spectra measurement" technique [112].

7.6 Concluding remarks

Until recently, no theory could describe the TE process in a unified way, from low to high impact energies. Instead, for low collision energies the TE mechanism was described by a semiclassical approximation (SCA), while for high collision energies, the Impulse Approximation was used. For a complete treatment of the total TE cross sections, results from these two calculations were just added together incoherently. A unified treatment of both RTE and NTE has only been given for the He^+ + H system in a correlated two-electron AO+ coupled channel calculation [43] which gave TE cross sections larger than experiment by factors of 4-6 [127].

Here, the results of a new three-electron nonperturbative treatment of TE in energetic collisions of He-like ground state ions with helium were presented. All coupling schemes populating the same doubly excited state are included in one uniform and coherent treatment. This thesis focused on the production of carbon and oxygen Li-like ($1s2p^2\,^2D$) state produced in collisions of He-like ($1s^2$) carbon and oxygen with helium target.

In the case of $C^{3+}(1s2p^2\,^2D)$, the theoretical single differential cross sections show a distinctive two-peak structure as a function of the collision energy. Also, $C^{3+}(1s2p^2\,^2D)$ single differential cross sections based on high resolution Auger electron measurements were presented. For the high-energy peak, there is excellent agreement between experiment and theory in the energy range where they overlap, i.e., at resonance 6 MeV, and above. Using simplifying two-level models, the underlying mechanisms essentially responsible for these two peaks were exposed. The high-energy peak arises predominantly from the two-center electron-electron interaction in soft collisions, i.e., at large impact parameters, validating therefore the present understanding. However, the low-energy peak is found to arise mainly from a one-step mechanism. It is mediated by a single electron-nucleus interaction responsible for excitation correlated to an electron transfer in head-on collisions, i.e., at small impact parameters, where the target and projectile electronic clouds largely overlap. Finally, concerning the interferences advocated in the past, these calculations inherently include them in this coherent treatment, but the total cross sections do not show any significant evidence of their presence.

Towards an isoelectronic study of TE process, $O^{5+}(1s2p^2\,^2D)$ was also studied in the same collision energy range as carbon, obtaining experimental and theoretical single differential cross sections. The FCC theoretical results here appear slightly shifted in energy, but fairly close to the experimental results, for reasons not yet understood.

It is indeed fascinating that after almost 40 years since the introduction of the RTE and NTE mechanisms to explain transfer-excitation, the presence of a new, additional one-step mechanism is revealed by a full quantum mechanical treatment, providing further insights into bielectronic processes in many-body quantum systems.

Chapter 8

Projectile Excitation: Production of the $2s2p\,^3P$ and $2s2p\,^1P$ states, experiment and theory

Overview

Atomic excitation in energetic ion-atom collisions remains, together with ionization and transfer, is one of the fundamental processes pervading most of atomic physics.

In this thesis, the projectile inner-shell excitation is studied, mostly attributed to the Coulomb interaction between the target nucleus and the projectile electrons. This is expected when the relative impact energy is larger than the required excitation energy ΔE [158]. The probability for such an electron-nucleus excitation (enE) is expected to scale with Z_t^{*2}, where Z_t^* is the effective target nuclear charge, i.e., the charge value corresponding to the target nuclear charge screened by the surrounding target electrons, and is expected to reach its maximum value at projectile velocities near the velocity of the excited electron, while it remains practically constant with further increase of the projectile energy.

In addition, projectile excitation can also be attributed to the interaction between target and projectile electrons. In the case of free electrons this process is known as electron-impact excitation (eIE) [159]. In the case of bound electrons as in the case of ion-atom collisions, this process is referred as electron-electron excitation (eeE). Here, the projectile energy threshold for excitation is equal to $(M_p/m)\Delta E$ where M_p/m is the ratio of the projectile to electron masses. In the case of free electron impact, the excitation cross section presents a sharp threshold at the matching projectile velocity to the required excitation energy ΔE. However, in the case of a bound electron this is expected to be washed out by the target electron's orbital velocity distribution. Here, the probability for electron-electron excitation is expected to be lower than enE by a factor $1/Z_t^{*2}$ [160]. In an attempt to distinguish the contribution from each interaction low-Z targets are used in order to minimize the enE with respect to the eeE process. Furthermore, the eeE threshold is expected to lie at

much higher energies than enE, thus, possibly providing another way to distinguish the eeE from the enE. Other processes that can contribute to the production of the same states include also double-excitation (DE) and transfer-loss (TL). In general, single step mechanisms that do not require an electron spin flip should be more probable than mechanisms that are two-step or require an electron spin flip. TL can be expected to be more important at lower energies as the capture cross section falls rapidly with increasing projectile energy.

In the past, projectile excitation has been studied experimentally in collisions of Li-like oxygen and fluorine ions with H_2 and He targets [156, 160, 161], while being theoretically approached by the PWBA and the IA [162].

In this chapter we study the projectile excitation mechanisms leading to the production of the $2s2p\,^3P$ and ^1P states in 0.5-1.5 MeV/u collisions of He-like carbon and oxygen with He targets. The incident ion beam is in a mixture of the ground state $1s^2\,^1S$ and the metastable $1s2s\,^3S$ and $1s2s\,^1S$ states as usual which must all be properly taken into account when considering the possible production mechanisms of these states. Clearly, the measured absolute electron yields will also be consequently influenced by the amount of each initial beam component. Atomic orbital close-coupling calculations involving three active electrons are also included, modelling the He target by a one-electron atom, as usual. A very large number of channels are taken into account. The processes for the production of the $2s2p\,^3P$ or $2s2p\,^1P$ states can be expressed as:

$$\mathrm{C}^{4+}(1s^2\,^1S, 1s2s\,^{1,3}S) + \mathrm{He} \rightarrow \mathrm{C}^{4+}(2s2p\,^{1,3}P) + \mathrm{He(All)} \tag{8.1}$$

$$\mathrm{O}^{6+}(1s^2\,^1S, 1s2s\,^{1,3}S) + \mathrm{He} \rightarrow \mathrm{O}^{6+}(2s2p\,^{1,3}P) + \mathrm{He(All)} \tag{8.2}$$

where again He(All) includes all target excited states as previously.

8.1 Electron-nucleus Excitation (enE)

The electron-nucleus Excitation (enE) shown schematically in Fig. 8.1, is considered the primary electron excitation process: a projectile electron is excited due to its interaction with the target nuclear charge $Z_t^\star$, whose strength is reduced due to its screening by the surrounding electrons. In the PWBA theory, it is referred to as the screening mechanism, with the target electrons remaining in the ground state [163, 164] during the projectile excitation process.

8.2 Electron-electron Excitation (eeE)

In the eeE process shown in Fig. 8.2 projectile electron and a target electron interact during the collision process, result in the mutual excitation of both projectile and target electrons. This interaction is also refereed in the bibliography as antiscreening [165–167]. The target electron in this case is considered to be loosely bound

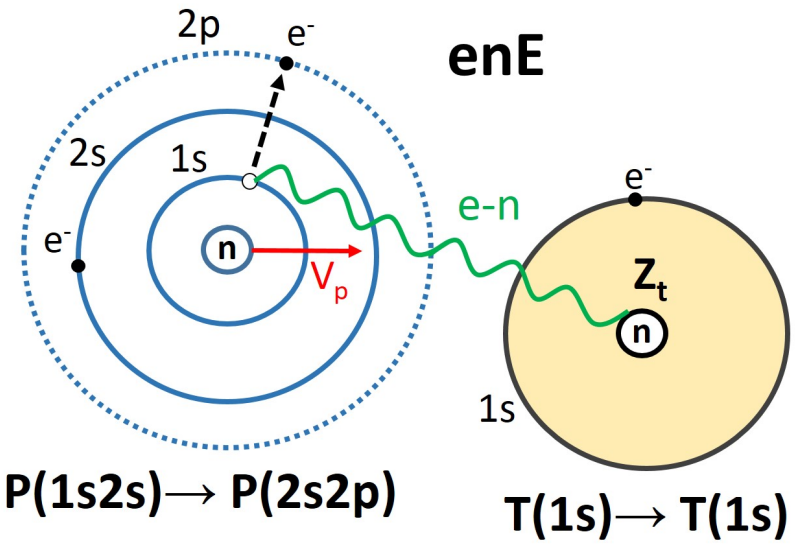

Figure 8.1: In the electron-nucleus excitation (enE) a projectile electron interacts with the target nucleus (green curvy line), leading to its excitation. Depending on whether the initial state of the projectile is $1s2s\,^3S$ or $1s2s\,^1S$, the $1s \rightarrow 2p$ excitation leads to the formation of $2s2p\,^3P$ or ^1P state, respectively. The target's nuclear charge Z_t is screened by the surrounding electron (yellow area)

to the nucleus, participating independently in the collision, being able to transfer sufficient momentum to a projectile electron leading to its excitation or ionization.

According to the IA, for swift enough collisions, the interacting target electron can be considered to scatter as a free particle whose impact energy is broadened due to its initial momentum distribution when bound to the target known as the Compton profile [168]. Therefore this process is seen to be analogous to electron impact excitation and can occur only when the kinetic energy transferred from one electron to the other is larger than the $1s \rightarrow 2p$ excitation energy ΔE. Antiscreening is thus expected to primarily contribute in the collision energy region above this threshold. The projectile energy threshold for eeE is then given by:

$$\frac{1}{2} m V_p^2 \geq \Delta E, \tag{8.3}$$

where V_p is the projectile velocity and ΔE is the $1s \rightarrow 2p$ excitation energy. Therefore, the minimum kinetic energy required for eeE is:

$$E_p^{ee} = \frac{M_p}{m} \Delta E \tag{8.4}$$

M_p and m are the projectile and electron masses, while E_p^{ee} and ΔE are in eV [9]. In Table 8.1 the $1s \rightarrow 2p$ excitation channels from the different components of the He-like $1s2s$ incident beam are presented together with the excitation energy ΔE and the projectile kinetic energy threshold. Below threshold the eeE channel is closed. The $e-e$ effects are expected to appear at energies higher than the threshold

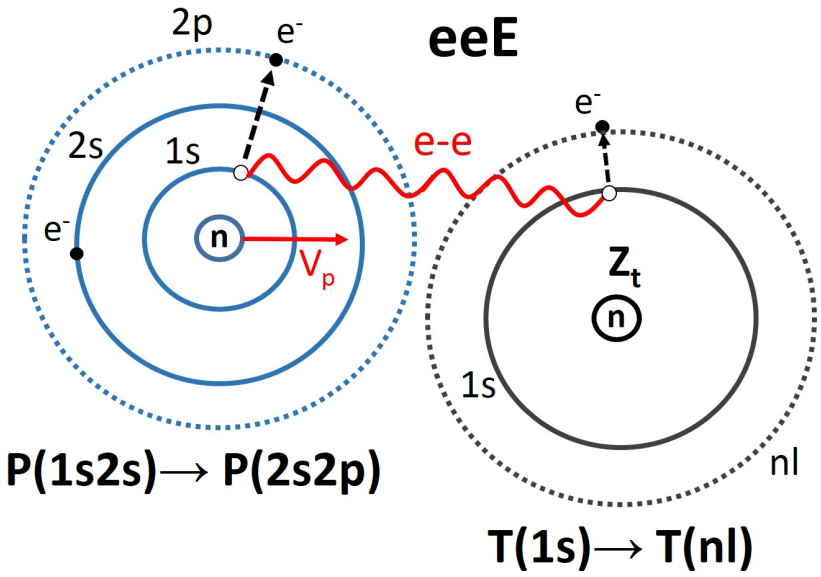

Figure 8.2: In electron-electron excitation (eeE) a projectile electron and a target electron interact (red curvy line), leading to the projectile's electron excitation. Depending on whether the initial state of the projectile is $1s2s\,^3S$ or $1s2s\,^1S$, the $1s \rightarrow 2p$ excitation leads to the formation of $2s2p\,^3P$ or ^1P state, respectively. The target electron is simultaneously typically excited or ionized according to the PWBA description [134].

calculated from Eq. (8.4) [9], while the enE channel is open from very low energies.

8.3 Double excitation (DE) and Transfer-Loss (TL)

Double excitation (DE) and transfer-loss (TL) mechanisms refer to mostly lower probability processes since they involve the simultaneous excitation of both projectile and target due to projectile and target $e - n$ interactions. As already shown by Montenegro et al [169], these become important mostly at the lowest collision energies.

Table 8.1: Excitation energies ΔE and corresponding E_p^{ee} electron impact thresholds in collisions with He target computed in the impulse approximation [9] from each of the three initial projectile ion states to each of the two final ion states.

Final	Carbon[1]						Oxygen[1]					
	$2s2p\,^3P$			$2s2p\,^1P$			$2s2p\,^3P$			$2s2p\,^1P$		
	ΔE (eV)	E_p^{ee} [3] (MeV)	(MeV/u)	ΔE (eV)	E_p^{ee} [3] (MeV)	(MeV/u)	ΔE (eV)	E_p^{ee} [3] (MeV)	(MeV/u)	ΔE (eV)	E_p^{ee} [3] (MeV)	(MeV/u)
Initial												
$1s2s\,^3S$	359.1	7.90	0.66	366.8	8.06	0.67	642.4	18.83	1.18	653.4	19.15	1.20
$1s2s\,^1S$	353.6	7.77	0.65	361.3	7.94	0.66	634.5	18.60	1.16	645.5	18.92	1.18

[1]Computed from NIST. I.P. values are relative to the $1s^2$ also using the $2s2p\,^{3,1}P$ Auger energies (see Table A.1, A.2).
[2]The excitation threshold for electron impact excitation is given by
$E_p^{ee}(\mathrm{MeV}) \approx 10^{-6}\,(M_p/m)\Delta E(eV)$, where ΔE is the $1s \rightarrow 2p$ excitation energy, while M_p and m are the masses of the projectile and the electron, respectively.

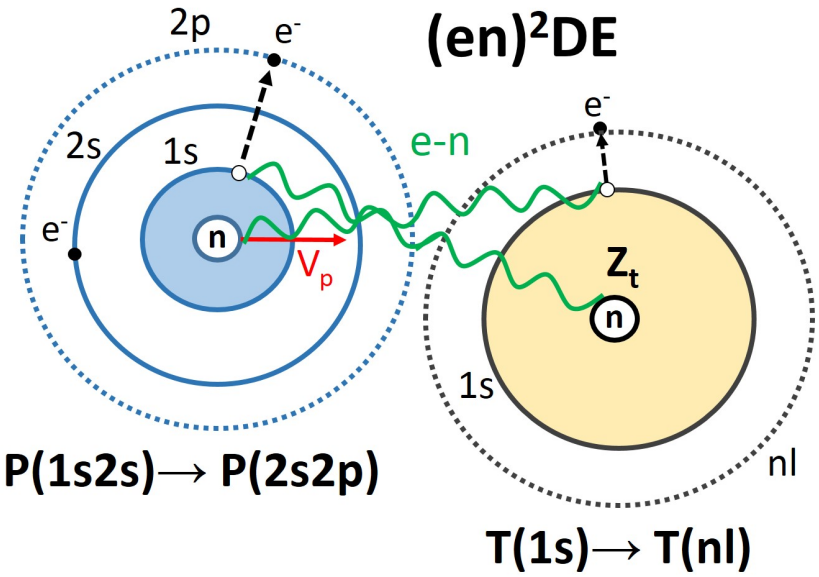

Figure 8.3: The $2s2p^{3,1}P$ can be formed also by $1s \rightarrow 2p$ excitation from the $1s2s^{3,1}S$ states respectively, with a simultaneous target excitation resulting in an overall double excitation of both partners.

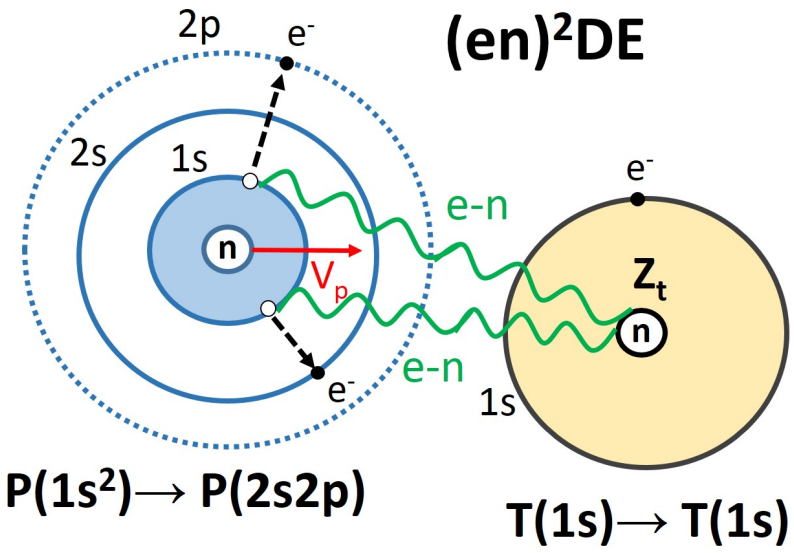

Figure 8.4: The $2s2p\,^{3,1}P$ can be formed also by $1s \rightarrow 2s$ and $1s \rightarrow 2p$ double projectile excitation from the $1s^2$ ground state, while the target electron remains in its ground state. This is a two step process and therefore of low probability.

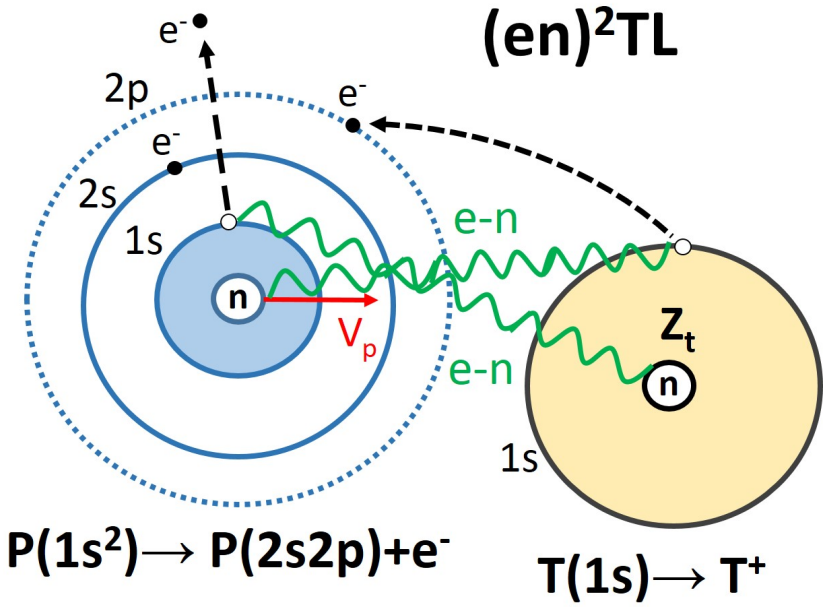

Figure 8.5: In transfer-loss (TL) the projectile loses an electron through ionization, and captures another electron from the target. Again the $2s2p\,^3P$ or ^1P states can be produced whether the initial state of the projectile is $1s2s\,^3S$ or ^1S. This is also a two step process and therefore of low probability.

8.4 $2s2p\,^{3,1}P$ DDCS Auger electron spectra

Both $2s2p\,^3P$ and $2s2p\,^1P$ excitation lines are clearly seen to lie a bit higher in electron energy than the previously discussed $1s2s2l'$ KLL Auger lines produced by SEC [129, 152] or TE [11] as shown in Fig. 5.1. Here, C^{4+} and O^{6+} $2s2p\,^{3,1}P$ DDCS spectra are presented after being transformed from counts versus channel number to projectile rest frame DDCS versus Auger energy. The $2s2p\,^3P$ appears (see Figs. 8.6, 8.7, 8.8, and 8.9) quite strong in all of the spectra and is easily identified and fitted, while this is not the case for the $2s2p\,^1P$ which appears, in the case of C^{4+}, blended in with the $(1s2s\,^3S)3d\,^2D$ state and quite close to the emerging $(1s2s\,^3S)3s\,^2S$ and $(1s2s\,^3S)3p\,^2P$ states, making the determination of the SDCS fit more difficult.

8.4.1 C^{4+} + He $2s2p\,^{3,1}P$ DDCS measurements

In this section, we present the DDCS Auger electron spectra in the projectile rest frame, produced in collisions between a two-electron mixed-beam C^{4+} ($1s^2\,^1S$, $1s2s\,^{3,1}S$) and helium target in the energy region 6-18 MeV according to the processes:

$$C^{4+}(1s^2, 1s2s\,^{3,1}S) + \mathrm{He} \rightarrow C^{4+}(2s2p\,^{3,1}P) + \mathrm{He(All)} \tag{8.5}$$

$$\hookrightarrow C^{5+}(1s) + e_A^-(\theta = 0^\circ), \tag{8.6}$$

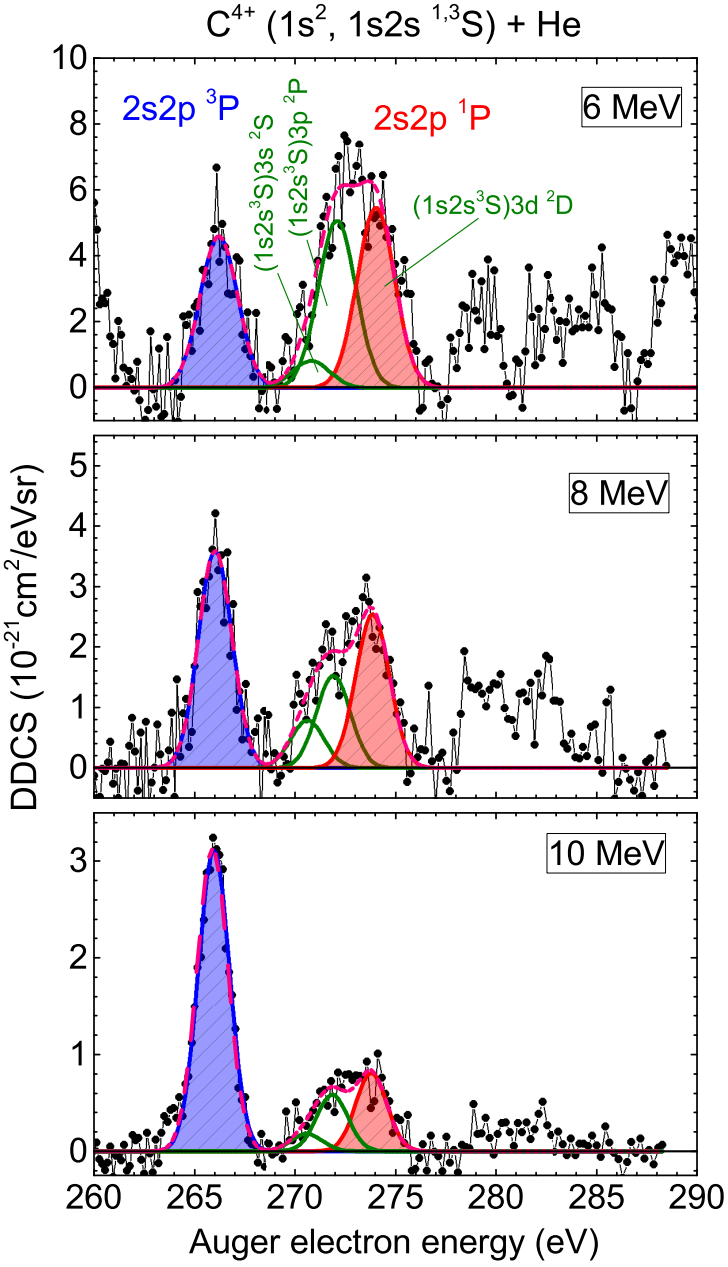

Figure 8.6: DDCS ZAPS spectra in the projectile rest frame as a function of electron energy at the selected projectile energies $E_p = 6, 8, 10$ MeV in collisions of $C^{4+}(1s^2, 1s2s\,^{3,1}S)$ ion beams with helium gas target. Identified are both the $2s2p\,^3P$ (blue shaded area) and $2s2p\,^1P$ (pink shaded area) Auger lines. The stripping method and the extracted results at the corresponding value of E_p are listed in Tables 8.6 and 8.8. Also shown (green Gaussians) are the three near-lying Auger lines $(1s2s\,^3S)3l\,^2L$ with $l = 0, 1, 2$ and $L = l$ due to $3l$ capture to the $1s2s\,^3S$ component, whose energies are also listed in Table A.1. Particularly the $(1s2s\,^3S)3d\,^2D$ line lies within the pink shaded area and cannot be resolved. $3l$ capture is seen to drop rapidly with projectile energy.

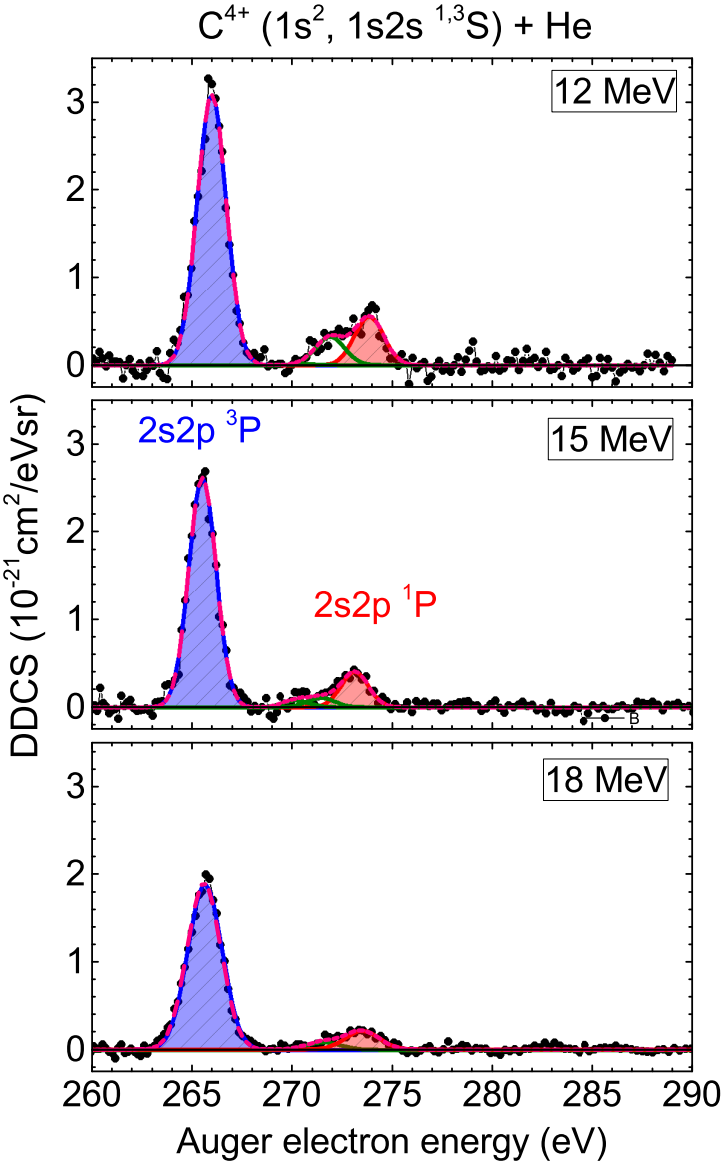

Figure 8.7: Same as Fig. 8.6, but for the selected projectile energies $E_p = 12, 15, 18$ MeV.

8.4.2 O^{6+} + He $2s2p\,^{3,1}P$ DDCS measurements

Similarly to the carbon excitation processes Eqs. 8.5 and 8.6, we have also for oxygen:

$$O^{6+}(1s^2, 1s2s\,^{3,1}S) + \mathrm{He} \rightarrow O^{6+}(2s2p\,^{3,1}P) + \mathrm{He(All)} \tag{8.7}$$

$$\hookrightarrow O^{7+}(1s) + e_A^-(\theta = 0°). \tag{8.8}$$

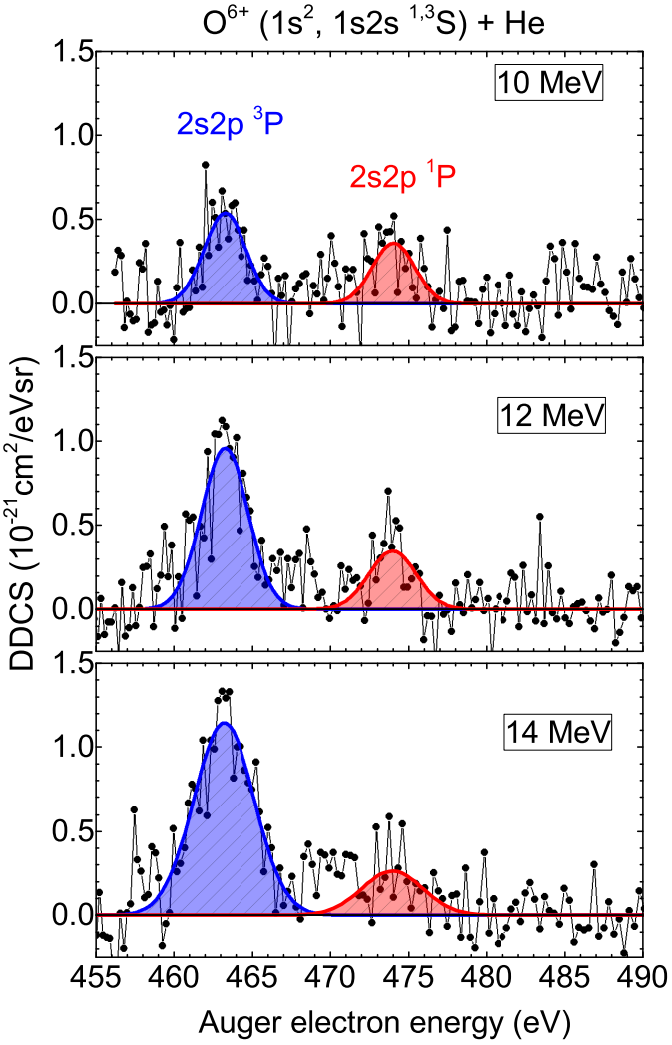

Figure 8.8: Same as Fig. 8.6, but for oxygen at the selected projectile energies $E_p = 10, 12, 14$ MeV of $O^{6+}(1s^2,\ 1s2s\,^{3,1}S)$ ion beam with He gas target. The stripping method and the extracted results at the corresponding value of E_p are listed in Tables 8.7 and 8.9. For oxygen there are no other Auger lines lying in between the two excitation lines as in the case of carbon.

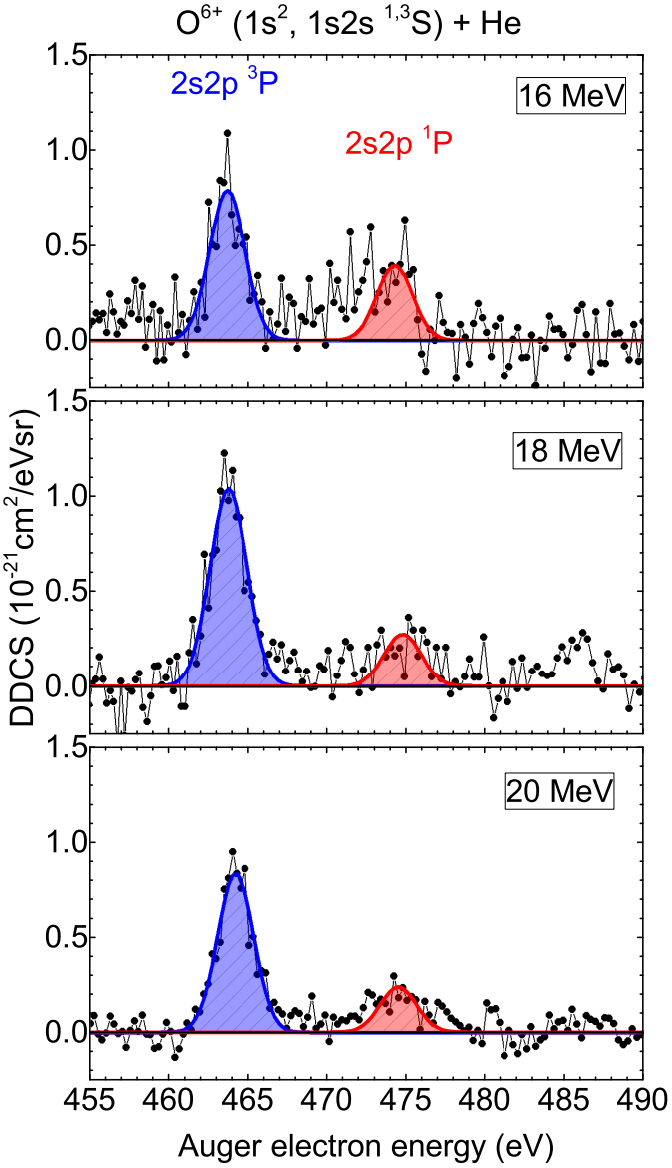

Figure 8.9: Same as Fig. 8.8, but for selected projectile energies $E_p = 16, 18, 20$ MeV.

8.5 $2s2p\,^{3,1}P$ 3eAOCC SDCS results

To obtain theoretical cross sections for the excitation processes the 3eAOCC method was used, as already described in chapter 6 [130, 132, 170], and used successfully for transfer-excitation [11] and single electron capture [85, 129, 152] investigations in C^{4+} (and O^{6+})+He MeV collisions. The excitation results were obtained within the same 3eAOCC calculation used to also obtain the previous results on TE and capture.

The cross sections stemming from the close-coupling computations and shown in the following are inclusive cross sections, i.e., cross sections for excitation to C^{4+}(2s2p) and O^{6+}(2s2p), whatever the final state of the helium target. This is mandatory since the target is not analyzed experimentally after collision and the

calculations show that He excitation and ionization are very important channels, especially for initial metastable ($1s2s\,^{1,3}S$) helium-like ions. The cross sections for production of excited and ionized He, with the projectile staying in its initial state, are about two orders of magnitude larger for C^{4+}+He collisions (and even more for the O^{6+} projectiles) than those for the process under consideration, so the simultaneous inelastic processes acting on both centres in the cross sections were carefully included and are presented in the following.

Note that in previous works [11, 85, 129, 152] concerning processes in which one electron was transferred from the target to the projectile, the use of a one-electron representation of the helium target implies a multiplication of the cross sections by a factor two, to take into account also the second He electron within the independent particle approximation. In the present study of projectile excitation in which the target electrons are not directly involved, such a factor is not used since the TCee interaction is included in the calculations, first through the Coulomb and exchange bi-electronic couplings involving the active target electron and, second, through the potential modelling the He^+-electron interaction taking into account both target electrons.

Since the He-like X^{q+} ions are in a mixture of the $1s^2$ (the ground state) and the two long-lived (metastable) states $1s2s\,^3S$ and $1s2s\,^1S$, three independent calculations had to be performed, one for each initial state. Thus, production cross sections for the following different excitation processes were calculated:

Single ($1s \to 2p$) excitation without spin exchange:

$$X^{q+}(1s2s\,^3S) + He(1s) \to X^{q+}(2s2p\,^3P) + He(All) \tag{8.9}$$
$$X^{q+}(1s2s\,^1S) + He(1s) \to X^{q+}(2s2p\,^1P) + He(All) \tag{8.10}$$

Single ($1s \to 2p$) excitation with spin exchange:

$$X^{q+}(1s2s\,^1S) + He(1s) \to X^{q+}(2s2p\,^3P) + He(All) \tag{8.11}$$
$$X^{q+}(1s2s\,^3S) + He(1s) \to X^{q+}(2s2p\,^1P) + He(All) \tag{8.12}$$

Double ($1s \to 2p$, $1s \to 2s$) excitation with spin exchange:

$$X^{q+}(1s^2\,^1S) + He(1s) \to X^{q+}(2s2p\,^3P) + He(All) \tag{8.13}$$

Double ($1s \to 2p$, $1s \to 2s$) excitation without spin exchange:

$$X^{q+}(1s^2\,^1S) + He(1s) \to X^{q+}(2s2p\,^1P) + He(All) \tag{8.14}$$

where He(All) signifies that all final states (included in the calculation) of the He target were considered in the calculation, including the He($1s$), He(nl), and even

ionization, i.e., He^+. In the excitation process with spin exchange the excited projectile state is seen to change spin, while in the process without spin exchange, i.e., direct excitation, the initial spin state is conserved. It is also worth noting that the above single excitation processes can also go through via the two-step process of transfer-loss (TL) (e.g. capture to the $2p$ with simultaneous projectile $1s$ ionization), especially competitive with the weaker process of single excitation with spin exchange. The 3eAOCC calculations certainly also include this transfer-loss channel, but its contribution cannot be separated from excitation. In Li-like ion-atom collisions, TL is thought to play an important role in the production of $1s2s2p\,^4P$ states at low collision energies of Li-like ions [160], but detailed calculations have not been performed to date.

The computed partial cross sections, $\sigma_i[M] = 0$ and total $1s \rightarrow 2p$ projectile excitation cross sections cross sections $\sigma_i^{\rm tot}$ are listed in Tables 8.2 and 8.3 for ^3P, and Tables 8.4 and 8.5 for ^1P, for carbon and oxygen ion beams, respectively, where i signifies production from one of the three initial ion states, i.e., g for ground state, ^3S and ^1S. In Figs. 8.10 to 8.13 the energy dependence of the cross sections is shown.

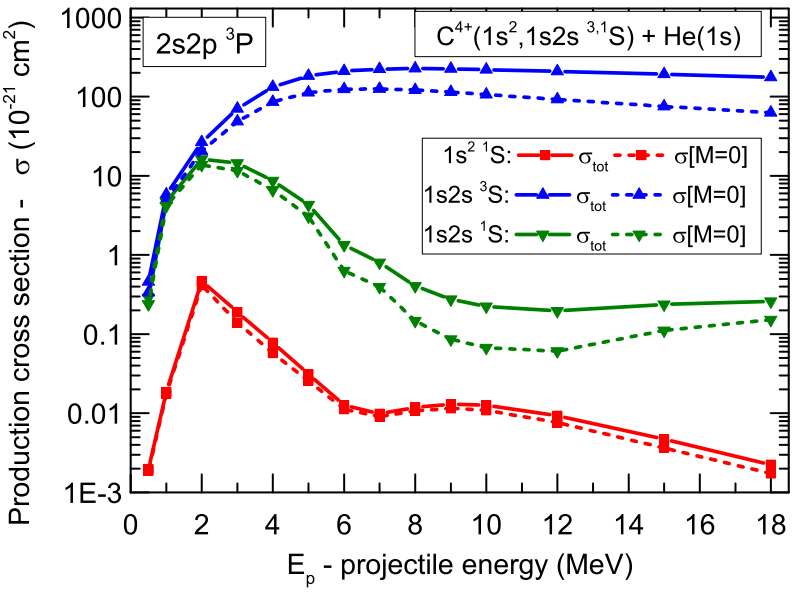

Figure 8.10: $C^{4+}(2s2p\,^3P)$ 3eAOCC production cross sections as a function of projectile energy E_p from each of the three different C^{4+} ion beam components: The $C^{4+}(1s2s\,^3S)$ state (blue lines with triangles), the $C^{4+}(1s2s\,^1S)$ state (green lines with inverted triangles) and the $C^{4+}(1s^2)$ ground state (red lines with squares). The full lines correspond to total cross sections (sum over all partial cross sections), while the dashed lines to just the $M = 0$ partial cross sections, $\sigma[M = 0]$, as also listed in Table 8.2.

Table 8.2: Calculated cross sections for the production of the $2s2p\,^3P$ state in collisions of mixed-state $C^{4+}(1s^2,^{3,1}S)$ ion beams with He as a function of projectile energy E_p. Listed from left to right are the projectile velocity V_p and energy E_p, the 3eAOCC partial cross section for $M = 0$, $\sigma[M = 0]$, and the total production cross sections $\sigma^{\rm tot} = \sigma[M = 0] + 2\sigma[M = 1]$. An uncertainty of about 15% is assigned to all computed cross sections. The notation 4.31[-1] stands for 4.31×10^{-1}.

		$C^{4+}(1s^2, 1s2s\,^{3,1}S) + He(1s) \rightarrow C^{4+}(2s2p\,^3P) + He(All)$					
		$C^{4+}(1s^2)$		$C^{4+}(1s2s\,^3S)^2$		$C^{4+}(1s2s\,^1S)$	
V_p [1]	E_p	$\sigma[M{=}0]$	$\sigma^{\rm tot}$	$\sigma[M{=}0]$	$\sigma^{\rm tot}$	$\sigma[M{=}0]$	$\sigma^{\rm tot}$
(a.u.)	(MeV)	[$\times 10^{-21}$ cm^2]					
$2s2p\,^3P$:							
1.291	0.5	1.87[-3]	1.99[-3]	3.36[-1]	4.59[-1]	2.40[-1]	2.89[-1]
1.826	1	1.76[-2]	1.86[-2]	4.95	5.82	4.19	4.67
2.582	2	4.16[-1]	4.70[-1]	2.06[1]	2.67[1]	1.38[1]	1.63[1]
3.162	3	1.41[-1]	1.89[-1]	4.87[1]	7.02[1]	1.16[1]	1.45[1]
3.652	4	5.77[-2]	7.79[-2]	8.61[1]	1.32[2]	6.62	8.70
4.082	5	2.57[-2]	3.13[-2]	1.13[2]	1.83[2]	3.08	4.33
4.472	6	1.13[-2]	1.27[-2]	1.24[2]	2.11[2]	6.32[-1]	1.34
4.830	7	9.10[-3]	9.88[-3]	1.25[2]	2.24[2]	3.95[-1]	8.04[-1]
5.164	8	1.07[-2]	1.18[-2]	1.21[2]	2.27[2]	1.48[-1]	4.07[-1]
5.477	9	1.16[-2]	1.30[-2]	1.14[2]	2.24[2]	8.60[-2]	2.75[-1]
5.774	10	1.09[-2]	1.26[-2]	1.06[2]	2.20[2]	6.72[-2]	2.23[-1]
6.325	12	7.63[-3]	9.32[-3]	9.20[1]	2.09[2]	6.12[-2]	1.96[-1]
7.071	15	3.64[-3]	4.69[-3]	7.53[1]	1.92[2]	1.12[-1]	2.36[-1]
7.746	18	1.74[-3]	2.25[-3]	6.26[1]	1.76[2]	1.52[-1]	2.59[-1]

[1] V_p(a.u.) $\approx 2\sqrt{10\,E_p(\text{MeV})/M_p(\text{u})}$

[2] From the $C^{4+}(1s2s\,^3S)$ initial beam component the partial cross sections $\sigma[M]$ are the mean of the two contributions from the doublet and quartet total spin of the collision partners $\mathbf{S}_{\rm tot}$, i.e., $\sigma_{^3S}(M) = 0.5\sigma_{^3S}[M, \mathbf{S}_{\rm tot} = 3/2] + 0.5\sigma_{^3S}[M, \mathbf{S}_{\rm tot} = 1/2]$, when using a one-electron model for the He target (see text)

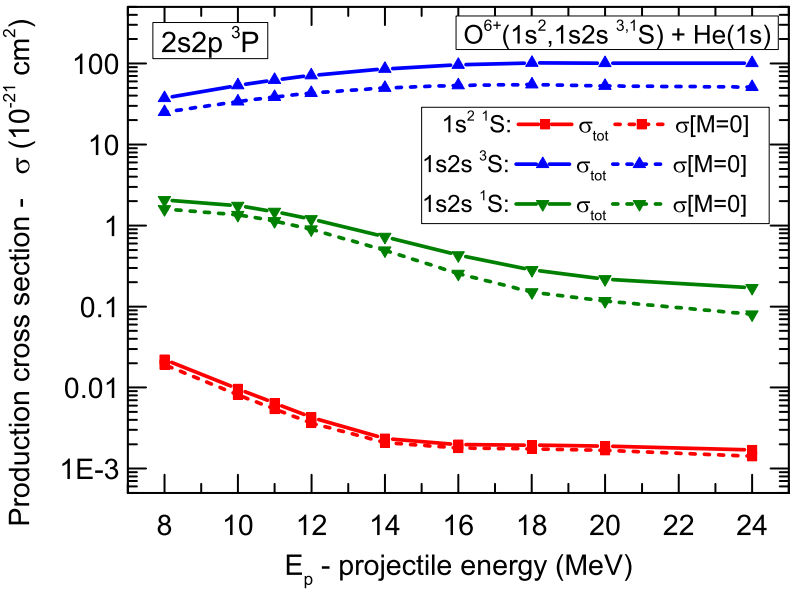

Figure 8.11: Production cross sections as in Fig. 8.10, but for O^{6+} collisions with He.

Table 8.3: Same as Table 8.2, but for oxygen. Footnotes same as Table 8.2.

		$O^{6+}(1s^2, 1s2s\,^{3,1}S) + He(1s) \rightarrow O^{6+}(2s2p\,^3P) + He(All)$					
		$O^{6+}(1s^2)$		$O^{6+}(1s2s\,^3S)^2$		$O^{6+}(1s2s\,^1S)$	
V_p [1]	E_p	$\sigma[M{=}0]$	σ^{tot}	$\sigma[M{=}0]$	σ^{tot}	$\sigma[M{=}0]$	σ^{tot}
(a.u.)	(MeV)	$[\times 10^{-21}$ cm$^2]$					
$2s2p\,^3P$:							
4.472	8	1.91[-2]	2.22[-2]	2.51[1]	3.74[1]	1.59	2.06
5.000	10	8.11[-3]	9.63[-3]	3.39[1]	5.37[1]	1.35	1.75
5.244	11	5.42[-3]	6.42[-3]	3.87[1]	6.26[1]	1.14	1.49
5.477	12	3.67[-3]	4.29[-3]	4.32[1]	7.13[1]	8.97[-1]	1.20
5.916	14	2.09[-3]	2.35[-3]	5.01[1]	8.60[1]	4.94[-1]	7.26[-1]
6.325	16	1.79[-3]	1.98[-3]	5.38[1]	9.58[1]	2.55[-1]	4.29[-1]
6.709	18	1.76[-3]	1.94[-3]	5.50[1]	1.01[2]	1.51[-1]	2.82[-1]
7.071	20	1.68[-3]	1.89[-3]	5.29[1]	1.01[2]	1.17[-1]	2.18[-1]
7.746	24	1.42[-3]	1.69[-3]	5.11[1]	1.04[2]	7.98[-2]	1.70[-1]

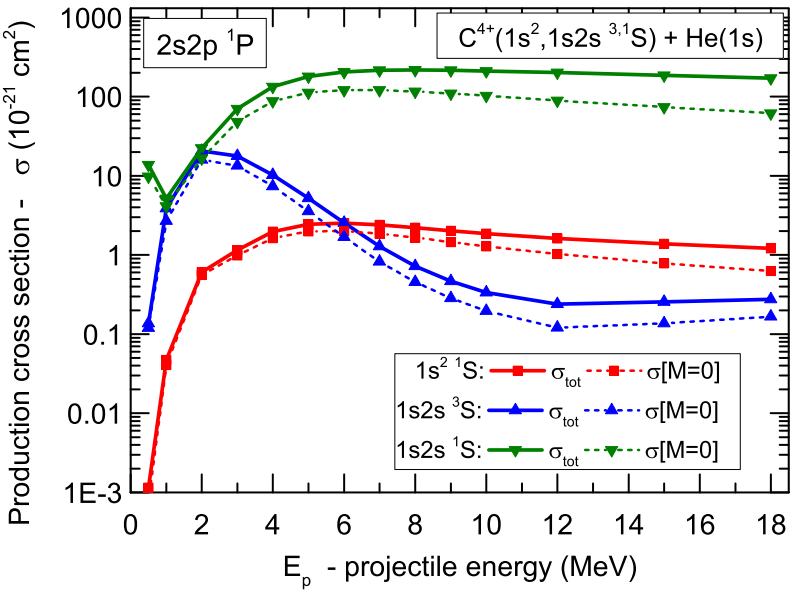

Figure 8.12: Same as Fig. 8.10, but for the production of the $2s2p\,^1P$ state. Again, direct $1s \rightarrow 2p$ excitation, but from the $1s2s\,^1S$ state (green lines with inverted triangles) is seen to be the dominant excitation mode, followed by $1s \rightarrow 2p$ excitation with exchange (blue lines with triangles) and double excitation (red lines with squares). Double excitation is seen to become larger than excitation with exchange as the collision energy E_p increases and the time allowed for spin exchange is correspondingly reduced.

Table 8.4: Same as Table 8.2, but for $2s2p\,^1P$.

		$C^{4+}(1s^2, 1s2s\,^{3,1}S) + He(1s) \rightarrow C^{4+}(2s2p\,^1P)$ + He(All)					
		$C^{4+}(1s^2)$		$C^{4+}(1s2s\,^3S)$[2]		$C^{4+}(1s2s\,^1S)$	
V_p [1]	E_p	$\sigma[M{=}0]$	σ^{tot}	$\sigma[M{=}0]$	σ^{tot}	$\sigma[M{=}0]$	σ^{tot}
(a.u.)	(MeV)	[$\times 10^{-21}$ cm^2]					
$2s2p\,^1P$:							
1.291	0.5	7.48[-4]	1.15[-3]	1.20[-1]	1.36[-1]	9.80	1.38[1]
1.826	1	4.08[-2]	4.73[-2]	2.70	3.88	4.13	5.17
2.582	2	5.61[-1]	6.09[-1]	1.60[1]	2.06[1]	1.66[1]	2.25[1]
3.162	3	9.88[-1]	1.15	1.34[1]	1.78[1]	4.82[1]	7.02[1]
3.652	4	1.63	1.96	7.36	1.03[1]	8.77[2]	1.34[2]
4.082	5	1.98	2.44	3.58	5.19	1.12[2]	1.80[2]
4.472	6	2.01	2.52	1.69	2.54	1.21[2]	2.05[2]
4.830	7	1.86	2.41	8.25[-1]	1.28	1.21[2]	2.15[2]
5.164	8	1.65	2.22	4.53[-1]	7.22[-1]	1.17[2]	2.17[2]
5.477	9	1.45	2.03	2.85[-1]	4.66[-1]	1.10[2]	2.15[2]
5.774	10	1.28	1.86	1.96[-1]	3.36[-1]	1.03[2]	2.11[2]
6.325	12	1.03	1.62	1.21[-1]	2.39[-1]	8.94[1]	2.02[2]
7.071	15	7.85[-1]	1.38	1.36[-1]	2.55[-1]	7.38[1]	1.87[2]
7.746	18	6.27[-1]	1.21	1.67[-1]	2.76[-1]	6.17[1]	1.71[2]

[1] $V_p(\text{a.u.}) \approx 2\sqrt{10\,E_p(\text{MeV})/M_p(\text{u})}$

[2] From the $C^{4+}(1s2s\,^3S)$ initial beam component the partial cross sections $\sigma[M]$ are the mean of the two contributions from the doublet and quartet total spin of the collision partners $\mathbf{S}_{tot}$, i.e., $\sigma_{^3S}(M) = 0.5\sigma_{^3S}(M, \mathbf{S}_{tot} = 3/2) + 0.5\sigma_{^3S}(M, \mathbf{S}_{tot} = 1/2)$, when using a one-electron model for the He target (see text)

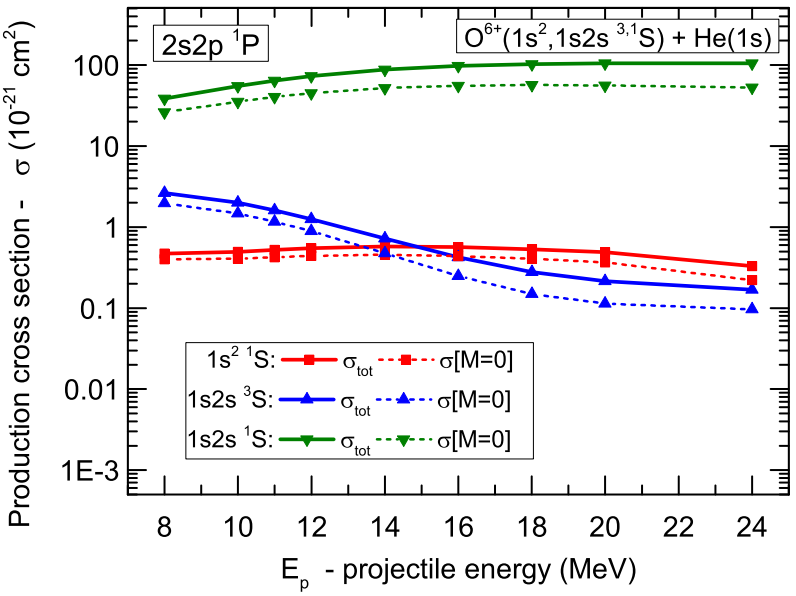

Figure 8.13: Production cross sections as in Fig. 8.12, but for O^{6+} collisions with He.

Table 8.5: Same as Table 8.4, but for oxygen. Footnotes same as Table 8.4.

		$O^{6+}(1s^2, 1s2s\,^{3,1}S) + He(1s) \rightarrow O^{6+}(2s2p\,^1P) + He(All)$					
		$O^{6+}(1s^2)$		$O^{6+}(1s2s\,^3S)^2$		$O^{6+}(1s2s\,^1S)$	
V_p [1]	E_p	$\sigma[M{=}0]$	σ^{tot}	$\sigma[M{=}0]$	σ^{tot}	$\sigma[M{=}0]$	σ^{tot}
(a.u.)	(MeV)	$[\times 10^{-21}$ cm$^2]$					
$2s2p\,^1P$:							
4.472	8	4.01[-1]	4.69[-1]	1.97	2.63	2.61[1]	3.86[1]
5.000	10	4.08[-1]	4.96[-1]	1.47	1.99	3.53[1]	5.51[1]
5.244	11	4.23[-1]	5.21[-1]	1.17	1.60	4.03[1]	6.42[1]
5.477	12	4.40[-1]	5.47[-1]	8.89[-1]	1.25	4.50[1]	7.31[1]
5.916	14	4.54[-1]	5.75[-1]	4.76[-1]	7.21[-1]	5.20[1]	8.77[1]
6.325	16	4.39[-1]	5.66[-1]	2.49[-1]	4.24[-1]	5.56[1]	9.73[1]
6.709	18	4.06[-1]	5.32[-1]	1.49[-1]	2.79[-1]	5.67[1]	1.03[2]
7.071	20	3.67[-1]	4.88[-1]	1.13[-1]	2.15[-1]	5.61[1]	1.05[2]
7.746	24	2.23[-1]	3.30[-1]	9.66[-2]	1.69[-1]	5.27[1]	1.05[2]

8.6 $2s2p\,^{3,1}P$ Auger normalized yields $\frac{dY}{d\Omega'}(0°)$

Experimental normalized $\theta = 0°$ Auger electron yields $dY^{exp}(0°)/d\Omega'$ for each of the ^3P and ^1P states, were obtained by integrating the fitted area under the Auger lines of interest. The experimental results here, contain information for the production of the ^3P and ^1P states with all the possible processes (see Eqs. 8.9 - 8.14) from each of the initial states $1s^2, 1s2s\,^{3,1}S$. Contrary to the $1s2p^2\,^2D$, which Auger transition

rules dictate to be predominantly produced from the $1s^2$ through the TE process, the $2s2p\,^3P$ and $2s2p\,^1P$ states can be produced through different processes, such as excitation (single or double) and transfer-loss, from all three $1s^2, 1s2s\,^{3,1}S$ ion beam components, with one-step processes seeming more probable, but still possible, two-step processes, especially in the case of ^1P.

For this reason, it appears to be more practical to transform the theoretical σ_i production cross sections provided, calculated for transitions from each of the initial $i = g,^3S,^1S$ components to the $2s2p\,^{3,1}P$ levels, to normalized $\theta = 0^\circ$ Auger electron yields and adding them to compare directly to the experimental normalized $\theta = 0^\circ$ Auger electron yields $dY^{exp}(0^\circ)/d\Omega'$.

8.6.1 The $2s2p\,^{3,1}P$ Auger SDCS and angular distributions

The Auger electron SDCSs for ^3P and ^1P states can be expressed as a sum over *even* (due to parity conservation) Legendre polynomials $P_k(\cos\theta'_e)$ given by [129] using the Eq. (6.10) as:

$$\frac{d\sigma^i_A}{d\Omega'}(\theta) = \bar{\xi}\frac{\sigma^{tot}_i}{4\pi}\left(1 + \sum_{k=2,4,\ldots}^{2L} a^i_k P_k(cos\theta)\right) \tag{8.15}$$

where as usual the index $i = g,^3S,^1S$, refers to the three different initial components of the ion beam and σ_i the production cross sections from each of these components to the $2s2p\,^{3,1}P$ levels. The coefficients a^i_k can be theoretically computed in various approximations, $\sigma^{\rm tot}_i$ is the total state production cross section, while $\overline{\xi}$ is the mean Auger yield given in Tables 8.6-8.9 for the two states.

For unresolved LSJ multiplets one has to sum over the various J states in various formulations depending on whether the fine structure is in principle resolvable or not. Furthermore, the Auger electron might have more than one allowed ℓ or j angular momenta, in which case, further complications arise since the different partial (l, j)-waves can interfere. Examples of calculations in the LSJ intermediate coupling approximation are given in Refs. [171, 172] and for LS coupling in Ref. [173].

In particular, for the P states of interest here, we have in Eq. (8.15) for $L = 1$ and $k = 2$ the coefficient a_2 given by:

$$a^i_2 = A^i_2 D_2, \tag{8.16}$$

with the anisotropy coefficient A^i_2 given by Table 6.3 [138]):

$$A^i_2 = 2\,\frac{\sigma_i[M=0] - \sigma_i[M=1]}{\sigma^{\rm tot}_i} \quad (i = g,^3S,^1S) \tag{8.17}$$

$$\sigma^{\rm tot}_i = \sigma_i[M=0] + 2\sigma_i[M=1], \tag{8.18}$$

and the dealignment factor D_2 (which accounts for the average loss of orbital align-

ment into spin alignment) is given by Eq. (6.14). The partial production cross sections $\sigma_i[M]$ depend on the magnetic quantum number M and are computed in the 3eAOCC approach for each of the three initial beam components. They are listed for the production of the $2s2p\,^3P$ and ^1P states in Tables 8.2 and 8.4 for collisions of carbon, and Tables 8.3 and 8.5 for oxygen ions with the modelled one-electron He($1s$) target as already discussed in section 6.1. The anisotropy parameter is seen to take values from $A_2 = 2$, when $\sigma[M = 1] = 0$ to $A_2 = -1$ when $\sigma[M = 0] = 0$ and thus is an indicator for alignment. And of course, when all partial cross sections are equal, then $A_2 = 0$ and we have isotropy.

Evaluating Eq. (8.15) at the laboratory observation angle $\theta = 0^\circ$ (for which $\theta'_e = 0^\circ$ or 180° - see Eq. (27) in Ref. [129]), we then obtain for the Auger SDCS:

$$\frac{d\sigma^i_A}{d\Omega'}(0^\circ) = \overline{\xi}\,\frac{\sigma_i[M=0](1+2D_2) + 2\sigma_i[M=1](1-D_2)}{4\,\pi}. \tag{8.19}$$

For the 2s2p $^3P_{2,1,0}$ Auger decay we obtain using published fine-structure results $\xi = 0.951$ and $D_2 = 0.321$ for carbon [174], while for oxygen [71], we have $\xi = 0.850$ and $D_2 = 0.283$. For no dealignment, i.e., $D_2 = 1$ [138], and we get the well-known LS-coupling result:

$$\frac{d\sigma^i_A}{d\Omega'}(0^\circ) = \overline{\xi}\,\frac{3\,\sigma_i[M=0]}{4\,\pi}, \qquad (D_2 = 1) \tag{8.20}$$

while if all partial cross sections are equal, i.e., $\sigma_i[M = 0] = \sigma_i[M = 1] = \sigma_i[M = -1] = \sigma_i$, then $\sigma_i^{\rm tot} = 3\sigma_i$ and we have the case of isotropy as expected (independent of dealignment):

$$\frac{d\sigma^i_A}{d\Omega'}(0^\circ) = \overline{\xi}\,\frac{\sigma_i^{\rm tot}}{4\,\pi}, \qquad \text{(isotropic)} \tag{8.21}$$

For the $2s2p\,^1P$ only $D_2 = 1$ is possible since there is not fine structure in this state.

8.6.2 $2s2p\,^{3,1}P$ theoretical normalized yields $\frac{dY}{d\Omega'}(0^\circ)$

Comparisons to the measured (normalized) $\theta = 0^\circ$ Auger yield, $dY^{exp}(0^\circ)/d\Omega'$ require the computation of the corresponding theoretical normalized yields. The theoretical Auger single differential cross sections $d\sigma^i_A(0^\circ)/d\Omega'$, is transformed to theoretical Auger ($\theta = 0^\circ$) normalized yield $dY^i(0^\circ)/d\Omega'$ as:

$$\frac{dY^i}{d\Omega'}(0^\circ) = f_i\frac{d\sigma^i_A}{d\Omega'}(0^\circ) \tag{8.22}$$

where f_i are the determined fractional components of the ion beam, i.e., f_g, $f_{^3S}$, $f_{^1S}$. The total theoretical Auger ($\theta = 0^\circ$) normalized yield will be:

$$\frac{dY^{sum}}{d\Omega'}(0^\circ) = \sum \frac{dY^i}{d\Omega'}(0^\circ) = f_g \frac{d\sigma_A^g}{d\Omega'}(0^\circ) + f_{^3S} \frac{d\sigma_A^{^3S}}{d\Omega'}(0^\circ) + f_{^1S} \frac{d\sigma_A^{^1S}}{d\Omega'}(0^\circ) \qquad (8.23)$$

which is directly comparable to the experiment.

8.6.3 $2s2p\,^3P$ experimental and theoretical $\frac{dY}{d\Omega'}(0^\circ)$

In Figs. 8.14 and 8.15 experimental C^{4+} and O^{6+} $2s2p\,^3P$ zero-degree Auger normalized yields $dY^{\exp}/d\Omega'$ are presented together with theoretical calculations $dY/d\Omega'$ from each of the initial three ion beam components, together with their sum, for dealignment factor $D_2 = 0.321$ for carbon and $D_2 = 0.283$ for oxygen, are presented. The theoretical results for each initial state have been multiplied with the corresponding ion beam component fractional amount.

In Tables 8.6 and 8.7 the theoretical and experimental results for the production of the $2s2p\,^3P$ in collisions of mixed-state $C^{4+}(1s^2,^{3,1}S)$ and $O^{6+}(1s^2,^{3,1}S)$ ion beams with He as a function of projectile energy E_p are presented together with the ion beam stripping combinations used in the measurements and the fractional composition of the three ion beam components $f_g, f_{^3S}, f_{^1S}$ determined according to the three-component formulation already presented in section 5.3.2.

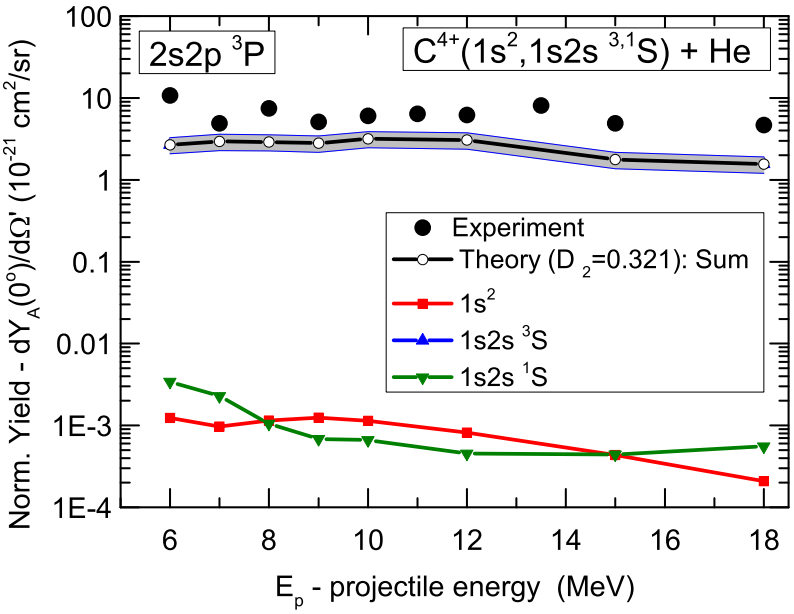

Figure 8.14: Zero-degree Auger normalized yields for the production of the $2s2p\,^3P$ from each of the three ion beam components for $D_2 = 0.321$. Contributions from the $1s2s\,^3S$ beam component (blue line with triangles) dominate as the sum of the three contributions (black line with circles) hides the contribution of the $1s2s\,^3S$ beam component. The shaded area corresponds to the uncertainty in the theoretical results and includes the uncertainties in the beam component fractions (∼15%) and the 3eAOCC cross sections (∼15%) added in quadrature. Error bars shown on the experimental values correspond to the statistical uncertainty.

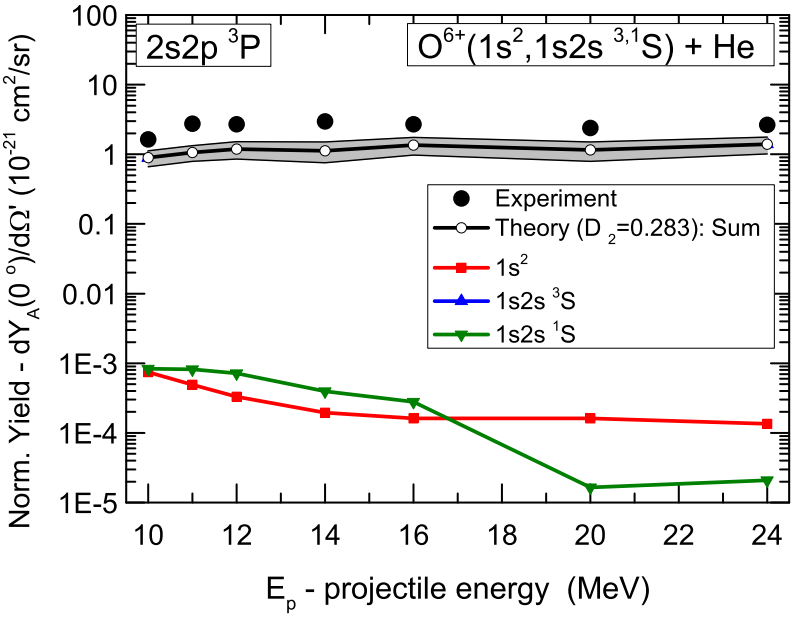

Figure 8.15: Same as Fig. 8.14, but for oxygen with $D_2 = 0.283$.

Table 8.6: Theoretical and experimental results for the production of the $2s2p\,^3P$ state in collisions of mixed-state $C^{4+}(1s^2,^{3,1}S)$ ion beams with He as a function of projectile energy E_p. Listed from left to right are the projectile energy E_p, the ion beam stripping combinations used in the measurements, the fractional composition of the three ion beam components $f_g, f_{^3S}, f_{^1S}$, the sum of the 0° normalized yields $\sum_i dY_i/d\Omega'$ contributions from each of component i ($i = g,^3S,^1S$) and the experimentally determined 0° normalized Auger electron yields, $dY^{\rm sum}/d\Omega'$ and $dY^{\rm exp}/d\Omega'$, respectively. Uncertainties in $dY^{\rm exp}/d\Omega'$ include just the statistical error, while uncertainties in the theoretical $dY^{\rm sum}/d\Omega'$ include both the computational uncertainty of 15% and the listed experimental uncertainties in the ion beam fractions added in quadrature. Entries indicated by – means no result was acquired, while an empty (blank) entry means this entry is the same as in the previous line and column.

$C^{4+}(1s^2, 1s2s\,^{3,1}S)$ + He → $C^{4+}(2s2p\,^3P)$ + He(All)		Ion beam fractions[1]			Theory[2]			Experiment
					$dY^{\rm sum}(0°)/d\Omega'$			$dY_A^{\rm exp}(0°)/d\Omega'$
E_p	Stripping[3]	f_g[4]	$f_{^3S}$[5]	$f_{^1S}$[6]	Isotropic	D_2=1	D_2=0.321	
(MeV)	Method	(%)			[$\times 10^{-21}$ cm^2/sr]			
					$2s2p\,^3P$ ($\bar{\xi} = 0.951$)[7]			
6	GTS-FPS	84±2	13±2	3.0±0.4	2.15±0.46	3.79±0.80	2.68±0.57	10.71±0.70
7	GTS-FPS	(83±2)	(14±2)	(3.3±0.5)	2.41±0.51	4.06±0.86	2.94±0.62	4.89±0.30
8	GTS-FPS	(83±2)	(14±2)	(3.3±0.5)	2.43±0.52	3.90±0.83	2.90±0.62	7.49±0.52
9	GTS-FPS	83±2	14±2	3.4±0.5	2.40±0.51	3.66±0.78	2.80±0.59	5.11±0.12
10	GTS-FPS	(79±3)	(17±2)	(4.0±0.6)	2.77±0.59	4.02±0.85	3.17±0.67	6.05±0.13
11	FTS	-	-	-	-	-	-	6.41±0.08
12	FTS	79±3	18±3	3.1±0.5	2.78±0.59	3.67±0.78	3.07±0.65	6.21±0.5
13.5	FTS	(79±3)	(17±3)	(3.0±0.5)	-	-	-	8.10±0.06
15	FTS	86±2	12±2	2.2±0.3	1.68±0.36	1.97±0.42	1.77±0.38	4.90±0.4
18	FTS	(86±2)	(11±2)	(2.3±0.3)	1.52±0.32	1.62±0.34	1.55±0.33	4.65±0.3

[1] Both $2s2p\,^3P$ and $2s2p\,^1P$ Auger lines were measured in the same spectrum so ion beam conditions were the same for both.
[2] Normalized yields, $\frac{dY}{d\Omega'}^{\rm sum}$, given by Eq. (8.23) for each of the three conditions expressed by Eqs. 8.21 (isotropic), 8.20 ($D_2 = 1$) and 8.19 ($D_2 = 0.321$).
[3] GTS: gas terminal stripper, GPS: gas post-stripper, FTS: foil terminal stripper, FPS: Foil post-stripper. Parentheses [e.g. (FTS)] indicate that the ion beam fractions for this E_p energy were interpolated from the measured values (no parentheses) which were experimentally determined using the "two-spectra measurement" technique [94, 112].
[4] Ground state fraction $f_g = 1 - f_{^3S} - f_{^1S}$ with uncertainty $\Delta f_g = \sqrt{(\Delta f_{^3S})^2 + (\Delta f_{^1S})^2}$.
[5] Experimentally determined metastable fraction $f_{^3S}$ was assigned a mean overall uncertainty of 15%, i.e., $\Delta f_{^3S}/f_{^3S} = 0.15$ (see text).
[6] Metastable fraction $f_{^1S}$ determined from $f_{^3S}$ according to Eq.(5.26) with an uncertainty $\Delta f_{^1S}/f_{^1S} = \Delta f_{^3S}/f_{^3S} = 0.15$.
[7] Mean Auger yield $\bar{\xi}$ computed from values given in Müller et al [174].
[8] Auger yield $\xi = 1 - K$ computed from values of $K = 0.00524$, the radiative branching ratio given in Goryaev et al. [71]. A similar value of $K = 0.0052$ is also given by van der Hart and Hansen [175].

Table 8.7: Same as Table 8.6, but for O^{6+}. Footnotes same as in Table 8.6, except where noted.

$O^{6+}(1s^2, 1s2s\,^{3,1}S) + He \rightarrow O^{6+}(2s2p\,^3P)$ +He(All)					Theory[1]			Experiment
		Ion beam fractions			$dY^{\rm sum}(0°)/d\Omega'$			$dY_A^{\rm exp}(0°)/d\Omega'$
E_p	Stripping	f_g	$f_{^3S}$	$f_{^1S}$	Isotropic	D_2=1	D_2=0.283	
(MeV)	Method		(%)			$[\times 10^{-21}$ cm^2/sr]		
					$2s2p\,^3P$ ($\overline{\xi} = 0.850$)[2]			
10	FTS-FPS	80±4	20±4	0.51±0.10	0.71±0.17	1.35±0.33	0.89±0.22	1.64±0.16
11	GTS-FPS	(79±4)	(20±4)	(0.60±0.12)	0.86±0.21	1.59±0.39	1.06±0.26	2.76±0.26
12	GTS-FPS	79±4	20±5	0.65±0.15	0.96±0.26	1.75±0.47	1.19±0.32	2.70±0.16
14	FTS-FPS	83±5	16±5	0.62±0.17	0.93±0.30	1.63±0.52	1.13±0.36	2.97±0.12
16	GTS-FPS	82±4	18±4	0.79±0.18	1.14±0.31	1.92±0.52	1.36±0.37	2.70±0.19
20	FTS	85±4	14±4	0.10±0.03	0.99±0.30	1.56±0.47	1.15±0.35	2.40±0.07
24	FTS	82±4	17±4	0.16±0.03	1.19±0.31	1.81±0.47	1.39±0.36	2.65±0.05

[1]Normalized yields, $\frac{dY}{d\Omega'}^{\rm sum}$, given by Eq. (8.23) for each of the three conditions expressed by Eqs. 8.21 (isotropic), 8.20 ($D_2 = 1$) and 8.19 ($D_2 = 0.283$).
[2]Mean Auger yield $\overline{\xi}$ computed from values given in Goryaev et al. [71].
[3]Auger yield $\xi = 1 - K$ computed from values of $K = 0.0152$, the radiative branching ratio given in Goryaev et al. [71].

8.6.4 $2s2p\,^1P$ experimental and theoretical $\frac{dY}{d\Omega'}(0^\circ)$

In Figs. 8.16 and 8.17 experimental C^{4+} and O^{6+} $2s2p\,^1P$ zero-degree Auger normalized yields are presented together with theoretical Auger normalized yields for the production of the $2s2p\,^1P$ from each of the three ion beam components are presented. For the $2s2p\,^1P$ only $D_2 = 1$ is possible since there is no fine structure in this state. Again here, the theoretical results for each initial state have been multiplied with the corresponding ion beam component fractional amount.

In Tables 8.8 and 8.9 the theoretical and experimental results for the production of the $2s2p\,^3P$ in collisions of mixed-state $C^{4+}(1s^2, 1s2s\,^{3,1}S)$ and $O^{6+}(1s^2, 1s2s\,^{3,1}S)$ ion beams with He as a function of projectile energy E_p are presented together with the ion beam stripping combinations used in the measurements and the fractional composition of the three ion beam components $f_g, f_{^3S}, f_{^1S}$ determined according to the three-component formulation already presented in section 5.3.2.

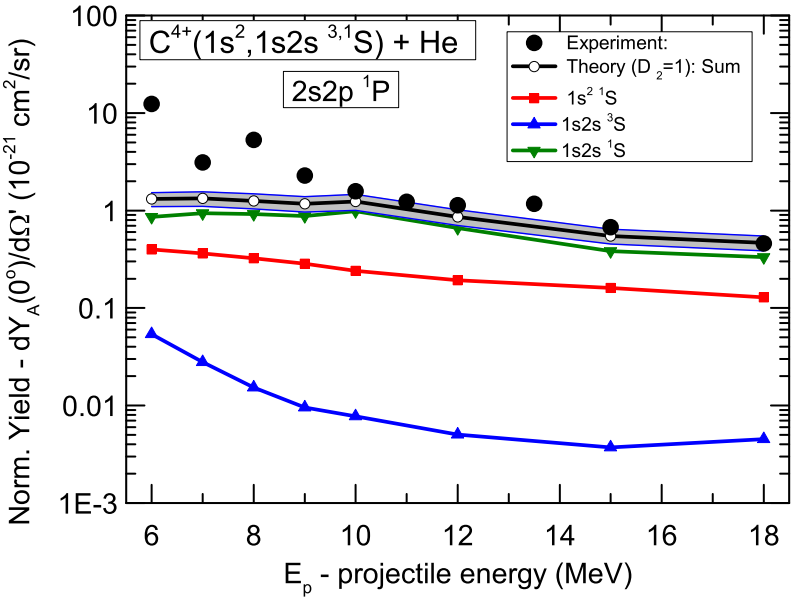

Figure 8.16: Same as Fig. 8.14, but for the carbon $2s2p\,^1P$ and $D_2 = 1$. In this case contributions from the $1s2s\,^1S$ are seen to be the most important, but the ground state contributions cannot be neglected as they are seen to be only about a factor 3-5 smaller.

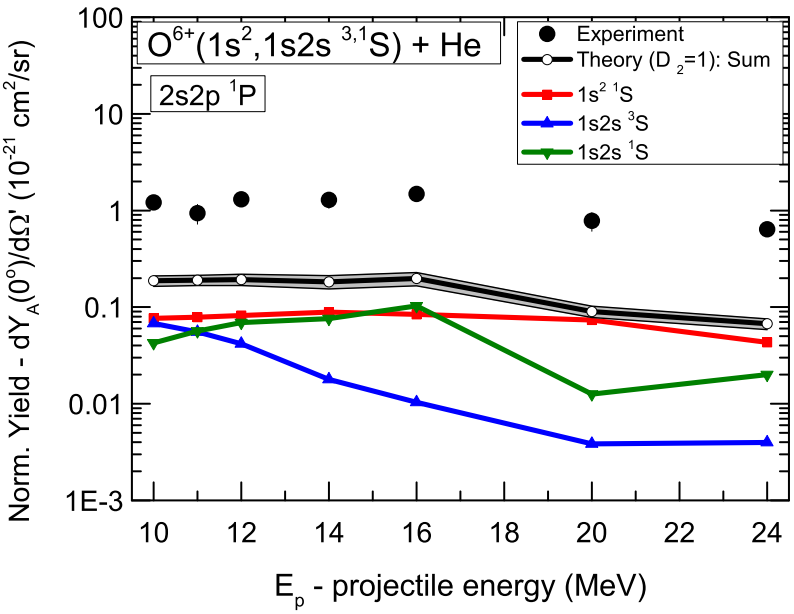

Figure 8.17: Same as Fig. 8.16, but for oxygen. Here it is seen that the contributions from the $1s^2$ are actually the strongest, primarily due to the much smaller $1s2s\,^1S$ component reaching the target, due to its much shorter lifetime.

Table 8.8: Theoretical and experimental results for the production of the $2s2p\,^1P$ state in collisions of mixed-state $C^{4+}(1s^2,^{3,1}S)$ ion beams with He as a function of projectile energy E_p. Listed from left to right are the projectile energy E_p, the ion beam stripping combinations used in the measurements, the fractional composition of the three ion beam components $f_g, f_{^3S}, f_{^1S}$, the sum of the 0° normalized yields $\sum_i dY_i(0°)/d\Omega'$ contributions from each of component i ($i = g,^3S,^1S$) and the experimentally determined 0° normalized Auger electron yields, $dY^{\rm sum}(0°)/d\Omega'$ and $dY_A^{\rm exp}(0°)/d\Omega'$, respectively. Uncertainties in $dY_A^{\rm exp}(0°)/d\Omega'$ include just the statistical error, while uncertainties in the theoretical $dY^{\rm sum}(0°)/d\Omega'$ include both the computational uncertainty of 15% and the listed experimental uncertainties in the ion beam fractions added in quadrature. Entries indicated by − means no result was acquired, while an empty (blank) entry means this entry is the same as in the previous line and column.

$C^{4+}(1s^2, 1s2s\,^{3,1}S) + He \rightarrow C^{4+}(2s2p\,^1P)$+ He(All)		Ion beam fractions[1]			Theory[2]		Experiment
					$dY^{\rm sum}(0°)/d\Omega'$		$dY_A^{\rm exp}(0°)/d\Omega'$
E_p	Stripping[3]	f_g[4]	$f_{^3S}$[5]	$f_{^1S}$[6]	Isotropic	D_2=1	
(MeV)	Method	(%)			[$\times 10^{-21}$ cm^2/sr]		
					$2s2p\,^1P$ ($\xi = 0.9948$)[8]		
6	GTS-FPS	84±2	13±2	3.0±0.4	0.68±0.11	1.31±0.19	12.35±0.72
7	GTS-FPS	(83±2)	(14±2)	(3.3±0.5)	0.73±0.12	1.33±0.21	3.12±0.27
8	GTS-FPS	(83±2	(14±2)	(3.3±0.5)	0.72±0.12	1.26±0.20	5.32±0.51
9	GTS-FPS	83±2	14±2	3.4±0.5	0.71±0.12	1.17±0.19	2.29±0.12
10	GTS-FPS	(79±3)	(17±2)	(4.0±0.6)	0.80±0.14	1.24±0.21	1.57±0.11
11	FTS	-	-	-	-	-	1.23±0.06
12	FTS	79±3	18±3	3.1±0.5	0.60±0.11	0.86±0.14	1.13±0.04
13.5	FTS	(79±3)	(17±3)	(3.0±0.5)	-	-	1.18±0.04
15	FTS	86±2	12±2	2.2±0.3	0.42±0.07	0.55±0.08	0.68±0.03
18	FTS	(86±2)	(11±2)	(2.3±0.3)	0.39±0.07	0.47±0.07	0.46±0.02

[1] Both $2s2p\,^3P$ and $2s2p\,^1P$ Auger lines were measured in the same spectrum so ion beam conditions were the same for both.
[2] Normalized yields, $\frac{dY}{d\Omega'}^{\rm sum}$, given by Eq. (8.23) for each of the conditions expressed by Eqs. 8.21 (isotropic) and 8.20 ($D_2 = 1$). For the $2s2p\,^1P$ only $D_2 = 1$ is possible since there is not fine structure in this state.
[3] GTS: gas terminal stripper, GPS: gas post-stripper, FTS: foil terminal stripper, FPS: Foil post-stripper. Parentheses [e.g. (FTS)] indicate that the ion beam fractions for this E_p energy were interpolated from the measured values (no parentheses) which were experimentally determined using the "two-spectra measurement" technique [94, 112].
[4] Ground state fraction $f_g = 1 - f_{^3S} - f_{^1S}$ with uncertainty $\Delta f_g = \sqrt{(\Delta f_{^3S})^2 + (\Delta f_{^1S})^2}$.
[5] Experimentally determined metastable fraction $f_{^3S}$ was assigned a mean overall uncertainty of 15%, i.e., $\Delta f_{^3S}/f_{^3S} = 0.15$ (see text).
[6] Metastable fraction $f_{^1S}$ determined from $f_{^3S}$ according to Eq.(5.26) with an uncertainty $\Delta f_{^1S}/f_{^1S} = \Delta f_{^3S}/f_{^3S} = 0.15$.
[7] Mean Auger yield $\bar{\xi}$ computed from values given in Müller et al [174].
[8] Auger yield $\xi = 1 - K$ computed from values of $K = 0.00524$, the radiative branching ratio given in Goryaev et al. [71]. A similar value of $K = 0.0052$ is also given by van der Hart and Hansen [175].

Table 8.9: Same as Table 8.8, but for O^{6+}. Footnotes same as in Table 8.8, except where noted.

$O^{6+}(1s^2, 1s2s\,^{3,1}S) + He \rightarrow O^{6+}(2s2p\,^1P) +$ He(All)		Ion beam fractions			Theory[1]		Experiment
					$dY^{sum}(0°)/d\Omega'$		$dY_A^{exp}(0°)/d\Omega'$
E_p	Stripping	f_g	$f_{^3S}$	$f_{^1S}$	Isotropic	D_2=1	
(MeV)	Method	(%)			[$\times 10^{-21}$ cm^2/sr]		
					$2s2p\,^1P$ ($\xi = 0.9848$)[3]		
10	FTS-FPS	80±4	20±4	0.51±0.10	0.08±0.01	0.19±0.02	1.21±0.17
11	GTS-FPS	(79±4)	(20±4)	(0.60±0.12)	0.09±0.01	0.19±0.02	0.94±0.22
12	GTS-FPS	79±4	20±5	0.65±0.15	0.09±0.01	0.19±0.03)	1.31±0.20
14	FTS-FPS	83±5	16±5	0.62±0.17	0.09±0.02	0.18±0.03	1.29±0.24
16	GTS-FPS	82±4	18±4	0.79±0.18	0.10±0.02	0.20±0.03	1.49±0.18
20	FTS	85±4	14±4	0.10±0.03	0.04±0.01	0.09±0.01	0.69±0.7
24	FTS	82±4	17±4	0.16±0.03	0.04±0.01	0.07±0.01	0.64±0.5

[1] Normalized yields, $\frac{dY^{sum}}{d\Omega'}$, given by Eq. (8.23) for each of the conditions expressed by Eqs. 8.21 (isotropic) and 8.20 ($D_2 = 1$). For the $2s2p\,^1P$ only $D_2 = 1$ is possible since there is not fine structure in this state.
[2] Mean Auger yield $\bar{\xi}$ computed from values given in Goryaev et al. [71].
[3] Auger yield $\xi = 1 - K$ computed from values of $K = 0.0152$, the radiative branching ratio given in Goryaev et al. [71].

8.7 Concluding remarks

In Figs. 8.10 and 8.11, the theoretical production cross sections for the carbon and oxygen $2s2p\,^3P$ are shown as a function of projectile energy E_p. Single (direct) 1s→2p excitation from $1s2s\,^3S$ is by almost two-orders of magnitude the dominant production mechanism exhibiting the well-known excitation E_p dependence: a low energy threshold followed by an increasing cross section eventually dropping off slowly with increasing energy E_p. Similar features are also seen for oxygen in Fig. 8.11, even though the low E_p energy region close to threshold is not covered. This characteristic E_p dependence is also seen to be followed by single 1s→2p excitation with spin exchange from $1s2s\,^1S$ (green triangles), albeit about two orders of magnitude smaller. However, excitation with spin exchange, while having a similar low E_p behavior, falls off much more rapidly than direct excitation at high E_p energies. Double-excitation with spin exchange (red squares) from the ground $1s^2\,^1S$ is the process with the lowest contribution, almost four orders of magnitude lower than direct excitation. Overall, the double-excitation process is by far the weakest, followed by excitation with exchange, while the largest cross sections are seen to be due to direct excitation.

In Figs. 8.14 and 8.15 the experimental and theoretical zero-degree Auger normalized yields are shown as a function of projectile energy E_p. Here, the He-like fractional ion beam component amount surviving to the target affects directly the produced normalized yields. In the case of $2s2p\,^3P$ production the $1s2s\,^3S$ is seen to predominantly contribute to its formation, while the contribution from $1s2s\,^1S$ and $1s^2\,^1S$ remain three orders of magnitude smaller. The experimental results for both

carbon and oxygen are seen to lie 2-3 times higher than theory.

In analogy to the $2s2p\,^3P$ results, in Figs. 8.12 and 8.13, the theoretical production cross sections for the carbon and oxygen $2s2p\,^1P$ are shown as a function of projectile energy E_p. Here, direct single 1s→2p excitation from $1s2s\,^1S$ (green triangles) appears to be the dominant process, with the single 1s→2p excitation from $1s2s\,^3S$ with spin flip and double-excitation (red squares) from the ground $1s^2\,^1S$ being again the process with the lowest contribution.

Interestingly though, for the ^1P and E_p energies larger than about 6 MeV (0.5 MeV/u) for carbon, double-excitation without spin exchange becomes more efficient than single-excitation with exchange. Similar behavior is also seen for oxygen in Fig. 8.13, but with the crossing point now occurring around 16 MeV (1 MeV/u). TL can also be expected to contribute to the observed maximum of the cross sections for spin-exchange processes since transfer can be expected to be large at the lowest E_p.

However, when it comes to comparing normalized yields shown in Figs. 8.16 and 8.17, the contributions to the production of the $2s2p\,^1P$ from the $1s2s\,^1S$ and $1s^2\,^1S$ appear to be of equal importance due to their large difference between the amount of each of these two components surviving to the target, with more than 80% of the ion beam being in the $1s^2\,^1S$. Now, comparing theory with experiment, in the case of carbon theory manages to reproduce the experiment quite satisfactory, especially in the 10-18 MeV region, while for lower energies, the experiment stands significantly higher. This can be explained both by the presence of TL in this energy region, not fully taken into account in theory, and by the fact that at lower energies, the $2s2p\,^1P$ gets mixed with the emerging close lying $(1s2s\,^3S)3d\,^2D$, $(1s2s\,^3S)3s\,^2S$ and $(1s2s\,^3S)3p\,^2P$ lines, making it impossible to cleanly resolve the $2s2p\,^1P$ area alone. In the case of oxygen a slight drop of the experimental normalized yields is observed with increasing collision energy, with the experimental data appearing 6-9 times higher than theory over the entire energy region.

It is interesting to note that in the above three-component model, the contribution from $1s2s\,^1S$ for oxygen is very small, due to the very low $f[^1S]$ value. However, an increase of this fraction by about a factor of 10, would decrease the gap between theory and experiment greatly, without affecting much the other results which depend on the other two fractional components. Thus, for example, at 1 MeV/u (16 MeV) for the case of $D_2 = 1$ (see Table 8.9, a value of about $f[^1S] = 10.7\%$ (rather than just 0.79%, i.e., an increase by a factor of 13.5) would give a $2s2p\,^1P$ theoretical normalized yield equal to the experimental, i.e., 1.49×10^{-21} cm^2/sr, while the corresponding changes to the other two fractions would give $f[1s^2] = 73.4\%$ and $f[^3S] = 15.9\%$, a small change from their original values of $f[1s^2] = 82\%$ and $f[^3S] = 18\%$ having only a minimal effect on the corresponding theoretical normalized yields for $2s2p\,^3P$ and $1s2p^2\,^2D$ [11]. This example clearly demonstrates the sensitivity of the $2s2p\,^1P$ results to $f[^1S]$, while only minimally affecting the other fractions. In the three-component model presented in this thesis it is assumed

that the production of the ^1S is tied to the production of ^3S in a ratio of 1 to 3 (see Eq. (5.21)) dictated by spin statistics. However, this assumption could well be incorrect since our actual experimental knowledge on this fraction is totally lacking.

In conclusion, in all cases the measured yields were found to be larger than theory. In the case of carbon by factors ranging from 2 to 4 for the $2s2p\,^3P$ state and from 1.3 to 9 for the $2s2p\,^1P$ state. In the case of oxygen these factors ranged from 1.8 to 2.6 for the $2s2p\,^3P$ and from 4.9 to 9 for the $2s2p\,^1P$ states. The large disagreements for the $2s2p\,^1P$ states could be the result of an underestimation of the $f[^1S]$ fraction. In addition, another uncertainty might arise due to the fact that only one active electron was used on the target in the calculations. Thus, an additional overall factor of 2 could be justifiable in the context of the three-active electron approach. As a result, further investigation is clearly needed.

Chapter 9

Summary and conclusions

In this thesis, the unique infrastructure of the 5.5 MV tandem Van de Graaff accelerator of N.C.S.R. "Demokritos" was utilized to deliver highly charged ions for energetic, state selective ion-atom collision experiments, using the state-of-the-art zero-degree Auger spectrometer of the APAPES setup. More specifically, the atomic processes of transfer-excitation (TE) and single as well as double excitation processes were studied in a wide energy range from 0.5 to 1.5 MeV/u, through collisions between He-like C^{4+} and O^{6+} projectile ions and He targets. The experimental results are accompanied by state-of-the art 3eAOCC calculations, performed by the collaborating group of Prof. Alain Dubois in Paris. He-like ion beams were specifically selected, as the collision systems become amenable to this new three active electron theoretical treatment.

The TE processes were initially studied experimentally through the production of the $C^{3+}(1s2p^2\,{}^2D)$ state in collisions of $C^{4+}(1s^2)$ with helium, obtaining $C^{3+}(1s2p^2\,{}^2D)$ single differential cross sections, based on high resolution Auger electron measurements. In parallel, theoretical single differential cross sections provided by the 3eAOCC approach, showed a distinctive two-peak structure as a function of the collision energy. For the high-energy peak, there is excellent agreement between experiment and theory in their overlapping energy range, i.e., at resonance (6 MeV) and above. Using simplifying two-level models, the underlying mechanisms essentially responsible for these two peaks were exposed. The high-energy peak is considered to arise predominantly from the two-center electron-electron interaction in soft collisions, i.e., at large impact parameters, validating therefore the present understanding. However, the low-energy peak is found to arise mainly from a one-step mechanism. This mechanism is mediated by a single electron-nucleus interaction responsible for excitation correlated to an electron transfer in head-on collisions, i.e., at small impact parameters, where the target and projectile electronic clouds largely overlap.

In addition, towards an isoelectronic study of the TE process, single differential cross sections for $O^{5+}(1s2p^2\,{}^2D)$ were also obtained through collisions of $O^{6+}(1s^2)$ with helium in the same energy range as carbon. Theoretical single differential cross

sections were once again provided by the 3eAOCC for the same energy range. In the case of oxygen, the theoretical results for $O^{5+}(1s2p^2\,{}^2D)$ are fairly close to the experimental results, although they appear slightly shifted in energy.

Overall, through this work, the presence of an additional one-step mechanism to explain TE apart from of the RTE and NTE was revealed by a full quantum mechanical treatment providing further insights into bielectronic processes in many-body quantum systems. Towards a deeper understanding of transfer excitation in the future, two directions of interest exist. The study of other He-like ions, particularly in the low collision energy range, and investigations of differential cross sections as a function of scattering angle, e.g., possibly using recoil ion momentum spectroscopy [176].

Next, the electron excitation process was studied through the production of $2s2p\,{}^3P$ and $2s2p\,{}^1P$ states in 0.5-1.5 MeV/u collisions of He-like mixed-state ($1s^2$, $1s2s\,{}^3S$ and $1s2s\,{}^1S$) carbon and oxygen ion beams with He targets. In parallel, the 3eAOCC treatment was used to calculate the cross sections for the production of these doubly excited states from each of the three possible initial ionic states with the helium target modelled by a single electron and all coupling schemes included in one uniform and coherent treatment. The $1s2s\,{}^3S$ metastable component was also determined experimentally, while the $1s2s\,{}^1S$ component was assumed to be statistically populated in the ratio of 3:1 according to the $1s2s\ {}^3S$ to ${}^1S$ spin degeneracies and was included in a more complete three-component analysis. The effects of dealignment due to fine structure splitting were also included in the Auger angular distributions at the observation angle of $\theta = 0°$. Thus, using this three-component fractional composition the $\theta = 0°$ theoretical normalized yields were determined and compared to the directly measured mixed-stated normalized yields.

In all cases the measured yields were found to be larger than theory. For carbon by factors ranging from 2 to 4 for the $2s2p\,{}^3P$ state and from 1.3 to 9 for the $2s2p\,{}^1P$ state. For oxygen these factors ranged from 1.8 to 2.6 for the $2s2p\,{}^3P$ and from 4.9 to 9 for the $2s2p\,{}^1P$ states with the disagreement for the $2s2p\,{}^1P$ production clearly larger than that for the $2s2p\,{}^3P$. The larger disagreement for the $2s2p\,{}^1P$ states could be the result of too small a $f[{}^1S]$ fraction introduced in the current three-component model. In addition, a more fundamental uncertainty might arise due to the fact that only one active electron was used on the target. However, such an additional overall factor of 2 is not so clearly justifiable in the context of the three-active electron approach.

Overall, the 3eAOCC calculations are the most advanced of their kind to date and applied for the first time to also describe excitation. However, they seem to be not as successful as when applied to transfer [129, 152] or transfer-excitation [11]. Clearly, more systematic isoelectronic investigations are needed to shed further light on these new results and the observed disagreement with experiment. In addition, more work on better defining the amount of the $f[{}^1S]$ fraction in He-like ion beams either theoretically or experimentally would clearly also be very helpful.

Abbreviations and Acronyms

ADC	Analogue - to - Digital Converter
APAPES	Atomic Physics with Accelerators: Projectile Electron Spectroscopy
BEe	Binary Encounter electrons
BCI	Beam Current Integrator
BPM	Beam Profile Monitor
CALIBRA	Cluster of Accelerator Laboratories for Ion-Beam Research and Applications
DAQ	Data Acquisition
DE	Double Excitation
DSP	Digital Signal Processor
eeE	electron-electron Excitation
enE	electron-nucleus Excitation
FC	Faraday Cup
FTS	Foil Terminal Stripper
FPS	Foil Post-Stripper

FWHM	Full Width at Half Maximum
GPS	Gas Post-Stripper
GTOs	Gaussian type orbitals
GTS	Gas Terminal Stripper
HDA	Hemispherical Deflector Analyzer
IA	Impulse Approximation
INPP	Institute of Nuclear and Particle Physics
MCP	Microchannel Plate
NCTE	Non-Resonant Coherent Transfer Excitation
NCSRD	National Centre for Scientific Research "Demokritos"
NEC	National Electrostatics Corporation
NTE	Non-Resonant Transfer Excitation
PSD	Position Sensitive Detector
PWBA	Plane-Wave Born Approximation
RAE	Resistive Anode Encoder
RC	Radiationless Capture
RTE	Resonant Transfer Excitation
SCC	Single-Collision Conditions
SDCS	Single Differential cross section
SNICS	Source of Negative Ions by Cesium Sputtering

tandem-PPA	tandem - Parallel Plate Analyzers
TE	Transfer Excitation
TL	Transfer-Loss
TORVIS	Toroidal Volume Ion Source
3eAOCC	Three Electron Atomic Orbital Close-Coupling
ZAPS	Zero-degree Auger Projectile Spectroscopy

Appendix A

Auger line identification

In this section the calculated electron energies of $1s2lnl' \rightarrow 1s^2$ and $2l2l' \rightarrow 1s$ Auger transitions are presented for the identification of the carbon and oxygen K-Auger lines. Some of them have already been used for energy calibration as seen in section 4.1. In Figs. A.1 and A.2 the carbon and oxygen levels according to their absolute binding energy are shown, together with some of the Auger transitions with their energies in eV. In Tables A.1 and A.2 lists of carbon and oxygen K-Auger energies are shorted in increasing energy (eV) resulting from $1s2lnl' \rightarrow 1s^2$ and $2l2l' \rightarrow 1s$ Auger transitions used for the line identification of in the recorded Auger spectra.

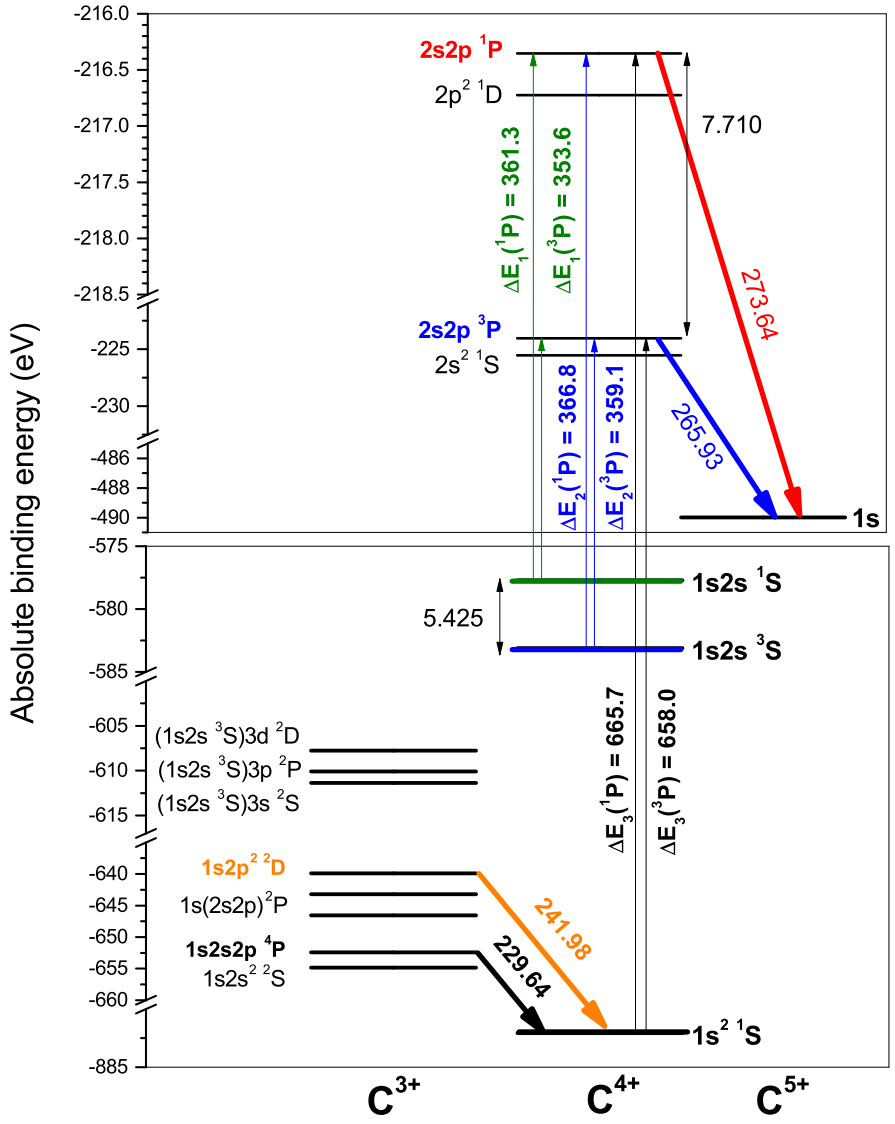

Figure A.1: Absolute binding energies of relevant carbon levels. Auger transitions and their energies in eV (downward arrows slanted to the right). Bottom panel: Black $C^{3+}(1s2s2p\,^4P)$ calibration line [177], orange $C^{3+}(1s2p^2\,^2D)$. Top panel: Blue $C^{4+}(2s2p\,^3P)$ and red $C^{4+}(2s2p\,^1P)$. The six excitation energies from each of the three initial ion beam components $1s^2$, $1s2s\,^3S$ and $1s2s\,^3S$ to the two final states $2s2p^1P$ and $2s2p^3P$ are also shown (thin upward pointing arrows).

Table A.1: Carbon K-Auger energies ε_A listed in increasing energy (eV) resulting from $1s2lnl' \rightarrow 1s^2$ and $2l2l' \rightarrow 1s$ Auger transitions used in the identification of the observed Auger lines in this thesis. The former are used also for energy calibration, while the latter are in the vicinity of the $2s2p\,^{3,1}P$ lines. There are no NIST [178] recommended values for the energy levels of these doubly excited states. Entries indicated by $-$ means no result was acquired. The footnote in the header of each column gives the reference from which the values shown in the column were obtained, unless otherwise indicated. Experimental uncertainties as reported in the corresponding reference. For conversions to eV, we have used the NIST equivalents, 1 a.u. $= 27.211386245988(53)$ eV and $1\,cm^{-1} = 1.239842\times10^{-4}$ eV, unless otherwise indicated.

	Experiment						Theory					
State	This work[1]	Rod79[2]	Mac87[3]	Mann87[4]	Kil93[5]	Calibration Values	Aln02[7]	Kar09[8]	Gor17[9]	Yer17[10]	Man22[11]	Man22[12]
$1s2s^2\,^2S$	227.2(6)	227.6(5)	227.06(9)	227.1(2)	-	227.23(30)[6]	227.1	-	227.00	227.208	-	-
$1s2s2p\,^4P$	229.6(5)	229.7(5)	229.639[16]	229.6(2)	-	229.64[6]	229.5	-	229.80	229.695	-	-
$1s2s2p\,^2P_-$	235.5(6)	235.5(5)	235.40(4)	235.5(2)	234.3(1)	235.44(20)[6]	235.3	-	235.41	235.572	-	-
$1s2s2p\,^2P_+$	238.8(6)	238.9(5)	238.92(4)	238.8(2)	237.8(3)	238.86(20)[6]	239.0	-	238.97	239.024	-	-
$1s2p^2\,^2D$	242.2(6)	242.2(6)	241.98(4)	242.1(2)	241.4(1)	242.15(20)[6]	242.0	-	242.18	242.099	-	-
$2s^2\,^1S$	264.4(6)	-	-	-	-	-	264.2	264.457	264.30	264.45[13]	263.936	264.417
$2s2p\,^3P$	265.9(6)	-	-	-	-	265.954(1)[14]	265.7	-	265.94	266.02[13]	265.837	265.962
$(1s2s\,^3S)3s\,^2S$	270.6(6)	-	270.70(15)	270.7(2)	-	-	271.5	-	270.57	-	-	-
$(1s2s\,^3S)3p\,^2P$	271.9(6)	-	271.98(10)	271.8(2)	-	272.1[6]	272.4	-	271.50	-	-	-
$2p^2\,^1D$	273.1(6)	-	-	-	-	-	272.4	273.157	272.99	273.27[15]	273.81	273.141
$2s2p\,^1P$	273.8(7)	-	-	-	-	-	273.5	273.927	273.64	273.92[13]	274.289	273.741
$(1s2s\,^3S)3d\,^2D$	274.2(6)	-	274.29(10)	274.2(2)	-	274.1[6]	-	-	274.02	-	-	-
$2p^2\,^1S$	-	-	-	-	-	-	-	-	283.029	281.810		
$(1s2s\,^1S)3s\,^2S$	274.8(6)	-	-	-	-	-	-	-	274.59	-	-	-
$(1s2s\,^1S)3p\,^2P$	276.9(6)	-	-	-	-	-	-	-	276.52	-	-	-
$(1s2s\,^1S)3d\,^2D$	278.5(6)	-	-	278.9(2)	-	278.7[6]	-	-	278.43	-	-	-

[1]Fitted Auger line peak energies after energy calibration of PSD channels according to the $1s2l2l'$ calibration values proposed by Bruch et al. [177] and listed in column seven.
[2]Rodbro et al. 1979 [75] in 300 keV $C^+ + CH_4$.
[3]Mack 1987 [179] weighted averages (Table 3) calibrated to the $1s2s2p\,^4P$ calculation of K.T. Chung [180].
[4]Mann 1987 [181].
[5]Kilgus etl 1993 [182] - Dielectronic Recombination (DR) measurements at the Heidelberg Test Storage Ring (TSR).
[6]Bruch et al. 1985 [177] - Proposed calibration of carbon K-Auger energies based on the measurements by Rodbro et al. [75] and theory.
[7]Alnaser 2002 [183] (from Tables 1 and 6) using $\varepsilon_A = Z_p^2 E_0 + Z_p E_1 + E_2$ with coefficients for each state E_0, E_1, E_2 from Rodbro et al [75].
[8]Kar and Ho 2009 [184] - Stabilization method: $2l2l'\,^1L$ levels in a.u.
[9]Goryaev et al. 2017 [71] - MZ code with relativistic corrections: $1s2l2l'$ and $2l2l'$ levels in keV.
$\varepsilon_A(1s2snl) = \Delta E_x(1s2snl \rightarrow 1s^2 2p) + E(1s^2 2p) - E(1s^2)$,
$\varepsilon_A(2s2p) = \Delta E_x(2s2p\,^{3,1}P_J \rightarrow 1s2s\,^{3,1}S) + E(1s2s\,^{3,1}S) - E(1s)$, where ΔE_x is the value of the x-ray transition energy given in Ref. [71] and $E(1s^2), E(1s), E(1s2s\,^{3,1}S)$ and $E(1s^2 2p)$ the energy levels with respect to the $1s^2$ and $1s^2 2s$ level .
[10]Yerokhin et al 2017 [185, 186] - Relativistic configuration-interaction calculation of transition wavelengths. Used $hc = 1.23984198\times10^{-4}$ eV-cm to convert wavelength (cm) to energy (eV). See also similar but older MCDF results by Safronova and Bruch 1994 [70].
[11]Manai et al 2022 [73] $E_{\rm FAC}$ energy levels computed with respect to the $1s^2$ ground state using the Flexible Atomic code (FAC) [187]. $\varepsilon_A(2l2l'\,^{3,1}L_J) = E_{\rm FAC}(2l2l'\,^{3,1}L_J) + E(1s^2) - E(1s)$.
[12]Manai et al 2022 [73] $E_{\rm AMBiT}$ energy levels computed with respect to the $1s^2$ ground state using the AMBiT code [188] (Particle–hole configuration interaction with many-body perturbation theory (CI+MBPT) for fully relativistic calculations of atomic energy levels). $\varepsilon_A(2l2l'\,^{3,1}L_J) = E_{\rm AMBiT}(2l2l'\,^{3,1}L_J) + E(1s^2) - E(1s)$.
[13]Ho 1981 [189] - complex rotation calculations as quoted in Table 4.5 of Mack 1987 [190].
[14]Müller et al 2018 [174] - The $2s2p\,^3P_J$ resonance energies were obtained in photo-ionization measurements of $C^{4+}(1s2s\,^3S)$ ions after fitting to theory. This is probably the most accurate determination to date and should be used for calibration.
[15]Peacock et al 1973 [191] - Hartree-Fock type calculations as quoted in Table 4.5 of Mack 1987 [190].
[16]K.T. Chung [180].

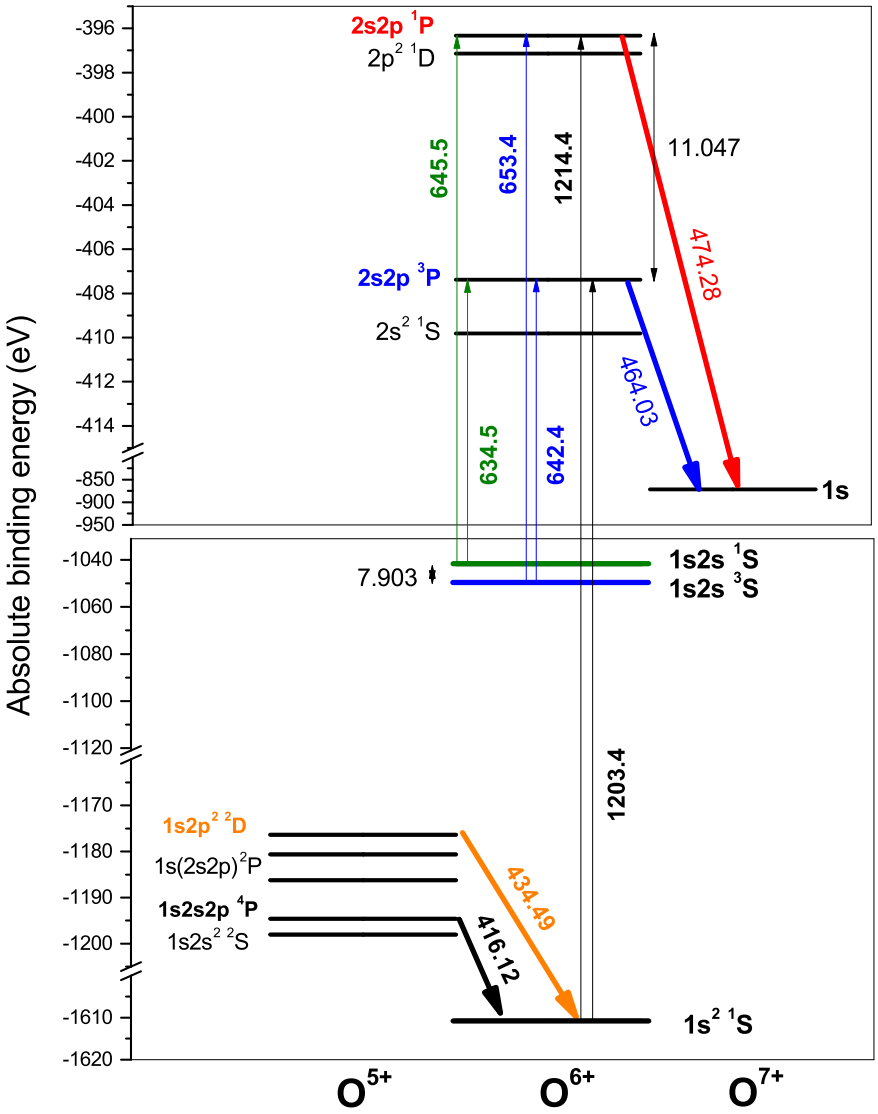

Figure A.2: Same as Fig. A.1, but for oxygen. The levels $1s2s3l$ are not indicated as in carbon because as shown in Table A.2 their Auger energies are quite a bit larger than the $2s2p^{3,1}P$ and therefore not a problem as in the case of carbon.

Table A.2: Same as Table A.1, but for oxygen. Auger energies computed from NIST recommended energy level values are listed in the last column.

	Experiment				Theory								
State	This work[1]	Mac87[2]	Bru87[3]	Kil90[4]	Bru87[3]	Ho81[5]	Aln02[6]	Kar09[7]	Gor17[8]	Yer17[9]	Man22[10]	Man22[11]	NIST[12]
$1s2s^2\,^2S$	412.3(7)	412.67(8)	412.7(2)	-	412.63	-	412.4	-	412.50	412.603	-	-	-
$1s2s2p\,^4P$	416.4(7)	416.08	416.0(2)	-	416.02	-	415.5	-	416.12	415.973	-	-	416.124
$1s2s2p\,^2P_-$	425.1(7)	424.81(8)	425.0(2)	-	424.99	-	424.4	-	424.91	424.945	-	-	424.474
$1s2s2p\,^2P_+$	428.8(7)	429.38(15)	429.6(2)	-	429.71	-	429.4	-	429.63	429.601	-	-	430.094
$1s2p^2\,^2D$	434.6(7)	434.31(8)	434.4(2)	-	434.38	-	434.6	-	434.49	434.313	-	-	434.382
$2s^2\,^1S$	461.5(7)	-	463(2)[13]	461.9(9)	462.3[13]	-	-	462.080	461.60	-	461.197	461.924	-
$2s2p\,^3P$	463.7(7)	-	466(2)[13]	463.9(1)	464.4[13]	464.25	463.3	-	463.78	-	463.677	464.002	464.029
$2p^2\,^1D$	473.8(7)	-	471[13]	474.1(1)	474.8[13]	-	-	474.145	473.86	-	474.583	474.143	474.275
$2s2p\,^1P$	474.7(7)	-	477(2)[13]	476.5(12)	476.0[14]	475.23	474.1	475.230	474.79	-	475.299	475.034	475.076
$2p^2\,^1S$	485.7(7)	-	-	485.8(1)	-	-	-	-	485.73	-	487.042	485.971	480.204
$(1s2s\,^3S)3s\,^2S$	500.3(7)	500.4(2)	-	-	500.5[13]	-	500.8	-	-	-	-	-	-
$(1s2s\,^3S)3p\,^2P$	501.8(7)	501.9(1)	-	-	502.7[13]	-	502.2	-	-	-	-	-	-
$(1s2s\,^3S)3d\,^2D$	505.5(7)	505.6(1)	-	-	506.1[13]	-	-	-	-	-	-	-	-
$(1s2s\,^1S)3s\,^2S$	-	-	-	-	506.2[13]	-	-	-	-	-	-	-	-
$(1s2s\,^1S)3p\,^2P$	-	-	-	-	509.9[13]	-	-	-	-	-	-	-	-
$(1s2s\,^1S)3d\,^2D$	-	-	-	-	512.7[13]	-	-	-	-	-	-	-	-

[1]Fitted Auger line peak energies after energy calibration of PSD channels according to the values Mack 1987 [179], listed in the 2nd column.
[2]Mack 1987 [179] - see Table A.1.
[3]Bruch et al. 1987 [192] - Zero-degree Auger projectile spectroscopy measurements and saddle-point technique [193, 194] with relativistic corrections.
[4]Kilgus et al. 1990 [195] - Dielectronic Recombination (DR) measurements at the Heidelberg Test Storage Ring (TSR).
[5]Ho 1981 [189] - complex rotation method.
[6]Alnaser 2002 [183] - see Table A.1.
[7]Kar and Ho 2009 [184] - Stabilization method: $2l2l'\,^1L$ levels in a.u.
[8]Goryaev et al. 2017 [71] - see Table A.1.
[9]Yerokhin et al. 2017 [185, 186] - see Table A.1.
[10]Manai et al [73] using FAC code - see Table A.1.
[11]Manai et al [73] using AMBiT code - see Table A.1.
[12]$\varepsilon_A(1s2l2l') = E(1s2l2l') - E(1s^2) + E(1s^22s)$ or $\varepsilon_A(2l2l') = E(2l2l') - E(1s) + E(1s^2)$, where $E(1s2l2l')$ and $E(2l2l')$ are the given NIST energies with respect to $1s^22s$ or $1s^2$, respectively [178].
[13]Bruch et al. 1979 [196] - 23.7° ESCA measurements and semiempirical + ab initio theoretical methods.

Appendix B

Auger transitions selection rules

In Table B.1 the Auger transitions selection rules are presented [10]. In Tables B.2, B.3 and B.4, the allowed Auger transitions together with the interaction mechanisms for the $2s2p\,^3P$, $2s2p\,^1P$ and $1s2p^2\,^2D$ are presented.

Table B.1: Selection rules for auto-ionization. ΔL, ΔS and ΔJ are the differences in total orbital angular momentum, total spin and total angular momentum between the initial and final states. α denotes the Sommerfield fine-structure constant, while m and M are the electron and proton masses , respectively. Table from Ref [10]

Interaction	ΔL	ΔS	ΔJ	Parity change	Relative transition rate
Coulomb	0	0	0	No	1
Spin-orbit	0,±1	0,±1,±2	0	No	α^4
Spin-other-orbit	0,±1	0,±1,±2	0	No	α^4
Spin-spin	0,±1,±2	0,±1,±2	0	No	α^4
Hyperfine	0,±1,±2	0,±1	0,±1	No	$\alpha^4(\mathrm{m}/\mathrm{M})^2$

Table B.2: Auger transitions for $2s2p\,^3P$

Initial state-i					Final state-f											Final - Initial				
Initial ion					Final ion				Auger electron			Total Ion + Auger								
i-state	Π	J	L	S	f-state	L_f	S_f	J_f	j	s	l	Π_f	J_f	L_f	S_f	$\Delta\Pi$	ΔJ	ΔL	ΔS	Interaction
$2s2p\,^3P_0$	-1	0	1	1	$1s\,^2S$	0	1/2	1/2	1/2	1/2	1	-1	0	1	1	0	0	0	0	Coulomb
$2s2p\,^3P_1$	-1	1	1	1	$1s\,^2S$	0	1/2	1/2	3/2	1/2	1	-1	1	1	1	0	0	0	0	Coulomb
$2s2p\,^3P_1$	-1	1	1	1	$1s\,^2S$	0	1/2	1/2	1/2	1/2	1	-1	1	1	1	0	0	0	0	Coulomb
$2s2p\,^3P_2$	-1	2	1	1	$1s\,^2S$	0	1/2	1/2	3/2	1/2	1	-1	2	1	1	0	0	0	0	Coulomb
$2s2p\,^3P_2$	-1	2	1	1	$1s\,^2S$	0	1/2	1/2	5/2	1/2	3	-1	2	3	1	0	0	2	0	spin-spin

Table B.3: Auger transitions for $2s2p\,^1P$

Initial state-i					Final state-f											Final - Initial				
Initial ion					Final ion				Auger electron			Total Ion + Auger								
i-state	Π	J	L	S	f-state	L_f	S_f	J_f	j	s	l	Π_f	J_f	L_f	S_f	$\Delta\Pi$	ΔJ	ΔL	ΔS	Interaction
$2s2p\,^1P_1$	-1	1	1	0	$1s\,^2S$	0	1/2	1/2	1/2	1/2	1	-1	1	1	0	0	0	0	0	Coulomb
$2s2p\,^1P_1$	-1	1	1	0	$1s\,^2S$	0	1/2	1/2	3/2	1/2	1	-1	1	1	0	0	0	0	0	Coulomb
$2s2p\,^1P_1$	-1	1	1	0	$1s\,^2S$	0	1/2	1/2	1/2	1/2	1	-1	1	1	1	0	0	0	1	spin-orbit
$2s2p\,^1P_1$	-1	1	1	0	$1s\,^2S$	0	1/2	1/2	3/2	1/2	1	-1	1	1	1	0	0	0	1	spin-orbit

Table B.4: Auger transitions for $1s2p^2\ ^2D$

Initial state-i					Final state-f											Final - Initial				
Initial ion					Final ion				Auger electron			Total Ion + Auger								
i-state	Π	J	L	S	f-state	L_f	S_f	J_f	j	s	l	Π_f	J_f	L_f	S_f	$\Delta\Pi$	ΔJ	ΔL	ΔS	Interaction
$1s2p^2\ ^2D_{3/2}$	1	3/2	2	1/2	$1s^2$	0	0	0	3/2	1/2	2	1	3/2	2	1/2	0	0	0	0	Coulomb
$1s2p^2\ ^2D_{3/2}$	1	3/2	2	1/2	$1s^2$	0	0	0	1/2	1/2	0	1	1/2	0	1/2	0	1	2	0	LSJ forbiden[1]
$1s2p^2\ ^2D_{3/2}$	1	3/2	2	1/2	$1s^2$	0	0	0	5/2	1/2	2	1	5/2	2	1/2	0	1	0	0	LSJ forbiden[1]
$1s2p^2\ ^2D_{5/2}$	1	5/2	2	1/2	$1s^2$	0	0	0	5/2	1/2	2	1	5/2	2	1/2	0	0	0	0	Coulomb
$1s2p^2\ ^2D_{5/2}$	1	5/2	2	1/2	$1s^2$	0	0	0	3/2	1/2	2	1	3/2	2	1/2	0	1	0	0	LSJ forbiden[1]

[1]Allowed only through hyperfine interaction.

Bibliography

[1] O. H. Dupac, Int. J. Mat. Res. (formerly Z. Metallkd.) **100**, 1162 (2009).

[2] M. O. Krause, J. Phys. Chem. Ref. Data **8**, 307 (1979).

[3] D. L. Matthews, *Ion-induced* A*uger electron spectroscopy* (Academic Press, New York, 1980), vol. 17 of *Methods of Experimental Physics*, pp. 433–527.

[4] M. Prost (1980).

[5] O. Sise, G. Martinez, I. Madesis, A. Laoutaris, A. Dimitriou, M. Fernandez-Martin, and T. J. M. Zouros, J. Electron Spectrosc. and Relat. Phenom. **211**, 19 (2016).

[6] O. Sise and T. J. M. Zouros, Journal of Spectroscopy **2015**, 20 (2015).

[7] E. P. Benis, M. Zamkov, P. Richard, and T. J. M. Zouros, Phys. Rev. A **65**, 064701 (2002).

[8] M. Zamkov, H. Aliabadi, E. P. Benis, P. Richard, H. Tawara, and T. J. M. Zouros, Phys. Rev. A **64**, 052702 (2001).

[9] T. J. M. Zouros, Comm. At. Mol. Phys. **32**, 291 (1996).

[10] P. Feldman and R. Novik, Phys. Rev. **160**, 143 (1967).

[11] A. Laoutaris, S. Nanos, I. Madesis, S. Passalidis, E. P. Benis, A. Dubois, and T. J. M. Zouros, Phys. Rev. A **106**, 022810 (2022).

[12] P. Auger, Compt. Rend. **177**, 169 (1923).

[13] P. Auger, Compt. Rend. **180**, 65 (1925).

[14] N. Stolterfoht, Phys. Rep. **146**, 315 (1987).

[15] S. Rosseland, Z. Phys. **14**, 173 (1923), first prediction of Auger process from Kopenhagen.

[16] H. R. Robinson, A. M. Cassie, and C. G. Barkla, Proceedings of the Royal Society of London. Series A, Containing Papers of a Mathematical and Physical Character **113**, 282 (1926).

[17] G. Wenzel, Physik **43**, 524 (1928).

[18] P. Burke (Elsevier, Amsterdam, Netherlands, 1968), vol. 4 of *Advances in Atomic and Molecular Physics*, pp. 173 – 219.

[19] W. N. Asaad and E. H. S. Burhop, Proc. Phys. Soc. **71**, 369 (1958).

[20] D. Chattarji, *Theory of* A*uger transitions* (Academic Press, London, 1976).

[21] E. McGuire, in *Atomic Inner-Shell Processes*, edited by B. Crasemann (Academic Press, 1975), pp. 293–330.

[22] T. Åberg and J. Utriainen, Phys. Rev. Lett. **22**, 1346 (1969).

[23] T. Åberg and G. Howat, *Handbuch der Physik*, vol. 31 (Springer Verlag, Berlin, 1982), s. fhigge and w. mehlhorn ed.

[24] M. E. Rudd, Phys. Rev. Lett. **13**, 503 (1964).

[25] M. E. Rudd, Phys. Rev. Lett. **15**, 580 (1965).

[26] N. Stolterfoht, in *Topics in Current Physics, Vol. 5: Structure and Collisions of Ions and Atoms*, edited by I. A. Sellin (Springer Verlag, Berlin, 1978), pp. 155–200.

[27] D. Berényi, Adv. Electr. and Electron Phys. **56**, 411 (1981).

[28] M. E. Rudd, T. V. Goffe, A. Itoh, and R. D. DuBois, Phys. Rev. A **32**, 829 (1985).

[29] A. Itoh, T. Schneider, G. Schiwietz, Z. Roller, H. Platten, G. Nolte, D. Schneider, and N. Stolterfoht, J. Phys. B **16**, 3965 (1983).

[30] A. Itoh and N. Stolterfoht, Nuclear Instruments and Methods in Physics Research Section B: Beam Interactions with Materials and Atoms **10-11**, 97 (1985).

[31] A. Itoh, D. Schneider, T. Schneider, T. J. M. Zouros, G. Nolte, G. Schiwietz, W. Zeitz, and N. Stolterfoht, Phys. Rev. A **31**, 684 (1985).

[32] A. Itoh, T. J. M. Zouros, D. Schneider, U. Stettner, W. Zeitz, and N. Stolterfoht, J. Phys. B **18**, 4581 (1985).

[33] T. J. M. Zouros and D. H. Lee, in *Accelerator-Based Atomic Physics: Techniques and Applications*, edited by S. M. Shafroth and J. C. Austin (AIP, Woodbury, NY, 1997), chap. 13, pp. 426–479.

[34] J. A. Tanis, S. M. Shafroth, J. E. Willis, M. Clark, J. Swenson, E. N. Strait, and J. R. Mowat, Phys. Rev. Lett. **47**, 828 (1981).

[35] A. Burgess, ApJ. **139**, 776 (1964).

[36] A. Burgess, ApJ. **141**, 1588 (1965).

[37] C. L. Cocke and E. C. Montenegro, Comm. At. Mol. Phys. **32**, 131 (1996).

[38] J. A. Tanis, E. M. Bernstein, W. G. Graham, M. Clark, S. M. Shafroth, B. M. Johnson, K. W. Jones, and M. Meron, Phys. Rev. Lett. **49**, 1325 (1982).

[39] J. K. Swenson, Y. Yamazaki, P. D. Miller, H. F. Krause, P. F. Dittner, P. L. Pepmiller, S. Datz, and N. Stolterfoht, Phys. Rev. Lett. **57**, 3042 (1986).

[40] T. J. M. Zouros, D. H. Lee, P. Richard, J. M. Sanders, J. L. Shinpaugh, S. L. Varghese, K. R. Karim, and C. P. Bhalla, Phys. Rev. A **40**, 6246 (1989).

[41] D. Brandt, Phys. Rev. A **27**, 1314 (1983).

[42] E. P. Benis, T. J. M. Zouros, T. W. Gorczyca, A. D. González, and P. Richard, Phys. Rev. A **73**, 029901(E) (2006).

[43] W. Fritsch and C. D. Lin, Phys. Rev. Lett. **61**, 690 (1988).

[44] A. Jain, R. Shingal, and T. J. M. Zouros, Phys. Rev. A **43**, 1621 (1991).

[45] J. M. Feagin, J. S. Briggs, and T. M. Reeves, J. Phys. B **17**, 1057 (1984).

[46] M. Benhenni, S. M. Shafroth, J. K. Swenson, M. Schulz, J. P. Giese, H. Schöne, C. R. Vane, P. F. Dittner, and S. Datz, Phys. Rev. Lett. **65**, 1849 (1990).

[47] D. K. W. M. J. F. J. F. M A Bennett, P A Smith and J. F. Williams, Rev. Sci. Instrum. **63**, 1922 (1992).

[48] M. Benhenni, S. M. Shafroth, and J. K. Swenson, Nucl. Instrum. Methods Phys. Res. Sect. B **86**, 28 (1994).

[49] M. Ourdane, H. Bachau, R. Gayet, and J. Hanssen, J. Phys. B **32**, 2041 (1999).

[50] I. Bray, H. Hayat, D. V. Fursa, A. S. Kadyrov, A. W. Bray, and M. Cytowski, Phys. Rev. A **101**, 022703 (2020).

[51] A. Müller, Adv. At. Mol. & Opt. Phys. **55**, 293 (2008).

[52] A. C. K. Leung and T. Kirchner, Eur. Phys. J. D **73**, 246 (2019).

[53] K. H. Spicer, C. T. Plowman, I. B. Abdurakhmanov, A. S. Kadyrov, I. Bray, and S. U. Alladustov, Phys. Rev. A **104**, 032818 (2021).

[54] J. Faulkner, I. B. Abdurakhmanov, S. U. Alladustov, A. S. Kadyrov, and I. Bray, Plasma Physics and Controlled Fusion **61**, 095005 (2019).

[55] T. J. M. Zouros, K. L. Wong, S. Grabbe, H. I. Hidmi, P. Richard, E. C. Montenegro, J. M. Sanders, C. Liao, S. Hagmann, and C. P. Bhalla, Phys. Rev. A **53**, 2272 (1996).

[56] M. E. Rudd, T. Jorgensen, and D. J. Volz, Phys. Rev. Lett. **16**, 929 (1966).

[57] D. J. Pegg, *Radiative and* A*uger beam-foil measurements* (Academic Press, New York, 1980), vol. 17 of *Methods of Experimental Physics*, pp. 529–606.

[58] I. A. Sellin, in *Topics in Current Physics*, edited by S. Bashkin (Springer, Heidelberg, 1976), vol. 1, p. 265.

[59] E. P. Benis, Ph.D. dissertation, Dept. of Physics, University of Crete (2001), (unpublished).

[60] N. Stolterfoht, D. Schneider, D. Burch, B. Aagaard, E. Bøving, and B. Fastrup, Phys. Rev. A **12**, 1313 (1975).

[61] M. W. Lucas and K. G. Harrison, J. Phys. B **5**, L20 (1972).

[62] G. B. Crooks and M. E. Rudd, Phys. Rev. Lett. **25**, 1599 (1970).

[63] K. G. Harrison and M. W. Lucas, Phys. Lett. **33A**, 142 (1970).

[64] K. Dettmann, K. G. Harrison, and M. W. Lucas, J. Phys. B **7**, 269 (1974).

[65] P. Bisgaard, P. Dahl, B. Fastrup, and W. Mehlhorn, J. Phys. B **14**, 2023 (1981).

[66] E. P. Benis, K. Zaharakis, M. M. Voultsidou, T. J. M. Zouros, M. Stöckli, P. Richard, and S. Hagmann, Nucl. Instrum. Methods Phys. Res. B **146**, 120 (1998).

[67] D. H. Lee, T. J. M. Zouros, J. M. Sanders, J. L. Shinpaugh, T. N. Tipping, S. L. Varghese, B. D. DePaola, and P. Richard, Nucl. Instrum. Methods Phys. Res. Sect. B **40-41**, 1229 (1989).

[68] E. P. Benis, T. J. M. Zouros, H. Aliabadi, and P. Richard, Phys. Scr. **T80B**, 529 (1999).

[69] I. Madesis, A. Laoutaris, T. J. M. Zouros, S. Nanos, and E. P. Benis, in *State-of-the-Art Reviews on Energetic Ion-Atom and Ion-Molecule Collisions*, edited by D. Belkić, I. Bray, and A. Kadyrov (World Scientific, Singapore, 2019), vol. 2 of *Interdisciplinary Research on Particle Collisions and Quantitative Spectroscopy*, chap. 1, pp. 1–31.

[70] U. I. Safronova and R. Bruch, Phys. Scr. **50**, 45 (1994).

[71] F. F. Goryaev, L. A. Vainshtein, and A. M. Urnov, At. Data & Nucl. Data Tables **113**, 117 (2017).

[72] M. H. Chen, At. Data & Nucl. Data Tables **34**, 301 (1986).

[73] S. Manai, D. E. Salhi, S. B. Nasr, and H. Jelassi, Results in Phys. **37**, 105487 (2022).

[74] S. Doukas, I. Madesis, A. Dimitriou, A. Laoutaris, T. J. M. Zouros, and E. P. Benis, Rev. Sci. Instrum. **86**, 043111 (2015).

[75] M. Rødbro, R. Bruch, and P. Bisgaard, J. Phys. B **12**, 2413 (1979).

[76] P. Hvelplund, Phys. Rev. A **11**, 1921 (1975).

[77] T. J. M. Zouros, D. Schneider, and N. Stolterfoht, Nucl. Instrum. Methods Phys. Res. Sect. B **31**, 349 (1988).

[78] Nuclear Instruments and Methods in Physics Research Section B: Beam Interactions with Materials and Atoms **541**, 93 (2023).

[79] T. J. M. Zouros, S. Nikolaou, I. Madesis, A. Laoutaris, S. Nanos, A. Dubois, and E. P. Benis, Atoms **8**, 61 (2020).

[80] E. P. Benis, S. Doukas, T. J. M. Zouros, P. Indelicato, F. Parente, C. Martins, J. P. Santos, and J. P. Marques, Nucl. Instrum. Methods Phys. Res. Sect. B **365**, 457 (2015).

[81] S. Harissopulos, M. Andrianis, M. Axiotis, A. Lagoyannis, A. G. Karydas, Z. Kotsina, A. Laoutaris, G. Apostolopoulos, A. Theodorou, T. J. M. Zouros, et al., Eur. Phys. J. Plus **136**, 617 (2021).

[82] I. Madesis, A. Dimitriou, A. Laoutaris, A. Lagoyannis, M. Axiotis, T. Mertzimekis, M. Andrianis, S. Harissopulos, E. P. Benis, B. Sulik, et al., J. Phys: Conf. Ser. **583**, 012014 (2015).

[83] A. Dimitriou, A. Laoutaris, I. Madesis, S. Doukas, E. P. Benis, B. Sulik, O. Sise, A. Lagoyannis, M. Axiotis, and T. J. M. Zouros, J. Atom. Mol. Cond. Nano Phys. **3**, 125 (2016).

[84] A. Laoutaris, M.Sc. dissertation, Dept. of Physics, National Technical University of Athens (2015), (unpublished).

[85] I. Madesis, Ph.D. thesis, University of Crete, Department of Physics, Heraklion, Greece (2021).

[86] T. J. M. Zouros and E. P. Benis, J. Electron Spectrosc. and Relat. Phenom. **125**, 221 (2002).

[87] D. A. Dahl, J. E. Delmore, and A. D. Appelhans, Rev. Sci. Instrum. **61**, 607 (1990).

[88] M. Dogan, M. Ulu, G. G. Gennarakis, and T. J. M. Zouros, Rev. Sci. Instrum. **84**, 043105 (2013).

[89] E. P. Benis and T. J. M. Zouros, J. Electron Spectrosc. and Relat. Phenom. **163**, 28 (2008).

[90] G. Martínez, M. Fernández-Martín, O. Sise, I. Madesis, A. Dimitriou, A. Laoutaris, and T. Zouros, Nucl. Instrum. Methods Phys. Res. B **369**, 92 (2016).

[91] J. Ladislas Wiza, Nuclear Instruments and Methods **162**, 587 (1979).

[92] R. L. Lucke, Review of Scientific Instruments **47**, 766 (1976).

[93] C. W. Woods, R. L. Kauffman, K. A. Jamison, N. Stolterfoht, and P. Richard, Phys. Rev. A **13**, 1358 (1976).

[94] E. P. Benis, I. Madesis, A. Laoutaris, S. Nanos, and T. J. M. Zouros, Atoms **6**, 66 (2018).

[95] H.-D. Betz, Rev. Mod. Phys. **44**, 465 (1972).

[96] R. Sayer, Rev. Phys. Appl. (Paris) **12**, 1543 (1977).

[97] J. Rozet, C. Stéphan, and D. Vernhet, Nucl. Instrum. Methods Phys. Res. Sect. B **107**, 67 (1996).

[98] V. N. I.S. Dmitriev, Soviet Physics J.Exptl. Theoret. Phys. (U.S.S.R) **20**, 409 (1965).

[99] K. Shima, N. Kuno, M. Yamanouchi, and H. Tawara, At. Data & Nucl. Data Tables **51**, 173 (1992).

[100] G. Schiwietz, E. Luderer, G. Xiao, and P. Grande, Nucl. Instrum. Methods Phys. Res. Sect. B **175-177**, 1 (2001), twelfth International Conference of Ion Beam Modification of Materials.

[101] E.-M. Asimakopoulou, Technical Report, Institute of Nuclear and Particle Physics, Demokritos and Department of Physics, University of Athens (2014).

[102] G. W. F. Drake, G. A. Victor, and A. Dalgarno, Phys. Rev. **180**, 25 (1969).

[103] G. W. F. Drake, Phys. Rev. A **3**, 908 (1971).

[104] B. R. Turner, J. A. Rutherford, and D. M. J. Compton, J. Chem. Phys. **48**, 1602 (1968).

[105] U. Schiebel, B. L. Doyle, J. R. Macdonald, and L. D. Ellsworth, Phys. Rev. A **16**, 1089 (1977).

[106] E. H. Pedersen, Phys. Rev. Lett. **42**, 440 (1979).

[107] F. W. Meyer, C. C. Havener, K. J. Snowdown, S. H. Overbury, and D. M. Zehner, Phys. Rev. A **35**, 3176 (1987).

[108] R. F. Welton, T. F. Moran, and E. W. Thomas, J. Phys. B **24**, 3815 (1991).

[109] F. W. Bliek, R. Hoekstra, M. E. Bannister, and C. C. Havener, Phys. Rev. A **56**, 426 (1997).

[110] C. L. Cocke, S. L. Varghese, and B. Curnutte, Phys. Rev. A **15**, 874 (1977).

[111] D. H. Lee, T. J. M. Zouros, J. M. Sanders, P. Richard, J. M. Anthony, Y. D. Wang, and J. H. McGuire, Phys. Rev. A **46**, 1374 (1992).

[112] E. P. Benis and T. J. M. Zouros, J. Phys. B **49**, 235202 (2016).

[113] S. S. Hodgman, R. G. Dall, L. J. Byron, K. G. H. Baldwin, S. J. Buckman, and A. G. Truscott, Phys. Rev. Lett. **103**, 053002 (2009).

[114] R. D. Knight and M. H. Prior, Phys. Rev. A **21**, 179 (1980).

[115] D. Fischer, B. Feuerstein, R. D. DuBois, R. Moshammer, J. R. C. Lopez-Urrutia, I. Draganic, H. Lorch, A. N. Perumal, and J. Ullrich, J. Phys. B **35**, 1369 (2002).

[116] A. A. Saghiri, J. Linkemann, M. Schmitt, D. Schwalm, A. Wolf, T. Bartsch, A. Hoffknecht, A. Muller, W. G. Graham, A. D. Price, et al., Phys. Rev. A **60**, R3350 (1999).

[117] H. T. Schmidt, P. Forck, M. Grieser, D. Habs, J. Kenntner, G. Miersch, R. Repnow, U. Schramm, T. Schüssler, D. Schwalm, et al., Phys. Rev. Lett. **72**, 1616 (1994).

[118] P. A. Neill, E. Träbert, P. Beiersdorfer, G. V. Brown, C. L. Harris, S. B. Utter, and K. L. Wong, Phys. Scr. **62**, 141 (2000).

[119] J. R. Crespo López-Urrutia, P. Beiersdorfer, D. W. Savin, and K. Widmann, Phys. Rev. A **58**, 238 (1998).

[120] E. Träbert, A. Wolf, J. Linkemann, and X. Tordoir, J. Phys. B **32**, 537 (1999).

[121] E. Träbert, G. Gwinner, E. J. Knystautas, and A. Wolf, Can. J. Phys. **81**, 941 (2003).

[122] C. D. Lin, W. R. Johnson, and A. Dalgarno, Phys. Rev. A **15**, 154 (1977).

[123] C. D. Lin and W. R. Johnson, Phys. Rev. A **15**, 1046 (1977).

[124] A. S. Pearl, Phys. Rev. Lett. **24**, 703 (1970).

[125] R. S. Van Dyck, C. E. Johnson, and H. A. Shugart, Phys. Rev. A **4**, 1327 (1971).

[126] M. H. Prior and H. A. Shugart, Phys. Rev. Lett. **27**, 902 (1971).

[127] T. J. M. Zouros, in *Recombination of Atomic Ions*, edited by W. G. Graham, W. Fritsch, Y. Hahn, and J. Tanis, NATO Advanced Study Institute Series B: Physics (Plenum Publishing Corporation, New York, 1992), vol. 296, pp. 271–300.

[128] E. P. Benis, I. Madesis, A. Laoutaris, S. Nikolaou, A. Dubois, T. W. Gorczyca, and T. J. M. Zouros, X-Ray Spectrom. **49**, 54 (2020).

[129] I. Madesis, A. Laoutaris, S. Nanos, S. Passalidis, A. Dubois, T. J. M. Zouros, and E. P. Benis, Phys. Rev. A **105**, 062810 (2022).

[130] N. Sisourat and A. Dubois, in *Ion-Atom Collision - The Few-Body Problem in Dynamic Systems*, edited by M. Schultz (de Gruyter, Berlin/Boston, 2019), pp. 157–178.

[131] S. Passalidis, Ph.D. thesis (2022), thèse de doctorat dirigée par Dubois, Alain Chimie physique Sorbonne université 2022.

[132] J. W. Gao, Y. Wu, J. G. Wang, N. Sisourat, and A. Dubois, Phys. Rev. A **97**, 052709 (2018).

[133] L. F. Shampine and M. K. Gordon, *Computer Solution of Ordinary Differential Equations: The Initial Value Problem* (W. H. Freeman, San Francisco, 1975).

[134] A. Laoutaris, S. Nanos, A. Biniskos, S. Passalidis, E. P. Benis, A. Dubois, and T. J. M. Zouros, Phys. Rev. A **109**, 032825 (2024).

[135] W. Mehlhorn, *Electron spectrometry of* A*uger and autoionizing states: Experiment and Theory*, Univ. of Aarhus summer lecture notes (unpublished) (1978).

[136] B. Cleff and W. Mehlhorn, J. Phys. B **7**, 593 (1974).

[137] B. Cleff and W. Mehlhorn, J. Phys. B **7**, 605 (1974).

[138] W. Mehlhorn and K. Taulbjerg, J. Phys. B **13**, 445 (1980).

[139] T. J. M. Zouros, in *Applications of Particle and Laser Beams in Materials Technology*, edited by P. Misailides, NATO Advanced Study Institute Series E: Applied Sciences (Kluwer Academic Publishers, Netherlands, 1995), vol. 283, pp. 37–52.

[140] N. Stolterfoht, Nucl. Instrum. Methods Phys. Res. Sect. B **53**, 477 (1991).

[141] M. Clark, D. Brandt, J. K. Swenson, and S. M. Shafroth, Phys. Rev. Lett. **54**, 544 (1985).

[142] J. A. Tanis, E. M. Bernstein, M. W. Clark, W. G. Graham, R. H. McFarland, T. J. Morgan, B. M. Johnson, K. W. Jones, and M. Meron, Phys. Rev. A **31**, 4040 (1985).

[143] T. J. M. Zouros, E. P. Benis, A. González, T. G. Lee, P. Richard, and T. Gorczyca, in *Proceedings of CAARI 2002* (AIP Press, Melville, NY, 2003), vol. 680, pp. 24–27.

[144] J. A. Tanis, in *Recombination of Atomic Ions*, edited by W. G. Graham, W. Fritsch, Y. Hahn, and J. Tanis, NATO Advanced Study Institute Series B: Physics (Plenum Publishing Corporation, New York, 1992), vol. 296, pp. 241–257.

[145] P. L. Pepmiller, P. Richard, J. Newcomb, J. Hall, and T. R. Dillingham, Phys. Rev. A **31**, 734 (1985).

[146] E. P. Benis, T. J. M. Zouros, T. W. Gorczyca, A. D. González, and P. Richard, Phys. Rev. A **69**, 052718 (2004), Erratum, Phys. Rev. A **73**, 029901 (2006).

[147] M. Benhenni, S. M. Shafroth, J. K. Swenson, M. Schulz, J. Giese, H. Schone, C. Vane, P. F. Dittner, and S. Datz, in *Proceedings of the XVII ICPEAC held in Brisbane, Australia, 10-16 July 1991*, edited by M. S. W.R. McGillivray, I.E. McCarthy, 17th Int. Conf. on the Physics of Electronic and Atomic Collisions (Adam Hilger, Bristol [England], Philadelphia, 1992), pp. 693–698, invited paper.

[148] J. M. Anthony, S. M. Shafroth, M. Benhenni, E. N. Strait, T. J. M. Zouros, L. D. Hendrik, and D. M. Peterson, J. de Phys. (Paris) **48**, 301 (1987).

[149] R. A. Holt, M. H. Prior, K. L. Randall, R. Hutton, J. McDonald, and D. Schneider, Phys. Rev. A **43**, 607 (1991).

[150] T. J. M. Zouros, C. P. Bhalla, D. H. Lee, and P. Richard, Phys. Rev. A **42**, 678 (1990).

[151] A. Laoutaris, S. Nanos, I. Madesis, A. Biniskos, E.P. Benis, S. Passalidis, A. Dubois, and T. J. M. Zouros, Phys. Rev. A (2023), (in preparation).

[152] I. Madesis, A. Laoutaris, T. J. M. Zouros, E. P. Benis, J. W. Gao, and A. Dubois, Phys. Rev. Lett. **124**, 113401 (2020), and Supplemental Material.

[153] J. L. Fox and A. Dalgarno, Phys. Rev. A **16**, 283 (1977).

[154] C. A. Nicolaides and D. R. Beck, Phys. Rev. A **17**, 2116 (1978).

[155] D. Brandt, Nucl. Instrum. Methods **214**, 93 (1983).

[156] D. H. Lee, P. Richard, J. M. Sanders, T. J. M. Zouros, J. L. Shinpaugh, and S. L. Varghese, Nucl. Instrum. Methods Phys. Res. Sect. B **56-57**, 99 (1991).

[157] D. H. Lee, P. Richard, J. M. Sanders, T. J. M. Zouros, J. L. Shinpaugh, and S. L. Varghese, Phys. Rev. A **44**, 1636 (1991).

[158] U. Thumm, J. S. Briggs, and O. Schöller, J. Phys. B **21**, 833 (1988).

[159] N. R. Badnell, Phys. Rev. A **40**, 3579 (1989).

[160] T. J. M. Zouros, D. H. Lee, and P. Richard, Phys. Rev. Lett. **62**, 2261 (1989).

[161] T. J. M. Zouros, D. H. Lee, P. Richard, and J. M. Sanders, Nucl. Instrum. Methods Phys. Res. Sect. B **56/57**, 107 (1991).

[162] T. J. M. Zouros, D. H. Lee, J. M. Sanders, and P. Richard, Nucl. Instrum. Methods Phys. Res. Sect. B **79**, 166 (1993).

[163] J. H. McGuire, N. Stolterfoht, and P. R. Simony, Phys. Rev. A **24**, 97 (1981).

[164] N. Stolterfoht, Phys. Scr. **42**, 192 (1990).

[165] D. R. Bates and G. Griffing, Proc. Phys. Soc. Sect. A **67**, 663 (1954).

[166] D. R. Bates and G. Griffing, Proc. Phys. Soc. Sect. A **66**, 961 (1953).

[167] D. R. Bates and G. Griffing, Proc. Phys. Soc. Sect. A **68**, 90 (1955).

[168] J. S. Lee, J. Chem. Phys. **66**, 4906 (1977).

[169] E. C. Montenegro, W. S. Melo, W. E. Meyerhof, and A. G. de Pinho, Phys. Rev. Lett. **69**, 3033 (1992).

[170] N. Sisourat, I. Pilskog, and A. Dubois, Phys. Rev. A **84**, 052722 (2011).

[171] M. H. Chen, Phys. Rev. A **45**, 1684 (1992).

[172] S. Fritzsche, A. Surzhykov, A. Gumberidze, and T. Stöhlker, New J. Phys. **14**, 083018 (2012).

[173] N. M. Kabachnik, J. Tulkki, H. Aksela, and S. Ricz, Phys. Rev. A **49**, 4653 (1994).

[174] A. Müller, E. Lindroth, S. Bari, A. Borovik, P.-M. Hillenbrand, K. Holste, P. Indelicato, A. L. D. Kilcoyne, S. Klumpp, M. Martins, et al., Phys. Rev. A **98**, 033416 (2018).

[175] H. W. van der Hart and J. E. Hansen, J. Phys. B **26**, 641 (1993).

[176] R. Doerner, V. Mergel, O. Jagutzki, L. Spielberger, J. Ullrich, R. Moshammer, and H. Schmidt-Böcking, Phys. Rep. **330**, 95 (2000).

[177] R. Bruch, K. T. Chung, W. L. Luken, and J. C. Culberson, Phys. Rev. A **31**, 310 (1985).

[178] A. Kramida, Y. Ralchenko, J. Reader, and NIST ASD Team, NIST Atomic Spectra Database (ver. 5.9), [Online]. Available: `https://physics.nist.gov/asd` [2022, August 9]. National Institute of Standards and Technology, Gaithersburg, MD. (2021).

[179] M. Mack and A. Niehaus, Nucl. Instrum. Methods Phys. Res. Sect. B **23**, 291 (1987).

[180] K. T. Chung, Phys. Rev. A **29**, 682 (1984).

[181] R. Mann, Phys. Rev. A **35**, 4988 (1987).

[182] G. Kilgus, D. Habs, D. Schwalm, A. Wolf, R. Schuch, and N. R. Badnell, Phys. Rev. A **47**, 4859 (1993).

[183] A. S. Alnaser, Ph.D. thesis, Western Michigan University, Kalamazoo (2002), unpublished.

[184] S. Kar and Y. K. Ho, J. Phys. B **42**, 044007 (2009).

[185] V. A. Yerokhin, A. Surzhykov, and A. Müller, Phys. Rev. A **96**, 042505 (2017).

[186] V. A. Yerokhin, A. Surzhykov, and A. Müller, Phys. Rev. A **96**, 069901 (2017).

[187] M. F. Gu, Can. J. Phys. **86**, 675 (2008).

[188] E. Kahl and J. Berengut, Comp. Phys. Com. **238**, 232 (2019).

[189] Y. K. Ho, Phys. Rev. A **23**, 2137 (1981).

[190] E. M. Mack, Ph.D. thesis, Rijksuniversiteit te Utrecht (1987).

[191] N. J. Peacock, M. G. Hobby, and M. Galanti, J. Phys. B **6**, L298 (1973).

[192] R. Bruch, N. Stolterfoht, S. Datz, P. D. Miller, P. L. Pepmiller, Y. Yamazaki, H. F. Krause, and J. K. Swenson, Phys. Rev. A **35**, 4114 (1987).

[193] B. F. Davis and K. T. Chung, Phys. Rev. A **29**, 2586 (1984).

[194] K. T. Chung and B. F. Davis, Phys. Rev. A **29**, 1871 (1984).

[195] G. Kilgus, J. Berger, P. Blatt, M. Grieser, D. Habs, B. Hochadel, E. Jaeschke, D. Krämer, R. Neumann, G. Neureither, et al., Phys. Rev. Lett. **64**, 737 (1990).

[196] R. Bruch, D. Schneider, W. H. E. Schwarz, M. Meinhart, B. M. Johnson, and K. Taulbjerg, Phys. Rev. A **19**, 587 (1979).

[197] M. Ahmed and L. Lipsky, Phys. Rev. A **12**, 1176 (1975).

Dissemination

Ph.D. Publications

1. Projectile excitation to autoionizing states in swift collisions of open-shell He-like ions with helium, A. Laoutaris, S. Nanos, A. Biniskos, E.P. Benis, S. Passalidis, A. Dubois and T. J. M. Zouros, Phys. Rev. A109 (2024) 032825. https://journals.aps.org/pra/abstract/10.1103/PhysRevA.109.032825.

2. Coherent treatment of transfer-excitation processes in swift ion-atom collisions, A. Laoutaris, S. Nanos, I. Madesis, S. Passalidis, E.P. Benis, A. Dubois and T. J. M. Zouros, Phys. Rev. A 106 (2022) 022810. https://journals.aps.org/pra/abstract/10.1103/PhysRevA.106.022810.

Closely Related Publications

1. Cusp-electron production in collisions of open-shell He-like oxygen ions with atomic targets, S. Nanos, N. J. Esponda, P.-M. Hillenbrand, A. Biniskos, A. Laoutaris, M. A. Quinto, N. Petridis, E. Menz, T. J. M. Zouros, T. Stölker, R. D. Rivarola, J. M. Monti and E.P. Benis, Phys. Rev. A107 (2023) 062815. https://journals.aps.org/pra/abstract/10.1103/PhysRevA.107.062815.

2. Determination of the ion beam energy width in tandem Van de Graaff accelerators via Auger projectile spectroscopy, S. Nanos, A. Biniskos, A. Laoutaris, M. Andrianis, T.J.M. Zouros, A. Lagoyannis and E.P. Benis, Nucl. Instrum. Methods Phys. Res. Sect. B541 (2023) 93. https://ui.adsabs.harvard.edu/abs/2023NIMPB.541...93N/abstract.

3. State-resolved differential cross sections of single-electron capture in swift collisions of $C^{4+}(1s2s\,^3S)$ ions with gas targets, I. Madesis, A. Laoutaris, S. Nanos, S. Passalidis, A. Dubois, T. J. M. Zouros and E.P. Benis, Phys. Rev. A 105 (2022) 062810. https://journals.aps.org/pra/abstract/10.1103/PhysRevA.105.062810.

4. Subshell contributions to electron capture into the continuum in MeV/u collisions of deuterons with multielectron targets, S. Nanos, M. A. Quinto, I. Madesis, A. Laoutaris, T. J. M. Zouros, R. D. Rivarola, J. M. Monti, E.P.

Benis, Phys. Rev. A 105 (2022) 022806.
https://journals.aps.org/pra/abstract/10.1103/PhysRevA.105.022806.

5. The Tandem Accelerator Laboratory of NCSR "Demokritos": Current status and perspectives, S. Harissopulos, M. Andrianis, M Axiotis, A. Lagoyannis, A.G. Karydas, Z. Kotsina, A. Laoutaris, G. Apostolopoulos, A. Theodorou, T. J. M. Zouros, I. Madesis, E. P. Benis, Eur. Phys. J. Plus 136 (2021) 617.
https://link.springer.com/article/10.1140/epjp/s13360-021-01596-5.

6. Radiative cascade repopulation of $1s2s2p\,^4P$ states formed by single electron capture in 2-18 MeV collisions of $C^{4+}(1s2s\,^3S)$ with He, T. J. M. Zouros, S. Nikolaou, I. Madesis, A. Laoutaris, S. Nanos, A. Dubois, E. P. Benis, Atoms 8 (2020) 61.
https://www.mdpi.com/2218-2004/8/3/61.

7. Pauli shielding and break-down of spin statistics in multi-electron, multi-open-shell dynamical atomic systems, I. Madesis, A. Laoutaris, T. J. M. Zouros, E. P. Benis, J.W. Gao, A. Dubois, Phys. Rev. Lett. 124 (2020) 113401.
https://journals.aps.org/prl/abstract/10.1103/PhysRevLett.124.113401.

8. Population of the $1s2s(^3\mathrm{S})\mathrm{nl}\ ^2\mathrm{L}$ states in collisions of mixed-state ($1s^2\ ^1S$, $1s2s\,^3S$) B^{3+} and C^{4+} ion beams with He and H_2 targets, E. P. Benis, I. Madesis, A. Laoutaris, S. K. Nikolaou, A. Dubois, T. W. Gorczyca, T. J. M. Zouros, X-Ray Spectrometry 49 (2020) 54-59.
https://hal.science/hal-03963650v1.

9. Projectile electron spectroscopy and new answers to old questions. Latest results at the new atomic physics beamline in Demokritos, Athens, I. Madesis, A. Laoutaris, T.J.M. Zouros, S. Nanos, E.P. Benis, in State-of-the-Art Reviews on Energetic Ion-Atom and Ion-Molecule Collisions, Interdisciplinary Research on Particle Collisions and Quantitative Spectroscopy, Vol. 2, edited by D. Belkic, I. Bray, and A. Kadyrov (World Scientic, 2019).
https://doi.org/10.1142/9789811211614_ 0001.

10. Experimental determination of the effective solid angle of long-lived projectile states in zero-degree Auger projectile spectroscopy, E.P. Benis, I. Madesis, A. Laoutaris, S. Nanos, T.J.M. Zouros, Journal of Electron Spectroscopy and Related Phenomena 222 (2018) 31.
https://www.sciencedirect.com/science/article/pii/S0368204817301792.

11. Mixed-State Ionic Beams: An Effective Tool For Collision Dynamics Investigations, E.P. Benis, I. Madesis, A. Laoutaris, S. Nanos, T.J.M. Zouros, Atoms 6 (2018) 66.
https://www.mdpi.com/2218-2004/6/4/66.

12. Voltage optimization of a 4-element Injection Lens on a hemispherical spectrograph with virtual entry aperture, G. Martinez, M. Fernandez-Martin, O. Sise, I. Madesis, A. Dimitriou, A. Laoutaris and T.J.M. Zouros, Nuclear Instruments and Methods in Physics Research B 369 (2016) 92-94.
https://www.sciencedirect.com/science/article/pii/S0168583X15009891.

13. The voltage optimization of a four-element lens used on a hemispherical spectrograph with virtual entry for highest energy resolution, O. Sise, G. Martinez, I. Madesis, A. Laoutaris, A. Dimitriou, M. Fernandez-Martin and T.J.M. Zouros, Journal of Electron Spectroscopy and Related Phenomena 211 (2016) 19-31.
https://www.sciencedirect.com/science/article/pii/S0368204816300573.

14. High Resolution Auger Projectile Electron Spectroscopy of Li-like Ions Produced by Electron Capture in collision of He-like ions with Gaseous targets, A. Dimitriou, A. Laoutaris, I. Madesis, S. Doukas, E. P. Benis, B. Sulik, O. Sise, A. Lagoyannis, M. Axiotis, T. J. M. Zouros, Journal of Atomic, Molecular, Condensate and Nano Physics, Vol.3, No. 2, 125-131 (2016).
https://www.rgnpublications.com/journals/index.php/jamcnp/article/view/523.

15. Determination of the solid angle and response function of a hemispherical spectrograph with injection lens for Auger electrons emitted from long lived projectile states, S. Doukas, I. Madesis, A. Dimitriou, A. Laoutaris, T. J. M. Zouros and E. P. Benis, Review of Scientific Instruments 86 (2015) 043111.
https://pubs.aip.org/aip/rsi/article/86/4/043111/360584/Determination-of-the-solid-angle-and-response.

16. Evaluation of the effective solid angle of a hemispherical deflector analyser with injection lens for metastable Auger projectile states, E.P. Benis, S. Doukas, I. Madesis, A. Dimitriou, A. Laoutaris, T.J.M. Zouros, F. Parente, C. Martins, J. P. Marques and J. P. Santos, Nuclear Instruments and Methods in Physics Research 365B (2015) 457-461.
https://www.sciencedirect.com/science/article/pii/S0168583X15005844.